الجمهورية الجزائرية الديمقراطية الشعبية
MINISTERE DE L'ENSEIGNEMENT SUPERIEUR ET DE LA RECHERCHE SCIENTIFIQUE UNIVERSITE SETIF-1 FERHAT ABBAS FACULTE DES SCIENCES
DEPARTEMENT DE CHIMIE

THÈSE

Présentée par

M^me^ Wafa LAMIRI

En vue de l'obtention du diplôme de

DOCTORAT LMD

Option **: Chimie physique**

THEME

Elaboration, characterization and multiple properties Of new complexes based on 5-bromosalicylaldehyde

Soutenue le : 18/11/2024
Devant le jury composé de :

ISSAADI Saïfi	Professeur	Université. Ferhat Abbas Sétif-1	Président
BENGHANEM Fatiha	Professeur	Université. Ferhat Abbas Sétif-1	Examinatrice
BENAHMED Merzoug	Professeur	Université. Larbi Ben M'Hidi OEB	Examinateur
MESSASMA Zakia	MCA	Université. Ferhat Abbas Sétif-1	Examinatrice
KABOUB Lakhemici	Professeur	Université. Ferhat Abbas Sétif-1	Directeur de thèse
HANNACHI Douniazed	Professeur	Université de Batna-1	Invitée

ACKNOWLEDGEMENTS

First and foremost, I give thanks to God for providing me with the chance, fortitude, and endurance throughout the course of these protracted years of study to complete this job.
This work was carried out at the Laboratory of Chemistry, Molecular Engineering and Nanostructure (LCIMN), Faculty of Science, Department of Chemistry, Ferhat Abbas University – SETIF-1 under the direction of Professor **KABOUB Lalhemici**.

I extend my sincere thanks to my supervisor Pr.**KABOUB Lalhemici** who guided, followed the progress and execution of the work of this thesis by providing me with all possible help, and devoting me his precious time.

My profound gratitude is sent to Mrs **HANNACHI Douniazed**, a professor at the University of Batna-1, who taught me how to perform gaussin theoretical calculations.

I would like to express my gratitude to Dr. **BENSOUICI Chawki**, who oversees the biochemistry lab at the Research Center for Biotechnology of Constantine (CRBT), for allowing me to visit his lab, for his moral support, his consistent availability, his competence, and his scientific integrity.

My sincere thanks also go to Mr **Zouaoui Ahmed** , Professor at the Laboratory of Growth and Characterization of New Semiconductors, Department of Process Engineering, Faculty of Technology, Ferhat Abbas Setif University, for his valuable help in the electrochemical part.

I warmly thank Professor **BENAHMED Merzoug** of Larbi Ben M'Hidi University, agreed to travel from Oum El Bouaghi to judge this work as a member examiner, your presence honors me, as well as **ISSAADI Saïfi** and Mrs **BENGHANEM Fatiha**, Professors at Ferhat Abbas Sétif-1 University, **MESSASMA Zakia** lecturer class A at Ferhat Abbas Sétif-1 University, I am very pleased to send you my sincere thanks.

finally, and we always end up with the best, I address my warm remembrances to my dear **LAMIRI Mohand Ouramdan** and **MERIBOUT Leloucha** of former lecturers in the Department of Process Engineering and Department of technology, thank you for your unwavering wisdom and guidance as well as your unconditional support, both moral and economic, which allowed me to realize this nugget. Your support and guidance have been invaluable and I am truly grateful for your continued presence in my life.
I would like also to express my gratitude to **my spouse** for his presence and unfailing support towards me.

May these lines express my sincere gratitude and thanks to everyone who helped to build this work, whether directly or indirectly.

Summary

Summary

General Introduction 1

CHAPTER I

BIBLIOGRAPHY AND STATE OF THE ART ON THE THESIS SUBJECT

PART I: THEORETICAL REVIEW 6

I.1.Introduction 6

I.2. Theoretical review of Schiff bases 7

I.2.1. Definition of Schiff bases 7

I.2.2. Schiff basics training 8

I.2.3. Classification of Schiff bases 11

I.2.4. Areas of application of the Schiff bases 12

I.2.5. Complexing properties of Schiff bases 12

I.2.6 Sal(ph)en (non)symmetric metal complexes of Schiff bases 12

I.3. Theoretical studies 13

I.3.1. Density Functional Theory (DFT) 13

I.3.2. Foundations of DFT 13

I.3.3. Quantum parameters 14

I.3.4. Global descriptors 15

I.3.5. Gaussian calculation code 17

I.4. Non-linear optics (NLO) 17

I.4.1. the linear polarization 18

I.4.2. Non-linear polarization 18

I.5.The Hirshfeld surface 19

I.5.1. Foundations 19

I.5.2. Properties of surfaces de and di 20

I.5.3. Properties of dnorm surfaces 20

I.5.4. 2d fingerprints of Hirshfeld surfaces 21

I.5.5. Curvedness and Shape Index 22

I.6. Antioxidant activity 22

I.6.1. Oxygen 23

I.6.2. Oxidative stress 24
1.6.3. Consequence of oxidative stress 25
I.6.4. Free radicals 26
I.6.5. Production of free radicals 28
I.6.6. The body's antioxidant systems 30
I.6.7. Mechanisms of action of antioxidants 31
I.7. Literature on some Schiff-based compounds 32
I.8. Literature on some Schiff compounds derived from 5-Bromosalicylaldehyde 35
PART II: METHODS AND TECHNIQUES 37
I.9. Summary materials (Assembly of synthesis) 37
I.10. Theoretical background of experimental techniques used 37
I.10.1. Melting point 38
I.10.2. Thin Layer Chromatography (TLC) 38
I.10.3. Spectroscopic methods 38
I.10.3.1. UV-Visible Spectrophotometry 39
I.10.3.1.1 Beer-Lambert's Law 40
I.10.3.2. Infrared (IR) Spectroscopy 41
I.10.3.3. Nuclear Magnetic Resonance (NMR) Spectroscopy 41
I.10.3.4. X-ray diffraction 42
I.10.3.4.1. Crystallographic concepts 44
I.10.3.4.2. Single crystal X-ray diffraction 44
I.10.4. Characteristic electrochemical method by cyclic voltametrie 45
I.11. Methods for evaluating biological activities (antioxidant capacity) 46
I.11.1. Preparation of dilutions 47
I.11.2 DPPH 48
I.11.3. ABTS radical-cation reduction test•+ 49
I.12. Conclusion 50

CHAPTER II

Synthesis, characterization and biological study of 2,2'-((1E , E')-((2-hydroxypropane-1,3-diyl)bis(azanylylidene))bis(methanylylidene)bis(bis(4-bromophenol) (H2L1)

And its transition metal complexes Cu(II), Mn(II), Co(II) and Zn(II).

II.1. INTRODUCTION 60
PART I: SYNTHESIS AND CHARACTERIZATION 60
II.2. Synthesis of ligand 2,2'-((1E,E')-((2-hydroxypropane-1,3-diyl)bis(azanylylidene)) bis(methany lylidene))bis(bis(4-bromophenol) (H2L1) 60
II.3. Synthesis of Mn(III), Cu(II), Co(III) and Zn(II) complexes with ligand (H2L1) 61

II.4. Physical and analytical properties of ligand (H2L1) and these complexes 62
II. 5. Spectroscopic characterizations of ligand (H2L1) and its complexes 63
II.5.1. UV-Visible absorption spectrophotometry analysis 63
II.5.2. Infrared (IR) absorption spectrophotometry analysis 66
II.5.3. Proton (1H NMR) and Carbon (13C NMR) Nuclear Magnetic Resonance Spectroscopy 69
II.6. Study of electrochemical behaviour by cyclic voltatrie of ligand (H2L1) and its metal complexes 72
II.6.1. Ligand electrochemical behaviour (H2L1) 72
II.6.2. Electrochemical behaviour of Schiff metal-base complexes (H2L1) 73
PART II: STRUCTURAL STUDY BY THEORETICAL CALCULATION 75
II.7.1. Quantum chemistry calculations by DFT 75
II.7.2. Frontier molecular orbitals (OMF) 76
II.7.3. Mulliken atomic charges 79
II.7.4. Molecular Electrostatic Potential (MEP) 80
PART III: BIOLOGICAL STUDY, ANTIOXIDANT PROPERTIES 82
II.8.1. DPPH radical test 83
II.8.2. Anti-radical activity of ABTS+• 84
II.9. Conclusion 87

CHAPTER III

Synthesis, characterization, biological and optical study of 2,2'-((1E,11E)-5,8-dioxa-2,11-diazadodeca-1,12-diyl)bis(4-bromophenol) (H2L2)

And its transition metal complexes Cu(II), Mn(II), Co(II) and Zn(II).

III.1. Introduction 94
PART I: synthesis and characterization 94
III.2. Synthesis of ligand 2,2'-((1E,11E)-5,8-dioxa- 2,11-diazadodeca-1,12-diyl)bis(4-bromophenol) (H2L2) 94
III.3. Synthesis of Mn(III), Cu(II), Co(II) and Zn(II) complexes with ligand (H2L2) 95
III. 3. 1. Manganese complex synthesis 96
III. 3. 2. Synthesis of the Cuivric complex 96
III . 3.3. Zinc complex synthesis 97
III. 3. 4. Synthesis of Cobalt Complex 97
III.4. Physical and analytical properties of ligand (H2L2) and its complexes 97
III. 5. Spectroscopic characterizations of ligand (H2L2) and its complexes 98

III.5.1. UV-Visible Absorption Spectrophotometry Analysis 98

III.5.2. Infrared absorption spectrophotometry (IR) analysis 100

III.5.3. Proton (1H NMR) and Carbon (13C NMR) Nuclear Magnetic Resonance Spectroscopy 104

III.6. Study of electrochemical behaviour by cyclic voltammetry of ligand (H2L2) and its metal complexes 107

III.6.1. Ligand (H2L2) electrochemical behaviour 107

III.6.2. Electrochemical behaviour of Schiff metal-base complexes (H2L2) 108

III.7. CRYSTALLOGRAPHIC STUDY OF SINGLE CRYSTALS 111

III.7.1. Preparation and selection of single crystals 111

III.7.2. Recording of intensities 112

III.7.3. Resolution and refinement of crystal structure 112

III.7.4. Description of the structure 114

III.7.5. Connections and angles 114

III.7.6. Elementary Cell 117

III.7.7. Crystal lattice 118

III.8. Hirshfeld surface analysis 121

PART II: STRUCTURAL STUDY BY THEORETICAL CALCULATION 126

III.9. Quantum chemistry calculations by DFT 126

III.9.1. Frontier molecular orbitals (OMF) 126

III.9.2. Mulliken atomic charges 129

III.9.3. Molecular Electrostatic Potential (MEP) 131

III.10. Nonlinear optical properties (NLO) 132

PART III: BIOLOGICAL STUDY, ANTIOXIDANT PROPERTIES 134

III.11.1. DPPH radical test 134

III.11.2. ABTS radical test 136

III.12. Conclusion 138

CHAPTER IV

Synthesis, characterization and biological study of E-4-((5-bromo-2-hydroxyhybenzyl-idene)amino)butanoic acid (H2L3)

And its transition metal complexes Cu(II), Mn(II).

IV.1. INTRODUCTION 145

PART I: SYNTHESIS AND CHARACTERIZATION 145

IV.2. Synthesis of E-4-((5-bromo-2-hydroxyhybenzylidene)amino)butanoic acid (H2L3) 145
IV.3. Synthesis of Mn(III) and Cu(II) complexes with ligand (H2L3) 146
IV. 3. 1. Manganese complex synthesis 147
IV. 3. 2. Synthesis of the Cuivric complex 147
IV.4. Physical and analytical properties of ligand (H2L3) and its complexes 147
IV. 5. Spectroscopic characterizations of ligand (H2L3) and its complexes 148
IV.5.1. UV-Visible Absorption Spectrophotometry Analysis 148
IV.5.2. Infrared absorption spectrophotometry (IR) analysis 151
IV.5.3. Proton (1H NMR) Nuclear Magnetic Resonance Spectroscopy 153
IV.6. Study of electrochemical behaviour by cyclic voltammetry of ligand (H2L3) and its metal complexes 154
IV.6.1. Ligand electrochemical behaviour (H2L3) 155
IV.6.2. Electrochemical behaviour of Schiff metal-base complexes (H2L3) 156
IV.7. CRYSTALLOGRAPHIC STUDY OF SINGLE CRYSTALS 157
IV.7.1. Crystallographic characterization of ligand (H2L3) 158
IV.7.2. Crystallographic characterization of the Cu(II)L3 complex 165
IV.8. Hirshfeld surface analysis 171
PART II: STRUCTURAL STUDY BY THEORETICAL CALCULATION 173
IV.9. Quantum chemistry calculations by DFT 173
IV.9.1. Frontier molecular orbitals (OMF) 173
IV.9.2. Mulliken atomic charges 176
IV.9.3. Molecular electrostatic potential (MEP) 177
PART III: BIOLOGICAL STUDY, ANTIOXIDANT PROPERTIES 178
IV.10.1. Test du radical DPPH 179
IV.10.2. ABTS radical test 181
IV.11. Conclusion 183
General conclusion 189

List of tables

Table 1.1 Different types of reactive species[73]. 27
Table II.1. Physicochemical characteristics of prepared compounds. 62
Table II.2. UV-Vis ligand (H2L1) absorption bands and its complexes. 63
Table II.3. Major bands of ligand (H2L1) IR vibration and its complexes. 66
Table II.4. The electrochemical properties of ligand (H2L1) and its complexes were in-ves-tigated by cyclic voltammetry in DMF 72
Table II.5. Values of the HOMO, LUMO, HOMO-1, HOMO-2, LUMO+1, LU-MO+2 and the energy difference (ΔEGAP) of the ligand (H2L1) 77
Table II.6. Quantum parameters for ligand (H2L1). 80
Table II.7. Ligand Mulliken Atomic Charges (H2L1). 81
Table II.8. Antioxidant activity of ligand (H2L1) and its complexes by different meth-ods…… 82
Table III.1. Physical and chemical characteristics of ligand (H2L2) and its com-plexes…… 97
Table III.2. UV-Vis ligand (H2L2) absorption bands and its complexes. 100
Table III.3. Major bands of ligand (H2L2) IR vibration and its complexes. 104
Table III.4. The electrochemical properties of ligand (H2L2) and its complexes were in-vestigated by cyclic voltammetry in DMF1 07
Table III.5. Crystallographic data of the copper complex and details of structural refine-ment. 113
Table III.6. Bond lengths in the Cu(II)L2 complex. 115
Table III.7. Angles (°) in the Cu(II)L2 complex 116
Table III.8. Percentage contribution of different intermolecular interactions to the sur-face of Hirshfeld de Cu(II)L2. 124
Table III.9. Energy of frontier orbitals (eV) for the ligand (H2L2) 127
Table III.10. Quantum parameters for ligand (H2L2). 129
Table III.11. Mulliken atomic charges calculated for the ligand (H2L2). 130
Table III.12 . Non-linear optical properties (NLO) of the ligand (H2L2). 133
Table III.13. Antioxidant activity of ligand (H2L1) and its complexes by different meth-ods. 134
Table IV.1. Physico-chemical characteristics of the ligand (H2L3) and its complexes
Table IV.2. UV-Vis ligand (H2L3) absorption bands and its complexes. 148
Table IV.3. Main bands of ligand (H2L3) IR vibration and its complexes. 151

Table IV.4. The electrochemical properties of ligand (H2L3) and its complexes were investigated by cyclic voltammetry in DMF.....155
Table IV.5. Ligand Crystallographic Data (H2L3).....158
Table IV.6. Ligand bond lengths and angles (H2L3).....160
Table IV.7. Angles (°) of the intermolecular hydrogen bonds of the Cu(II)L3 complex…….....161
Table IV.8. Crystallographic data of the Cu(II)L3 complex.....166
Table IV.9. Interatomic distances and Cu(II)L3 complex bond angles. 167
Table IV.10.Lengths (Å) and angles (°) of Cu(II)L3 intermolecular hydrogen bonds.167
Table IV.11. Energy of the frontier orbitals (eV) for the ligand (H2L3) at the theoretical level B3LYP/6-311 G.....175
Table IV.12. Quantum parameters for ligand (H2L1). 176
Table IV.13. Mulliken atomic charges calculated for the ligand (H2L3).....176
Table IV.14. Theoretical (B3LPY/ 6-31G (d, p) ligand (H2L3) bond angles. 177
Table IV.15. Antioxidant activity of ligand (H2L3) and its two complexes by different methods. 179

List of Figures

Figure I.1. Schematic representation of the salen ligand accounting for the N2O2 coordination pocket.....07
Figure I.2. Examples of bioactive Schiff bases, natural product, natural product derived compounds, and non-natural compound. 08
Figure I.3. General reaction of Schiff base formation(R, R and R" = alkyl or aryl group)… 08
Figure I.4. Different types of Schiff bases. 11
Figure I.5. Non-symmetric salen ligand. 13
Figure I.6. Effect of an electric field on an atom and its electronic cloud. 18
Figure 1.7. Colours adapted to (dnorm) in the Hirshfeld surface 21
Figure I.8. Oxygen distribution in various organs. 24
Figure I.9. Different oxidative stress factors. 25
Figure I.10. Intracellular ROS production sites 28
Figure I.11. The neutralization of free radicals by an antioxidant agent is important to maintain a healthy cell. 31
Figure I.12. General diagram of the complex developed by Ameli .I.B and col. 34
Figure I.13. Structure of Schiff base metal complexes prepared by Krishna, G. A and al 35
Figure I.14. Four conformers of 5BSA molecule stadied by Bahçeli. S and col.....36
Figure I.15.Optimized structure of (E)-3-((5-bromo-2-hydroxybenzylidene)amino) propanoic acid prepared by Meenukutty M and col 36
Figure I.16. General structure of the 5BRSET ligand prepared by Priya, C. G and col 37
Figure I.17. All radiation constitutes the electromagnetic spectrum. 39
Figure 1.18. Schematic diagram of X-ray diffraction 43
Figure I.19. Principle of single crystal X-ray diffraction. 45
Figure I.20. Preparation of product dilutions in methanol. 48
Figure II.1. UV-Visible spectrum of (H2L1) and Mn(II)L1 in DMF. 64
Figure II.2. UV-Visible spectrum of (H2L1) and Cu(II)L1 in DMF. 64
Figure II.3. Spectre UV-Visible de (H_2L1) et de Zn(II)L1 dans le DMSO. 65
Figure II.4. UV-Visible spectrum of (H2L1) and Co(II)L1 in DMF. 65
Figure II.5. IR spectrum in KBr of (H2L1).....67

Figure II.6. IR spectrum in Mn (II)L1 KBr.....67
Figure II.7. IR spectrum in KBr of Cu(II)L1 and Co(II)L1.....68
Figure II.8. IR spectrum of Zn(II)L1 in KBr.....69
Figure II.9. H-RMN1 spectrum of (H2L1) in CDCl3. 70
Figure II.10. 13C NMR Spectrum of (H2L1) in CDCl3 71
Figure II.11. Cyclic Ligand Voltammetry (H2L1)(10-3M) in DMF+TBAP(10-1M) under nitrogen atmosphere at a scanning speed of 100 mV/s. 73
Figure II.12. Mn (II)L1(10-3M) cyclic voltammetry in FMD+TBAP(10-1M) under nitrogen atmosphere at a scanning speed of 100 mV/s.....73
Figure II.13. Cu (II)L1(10-3M) cyclic voltammetry in FMD+TBAP (10-1M) under nitrogen atmosphere at a scanning speed of 100 mV/s.....74
Figure II.14. Cyclic Voltammetry of Co (II)L1(10-3M) in FMD+TBAP(10-1M) under nitrogen atmosphere at a scanning speed of 100 mV/s.....75
Figure II.15. Cyclic voltammetry of Zn(II)L1(10-3M) in FMD+TBAP(10-1M) under nitrogen atmosphere at a scanning speed of 100 mV/s.....76
Figure II.16. Optimal molecular structure of the ligand (H2L1).....78
Figure II.17. Frontier molecular orbitals (OMF) of H2L1 ligand 81
Figure II.18. Cartographer of the molecular electrostatic potential of ligands H2L1 drawn on surfaces of total density (a): Front view and (b) Rear view.....83
Figure II.19.Kinetics of anti-radical activity of (H2L1), Mn(II)L1 , Cu(II)L1, Co(II)L1 and Zn(II)L1 with BHA and BHT standards. 84
Figure II.20. IC50 inhibitory concentration values in (µg/ml). Ligand (H2L1), complexes Mn(II)L1, Cu(II)L1, Co(II)L1, Z(II)L1 and standard BHA and BHT.....85
Figure II.21. Trapping effect of ABTS+ radical of H2L1, Mn(II)L1, Cu(II)L1 , Co(II)L , Zn(II)L1 and BHT and BHA standards. 86
Figure II.22. IC50 inhibitory concentration values in (µg/ml). From (H2L1), Mn(II)L1, Cu(II)L1, Co(II)L1, Zn(II)L1 and standard BHA and BHT towards ABTS.....87
Figure III.1. Spectre UV-Visible du ligand (H2L2) dans le DMF.....98
Figure III.2. UV-Visible Spectrum of Mn(II) L2 in DMF. 99
Figure III.3. UV-Visible Spectrum of Zn(II) L2 in DMF. 99
Figure III.4. UV-Visible Spectrum of Cu(II) L2 in DMF. 99
Figure III.5. UV-Visible Spectrum of Cu(II) L2 in DMF. 99
Figure III.6. IR ligand (H2L2) spectrum in KBr. 101
Figure III.7. Mn(II)L2 IR spectrum in KBr.....102

Figure III.8. Cu(II)L2 IR spectrum in KBr. 102
Figure III.9. Co(II)L2 IR Spectrum in KBr..... 103
Figure III.10. Zn(II)L2 IR spectrum in KBr..... 103
Figure III.11. H-RMN1 spectrum in CDCl3 of (H2L2). 105
Figure III.12. 13C NMR spectrum in CDCl3 of (H2L2)..... 106
Figure III.13. Cyclic Ligand Voltammetry (H2L2)(10-3M) in DMF+TBAP(10-1M) under nitrogen atmosphere at a scanning speed of 100 mV/s. 108
Figure III.14. Mn (II)L2(10-3M) cyclic voltammetry in FMD+TBAP(10-1M) under nitrogen atmosphere at a scanning speed of 100 mV/s..... 109
Figure III.15. Cu(II)L2(10-3M) cyclic voltammetry in FMD+TBAP(10-1M) under nitrogen atmosphere at a scanning speed of 100 mV/s..... 109
Figure III.16. Co(II)L2(10-3M) cyclic voltammetry in FMD+TBAP(10-1M) under nitrogen atmosphere at a scanning speed of 100 mV/s..... 110
Figure III.17. Zn(II)L2(10-3M) cyclic voltammetry in FMD+TBAP(10-1M) under nitrogen atmosphere at a scanning speed of 100 mV/s..... 111
Figure III.18. Representation of the Cu(II)L2 complex molecule..... 114
Figure III. 19. Representation of the Cu(II)L2 complex molecule with atom numbering 115
Figure III.20. Representation of the mesh with axes a, b and c of the Cu(II)L2 complex. 117
Figure III.21.Mesh in the plane a, b c of the complex Cu (II)L2 with symmetry elements 118
Figure III.22 . Crystalline molecular stacking of Cu(II)L2 in three crystallographic planes:(a) [100], (b) [010] and (c) [001]. 119
Figure III.23. Perspective view of the crystal lattice. 120
Figure III.24. Perspective projection visualizing the intermolecular interaction by hydrogen bond (C— H…X) presents between two molecules voisions. 120
Figure III.25. Hirshfeld surface of Cu(II)L2 plotted on (a) = dnorm , (b) = di , (c) = de , (d) = curvedness , (e) = shape index 121
Figure III.26. The Cu(II)L2 structure two-dimensional fingerprint type H…H. 122
Figure III.27. Br… H/H… Br and C…H/H… C two-dimensional fingerprints of the Cu(II)L2 structure..... 123
Figure III.28. Two-dimensional fingerprints type O…H/H…O and C…Br/Br…C of the Cu(II)L2 structure..... 123

Figure III.29. Two-dimensional fingerprints of type N…H/H…N and C…N/N…C of the Cu(II)L2 structure.....124
Figure III.30. The Hirshfeld surface of Cu(II)L mapped to dnorm showing interactions with nearby neighbors in three directions (x,y,z) at a distance of 3.8 Ao. 125
Figure III.31. Optimal molecular structure of the ligand (H2L2). 126
Figure III.32. Frontier molecular orbitals (FMOs) of H2L2 ligands.....128
Figure III.33. Cartograph of the molecular electrostatic potential of ligands H2L2drawn on surfaces of total density (a): Front view and (b) Rear view 132
Figure III.34. DPPH free radical scavenging activity of standard BHA, BHT and synthesized compounds.....134
Figure III.35. IC50 inhibitory concentration values expressed in (µg/ml). Ligand (H2L2), Mn(II)L2, Cu(II)L2, Co(II)L2, Zn(II)L2 complexes and BHA and BHT standards ..135
Figure III.36. ABTS anti-radical activity of synthesized molecules (H2L2), Mn(II)L2 , Cu(II)L2, Co(II)L2, Zn(II)L2 and BHA , BHT standards.....136
Figure III.37. IC50 inhibitory concentration values in (µg/ml). Du (H2L2), Mn(II)L2, Cu(II)L2, Co(II)L2, Zn(II)L2 and BHA , BHT standards towards ABTS. 137
Figure IV.1. UV-Visible Spectrum of Cu(II)L3 in DMF 149
Figure IV.2. UV-Visible Spectrum of ligand (H2L3) in DMF. 149
Figure IV.3. Mn(II)L3 UV-Visible Spectrum in DMF 150
Figure IV.4. UV-Visible Spectrum of (H2L3) and its corresponding complexes in DMF 150
Figure IV.5. IR spectrum of Cu(II)L3 in KBr. 152
Figure IV.6. IR spectrum OF Mn(II)L3 in KBr. 152
Figure IV.7. H-RMN1 spectrum in MeOH of (H2L3).....154
Figure IV.8. Cyclic Ligand Voltammetry (H2L3)(10-2M) in DMSO+(C2H5)4NBF4 (10-1M) under nitrogen atmosphere at a scanning speed of 100 mV/s. 155
Figure IV.9. Mn (II)L3(10-2M) Cyclic Voltammetry in DMSO+(C2H5)4NBF4 (10-1M) under nitrogen atmosphere at a scanning speed of 100 mV/s. 156
Figure IV.10. Cu(II)L3(10-2M) cyclic voltaromegram in DMSO+(C2H5)4NBF4 (10-1M) under nitrogen atmosphere at a scanning speed of 100 mV/s. 157
Figure IV.11. Molecule representation (H2L3). 158
Figure IV.12. Ligand crystal structure (H2L3) with numbering. 159
Figure IV.13. Projection of the elementary cell of (H2L3) along the three crystallographic axes a, b and c. 162

Figure IV.14. Mesh in a plane, b c of ligand (H2L3) with symmetry elements. 163
Figure IV.15. Molecular crystalline stack of (H2L3) in three crystallographic planes: (a) [100], (b) [010] and (c) [001]. 164
Figure IV.16. Perspective representation of the molecule Cu(II)L3. 165
Figure IV.17. Representation of the intermolecular interaction in the Cu(II)L3 crystal. 168
Figure IV.18. Representation of the mesh with axes a, b and c 168
Figure IV.19. Mesh in plane a, b c of Cu (II)L3 complex with symmetry elements. ... 169
Figure IV.20. Representation of the Cu(II)L3 crystal lattice..... 170
Figure IV.21. Hirshfeld surface of (H2L3) and Cu(II)L3 plotted on dnorm. 171
Figure IV.22. Two-dimensional fingerprints of each type of interaction in the structure of (H2L3) and Cu(II)l3. 172
Figure IV.23. Optimal molecular structure of the ligand (H2L3). 173
Figure IV.24. HOMO and LUMO molecular orbitals of the H2L3 ligand. 174
Figure IV.25. Cartograph of the molecular electrostatic potential of ligands H2L3 drawn on surfaces of total density (a): Front view and (b) Rear view..... 178
Figure IV.26. Kinetics of the anti-radical activity of the ligand (H2L3) and its metal complexes Mn(II)L3 , Cu(II)L3 with the BHA and BHT standards on the DPPH radical. 180
Figure IV.27. IC50 inhibitory concentration values in (µg/ml). Ligand (H2L3), Mn(II)L3 and Cu(II)L3 complexes and BHA and BHT standards..... 180
Figure IV.28. Trapping effect of the ABTS+ radical of H2L3, Mn(II)L3, Cu(II)L3 and BHT and BHA standards..... 182
Figure IV.29. IC50 inhibitory concentration values in (µg/ml). Ligand (H2L3), Mn(II)L3 and Cu(II)L3 complexes and BHA and BHT standards towards ABTS..... 182

List of Scheme

Scheme I.1. Synthesis of salen ligands. 06

Scheme I.2. General reaction of Schiff base formation (R, R and R" = alkyl or aryl group). 09

Scheme I.3. The reaction sequence for the synthesis of a Schiff base. 09

Scheme I.4. Mechanism of formation of a Schiff base 10

Scheme I.5. Various diseases related to reactive oxygenated species ERO 26

Scheme I.6. Origin of different oxygen free radicals and ROS involved in biology 27

Scheme I.7. Chemical drawings of synthesis and X-ray characterized structure of 6–8 studied by Mahira Memisevic et al 34

Scheme II.1. Reaction pattern of ligand formation (H2L1). 60

Scheme II.2. Basic Schiff (H2L1) synthesis reaction mechanism. 61

Scheme II.3. General ligand complexation reaction (H2L1) 62

Scheme III.1. Reaction scheme of ligand formation (H2L2). 94

Scheme III.2. Basic Schiff (H2L2) synthesis reaction mechanism. 95

Scheme III.3. General ligand complexation reaction (H2L2) 96

Scheme IV.1. Reaction pattern of ligand formation (H2L3) 145

Scheme IV.2. Basic Schiff Synthesis Reaction Mechanism (H2L3). 146

Scheme IV.3: General ligand complexation reaction (H2L3). 146

Abbreviations

DMSO : Dimethylsulfoxide C2H6OS

BHT : butylated hydroxytoluene C15H24O

BHA : butylated hydroxyanisole

DPPH : 2,2-diphenyl-1-picrylhydrazine C18H12N5O6

ABTS: 2,2-azinobis-(3ethylbenzothiazoline-6-sulfonic) acid ammonium salt

CI50 : Inhibitory concentration at 50%

EC50 : Effective mass concentration at 0.5

RLs : Free radicals.

DMF : N, N-diméthylformamide C3H7NO

DMSO: Diméthylsulfoxide.

Bu4NBF4: Tetrabutylammonium tetrafluoroborate (Electrolyte support)

$\mathbf{E_{HOMO}}$: The energy of the highest molecular orbital occupied

$\mathbf{E_{LUMO}}$: The energy of the first unoccupied molecular orbital

$\mathbf{\Delta E_{GAP}}$: gap Energy (eV)

I: ionisation energy (eV)

χ : Electronegativity (eV)

σ : Softness $(eV)^{-1}$

ω : Electrophilicity index (eV)

A : electronic affinity (eV)

η: Overall hardness (eV)

VC : Cyclic voltammetry

NMR : Nuclear magnetic resonance

IR : Infrared

ERO : Reactive oxygen species.

RNS : Reactive nitrogen species

GENERAL INTRODUCTION

General Introduction

The chemistry of transition metal complexes has progressed considerably due to the innovative and varied potential applications of these materials especially in photonics and optoelectronics. Several theoretical and experimental works have been carried out in these areas [1–4].

Because these two sciences are at the intersection of several industries and sectors, chemistry and biology are now a part of our everyday lives. Today's biological molecules, inorganic molecules, and macromolecules are all covered by the organic chemistry of yesterday. Up until the formation of a supramolecular chemistry, which is based on diverse interactions between molecules and explains their properties, it builds more or less complicated structures.

In this context, the development of the field of bio-inorganic chemistry has increased the interest of the Schiff base complexes, as they can serve as models of bio-logically important compounds [5–7] hence the interest for chemists to develop series of complexes in order to understand and optimize their reactivity.

Since transition metal compounds exhibit a broad range of pharmacological actions, which have led to extensive research into their potential for treating a variety of worries [6,8–10] that are closely tied to their capabilities, this interest has only grown [11]. For instance, lipophilia, which regulates the velocity of entrance into the cell, is altered during coordination; this lessens some of the negative effects and allows complexes to exhibit novel bioactive characteristics not present in the free ligand [12,13].

In addition, extensive research has revealed that Schiff base complexes containing one or more halogen atoms in their aromatic cycle have been extensively studied because of their antimicrobial properties [14]. However, much less information is available on Schiff bases derived from 5-Bromosalycilaldehyde with other amino compounds. This type of compound has not yet been systematically studied. There is little literature on the reactivity of 5-Bromosalycilaldehyde with various amino compounds [15,16]. In the extension of these studies, we are interested in the behavior of transition metal complexes at the level of biological activities.

In order to better understand the antioxidant biological capacity of copper (II), cobalt (II), manganese (II), and zinc (II) complexes and their corresponding methos, it appeared beneficial to synthesize the spectroscopic and crystallographic characterization of these compounds through this study endeavor. One of the aims of this work is to examine nonlinear optics after doing a theoretical calculation using the DFT.

In addition to the introduction and general conclusion, the thesis is divided into four chapters: The first chapter refers to the current bibliographic knowledge on the bases of Schiff and their metallic complexes followed by a bibliographic study concerning the antioxidant biological activity, their classification and their main characteristics , as well as a reminder of the bibliographic work carried out on the Schiff bases and their bioactivities This is followed by a description of the products and solvents used to produce the synthesis reactions of the ligands and complexes studied and those of the biological study. We also describe the different analytical techniques used to establish the structures of the obtained compounds.

In the second chapter we describe the synthesis of new ligand base of Schiff 2,2'-((1E,1'E)-((2-hydroxypropane-1,3-diyl)bis(azanylylidene)bis(methanyllylidene)bis(4-bromophenol) (H2L1) and their metal complexes with respect to transition metals Cu(II), Mn(II) ,Co(II), and Zn(II), we will detail their structural characterization by the usual spectroscopic methods UV-vis, IR, ^{1}H, ^{13}C NMR, DRX and by cyclic voltammetry as well as the evaluation of biological activities (antioxidant), which will be followed by a discussion of all the results obtained.

Chapter III is devoted to the synthesis and characterization of Schiff 2,2'-((1E,11E)-5,8-dioxa-2,11-diazadodeca-1,12-diyl)bis(4-bromophenol) (H2L2) and their metal complexes with respect to transition metals Cu(II), Mn(II), Co(II) and Zn(II) followed by antioxidant potency tests, ended with the interpretation and discussion of the results obtained .

Chapter IV describes the synthesis and characterization of E-4-((5-bromo-2-hydroxyhybenzylidene)amino)butanoic acid (H2L3) and their metal complexes with respect to Cu(II),Mn(II) transition metals with a well-detailed spectroscopic, electrochemical and crystallographic characterization, followed by biological tepists.

References

[1] A.B. Tamayo, B.D. Alleyne, P.I. Djurovich, S. Lamansky, I. Tsyba, N.N. Ho, R. Bau, M.E. Thompson, Synthesis and characterization of facial and meridional tris-cyclometalated iridium (III) complexes, J. Am. Chem. Soc. 125 (2003) 7377–7387.

[2] E. Baranoff, J.-H. Yum, M. Graetzel, M.K. Nazeeruddin, Cyclometallated iridium complexes for conversion of light into electricity and electricity into light, J. Organomet. Chem. 694 (2009) 2661–2670.

[3] Y.-J. Yuan, J.-Y. Zhang, Z.-T. Yu, J.-Y. Feng, W.-J. Luo, J.-H. Ye, Z.-G. Zou, Impact of ligand modification on hydrogen photogeneration and light-harvesting applications using cyclometalated iridium complexes, Inorg. Chem. 51 (2012) 4123–4133.

[4] C. Li, Y. Cai, M. Pang, X. Zhou, X. Luo, Z. Xiao, A coumarin-appended cyclometalated iridium (III) complex for visible light driven photoelectrochemical bioanalysis, Biosens. Bioelectron. 147 (2020) 111779.

[5] H. Keypour, A. Shooshtari, M. Rezaeivala, F.O. Kup, H.A. Rudbari, Synthesis of two new N2O4 macroacyclic Schiff base ligands and their mononuclear complexes: Spectral, X-ray crystal structural, antibacterial and DNA cleavage activity, Polyhedron 97 (2015) 75–82.

[6] R. Paulpandiyan, N. Raman, Oxovanadium (IV) complexes with Knoevenagel Schiff base condensate as impending chemotherapeutic agents: synthesis, characterization, biological screening and anti-proliferative assay, Bioorg. Chem. 73 (2017) 100–108.

[7] A.Z. El-Sonbati, M.A. Diab, A.A. El-Bindary, M.I. Abou-Dobara, H.A. Seyam, Molecular docking, DNA binding, thermal studies and antimicrobial activities of Schiff base complexes, J. Mol. Liq. 218 (2016) 434–456.

[8] K. Dhahagani, M.P. Kesavan, K.G.G. Vinoth, L. Ravi, G. Rajagopal, J. Rajesh, Crystal structure, optical properties, DFT analysis of new morpholine based Schiff base ligands and their copper (II) complexes: DNA, protein docking analyses, antibacterial study and anticancer evaluation, Mater. Sci. Eng. C 90 (2018) 119–130.

[9] V.P. Radha, S.J. Kirubavathy, S. Chitra, Synthesis, characterization and biological investigations of novel Schiff base ligands containing imidazoline moiety and their Co (II) and Cu (II) complexes, J. Mol. Struct. 1165 (2018) 246–258.

[10] K. Venkateswarlu, M.P. Kumar, A. Rambabu, N. Vamsikrishna, S. Daravath, K. Rangan, Crystal structure, DNA binding, cleavage, antioxidant and antibacterial studies of Cu (II), Ni (II) and Co (III) complexes with 2-((furan-2-yl) methylimino) methyl)-6-ethoxyphenol Schiff base, J. Mol. Struct. 1160 (2018) 198–207.

[11] S. Sangeeta, K. Ahmad, N. Noorussabah, S. Bharti, M.K. Mishra, S.R. Sharma, M. Choudhary, Synthesis, crystal structures, molecular docking and urease inhibition studies of Ni (II) and Cu (II) Schiff base complexes, J. Mol. Struct. 1156 (2018) 1–11.

[12] B. Iftikhar, K. Javed, M.S.U. Khan, Z. Akhter, B. Mirza, V. Mckee, Synthesis, characterization and biological assay of Salicylaldehyde Schiff base Cu (II) complexes and their precursors, J. Mol. Struct. 1155 (2018) 337–348.

[13] V.A. Joseph, J.H. Pandya, R.N. Jadeja, Syntheses, crystal structure and biological evaluation of Schiff bases and copper complexes derived from 4-formylpyrazolone, J. Mol. Struct. 1081 (2015) 443–448.

[14] M.P. Kumar, S. Tejaswi, A. Rambabu, V.K.A. Kalalbandi, Synthesis, crystal structure,

DNA binding and cleavage studies of copper (II) complexes with isoxazole Schiff bases, Polyhedron 102 (2015) 111–120.

[15] P. Tyagi, S. Chandra, B.S. Saraswat, D. Yadav, Design, spectral characterization, thermal, DFT studies and anticancer cell line activities of Co (II), Ni (II) and Cu (II) complexes of Schiff bases derived from 4-amino-5-(pyridin-4-yl)-4H-1, 2, 4-triazole-3-thiol, Spectrochim. Acta Part A Mol. Biomol. Spectrosc. 145 (2015) 155–164.

[16] L.H. Abdel-Rahman, N.M. Ismail, M. Ismael, A.M. Abu-Dief, E.A.-H. Ahmed, Synthesis, characterization, DFT calculations and biological studies of Mn (II), Fe (II), Co (II) and Cd (II) complexes based on a tetradentate ONNO donor Schiff base ligand, J. Mol. Struct. 1134 (2017) 851–862.

CHAPTER I
BIBLIOGRAPHY AND STATE OF THE ART ON THE THESIS SUBJECT

PART I: THEORETICAL REVIEW

I.1.Introduction

Schiff bases are a very intriguing family of ligands because they include a range of donor atoms, including sulfur, oxygen, and nitrogen. Due to their ease of synthesis with a very good yield and the variety of uses they have in relation to the relative stability of their complexes with most transition metals, researchers have recently placed a great deal of emphasis on the synthesis and characterization of Schiff base ligands and their metal complexes using various physicochemical and biological methods. These compounds are widely used in medical chemistry, coordination chemistry, and the field of optics. This class of chemicals has a wide range of potential applications in many aspects of life, particularly in the biological system, where they have been employed as antivirals, anticancer, antitubercular, anti-HIV, bactericides, fungicides, and in the treatment of a number of terminal illnesses. The outcome is an ideal pharmacological model.

Hugo Schiff made the discovery that carbonyl compounds can condense with primary amines to generate imines in 1864[1]. Since then, the Schiff family of chemicals has been used as its common name. Many branches of chemistry have shown a great deal of interest in Schiff's fundamental condensation due to its reversible nature and straightforward synthesis conditions. The tetradentate derivative, sometimes referred to as the Salen derivative, is a more frequently occurring structure in the literature. It is produced by combining salicylaldehyde with a diamine. The tetradentate Schiff base ligands of N, N, O, and O can be thought of as being modeled after these Salen structures (salicylethylenediamine).

Coordination chemistry has long effectively employed these N2O2-type tetradentate salen ligands (Scheme I.I.) as preferred ligands [2–4]. quite simple condensation between two readily accessible diamines and precursors of salicylaldehydes yields these adaptable ligands, which are quite easy to synthesis [2].

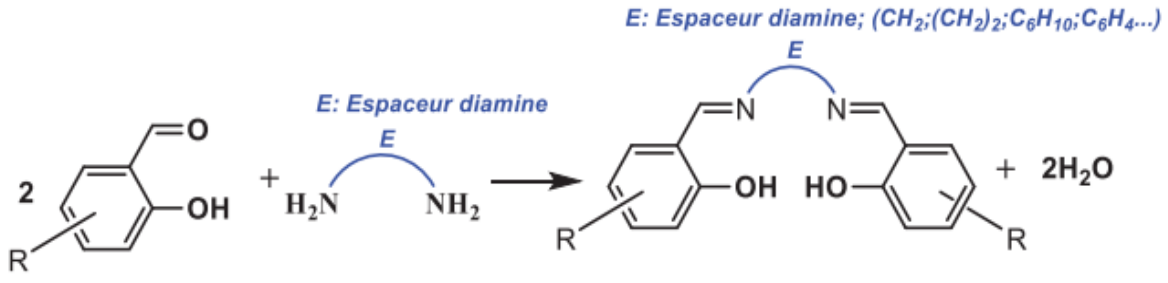

Scheme I.1. Synthesis of salen ligands

These ligands, through their internal coordination cavity N2O2, have a considerable capacity to coordinate metal ions and stable them in different oxidation states. In addition to these four coordination sites, these salen compounds additionally feature two axial sites that can be accessed by auxiliary ligands, contingent on the selected metal. With the benefit of simpler synthesis, their behavior is comparable to that of porphyrins due to the availability of sites.

Furthermore, the term "salen" describes ligands that are produced by condensation of 1,2-ethylenediamine and salicylaldehyde. Eventually, this term also encompasses ligands that have variable skeletons of diamines, such as "E," which is a spacer and a chain that connects the two aromatic cycles of the salt framework Figure 1. Consequently, in the literature, this term refers to the description of a so-called generic class of complexation of type N2O2.

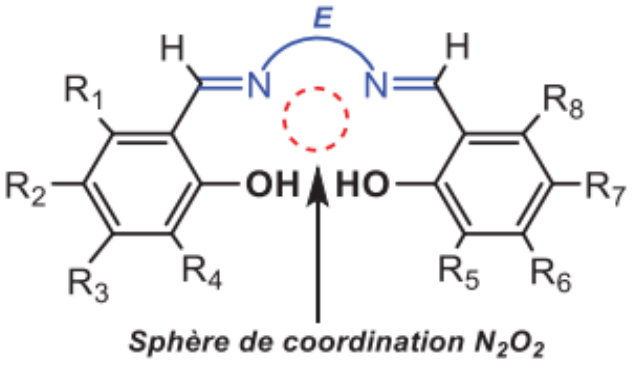

Figure I.1. Schematic representation of the salen ligand accounting for the N2O2 coordination pocket

I.2. Theoretical review of Schiff bases

Schiff's base ligands play a significant part in many branches of chemistry. In fact, a great deal of work has gone into creating procedures for the synthesis of these substances, which have long drawn the interest of several scientists due to their significance in the fields of biology, medicine, pharmacology, and industry.

I.2.1. Definition of Schiff bases

The bases of Schiff are really named after their inventor Hugo Schiff (1834-1915) who was the first chemist to synthesize this type of compounds in 1864 [1,5].

- A Schiff base is defined as any product with an imine function where one of the constituents on carbon or nitrogen is an aromatic group [6,7].

- A Schiff base is defined as the condensation of a primary amine with a ketone or aldehyde. By extension, Schiff base is any product with a double bond C=N resulting from the reaction between a nucleophilic nitrogen and a carbonylated compound [7,8].

The Schiff bases have the following general structure (Figure I.2):

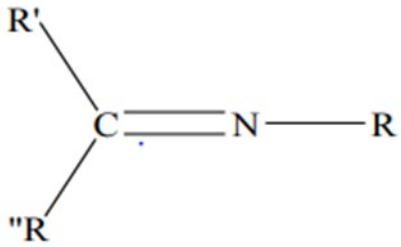

Figure I.2. General structure of a Schiff base. Where R' , R" and/or R= aryl or alkyl.

In fact, several natural products, compounds derived from natural sources, and synthetic compounds all include imine or azomethine groups; Figure I.3 provides some examples. It has been demonstrated that the imine group in these compounds is necessary for their biological actions [9–11].

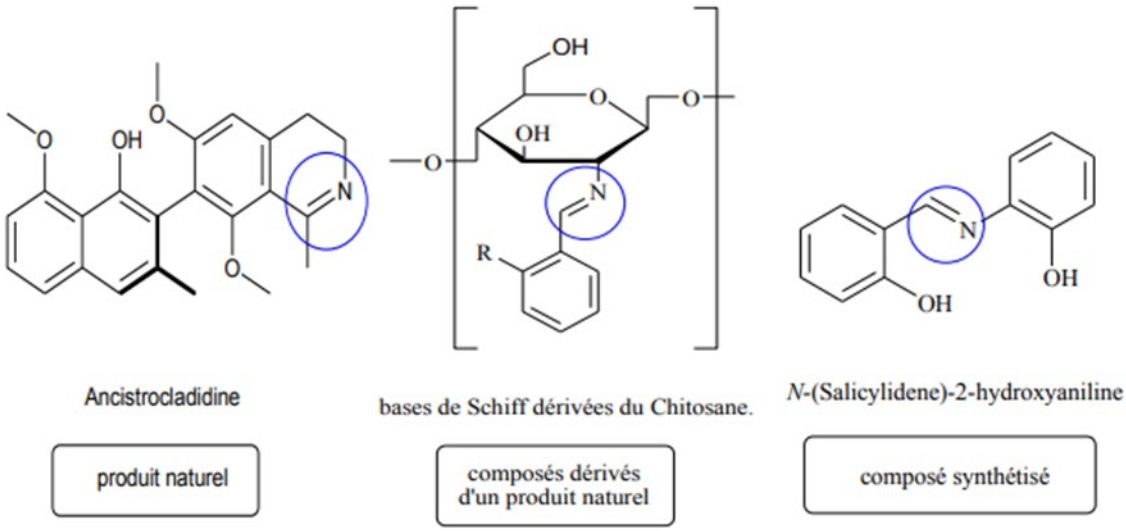

Figure I.3. Examples of bioactive Schiff bases, natural product, natural product derived compounds, and non-natural compound [12]**.**

I.2.2. Schiff basics training

The Schiff base is formed by a condensation reaction of an aldehyde or ketone on the primary amine whether aliphatic or aromatic as illustrated by the following Scheme:

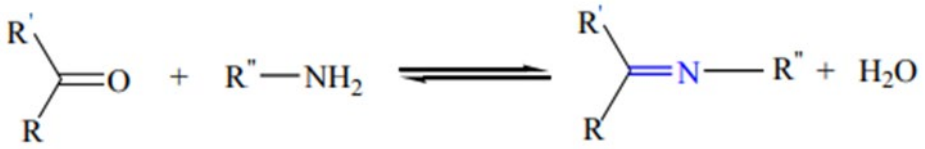

Scheme I.2. General reaction of Schiff base formation (R, R and R" = alkyl or aryl group).

Since the aryl group has a broader electronic delocalization on the molecule's surface, Schiff bases with this substituent are thought to be the most stable. Producing these is simple. The Schiff bases belonging to the aliphatic series exhibit comparatively lower stability when compared to their aromatic counterparts. Be aware that Schiff bases derived from aliphatic aldehyde condensation are more quickly polymerized and substantially less stable [13].

The process of forming Schiff bases from aldehydes or ketone is a reversible reaction that can be initiated by heating, acid or basic catalysis, or both [1,13]. Because of this reaction's reversibility, it is frequently necessary to remove water from the reaction medium in order to tip the balance in favor of the formation of the Schiff base.

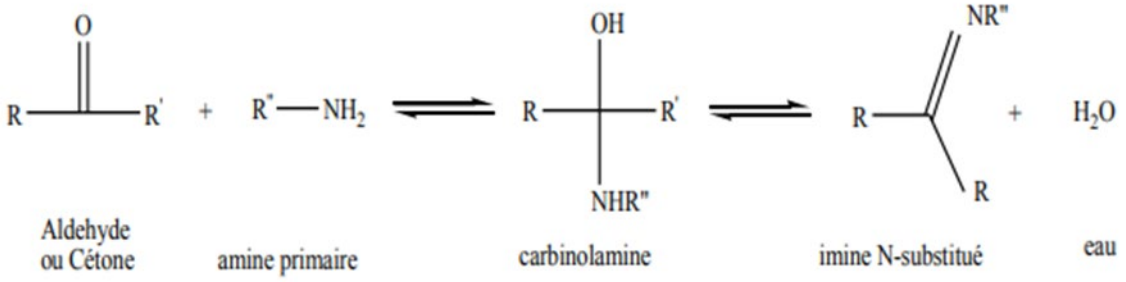

Scheme I.3. The reaction sequence for the synthesis of a Schiff base

The first step in this reaction is the nucleophilic attack of the nitrogen atom of the amine on the carbonyl carbon, which leads to an unstable intermediate named carbinolamine, of which a carbon atom is carrier of two eleccroattractor functions (hydroxyl function and amine NHR function)[13,14]

The reaction can take the opposite path leading to the formation of the starting products. Finally, when the hydroxyl group is eliminated, the imine function C=N is immediately formed and the Schiff base is then obtained. It should be noted that many factors can affect the course of this condensation reaction, for example solution pH, steric effect as well as electronic effects.

Since the amine is basic, it is rapidly protonated in the acid medium so that it can no longer function as a nucleophilic agent and therefore the reaction cannot take place. In addition, in a strongly basic medium, the reaction is prevented because of the absence of protons in the reaction medium that cause the attack of the carbinolamine hydroxyl leading to the formation of the Schiff base and water[13].

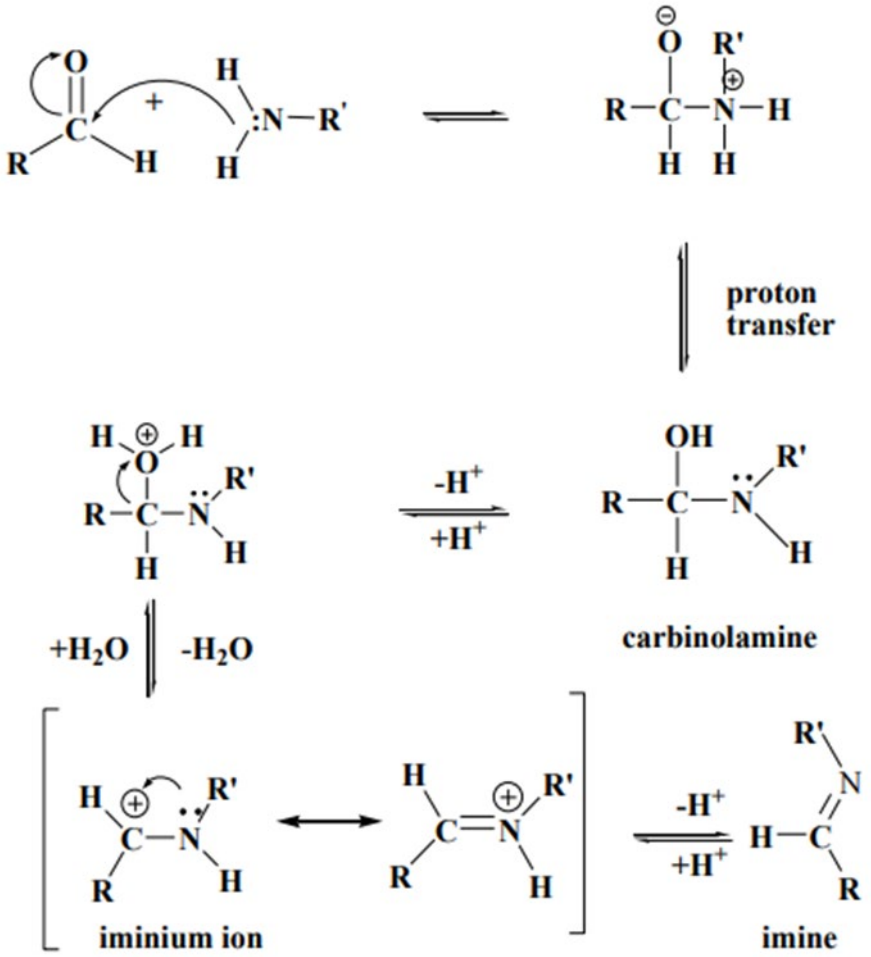

Scheme I.4. Mechanism of formation of a Schiff base[14]**.**

As is customary in catalytic reactions to use minute amounts of catalyst, this is indeed the case here in order to ensure the nucleophilic attack of the amine otherwise the Schiff base would never be formed.

Aldehydes generally react faster than ketones in these condensation reactions since the resulting Schiff base of aldehyde has fewer steric genes than those of a ketone. Moreover, the electron density on the carbon atom of the carbonyl group is lower in the case of ketone than in the case of aldehyde so that the efficiency of the nucleophilic attack of the amine is regulated as such [5,6].

I.2.3. Classification of Schiff bases

Depending on the reaction circumstances, Schiff's base ligands have the capacity to create co-ordination bonds with transition metals.

It is noteworthy that despite the intense research activity in the last two decades, when there has been an exceptionally fertile scientific production, the literature has devoted a great deal of effort to coordination chemistry. This effort has primarily focused on the complexation of Schiff base ligands with transition metals[6,11]. Usually, these ligands are organic compounds having electron-donor atoms that resemble Lewis structures. The number of ligand coordination sites in these compounds may subsequently be used to classify them as monodentate, bidentate, or polydentate[12].

The examples in Figure I.8 given below show the different types of structures of these Schiff bases.

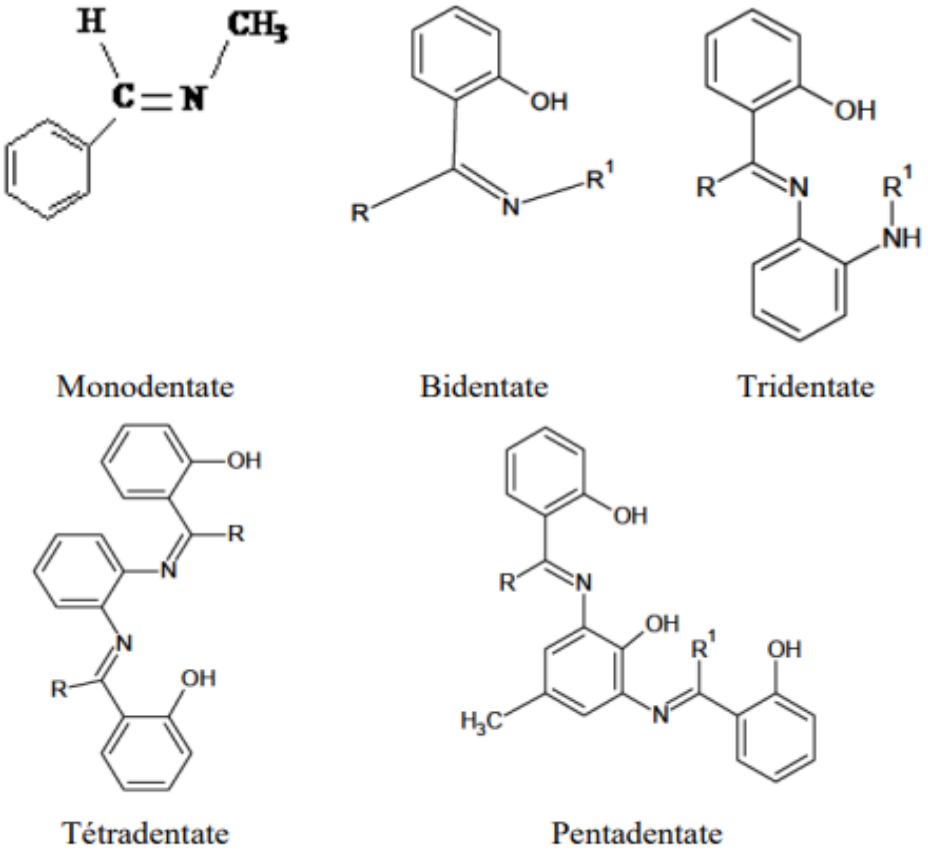

Figure I.4. Different types of Schiff bases.

I.2.4. Areas of application of the Schiff bases

The Schiff bases have a very wide range of applications in chemistry, the pharmaceutical industry, medicine, and biology, among other areas of daily life. These applications, which represent one of the most widely used novel systems in research, have been extended from the laboratory to the industrial scale.

In biology, many recent works on the bases of Schiff have highlighted for these systems, excellent antifungal properties, antibacterial, antimalarial, antiproliferative, anti-inflammatory, anticancer, cytotoxic, antiviral and antipyretic[15,16].

Organic and organometallic compounds have been the subject of several recent studies for nonlinear optics (NLO) applications. This work applies not only to the experimental domain but also to theoretical chemistry, i.e., the investigation of novel molecular classes through the use of ab initio quantum chemistry techniques. The chromophore's elongation, the variation of metals and associated ligands, the realization of clusters or aggregates, and the variation of donor groups and acceptors at the ends of the chromophores are all factors that contribute to the improvement of the ONL response in the materials under study[17].

I.2.5. Complexing properties of Schiff bases

The complexant properties of Schiff bases are closely related to their structures, their stability as well as their basic or acidic character. Many works and works have illustrated the complexant power of Schiff bases with respect to all kinds of metal cations, both in solution and in the solid state.

It should be mentioned that the number of coordination sites required to produce a stable complex is determined by the valence of the metal ion. This value is often more than the metal cation's typical valence [18]. First, the aniline salicylidene type Schiff bases were used to create the complexes, along with other metal ions such nickel(II), copper(II), and iron(III).

All these studies have highlighted a number of results concerning the coordination mode of these systems and their geometries[19]. In recent years, the development of this coordination chemistry has focused on the synthesis and characterization of this type of complexes.

I.2.6 Sal(ph)en (non)symmetric metal complexes of Schiff bases

The usual procedure for generating salt ligand of symmetry C2 with extremely high yields involves condensation of one diamine on two equivalents of salicylaldehydes with the identical

substitution groups on their lateral aromatic cycles. While using different salicylaldehydes might lead to some degree of ligand property variation, the range of structures that can be accessible in this manner is still restricted.

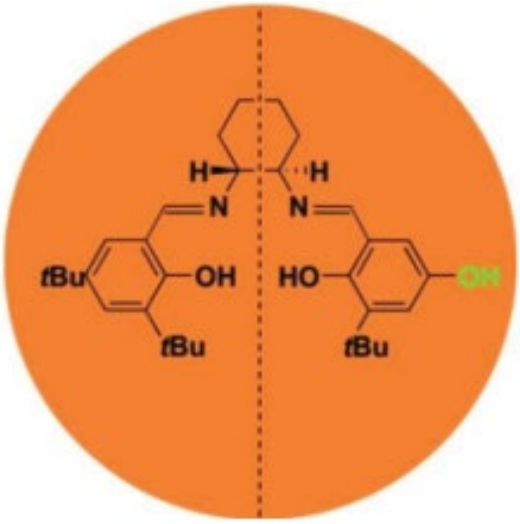

Figure I.5. Non-symmetric salen ligand.

I.3. Theoretical studies

I.3.1. Density Functional Theory (DFT)

Density functional theory, or DFT, replaces the wave function in the calculation of energy since its basic idea is to represent the energy of a multi-electron system from its electron density. This method is interesting because, regardless of the number of particles in the system, the electron density is a physically observable that depends only on the three variables (x, y, and z). As a result, it is not affected by the system's size. The complexity of an N-electron system rises with the number of variables, even though its wave function depends on 4N variables—3N space coordinates and N spin coordinates.

I.3.2. Foundations of DFT

The proposal put out by Thomas and Fermi in 1927[20,21] calls for using density as a variable rather than the wave function. A particular explicit density function was suggested as a model for the kinetic component in the Schrödinger equation. This method has a number of significant issues (it does not explain the covalent bond, for example). Several adaptations have been suggested, but they all have the drawback of include terms as and when subsequent approximations are taken into account—a problem that is already present in the Hartree-Fock method. Density,

however, results in fewer complicated solutions than when the wave function is used. Setting up a strict framework to overcome any approximation was made possible by Hohenberg and Kohna's method.

Density functional theory (DFT) uses the density ρ (r) as the fundamental variable and aims to characterize a system. The poly-electronic wave function Ψ (1,2,..., n) is used in methods from the Hartree-Fock (HF) framework. As a result, unlike the HF approaches, which study the n-electron issue in the space of dimension 3n, the DFT method studies it in the space of ρ (r), which is of dimension 3. The two theorems of Hohenberg and Kohn in 1964 [22] are credited with launching the DFT.

I.3.3. Quantum parameters

Chemists have traditionally used various variables, such as hardness or electronegativity, to explain chemical processes and occurrences. These values, however, did not correspond with any of the outcomes of computations using quantum chemistry.

Parr et al. connected the chemical potential μ to the reverse of electronegativity χ and to the energy derivative of the E system relative to the number of electrons N with constant external potential v(r) in a landmark paper[23] published in 1978.

$$\mu = \left(\frac{\partial E}{\partial N}\right)_{v(\vec{r})} = -\chi$$

Many more values, which we shall refer to as descriptors, have since been discovered. For example, molecular hardness η [24], which is the second derivative of energy with respect to electron count, has been found. Furthermore, it is the reverse of softness S:

$$\eta = \left(\frac{\partial^2 E}{\partial N^2}\right)_{v(\vec{r})} = \frac{1}{S}$$

The electronic density itself also proves to be an energy-related descriptor by its derivative in relation to the external potential:

$$\rho(\vec{r}) = \left(\frac{\delta E}{\delta v(\vec{r})}\right)_N$$

The Conceptual Density Functional Theory is based on these characteristics taken collectively (CDFT). Currently, many hundred descriptors have been suggested for various applications [25].

There are three types of descriptors:

• Global descriptors, which have a unique value for a given structure molecule,

• Local descriptors, whose value depends on the position in the space,

• Non-local descriptors, whose value depends on at least two positions in the space.

Among all these descriptors are descriptors derived from successive energy derivatives such as electronegativity or hardness mentioned below on, but also composite descriptors formed from the previous descriptors in order to reproduce certain phenomena, such as the electrophilic index. In practice, to calculate these descriptors, two main approaches are used:

• Frozen Molecular Orbitals (FMO) based on the properties (energy, density, etc.) of HOMO and LUMO in the N-electron system.

• Finite Difference Linearization (FDL) based on calculations of the N 1, N and N + 1 electron frozen geometry system.

These two approaches make it possible to evaluate the same descriptors but do not necessarily give the same values.

I.3.4. Global descriptors

I.3.4.1. Chemical Potential (μ)

The chemical potential μ mentioned above is defined as the first derivative of energy in relation to the number of electrons with constant external potential [23]. It is also the opposite of electronegativity χ.

It is a global descriptor indicating the ability of a molecule to gain or lose electrons: indeed, when two species A and B react and exchange electrons, with constant number of electrons N = NA + NB, the following relationship can be written for the system energy variation (first order):

$$\Delta E_{tot} = \Delta E_A + \Delta E_B = \mu_A \Delta N_A + \mu_B \Delta N_B = (\mu_A - \mu_B)\Delta N$$

In practice, μ is calculated either from the energies of the boundary orbitals, or from the energy of the system with a missing or additional electron:

$$\mu_{FMO} = EHOMO + ELUMO/\ 2$$

$$\mu_{FDL} = E(N + 1) + E(N - 1)/\ 2$$

I.3.4.2. Chemical hardness (η) and softness (S)

The definition of chemical hardness (η) was given by Parr and Pearson [23]in 1983. It is the primary derivative of the chemical potential in relation to the number of electrons with constant

external potential, and it is also the second derivative of energy. Additionally, it is the reverse of softness S:

$$\eta = (\partial^2 E / \partial N^2)_{v(\vec{r})} = (\partial \mu / \partial N)_{v(\vec{r})} = 1 / S$$

η is a global descriptor that represents the resistance of the system to electron transfer, while softness characterizes the opposite, the ability of the system to keep electrons.

η and S are also calculated either from the energies of the boundary orbitals, or from the energy of the system with a missing or additional electron:

$$\eta_{FMO} = I - A$$

I.3.4.5. Indices of electrophilia (ω) and nucleophilia (N)

Once fundamental notions like electronegativity have been identified, one may question if a descriptor characterizing the electrophilia and nucleophilia of reactive substances can be found. Parr and al.[26] developed a composite descriptor, which is not directly generated from an energy derivative but rather estimated from various descriptors, in response to Maynard et al.[27]'s connection of descriptors with the interaction energy in docking.

$$\omega = \mu^2 / 2\eta$$

ω is the electrophilic index and corresponds to the energy stabilization of the system during a charge transfer, more precisely the transfer of the optimum number of electrons to the electrophilic compound immersed in a sea of electrons at zero temperature and chemical potential and with constant external potential. Similar to hardness/softness, Domingo et al. [28] proposed defining a nucleophilia N index as the inverse of the electrophilic index:

$$N = 1 / \omega$$

I.3.4.6. Ionization potential (I)

This is the energy needed to pull an electron out of a system. That is, the energy needed to pass from the neutral molecule (n electrons) to the cation (n-1 electrons). The ionization potential is directly related to the highest occupied molecular orbital (HOMO) [29]. The ionization potential is defined as follows:

$$I = -E(HOMO)$$

I.3.4.7. Electronic Affinity (A)

It is defined as the energy gained by a system when it captures an electron. This energy gain accompanies the transition from a neutral system to an anion[30]. The electron affinity is directly related to the lowest unoccupied molecular orbital (LUMO). It is given by:

$$A = -E(LUMO)$$

I.3.5. Gaussian calculation code

Gaussian is a very general 'ab initio' quantum chemistry software originally created by John Pople and released in 1970 (Gaussian 70). It has since been constantly updated. This code takes its name from Pople's use of Gaussian orbitals to speed up computation compared to software using Slater orbitals. This facilitated the development of computational chemistry, particularly ab initio methods such as Hartree-Fock. Gaussian quickly became a very popular and widely used electronic structure program. Today, several high-level researchers are collaborating to enrich this quantum chemistry tool [31,32].

We can forecast the energies, molecule structures, vibration frequencies, and chemical characteristics of complex molecular systems using Gaussian, which is based on the fundamental rules of quantum mechanics. Both stable species and complicated compounds, as well as compounds that are hard to view experimentally, such ephemeral intermediates or transition states, can have their molecules and reactions examined under a variety of settings.

Our interest in chemical issues, such modeling reactivity, may be thoroughly investigated with Gaussian. For instance, it is possible to verify if projected stationary points are minima or transition structures (TS) in addition to quickly and accurately minimizing molecular structures and predicting transition state structures. Finding which reagents and products are related by a certain transition structure and following the intrinsic reaction coordinate (CRI) will allow you to compute the reaction route.

I.4. Non-linear optics (ONL)

Non-linear Optics (ONL) is the study of the optical response of materials when subjected to very intense radiation. ONL is a field that appeared shortly after the invention of the laser and the first observation of Second Harmonic Generation (GSH) by Franken et al. dates from 1961[33]. Before detailing the ONL approaches we must first define the linear polarization.

I.4.1. the linear polarization

The irradiation of an anisotropic material by a light wave characterized by an electric field E [$V.m^{-1}$] associated with a magnetic field H [$A.m^{-1}$], gives rise to the deformation of the electronic cloud by the coulomb force, which generates an induced polarization. The latter takes the linear character in the case where the electric field of the light wave is weak ($E < 10^5$ $V.m^{-1}$) compared to the electric fields of the valence electrons (10^{10} à 10^{11} $V.m^{-1}$)[34].

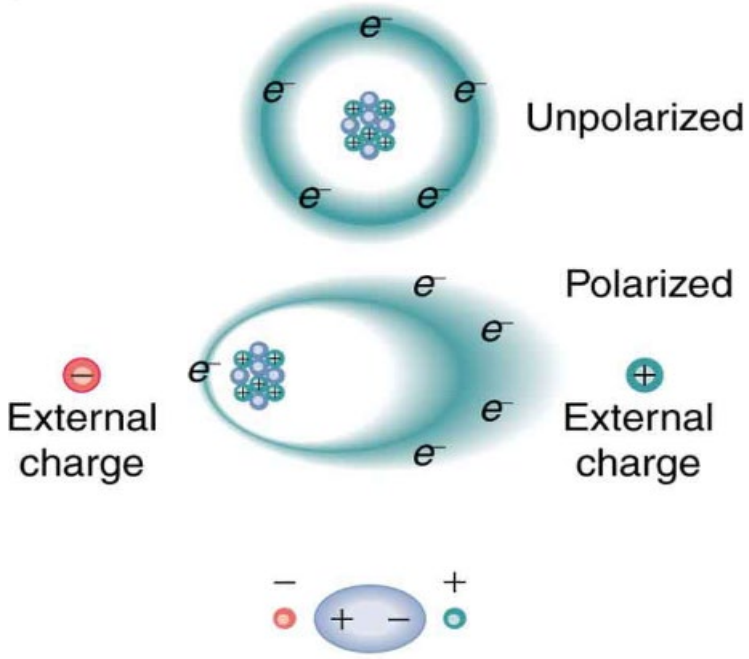

Figure I.6. Effect of an electric field on an atom and its electronic cloud.

I.4.2. Non-linear polarization

The interaction of the electric field E of a light wave and a dielectric medium (supposed non-magnetic) is governed by polarization P. This polarization represents the electric dipole moment density per unit volume and reflects the displacement of the weakly bound charges of the medium under the influence of the eclectic field. When this field is sufficiently intense ($E >> 10^5$ $V.m^{-1}$) the response of the medium (thus the polarization) is a non-linear function of the excitation[35] . ONL polarization is determined at the macroscopic or microscopic level.

I.4.2.1. Description at the microscopic level

The non-linearity at the microscopic scale is defined by the induced dipole moment of active materials in ONL, hence the total dipole moment is written as a series development of the E field in the semi-classical formalism as follows [36,37]:

$$\mu_i(E) = \mu_i^0 + \alpha_{ij}E_i + \beta_{ijk}E_jE_k + \Upsilon_{ijkl}E_jE_kE_l + \cdots$$

Where

μ^0 is the potential permanent dipole moment of the molecule in the absence of E

αij is the linear polarizability, or β_{ijk} , γ_{ijk}… are the hyperpolarisabilities respectively of the first (or quadratic) and the second order (or cubic).

The tensors α, β and γ are defined by the first, second and third leads of the induced dipole moment on the E field [38].

I.4.2.2. Description at the macroscopic level

At the macroscopic level, for a molecular population, which allows the interaction of several electric fields, and thereby modifies the frequency, phase or polarization of incident light. Dielectric polarization is similarly expressed by the following equation [39]:

$$P = \varepsilon_0\left(\chi^{(1)}E + \chi^{(2)}E^2 + \chi^{(3)}E^3 + \cdots\right)$$

The term $\chi^{(1)}$ represents linear susceptibility, The terms $\chi^{(2)}$ and $\chi^{(3)}$ are nonlinear susceptibilities of order two and three, respectively. ε_0 is the permittivity of vacuum [40].

I.5.The Hirshfeld surface

Among the main aims of this work is the study of intermolecular interactions in crystallographic structures of coordination complexes. For this purpose, a method dedicated to the study of the latter on the basis of calculations of molecular surfaces from the Hirshfeld partition[41], was adopted. Therefore, the different representations of surfaces (SH) will be analyzed to identify all the intermolecular contacts taking place within these crystals.

The Hirshfeld surface represents a characteristic property of each molecule belonging to a crystalline structure. Because the Hirshfeld surface depends on the molecular environment, there are several surfaces for a single molecule depending on the crystal structure to which it belongs.

I.5.1. Foundations

A molecule in a crystal may be represented by its Hirshfeld surface [42], which is created by segmenting the crystal's space into areas where the electronic distribution of a molecule's (the

promolécule) sum of spherical atoms dominates the equivalent total on the crystal (the procristal).

Considering ρA(r) as the average electron density of an atomic nucleus A centered on this nucleus, the Hirshfeld results from a distribution function ω(r) defined by the following equation:

$$\omega(\mathrm{r}) = \frac{\rho_{promolécule}(\mathrm{r})}{\rho_{procristal}(\mathrm{r})} = \frac{\sum \rho_A(\mathrm{r})[A \in molécule]}{\sum \rho_A(\mathrm{r})[A \in cristal]}$$

The Hirshfeld surface, surrounding a molecule, is defined when $\pm(\mathrm{r}) \geq 0.5$, which corresponds to the region where the contribution of the promolécule to the electronic density of the procristal exceeds that of the other molecules of the crystal. In order to obtain as much information as possible in practice, it is imperative to transpose the results in graphical form.

I.5.2. Properties of surfaces de and di

The simplest and most immediately useful property for mapping the surface is the distance between the surface and the nearest kernel external to the surface, which we call (de). This property provides an immediate picture of the nature of the intermolecular contacts in the crystal.

In the same way, we can define (di), the distance from the surface to the nearest core internal to the surface, which is useful when used in conjunction with (de).

The range of (de) and (di) across the Hirshfeld surface varies considerably depending on the atoms in the molecule (size dependence) and the particular type of in-termolecular interaction tested (interaction dependence).

Mapping the same range of all molecules would reduce color contrast for molecules with a small range of contact distances (such as hydrocarbons). To make the most of the color mapping on the surface, we choose a range of more suitable for each group of molecules in direct comparison

I.5.3. Properties of dnorm surfaces

Another way of illustrating Hirshfeld surfaces is to generate an im-plicate representation of normalized contact distances taking into account the van der Waals radius of the atoms involved in the analysis. This way of depicting the surface is named dnorm [43,44]. This property is constructed by summing the normalized contribution of (de) and (di) in relation to the van der Waals radius of the atoms involved in the expression. The term dnorm is given by the following equation:

$$d_{norm} = \frac{d_i - r_i^{vdW}}{r_i^{vdW}} + \frac{de - r_e^{vdW}}{r_e^{vdW}}$$

More concretely, this type of analysis makes it possible to illustrate graphically the relative position of neighboring atoms belonging to molecules interacting together.

Again, a color gradient is used to quantify the interactions between atoms within the studied crystal. The 3D image of the Hirshfeld surface which is represented by the value of (dnorm) where the color shades represent:

• Red: When atoms form intermolecular contacts shorter than the sum of their Van der Waals rays.

• White: Contacts around the sum of Van der Waals rays in the dnorm surface.

• Blue: The longest contacts of the sum of Van der Waals rays.

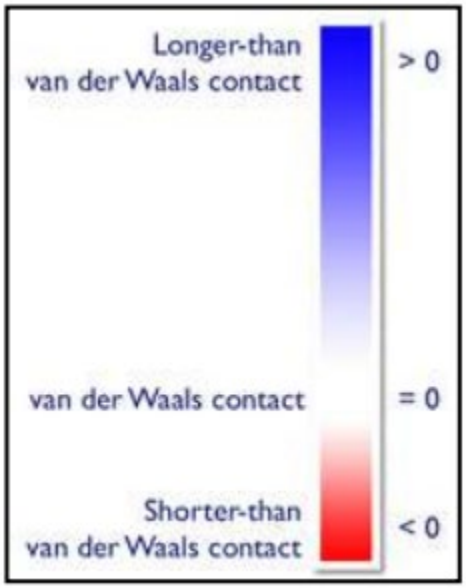

Figure 1.7. Colors adapted to (dnorm) in the Hirshfeld surface

I.5.4. 2d fingerprints of Hirshfeld surfaces

Another way to analyze the complex information contained in the structure of a molecular crystal is the 2D impression of Hirshfeld surfaces[45,46]. The graphic distribution of all pairs (di, de) highlights the types of interactions observed in the crystal as well as the frequency of overlaps. The diagrams that result from this type of analysis are a fingerprint of the intermolecular interactions in the crystal.

This kind of representation allows to characterize intermolecular interactions because several of them generate a particular pattern in the obtained graphs. In addition to listing all the contacts in the crystal, it is possible to isolate specific contacts between certain atoms. This allows to

highlight non-covalent interactions of type C− H… π, halogen… halogen, C− halogen… H and stacks π…. π taking place in the arrangements studied.

When studying this type of graph, it is important to pay particular attention to contacts whose values of di and approximate the size of the van der Waals rays of the observed atoms. For a pair (di, de), the sum of these components is equivalent to the distance separating the atoms contributing to this point

Close contacts are present when the sum of these components is smaller or equal to the sum of the van der Waals rays of the atoms involved. It should be noted that these contacts take the form of slides pointing to the origin of the graph studied. This criterion is expressed by the following equation [47]:

$$d_i + d_e \leq r_i^{vdW} + r_e^{vdW}$$

I.5.5. Curvedness and Shape Index

➢Curvedness

is dependent on the surface's mean-square curvature, and it applies to flat surfaces. The curvature of a Hirshfeld surface may be used to establish a coordination number in a crystal because Hirshfeld surfaces with high curvature tend to split the surface into contact plates with each neighboring molecule.

➢Shape Index

is a qualitative shape measure that can pick up on even the smallest variations in surface form, particularly in areas with extremely tiny overall curvature. Further troughs can be located using the form index maps on the Hirshfeld surface.

I.6. Antioxidant activity

The identification of radical chemical species that are typically found in the body has improved our comprehension of biological processes. Since these free radicals are beneficial to the body in moderation, they are produced by a variety of physiological processes. However, when these radicals are produced in excess or as a result of externally induced toxicity, the body must defend itself against these excesses using a variety of antioxidant systems[48].

Oxidative stress is linked to the emergence of diseases including Parkinson's and Alzheimer's [49], cancer and coronary diseases [50], and autoimmune disorders. Oxidative stress is caused by imbalances between the generation of free radicals and antioxidant enzymes. Numerous beneficial antioxidant elements, such as selenium, vitamins C and E, β-carotene and other carotenoids, and other polyphenolic chemicals from plant diets, have been found by epidemiological research .

Reactive oxygen species (ROS) are naturally produced during cellular respiration; most cells have the capacity to produce superoxides [51] . The term "endoglamiento respiratorio" (ERO) is a general term that encompasses both oxygen free radicals and some reactive non-badiar oxygen derivatives with notable toxicity [48,49]. These latter damage cell life by oxidizing lipids, proteins, and DNA [50]. The progression of this oxidation appears to be the source of numerous pathogenic and toxic phenomena and speeds up the aging process [52].

I.6.1. Oxygen

Oxygen (O2) is an essential element for life, it is used by all organs with varying proportions. O2 is one of the components of living matter. It plays a very important role in mitochondrial respiration in order to produce energy. The reduction of this species during the oxidation of endogenous or exogenous molecules will lead to the production of reactive oxygen species (ROS).

At low concentrations, ROS have a crucial function in normal physiology processes, as a second messenger in cell signaling. A surplus of these molecules is accompanied by deleterious effects on biomolecules [53,54], they are involved in the oxidation of nucleic acids, pro-teins, and thus in lipid peroxidation [55].

Every day, the body produces OERs, but the defense mechanism neutralizes them right away. This results in an equilibrium between antioxidants and oxy-ydants. The term "oxidative stress" refers to the condition that results when the body's defenses against these chemicals are inadequate.

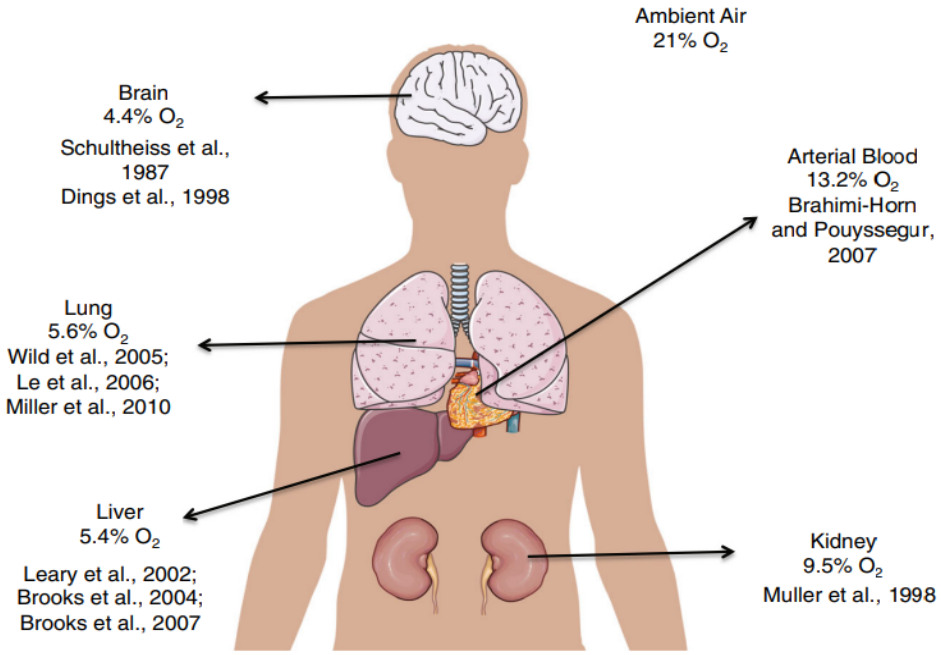

Figure I.8. Oxygen distribution in various organs.

I.6.2. Oxidative stress

The term "oxidative stress" was first used in 1991 by «Sies», who defined it as the body's incapacity to protect itself from the aggression of free radicals (ROS)—a term that refers to all free radicals and their precursors—after an imbalance that either increased the production of ROS or decreased the body's ability to fend off their attacks. When an organism, cell, or compartment of a cell's antioxidant defense system is overpowered by oxidants, a disruption in the cellular metabolic equilibrium is known as oxidative stress[56,57].

Nutritional inadequacies, excess antioxidants, or deficits are the causes of this syndrome [48]. excessive synthesis of prooxidant substances with an inflammatory origin inside the body [58], or exposure to prooxidant factors in the environment (pollution) such as alcohol, tobacco, narcotics, gamma rays, UV rays, herbicides, ozone, asbestos, and toxic metals [59]. Numerous illnesses, including diabetes mellitus, cancer, and cardiovascular disorders, may emerge as a result of an individual's increased oxidative stress. A nutritious diet that is high in fruits and vegetables is especially crucial for providing appropriate antioxidant defenses, which are necessary to avoid various disorders [60,61].

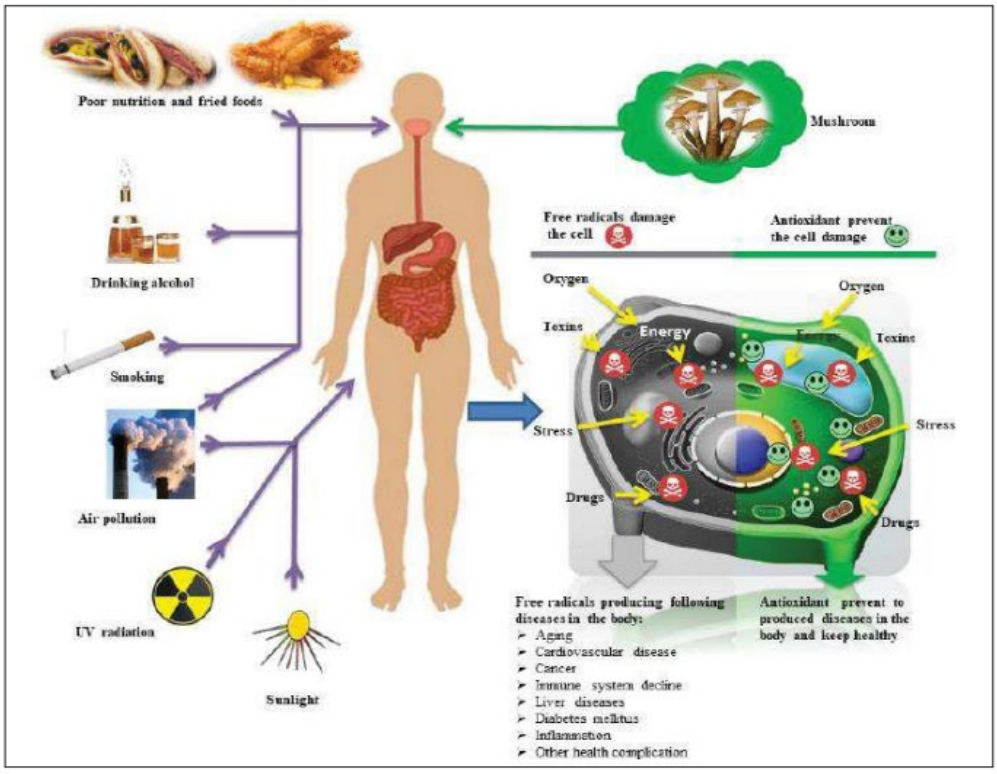

Figure I.9. Different oxidative stress factors [62]**.**

1.6.3. Consequence of oxidative stress

Antioxidant deficiency and/ or overproduction and uncontrolled ROS is not without harmful consequences in the body, because it often leads to oxidative stress which is defined as an imbalance between the antioxidant system and oxidant production (ROS) [63]. The main danger of these oxygenated molecules comes from the fact that they cause damage to different cellular components such as lipids, proteins, DNA etc... the degradation of cells and tissues [48,64,65]. Apart from these deleterious effects throughout the body, oxidative stress is largely involved in aging and in the appearance of certain pathologies (figure I.14) such as cancer, diabetes, atherosclerosis, osteoporosis, stroke, neurodegenerative diseases and inflammatory diseases [64,66–68].

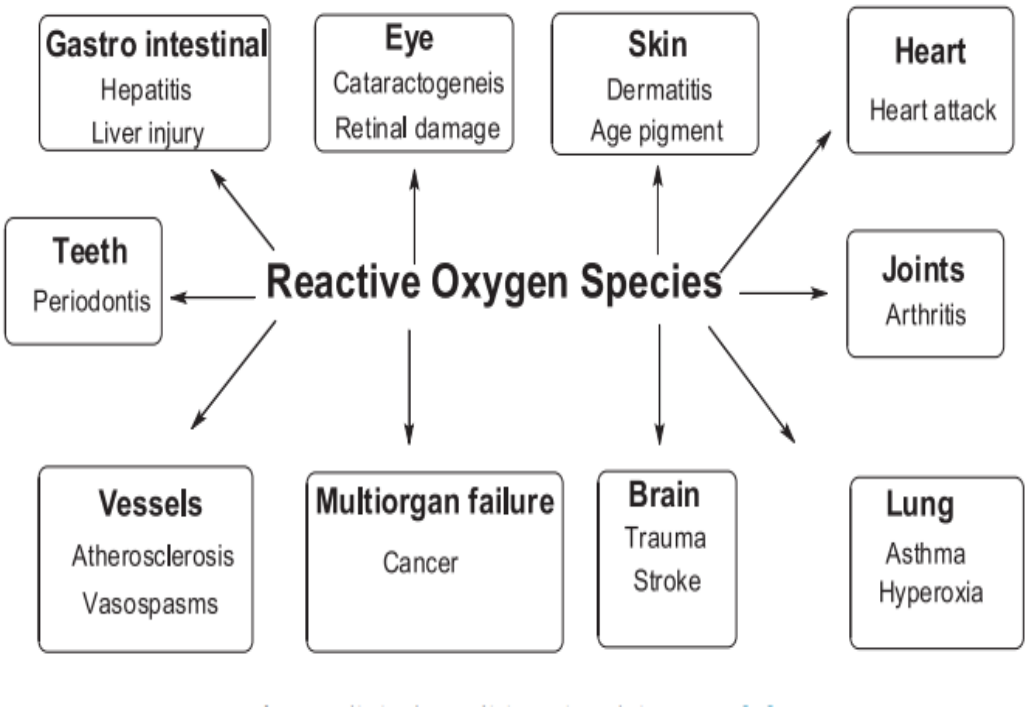

[69].

I.6.4. Free radicals

Free radicals are highly reactive atoms or molecules with an unpaired electron (single electrons). They have a very short existence of 10-9 to 10-12 seconds before colliding with another molecule and either capturing or giving an electron to become stable [70,71]. Distributed in reactive oxygen species (ROS) and reactive nitrogen species (RNS)[72]. In doing so, they generate a new radical from the molecule they collided with.

Under normal circumstances, the body produces free radicals, which damage lipids, proteins, and nucleic acids in cell membranes, regardless of the toxin that initiates the process [72]. The most harmful free radicals found in biological systems found in aerobic cells, such as those found in human cells, are radical oxygen species, which include hydrogen peroxide, superoxide anions, hydroxyl radicals, and transition metals.

Superoxide radicals seem to be less reactive than hydroxyl radicals, which are the most aggressive and harmful kind of oxidative stress[48,71] .Radical oxygen-induced tissue damage is commonly referred to as oxidative damage, and antioxidants are substances that shield tissue against radical oxygen-induced damage [70].

Table 1.1 Different types of reactive species[73].

Espèces radicalaires		Espèces non radicalaires	
Nom	**Symbole**	**Nom**	**Symbole**
Anion superoxyde	$O_2^{\bullet-}$	Acide hypochlorique	HOCl
Monoxyde d'azote	$NO^{\bullet}$	Oxygène singulet	$^1O_2$
Radical alkoxyle	$RO^{\bullet}$	Peroxyde d'hydrogène	H_2O_2
Radical hydroxyle	$OH^{\bullet}$	Peroxyde organique	ROOH
Radical peroxyle	$ROO^{\bullet}$	Peroxynitrite	$ONOO^-$

I.6.4.1 Reactive Oxygen Species (ROS)

In aerobiosis, oxygen (O2) is a vital component for living activities. Reactive oxygen species (ROS) are created when breathed oxygen is altered by at least 5%. According to Merksamer et al. (2013), reactive oxygen species (ROS) are a class of chemicals that result from partial molecular oxygen reduction. Produced in response to a variety of stimuli, such as growth factors, cytokines, and chemotactic factors, ROS are significant mediators of signaling throughout numerous biological processes [74].

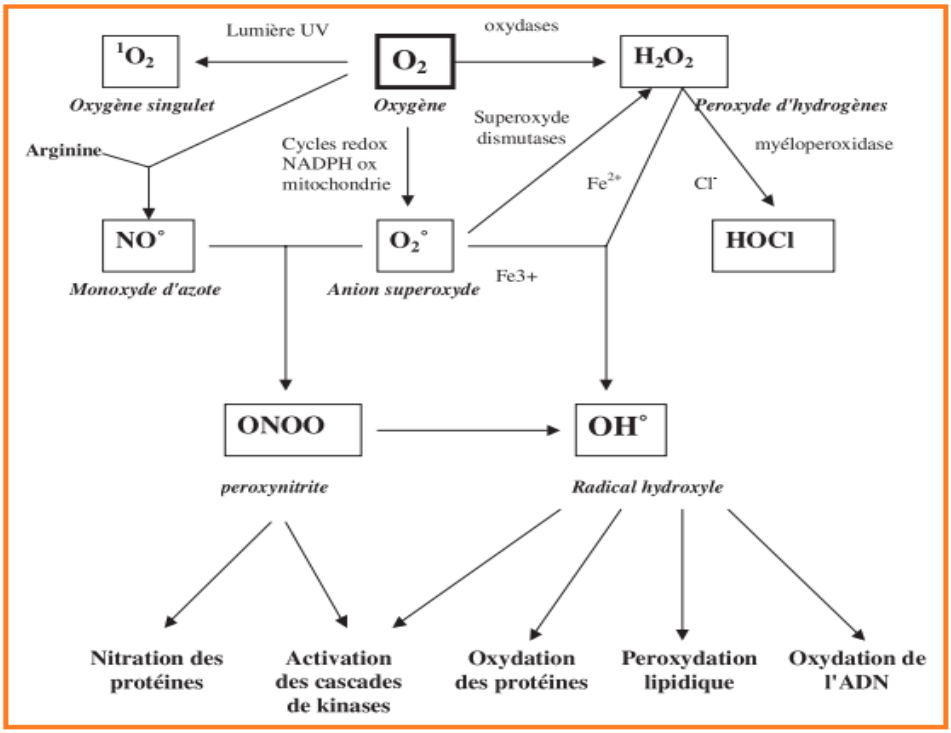

Scheme I.6. Origin of different oxygen free radicals and ROS involved in biology [48].

I.6.4.2 Reactive nitrogen species (RNS)

Nitric monoxide (NO•), an RNS, is endogenously produced from arginine, oxygen and NADPH (Nicotinamide adenine dinucleotide phosphate) by several nitric oxide synthase (NOS) enzymes in response to a number of physiological stimuli. NO• is a highly reactive species, it represents the ideal molecular messenger, it is involved in the regulation of a number of functions including blood pressure, phagocytes and antimicrobial activity, endothelial and neuronal homeostasis, platelet and leukocyte adhesion, and apoptosis induction [75].

Spontaneous generation of O2 •- and radical NO• promotes the formation of peroxynetrite (Equation below) which is a highly toxic product, a RNS itself capable of inducing lipid peroxidation and protein nitration [75].

$$O2 \bullet^- + NO\bullet \Longrightarrow ONOO^-$$

I.6.5. Production of free radicals

I.6.5.1. Intracellular production

The production of EOR in mammalian cells results from several possible sources (Figure I.16) but is essentially of enzymatic origin. It is mainly NAD(P)H membrane oxidase and mitochondrial enzymatic complex of the respiratory chain

.

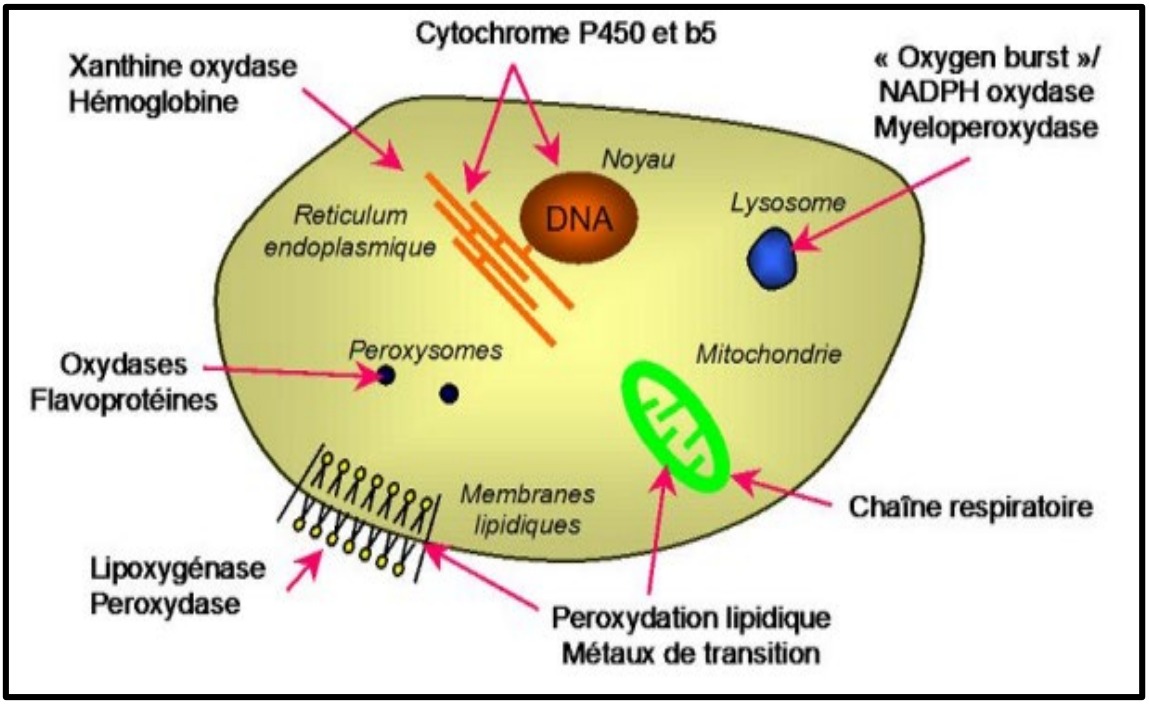

Figure I.10. Intracellular ROS production sites [76].

NAD(P)H oxidase is a membrane enzyme that catalyzes oxygen reduction according to:

$$NAD(P)H + 2\ O2 \rightarrow NAD(P) + + H+ + 2\ O2\ \cdot-$$

Cytochromes P450, terminal electron acceptors of the electron transport chain complex, located in the mitochondrial membrane, catalyze the reaction:

$$O2 + 4\ e- + 4\ H+ \rightarrow 2\ H2O$$

This transport chain releases a certain proportion of electrons, about 2%, which will partially reduce oxygen to lead to the formation of the superoxide radical:

$$O2 + 1\ e- \rightarrow O2\ \cdot-$$

Given the intense activity of the respiratory chain in aerobic organisms, this leakage of electrons seems to anticipate the activities of NAD(P)H. In addition, in mitochon dries, the oxidation of coenzymes, such as reduced flavoproteins, is accompanied by a loss of protons and electrons which, via the transport chain, are then transferred to the O2.

Other sources can also play a role in the production of radicals such as xanthine oxidase which reduces molecular oxygen to superoxide ion, peroxisomes which have several enzymes sources of hydrogen peroxide and lipo-oxygenases, in-zymes of the arachidonic acid pathway that notably allow the synthesis of prostaglandins, oxidize fatty acids to give unsaturated fatty acid hydroperoxides [63].

In addition, during antibacterial defense, phagocytic cells activated by an inflammatory reaction will produce a large number of ROS. In addition, there is mas-sive production of superoxide anion by the leukocyte mechanism. This is the respiratory outbreak. The NO synthases, at the origin of the NO• radical, may, under certain conditions, also produce superoxide anions [63,77].

I.6.5.2. Extracellular production

The environment and lifestyle are also responsible for the creation and accumulation of free radicals in the body. These environmental factors including non-genotoxic carcinogens can be directly or indirectly involved in the generation of free radicals (xenobiotics, leukocyte activation...). UV radiation induces the synthesis of O2 •- , OH• , O2 and H2O2 via photosensitizing agents [76]

Nitrogen oxide (NO) and nitrogen dioxide (NO2) present in our way of life (tobacco, ionizing radiation, electric fields, industrial pollutants), as well as unhealthy food (refined, rich in saturated fat and sugar, alcohol consumption, etc.), are all elements promoting the genesis of free radicals [78].

I.6.6. The body's antioxidant systems

Given the uncertainty surrounding the relationship between oxygen consumption and hazard, nature has evolved a robust system of antioxidant defenses to regulate metabolism as accurately as possible. Any chemical, whether manufactured or natural, that has the ability to prevent oxidation is an antioxidant. These molecules get involved in the oxidation process at various points. In order to prevent the formation of peroxides, it can act in a variety of ways, such as by trapping the compounds that start the radical reaction, neutralizing the super-oxide anion, completing the propagation reaction in the reacto-radicalization to lower the concentration of oxygen, and so on [69]. Antioxidants come in a wide variety of forms, both natural and synthetic:

I.6.6.1. Enzymatic systems

The body has a number of mostly endogenous enzyme compounds that are capable of battling ROS. This is glutathione peroxidase, which detoxifies hydrogen peroxide and other hydroperoxides [62,64,65] ; catalase, which catalyzes the transformation of hydrogen peroxide into water and molecular oxygen; and superoxide dismutase, which can help dismutate superoxide anion into hydrogen peroxide and molecular oxygen [64].The body's initial line of defense against oxidative stress is thought to be this mechanism.

I.6.6.2. Non-enzymatic Systems

Usually, eating brings them. These comprise polyphenols, vitamins A, C, and E, carotenoids, and trace elements (copper, zinc, selenium, magnesium, and manganese) [48,61,62]. These antioxidants work by preventing or reducing the production and propagation of free radicals [79]. Moreover, artificial antioxidants such tertiobutylhydroquinone (TBHQ), butyl-hydroxy-toluene (BHT), and butyl-hydroxy-anisole (BHA) have long been added to food products as possible lipid oxidation inhibitors [80].

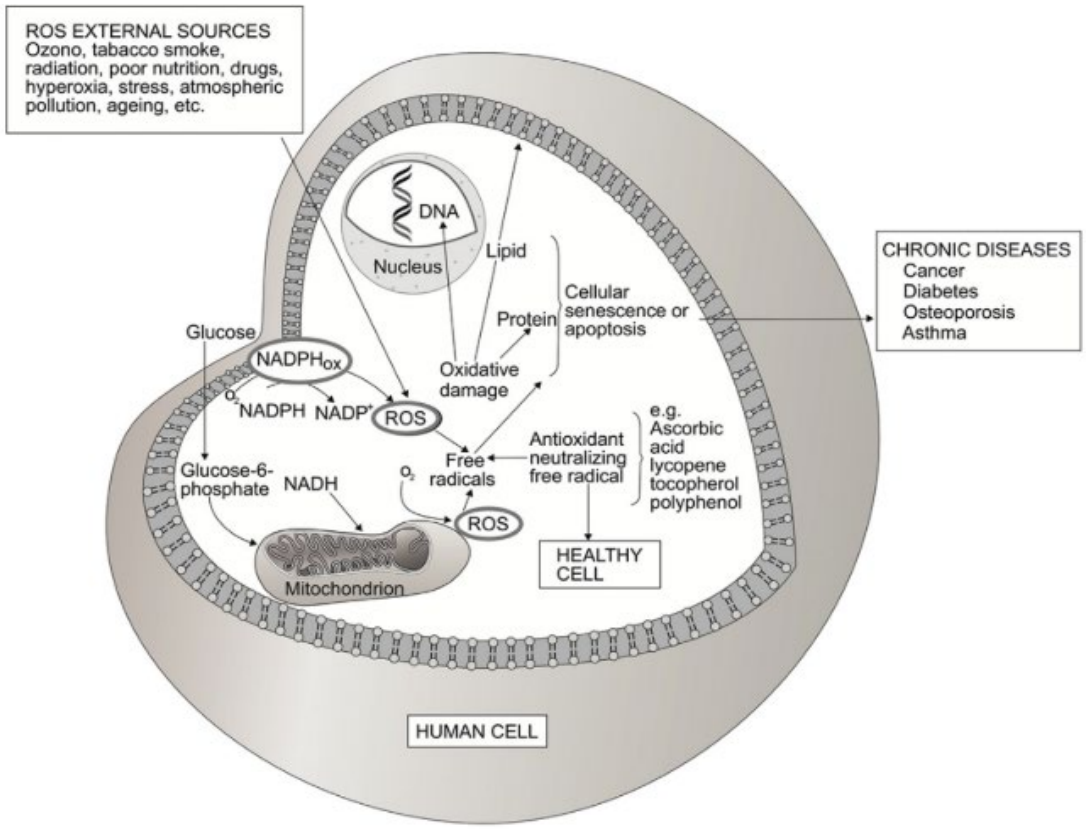

Figure I.11. The neutralization of free radicals by an antioxidant agent is important to maintain a healthy cell.

I.6.7. Mechanisms of action of antioxidants

Antioxidants work through a variety of processes, such as chelating transition metals, reducing radicals or peroxides, capturing singlet oxygen, and deactivating radicals by covalent addition reactions. Generally speaking, an antioxidant that oxidizes more quickly than one substrate can stop another substrate from oxidizing. This kind of impact is caused by a structure that contains donors of hydrogen atoms or electrons, frequently aromatic ones, as in the case of phenol derivatives. Their intermediate radicals are also comparatively stable because of resonant delocalization and a deficiency of molecular oxygen-attackable sites [71,81]. Antioxidants are divided into two groups based on how they function:

I.6.7.1. Primary or anti-radical antioxidants

By transferring a hydrogen atom and functioning as scavengers of lipid free radicals, these antioxidants can stop the autocatalytic cascade of oxidation. The antioxidant then turns into a carrier of a radical itself, but because it is less reactive than lipid radicals, it prevents the radical from spreading. Because of the remarkable stability that their aromatic cycle provides, phenolic

compounds make up practically the whole class of antioxidants. This category comprises plant polyphenols (flavonoids, phenolic acids, diterpenoids), tocopherols (vitamin E), and antioxidant additives (BHA, BHT, TBHQ, gallates) [79,82].

I.6.7.2. Secondary or preventive antioxidants

These antioxidants that can prevent the formation of free radicals work through a variety of indirect mechanisms, such as chelating oxidizing-promoting metals like iron and copper as lecithins and citric acid, breaking down hydroperoxide into non-radical species like alcohol, thiols (glutathione, sulfur amino acids), or disulfides, repairing primary antioxidants through the donation of hydrogen or electrons, deactivating singlet and triplet oxygen sequestrants like ascorbic acid, β-carotene, and lycopene, and absorbing UV radiation through carotenes [59,71].

I.7. Literature on some Schiff-based compounds

The synthesis of Schiff's foundations is a topical research theme that continues to attract numerous research teams around the world. This can be mainly associated with the importance and variety of applications of these types of compounds. Schiff bases are widely used in the biological and non-organic field. To this end we will briefly clarify the biological interest by citing some essential publications that lead to enrich the exploitation of certain imine compounds.

M. Dehar et al [83] synthesized original styrenic Schiff bases derived from heterocyclic amines such as 2-aminothiazole and 4-amino-1,2,4-triazole known to their biological and pharmacological activities. The comparative hydrolysis study of m and p N-vinylbenzylidene-4-amino-1,2,4-triazole was studied by UV-visible spectroscopy in homogeneous aqueous environment buffered at several pH at T = 25°C. The room temperature condensation reaction of aminothione on different commercial aromatic aldehydes in ethanol and in the presence of piperidine easily leads to the formation of imine (70-92%). The structure of all the compounds obtained was determined by spectroscopic methods (IR, NMR 1H and NMR 13C). The study of UV-Vis in methanol shows that some molecules presenting the phenomenon of delocalized electrons π are responsible for the bathochromic effect [84]. Pyrimidine compounds play an important role in coordination chemistry, they form Schiff base compounds with a carbonyl (aromatic and non-aromatic) [85]. Schiff bases are structurally characterized by the imine fragment, RHC = NR. Pyrimidinyl Schiff base ligands achieve better stability of complexes

metal with transition metal ions. Because of their easy preparation, solubility in polar and non-polar common solvents, stereochemical and chemical processing and electronic properties [86], pyrimidinyl derivatives have been associated with various biological activities such as antibacterial [87], antitumor/anticancer , anti-HIV , antioxidants [88].

M.Me and al [89] synthesized three new Schiff (I-III) base compounds by a condensation reaction in 1:2 M ratios of 4.40 -diaminodiphenyl sulphide and pyr-rol/thiopene/furan-2-carboxaldehyde in ethanol. The structural determinations of the Schiff bases were identified by means of an elemental analysis and confirmed by UV-Vis, FT-IR and 1 H NMR. Antibacterial and antifungal activities of the synthesized compounds were studied in vitro using the diffusion method. The individually synthesized Schiff bases showed varying degrees of inhibitory effects on growth of microbial species tested.

Ö. Altun and al [90] synthesized a Pt (II) [Pt (L1) (L2)] complex using a Schiff (L1) base derived from L-phenylalanine with furfuraldehyde in the presence of 8-hydroxyquinoline (L2). The structure of the complex was studied by Electrospray ionization mass spectrometry (ESI-MS), UV-visible spectroscopy, Fourier transform infrared spectroscopy (FT-IR), 1H nuclear magnetic resonance (NMR), 13C NMR, X-ray diffraction powder (XRD), Scanning Electron Microscopy (SEM), Analytical Energy dispersive X-ray (EDX) and thermogravimetric and differential thermal analysis (TG-DTA). Antimicrobial activities of L1 and the complex have shown that the compounds have significant antibacterial and antifungal properties. They also show significant cytotoxic effects against the growth of mouse embryo fibroblasts (MEF) and human prostate adenocarcinoma cancer cells (Du145). The tests of L1, L2 and the Pt (II) complex on antioxidant activity showed an effective core activity.

Amali.I.B and col [91] studied a series of metal complexes(II) [Cu(L)] (1), [Co(L)] (2), [Ni(L)] (3) and [Zn(L)] (4), as well as their structural characterizations with various analytical and spectroscopic techniques. Monocrystalline XRD studies suggested that prepared metal complexes (II) adopted a deformed tetrahedral geometry. The 1H NMR and FTIR data concluded that the Schiff H2L base ligand acts as a tetradentate ligand coordinating with the metal(II) ions through the oxygen atom of the phenolic group and the nitrogen atom of the azomethrin group. Complexes 1 and 4 have been shown to be effective in causing antimicrobial activity. The 3-(4,5-dimethyltrtryzol-2-yl)-2,5-diphenyltetrazolium bromide (MTT) assay showed remarkable

cytotoxicity of complex 1 (IC50 = 19 1,1 µg/mL) on human breast cancer MCF-7 cells compared to Schiff H2L base ligand and complexes 2-4. In addition, the AO/EB staining assay revealed cell death due to apoptosis in MCF-7 cells and the generation of ROS by the Schiff H2L base ligand and its metal (II) 1-4 derived complexes may be a possible cause of their cytotoxic activity.

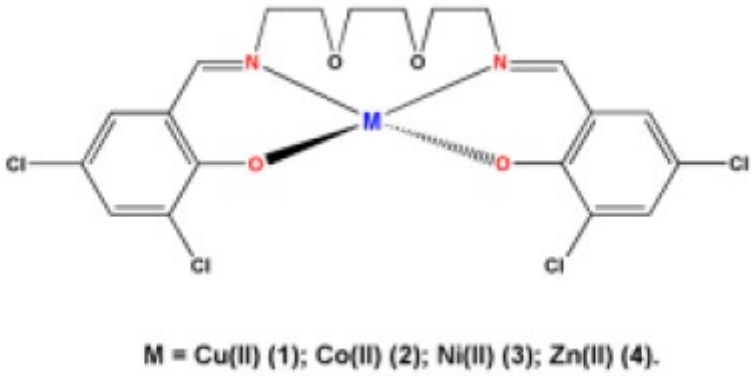

M = Cu(II) (1); Co(II) (2); Ni(II) (3); Zn(II) (4).

Figure I.12. General diagram of the complex developed by Ameli .I.B and col [91].

In 2021, Mahira Memisevic et al [92] have synthesized copper(II) complexes, [Cu(SB6-8)2] (6 – 8) by refluxing ethanolic solution of Cu (OAc)2·H2O with N-n-alkylsalicylidenimine Schiff bases (HSB6 -HSB8). 1, 2-Hydroxybenzaldehyde or its 5-chloro derivative is simply condensed with n-propyl- and n-butylamine in 100% ethyl alcohol to produce ligands. Single crystal X-ray analysis displays nearly perfect square planar CuO2N2 trans geometry of the complexes in which there is a bidentate mode of coordination of iminophenate to the metal ion by way of deprotonated phenolic oxygen and azomethine nitrogen

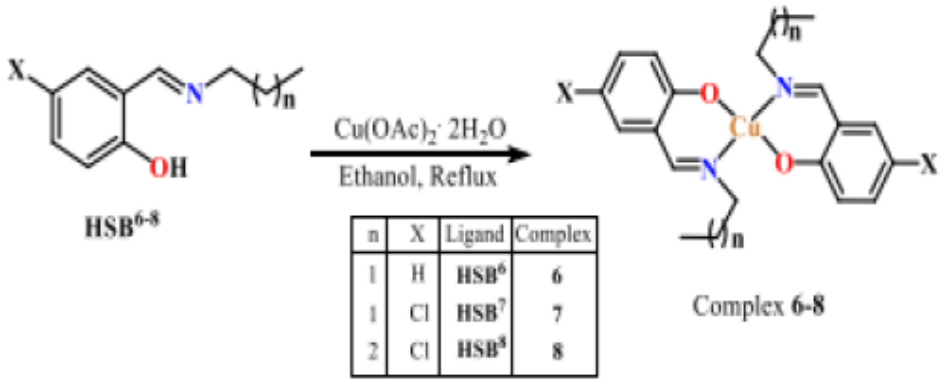

n	X	Ligand	Complex
1	H	HSB6	6
1	Cl	HSB7	7
2	Cl	HSB8	8

Scheme I.7. Chemical drawings of synthesis and X-ray characterized structure of 6–8 studied by Mahira Memisevic et al [92].

Krishna, G. A and al [93] prepared a flexible class of Ni(II) and Zn(II) complexes with a new Schiff base ligand containing a fraction of imidazole. The synthesized compounds were taken for separate structural characterizations. The coordination construction of the Ni(II) and Zn(II) complexes was found in octahedral and tetrahedral form where the metal ions Ni(II) and Zn(II) were composed of a nitrogen atom of azomethrin, an imidazole ring and an oxygen atom of acetate. All synthesized compounds were tested for their biochemical properties, including antioxidant, anti-inflammatory, antimicrobial activities, enzymatic inhibition and cytotoxicity. The antioxidant activity of the designed compounds was investigated by the technique of 1,1-diphenyl-2-picrylhydrazyl (DPPH) and all Schiff base ligands and some of its Ni(II)/Zn(II) complexes showed antioxidant activities close to standards (BHA, BHT and ascorbic acid).

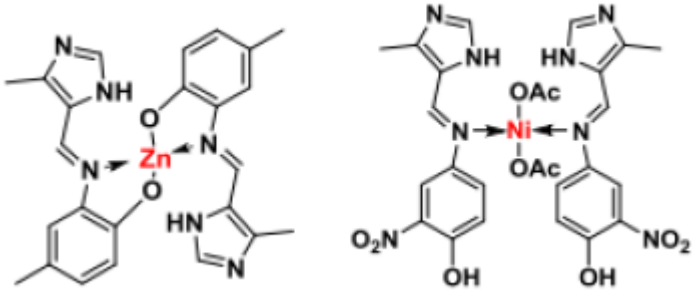

Figure I.13. Structure of Schiff base metal complexes prepared by Krishna, G. A and al[93].

I.8. Literature on some Schiff compounds derived from 5-Bromosalicylaldehyde

Bahçeli. S and col [94] are conducting a study on 5-bromosalicylaldehyde (5BSA) where they are evaluating its performance for application in organic solar cells. The possible conformists of the 5BSA were studied using the MMFF methodology in the Spartan software. The geometric optimization of the modifications for each conformation was calculated using the DFT approach for the function B3LYP/6-311+ +G(d,p).

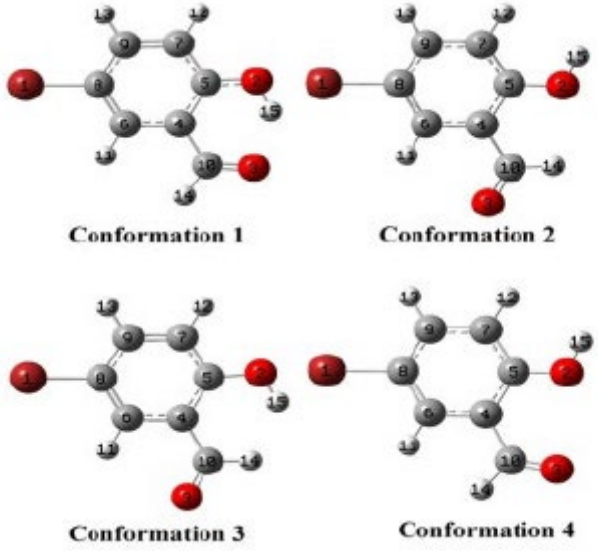

Figure I.14. Four conformers of 5BSA molecule stadied by Bahçeli. S and col [94].

a new base of Schiff, (E)-3-((5-bromo-2-hydroxybenzylidene)amino) propanoic acid was synthesized from 5-bromo salicylaldehyde and β-alanine by **Meenukutty M** and col [95]. This study investigates the evaluation of a novel Schiff base as an inhibitor against human breast cancer cell lines (pdb:3GEY) using 2-(dimethylamino)-N-(6-oxo-5,6-dihy drophenanthridine-2-yl) acetamide (DDA) as a native ligand.

The synthesized Ligand anchored in the B-chain of the PARP enzyme binding site to visualize the best posed and favorable ligand-protein binding interactions. The Swiss tool ADME determines the resemblance of the drug and strongly suggests that SBL may be a promising candidate for fighting breast cancer. DFT studies were performed to support the experimental results using B3LYP/6-311þG(d,p) and geometry optimization was performed. Various thermodynamic parameters and NLO properties were discovered. The ECD and VCD spectrum was explained using DFT studies.

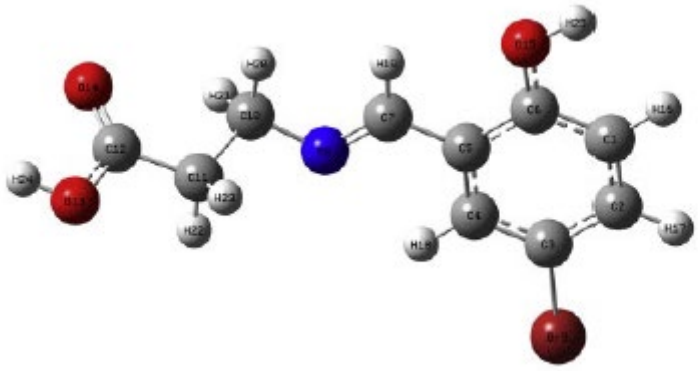

Figure I.15. Optimized structure of (E)-3-((5-bromo-2-hydroxybenzylidene)amino) propanoic acid prepared by Meenukutty M and col [95].

Priya, C. G and col [96] synthesized and characterized a Schiff base derived from m-bromo-salicylaldehyde. Using the DFT study, the compound structure was optimized. Local energy decomposition analysis (LED) calculated that the binding energy is -9.19 kcal/mol. The molecule (5BRSET) is an optical material, its wavelength is 512 nm and 784 nm respectively. three different solvents in summer used to calculate nonlinear optical studies, HOMO/LUMO and molecular electrostatic potential, when compared to other solvents, water has good activity. The study of non-covalent interactions confirms intermolecular and intermolecular hydrogen bonds. An anchoring study was performed on the molecule, and the results show that 5BRSET interacts well with the crystalline structure of the hypothetical protein (PDB ID: 2EA9). The molecule has moderate activity, confirmed by antimicrobial activity.

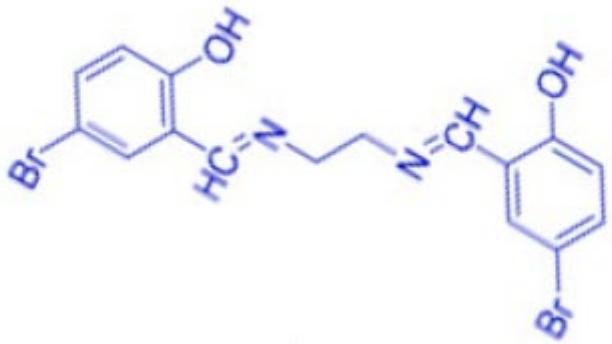

Figure I.16. General structure of the 5BRSET ligand prepared by Priya, C. G and col [96].

PART II: METHODS AND TECHNIQUES

Our work was carried out in the Laboratory of Chemistry, Molecular Engineering and Nanostructures, at the Ferhat Abbas Setif 1 University in order to synthesize new ligands based on Schiff that chelates subsequently by transition metals such as Cu(II), Mn(II) , Co(III) and Zn(II), and continue to the biochemistry laboratory of the Constantine Biotechnology Research Centre (CRBT) to assess the antioxidant activity of our products.

I.9. Summary materials (Assembly of synthesis)

The essential elements used for the experimental setup are:

- A balloon heater with magnetic agitation;
- A refrigerant used to condense the solvent during the reaction;
- A bi-neck ball with a magnetic bar.

All chemicals, reagents and solvents used in the preparation of Schiff base ligands and corresponding transition metal complexes come from Sigma-Aldrich.

I.10. Theoretical background of experimental techniques used

The study of the physicochemical behavior of different molecules is detected by several methods that are collected together to better frame the constitutive properties of the molecule.

I.10.1. Melting point

This term refers to the change of state of a material when it changes from a solid to a liquid state. The melting point is the exact temperature required for this transformation and its determination is very important since it is highly dependent on the purity of the material tested. This technique is therefore used to define the quality of a substance [97].

The melting points were determined on a digital heater bench from Köfler Bank 7779. It is a hot plate with a temperature gradient, the temperature varies from 40°C to 250°C, on which a sample is moved. The determination of the melting point is an important physical data for a substance.

I.10.2. Thin Layer Chromatography (TLC)

Chromatography is a physical technique for separating chemical species that allows the identification of the different compounds in a mixture. Its main interest is the rapid identification of compounds in a mixture. It is based on differences in the affinity of substances with respect to two phases, one stationary or fixed, the other mobile:

- stationary phase: is a thin layer of adsorbent material (usually silica gel, aluminum oxide).
- mobile or eluent phase: a solvent or a mixture of solvents which will cause the compounds to separate along the stationary phase by capillary action.

the substances migrate at a rate dependent on their nature and that of the solvent, characterized by a frontal ratio (Rf) defined by the expression:

$$\mathbf{Rf} = \mathbf{d}_{\text{substance}} / \mathbf{d}_{\text{solvant}}$$

dsubstance: Distance traveled by the compound

dsolvant: Distance travelled by solvent

Reaction monitoring and product purity control were performed by thin-film liquid chromatography (TLC). These chromatographic analyses were performed on 0.25 mm E Merck silica gel

plates (60F-254) and ethyl acetate/petroleum ether mixture (2/1) as eluent and the revelation was performed under ultraviolet lamp (wavelength 254 nm).

I.10.3. Spectroscopic methods

Spectroscopy is the study of electromagnetic radiation emitted, absorbed or diffused by atoms or molecules. It provides information on the identity, structure and energy levels of atoms and molecules through the analysis of the interaction of electromagnetic radiation with matter. Several types of excitation are obtained depending on radiation. The methods used in this work are:

- Ultraviolet-visible spectroscopy (UV-vis) (electronic excitation).
- Infrared (IR) spectroscopy (link deformation).
- Proton Nuclear Magnetic Resonance (1H NMR) (electron spin excitation)

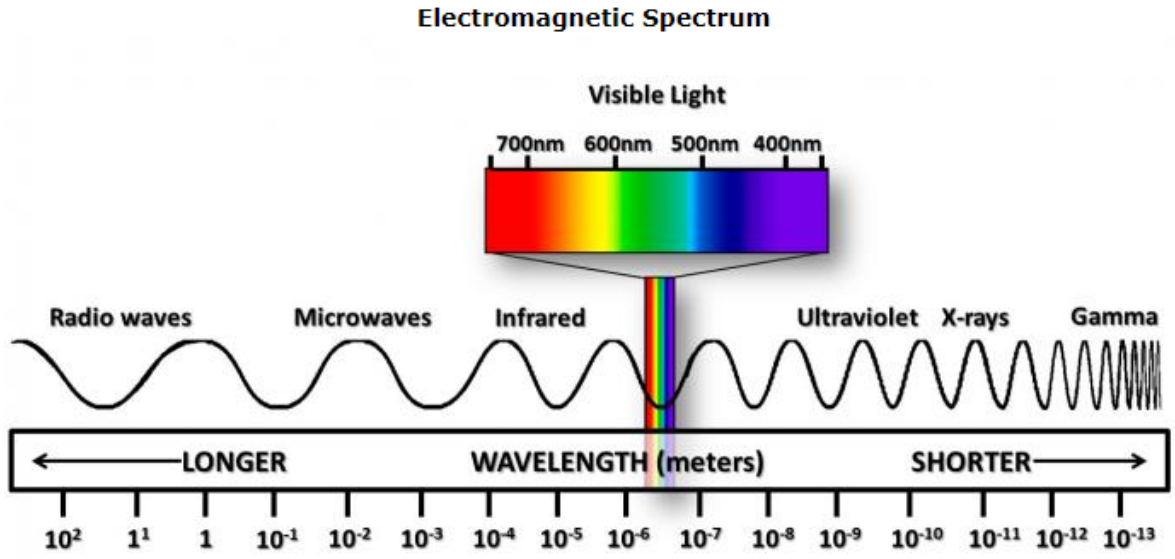

Figure I.17. All radiation constitutes the electromagnetic spectrum.

I.10.3.1. UV-Visible Spectrophotometry

Ultraviolet and visible absorption spectrophotometry (UV-Vis) is both a quantitative and qualitative analysis method. It is essentially based on the phenomenon of absorption of light energy by a substance. When a molecule absorbs part of the energy of electromagnetic radiation, it is automatically accompanied by an electronic transition from a fundamental level to a higher energy level [98].

These electronic transitions, occurring at the molecular scale, concern valences electrons. Energy absorptions are expressed by the law of BEER LAMBERT.

UV-Visible spectroscopy involves photons with wavelengths in the ultraviolet (200 nm – 400 nm), visible (400 nm – 800 nm) or near-infrared (750 nm -1 400 nm) range. Subjected to radiation in this wavelength range, molecules, ions or complexes are likely to undergo one or more electronic transitions. The substrates analyzed are most often in solution, the electronic spectrum is the function that connects the light intensity absorbed by the sample analyzed as a function of the wavelength.

It allows qualitative access to information on the nature of the bonds present in the sample (via the order of magnitude of λmax and εmax) and to determine quantitatively the concentration of absorbing species in this spectral domain.

The electron absorption spectra of the different ligands and complexes synthesized were performed on a Shimadzu Spectrophotometer UV-1800, using quartz tanks 1 cm thick. Spectra are recorded in different solutions of DMF, DMSO, Methanol (10-4 M) in the range of 200 to 800 nm.

I.10.3.1.1 Beer-Lambert's Law

The Beer-Lambert law indicates that the absorbance of a solution is proportional to its concentration and the thickness l of the sample. The Beer-Lambert relationship gives access to the molar extinction coefficient ε, which characterizes the absorption of the building under the conditions of the experiment. To this end the law of BEER LAMBERT is expressed by the following relation:

$$\boldsymbol{A = \varepsilon C l = log I_0 / I}$$

Where

I/I_0: is the transmittance of the solution (without unit).

A_λ: is the optical absorbance or density at a wavelength λ.

ε : is the molar extinction coefficient (in L.mol 1 cm 1).

l: is the length of the optical path in the through solution, it corresponds to the thickness of the bowl used (in cm).

C: is the molar concentration of the solution (in mol.L 1).

In the case of organic molecules, the electronic levels concerned by these transitions correspond to the valence orbitals of the building and their energy is dependent on their nature (σ, π) and their character (binder, antiliant, non binder).

Many transitions are possible but only those of lower energies lead to absorption in the UV-vis. The nature σ or π of the levels involved reflect the nature of the functional group present in the building. The various possible transitions are:

Transition σ→ σ*: this transition requires a lot of energy: it is located in the far UV. This is why saturated hydrocarbons, which have only bonds of this type, are transparent in the near UV region.

Transition n→ σ*: it usually occurs at wavelengths close to 200 nm and is observable in many compounds with simply bound heteroatoms, such as O-H, N-H… etc.

Transition n→ π*: this type of transition occurs in the case of molecules with a heteroatom belonging to an unsaturated system. The best known is that which corresponds to the carbonyl band.

Transition π →π*: compounds with an isolated double ethylene bond lead to a strong absorption band at 270 nm whose position depends on the presence of substituents.

I.10.3.2. Infrared (IR) Spectroscopy

Infrared spectroscopy (FT-IR) is a qualitative analytical technique for determining the presence or absence of functional groups. It expresses the electromagnetic interaction of radiation with different parts of the molecule. IR radiation causes the vibration of bonds between two atoms in an organic structure, since the atoms of organic molecules are bound together in a particular arrangement characterizing the functional groups. The IR spectrum of an organic substance displays several lines each expressing energy absorption. The position of an absorption band in the IR spectrum is expressed in units of wavelength (µm) or wave number (cm-1) with the advantage of being proportional to the absorbed energy ΔE.

The infrared spectra plots for all structures were made in the solid state. The infrared absorption spectra are obtained with a Perkin Elmer 1000-FTIR series, using a KBr tablet, in which the product was dispersed in 150mg of KBr at a concentration of 3% under a pressure of 80tons/cm^2. The frequency range used for this analysis is between 4000 and 400cm^{-1} with a spectral resolution of 4 cm^{-1}

I.10.3.3. Nuclear Magnetic Resonance (NMR) Spectroscopy

Nuclear Magnetic Resonance in liquid medium or NMR is an effective tool to highlight changes in the chemical environment of a particular nucleus, it is a spectroscopic technique commonly used for structural analysis of many chemical molecules. It is mainly used for the structural

determination of organic compounds, to follow the evolution of chemical reactions and to study the steric effect of substituted groups as well as the purity of a sample. By measuring the resonance frequency of the nuclear spins of certain atomic nuclei when placed in an intense magnetic field, the chemical environment of these atoms can be studied. This information makes it possible to identify the molecules, to determine their structure.

The method is based on nuclear magnetism, the nuclei of some atoms ^{1}H, ^{13}C, ... have a nuclear magnetic moment, ie they behave like microscopic magnets characterized by a quantum magnitude: the spin [99].

The ^{1}H and ^{13}C NMR spectra were recorded in MeOH and CDCL3 solution on the BRUKER AC 300P spectrometer (Wissembourg, France) at 300 MHz and 75 MHz respectively. Chemical displacements are expressed in part per million downstream of tetramethylsilane Si(CH3)4 (TMS) as the internal standard (internal reference). The coupling constants " j "are given in Hz.

I.10.3.4. X-ray diffraction

X-ray diffraction (XRD) is an experimental technique of choice for characterizing the three-dimensional structure of a crystalline state compound. X-ray diffraction on a single crystal sample remains the most effective technique for determining its crystallographic structure, since structural information cannot be obtained completely from powder diffraction. It should still be noted that it is still not easy to obtain the desired single crystal for a fundamental study.

The information provided by X-ray diffraction is almost null for gases, limited to the distribution of distances between objects diffracting for liquids and amorphous, on the other hand for the crystals one can find the precise position of the atoms in the crystal.

It is possible to localize the atomic locations that make up the crystalline molecular structure using X-ray diffraction on single crystals. The system's stable conformation can be described in terms of binding length, valence angle, and torsion angle. Additionally, weak bonds that may be involved in the ligand-receptor intermolecular interaction can be identified by examining the intermolecular forces that ensure crystal cohesion, such as hydrogen bridges, electrostatic interactions, and Van Der Waals interactions [100].

The diffraction of a parallel X-ray beam on a crystal's surface and its deep penetration into the crystal make up the measuring concept. The atoms that make up the nodes of the crystal lattice reflect back all directions the photons that hit them [101]. It is stated that X-rays are diffracted. Diffracted X-rays may therefore be seen in several directions, each of which corresponds to a distinct reticular plane of the crystalline structure. The diffracted radius intensity in a particular

direction only matters if there are several nodes in the corresponding reticular plane that may return X-rays.

The crystalline lattice atom arrangement and interatomic distances can be ascertained using X-ray diffraction [102] or X-ray diffractometry analysis. By irradiating materials with X-rays, one may determine its crystallographic character since the members of the lattice diffract X-rays in various ways after they are constructed.

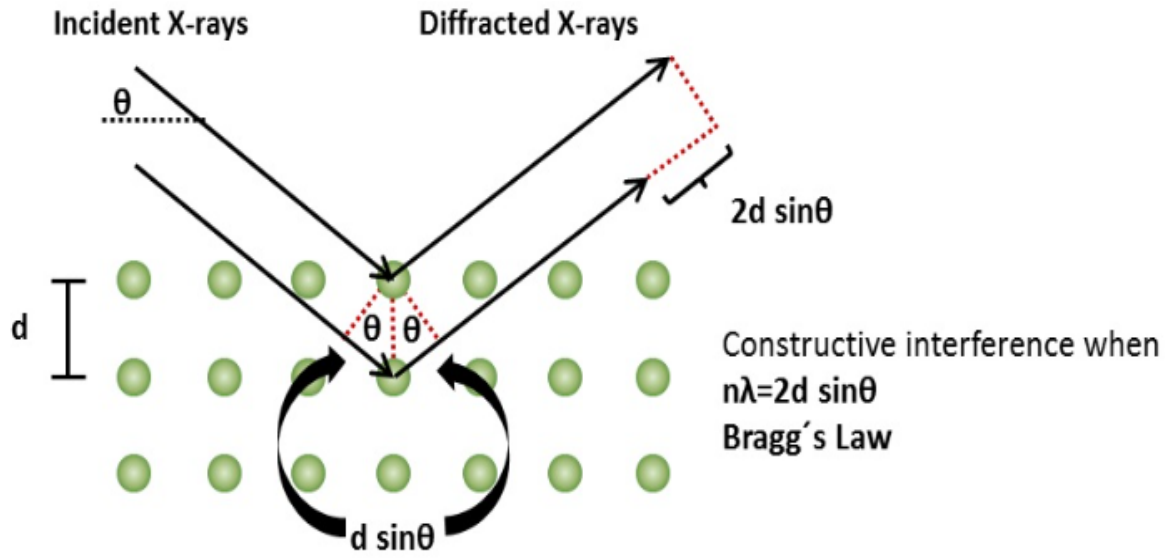

Figure 1.18. Schematic diagram of X-ray diffraction [103]**.**

Figure I.19 schematizes the X-ray diffraction by a family of reticular planes (hkl) illustrating the Bragg law, with d hkl the distance separating two atomic planes of the same family, and θ the Bragg angle as follows:

$$n\lambda = 2d_{hkl}\, sin(\theta)$$

With:

d_{hkl} is the inter-reticular distance of the family of planes (h k k l).

θ is the angle between the incident x-ray beam and the sample area.

λ this is the wavelength .

n is the diffraction order.

The wavelength of the probe beam must be of the order of magnitude of the inter-reticular distances. The intensity diffracted by a crystal is the product between a form factor and the structure factor:

$$\overrightarrow{I(R)} = \left|\overrightarrow{G(R)}\right|^2 = \left|\overrightarrow{F(R)} \times \overrightarrow{L(R)}\right|^2$$

Where:

(R) ⃗is the direction vector in the reciprocal network,

F is the structure factor.

L is the form factor. It depends on the shape and size of the crystal.

I.10.3.4.1. Crystallographic concepts

The physicochemical properties of a crystal are closely related to the spatial arrangement of atoms in matter. The crystalline state is defined by a periodic character and ordered at the atomic or molecular scale. The crystal is obtained by translation in all directions of a basic unit called the elementary cell.

Solid matter is composed of atoms, which can be seen as elementary balls that assemble. The balls can be arranged irregularly, we then have so-called amorphous or glassy matter, like glass, or they can pile up in an orderly way, it is then a crystal.

The crystal is a solid with structure consisting of atoms ordered in a periodic network and even tri-periodic and symmetrical. It has symmetry properties with direct and inverse rotation axes, mirrors, planes and centers of symmetry.

The elemental mesh is the smallest crystalline volume built on three shortest independent translations of the crystal. It is defined by three vectors that generate six mesh parameters: the three lengths of vectors a, b, c and the three angles between these vectors α, β, γ.

I.10.3.4.2. Single crystal X-ray diffraction

Crystallographic X-ray diffraction [46,104] is a unique technique for figuring out a molecule's three-dimensional structure. In fact, the electron cloud of the crystal's atoms is rayed with Xinteragissent. Since the crystal is a periodic material with three dimensions, the interference of these dispersed waves results in the diffraction phenomena. The Fourier components of the molecule's electron density may then be obtained by the measurement of these diffracted intensities. A structural determination entails locating the electronic density maxima that are integrated to the atomic locations via a series of computational procedures. Single crystal diffractometers [46,105] with electronic detectors (scintillation or proportional counters) are used to measure the intensities.

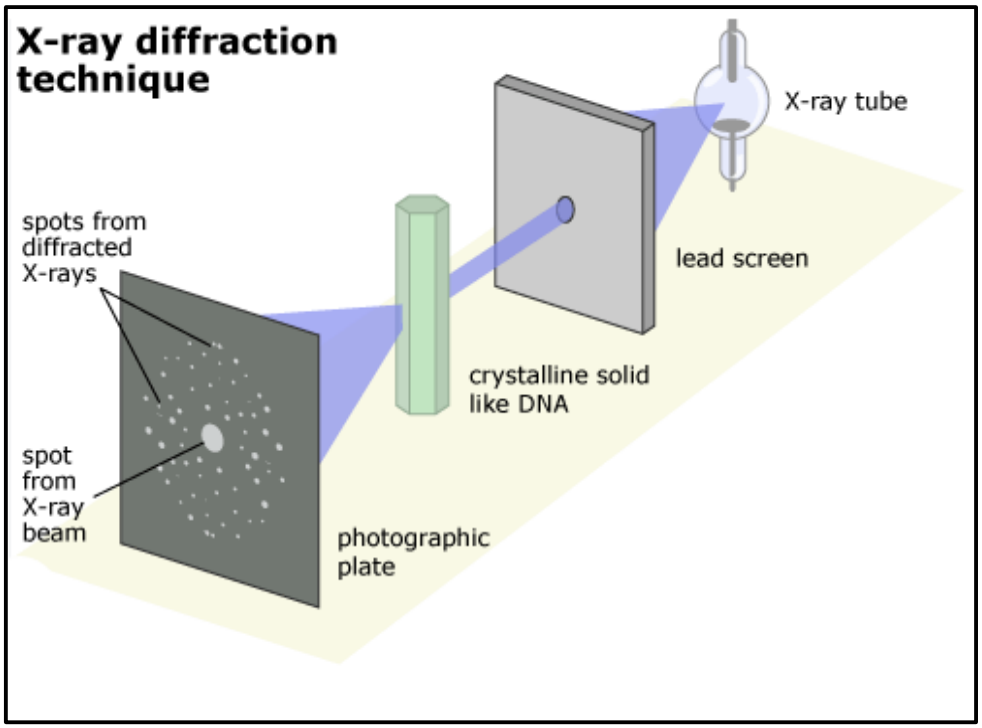

Figure I.19. Principle of single crystal X-ray diffraction.

An incident x-ray beam of wavelength λ will only be reflected by a family of planes (h, k, l) to the extent that it meets these planes at a certain angle θ called Bragg angle, and reflects the geometry of the direct network (crystal system, mesh parameters). Diffraction spots form the reciprocal lattice and are therefore named by their Miller indices (h, k, l). The intensities of the diffracted beams carry information about the atomic content of the mesh that makes up the crystal, which is defined as the convolution of this mesh (shape and atomic content) by the direct network.

DRX analysis of the single crystals Cu(II)L2, H2L3 and Cu(II)L3 was performed by a Bruker D8-VENTURE diffractometer equipped with a CCD Photon zone detector, which uses Mo-Kα monochromated graphite radiation (λ = 0.71073 Å). Data were collected at 298 K using APEX-III software, integrated with SAINT, and corrected for absorption using a multi-scan approach (SADABS).

I.10.4. Characteristic electrochemical method by cyclic voltammetry

Cyclic voltammetry is a potentiodynamic method widely used in electrochemistry for the preliminary study of electrochemical systems. It provides by a simple and fast experiment a lot of information on the behavior of the redox system fixed to the surface of the electrode [106]. It

is a transient electrochemical method in which the potential of the indicating electrode varies linearly with time depending on the relationship:

$E = Ei + \boldsymbol{\upsilon}. t$

E: Indicator electrode potential (volt).

Ei: Initial potential.

υ : Scan speed.

t: Time (s).

For active compounds in cyclic voltammetry, migration is always guaranteed by a support electrolyte; diffusion is the sole route of transport involved [107]. It is simple to watch the activity of the system and distinguish between the many electroactive species using this method, which is based on a round-trip linear scan of the potential [108]. The electrochemical behavior of the reagents and products, and therefore the reversibility of the processes, may be seen by the inversion of the potential's direction of change. Furthermore, the scanning speed offers a direct way to regulate the kinetic regime of reactions (irreversible, quasi-reversible, and reversible), and its variation enables the observation of reactions in various regimes and the diagnosis of their mechanistic aspects.

This technique is generally applicable to all types of electrodes and electrolytes. The shape of the intensity-potential curves obtained makes it possible to distinguish the different redox systems according to whether they are reversible, quasi-reversible or irreversible.

Mathematical expressions of peak current and potential were initially developed for a one-way sweep by Randels and Sevick for fast systems [109] and by Delahay for slow systems [110] . This theory is extended by Matsuda and Ayabe to semi-fast systems. The work of Nicholson and Shain allowed the development of relationships describing the experimental curves of cyclic scans.

In this research, we present the electrochemical behavior of synthesized ligands (H2L1), (H2L2), and (H2L3) and their complexes of Cu(II), Zn(II), Co(III), Mn(III). The study is carried out by cyclic voltammetry on vitreous carbon electrode in dimethylformamide medium (DMF) in the presence of tetrabutylammonium perchlorate (TBAP) 10-1M.

I.11. Methods for evaluating biological activities (antioxidant capacity)

There is no one-size-fits-all technique for precisely quantifying antioxidant activity due to the complexity of oxidation processes and the variety of antioxidants, which contain both hydro-

philic and hydrophobic components. While none of these techniques can fully describe oxidation or oxidation resistance, they all help to define the biological activities of the compounds or mixtures under evaluation in terms of their total biological activities. To get a fairly accurate estimate of the antioxidant capacity of the sample to be tested, it is typically required to integrate the results of several, complimentary assays. Conversely, there are two categories of techniques for determining antioxidant efficacy in vitro:

- Methods based on the transfer of a hydrogen atom or Hydrogen Atom Transfer (HAT) Such as: ORAC method (Oxygen Radical Absorbance Capacity), TRAP (Total Reactive Antioxidant Potential) etc... Most of these methods are dependent on the solvent used and pH, while the presence of metals may interfere with these methods [111].

- Methods based on the transfer of an electron or Single Electron Transfer (SET) in particular: DPPH method (2,2-Diphenyl-1-Picrylhydrazil) (also considered as HAT method, therefore mixed), TEAC (Trolox Equivalent Antioxidant Capacity) and FRAP (Ferric Reducing Antioxidant Power) [111]

To evaluate the antioxidant power of the various synthesized products, several tests were used, namely the DPPH• radical trapping test, the ABTS•+.

I.11.1. Preparation of dilutions

To prepare a series of dilutions, the different products are dissolved in methanol, DMF and DMSO, 500 µl of this stock solution are mixed with 500 µl of methanol, to arrive at a ½ dilution and so on. This procedure is repeated for subsequent dilutions until dilution 1/64 is achieved (Figure I.21).

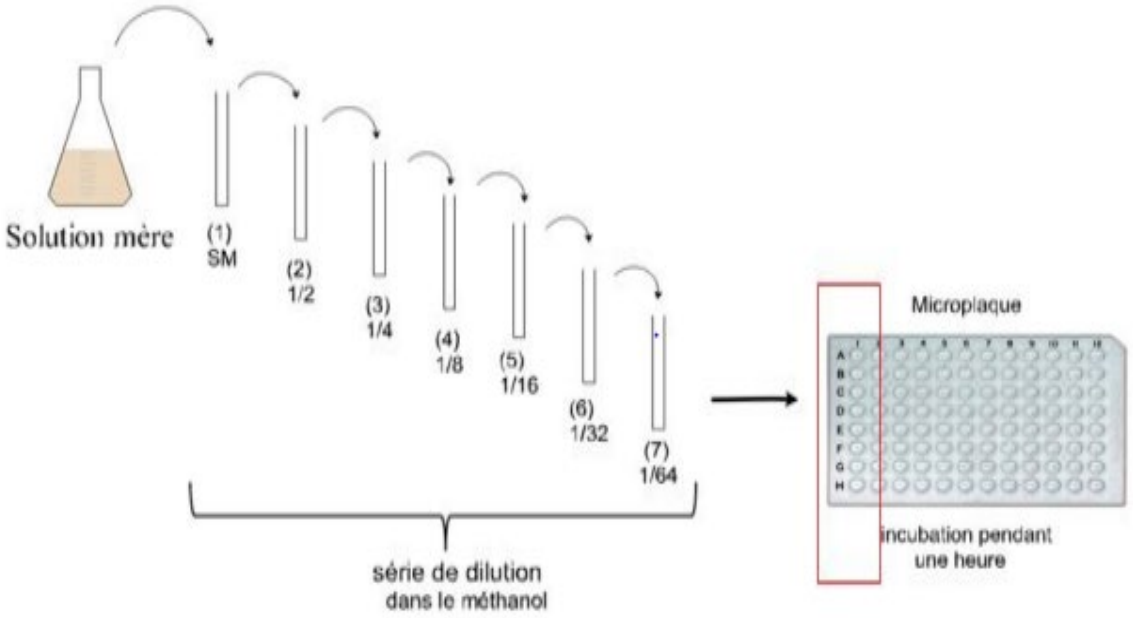

Figure I.20. Preparation of product dilutions in methanol.

I.11.2 DPPH

Antioxidant activity was assessed using the method described by Morel et al [112]. Schiff base ligands were solubilized in methanol, all Mn(II), Cu(II), Co(II) complexes were solubilized first in DMF, and Zn(II) was solubilized first in DMSO (4 mg/ml stock) before being diluted in absolute ethanol at different concentrations (1; 0.5 and 0.2 mg/ml) from the stock solution. Methanol was used as white and trolox was used as a calibration range at dilutions of 12.5, 25, 50 and 75 µM. BHA and BHT were used as a positive control. Then, 40 µl of the synthesized products were deposited in a 96-well triplicate plate for each concentration tested. Finally, 160 µl of the freshly prepared DPPH solution was added to trigger the reaction and have a final volume equal to 200 µl. The plate was incubated for 30 minutes at room temperature away from light (in aluminum foil). Absorbance was measured at 517 nm using a microplate reader (MDS Inc., Toronto, Canada). The results are the SEM mean of 3 independent experiments (3 wells/ concentration for each experiment) and are expressed in equivalents , and they are expressed as anti-radical activity where inhibition of free radicals, these are calculated as percentages (I %) by the following formula:

$$I\,\% = \frac{A_{blanc} - A_{echantillon}}{A_{blanc}} \times 100$$

With:

I%: Percentage of inhibition.

A white: Absorbance of white

A sample: Absorbance of the sample.

The concentration of the synthesized samples causing 50% inhibition (IC50) of the DPPH radical, is determined graphically by linear regression from the graph of the percentage inhibition as a function of concentration of the samples.

I.11.2.1. Assessment of antiradical potential: calculation of IC50

The antioxidant activity of the extracts is expressed in IC50. This parameter used to estimate antioxidant potency is defined as the effective concentration of the substrate that causes the loss of 50% of DPPH activity. IC50s are determined graphically by linear or logarithmic regressions of plotted graphs (percent inhibition as a function of extract concentration).

The antiradical power is inversely proportional to IC50 .

I.11.3. ABTS radical-cation reduction test•+

This anti-radical activity was measured by a microplate colorimetric method described by Re and al . The ABTS•+ solution was prepared from 2 aqueous solutions: ABTS (7 mM) and potassium persulfate K2S2O8 (2.45 mM), the mixture was kept out of light for 16 hours. This solution was used after dilution with distilled water. 160 µl of ABTS•+ solution was added to 40 µl of different extracts, which have different concentrations in a 96-well microplate. Absorbance was measured after 10 min at 734 using a microplate reader. Methanol and ABTS•+ were used as control. The percentage of radical inhibition is calculated as follows:

Percentage inhibition of ABTS•+(%): [C control- A sample/C control] ×100

Where:

C control: Control absorbance

A Sample : Sample absorbance.

I.12. Conclusion

During this bibliographic study we have highlighted the importance of the activity of Schiff bases and their complexes in biology, which shows that their synthesis continues to increase according to the literature. However, the biological activity of the Schiff base compounds deserves further study. Although research on this topic is in its early stages, a number of reports that attempt to disclose the effects of Schiff bases on pathogens of clinical interest have been recently reported. The creation of material clusters for the ONL application is the final and most significant application, aside from biological activities, that has been the primary goal of our work.

References

[1] H. Schiff, Mittheilungen aus dem Universitätslaboratorium in Pisa: eine neue Reihe organischer Basen, Justus Liebigs Ann. Chem. 131 (1864) 118–119.

[2] X.-B. Lu, D.J. Darensbourg, Cobalt catalysts for the coupling of CO 2 and epoxides to provide polycarbonates and cyclic carbonates, Chem. Soc. Rev. 41 (2012) 1462–1484.

[3] A. Dalla Cort, P. De Bernardin, G. Forte, F.Y. Mihan, Metal–salophen-based receptors for anions, Chem. Soc. Rev. 39 (2010) 3863–3874.

[4] X.-B. Lu, W.-M. Ren, G.-P. Wu, CO2 copolymers from epoxides: catalyst activity, product selectivity, and stereochemistry control, Acc. Chem. Res. 45 (2012) 1721–1735.

[5] W. DERAFA, Synthèse de nouveaux complexes de base de schiff de métaux de transition non symétriques (manganèse ou fer) contenant un résidu moléculaire électopolymérisable, (2014).

[6] K. OUARI, Synthèse de ligands bases de schiff tetradentates non symétriques et obtention de complexes de métaux de transition.-propriétés électro catalytiques appliquées au modèle cytochrome p450, (2014).

[7] F.Z. Chiboub Fellah, Synthèse et détermination structurale de complexes de métaux de transition et d'entités 3d-4f, (2008).

[8] L. Mugherli, Microarrays fonctionnels de gouttes: de la synthèse chimique combinatoire au criblage de molécules bioactives., (2006).

[9] Z. Guo, R. Xing, S. Liu, Z. Zhong, X. Ji, L. Wang, P. Li, Antifungal properties of Schiff bases of chitosan, N-substituted chitosan and quaternized chitosan, Carbohydr. Res. 342 (2007) 1329–1332.

[10] G. Bringmann, M. Dreyer, J.H. Faber, P.W. Dalsgaard, D. Stærk, J.W. Jaroszewski, H. Ndangalasi, F. Mbago, R. Brun, S.B. Christensen, Ancistrotanzanine C and related 5, 1 '-and 7, 3 '-coupled Naphthylisoquinoline alkaloids from Ancistrocladus t anzaniensis, J. Nat. Prod. 67 (2004) 743–748.

[11] A.O. de Souza, F. Galetti, C.L. Silva, B. Bicalho, M.M. Parma, S.F. Fonseca, A.J. Marsaioli, A.C.L.B. Trindade, R.P.F. Gil, F.S. Bezerra, Antimycobacterial and cytotoxicity activity of synthetic and natural compounds, Quim. Nova 30 (2007) 1563–1566.

[12] C.M. Da Silva, D.L. da Silva, L. V Modolo, R.B. Alves, M.A. de Resende, C.V.B. Martins, Â. de Fátima, Schiff bases: A short review of their antimicrobial activities, J. Adv. Res. 2 (2011) 1–8.

[13] R. Abdul, Synthesis and biological studies of some Schiff base compounds and their transition metal complexes, (2005).

[14] T.M. Tallon, Synthesis of imidazole schiff base ligands, their silver (I) complexes and their activities against candida albicans, (2010).

[15] C. Safia, Synthèse, caractérisation et étude de la réactivité électrochimique de nouvelles bases de Schiff non symétriques et de leurs complexes de métaux de transition, Université Ferhat Abbas Sétif-1 UFAS (Algérie), 2018. http://dspace.univ-setif.dz:8888/jspui/handle/123456789/2982.

[16] P. Przybylski, A.W. Huczyński, K.K. Pyta, B. Brzezinski, F. Bartl, Biological properties of Schiff bases and azo derivatives of phenols, Curr. Org. Chem. 13 (2009).

[17] E.A. MILOUD, Etude quantique des clusters de molécules push- pull. Structures et propriétés physiques. Soutenue, UNIVERSITE DJILLALI LIABES FACULTE DES

SCIENCES EXACTES SIDI BEL ABBÈS, 2018.
[18] B.M. Yazid, Doctorat en sciences en : Chimie Industrielle Option : Génie Chimique Synthèse , structurale et Etude du Comportement Dédicaces Je dédie ce travail A mes chers parents , (n.d.).
[19] W. Zhang, J.L. Loebach, S.R. Wilson, E.N. Jacobsen, Enantioselective epoxidation of unfunctionalized olefins catalyzed by salen manganese complexes, J. Am. Chem. Soc. 112 (1990) 2801–2803.
[20] E. Fermi, Statistical method to determine some properties of atoms, Rend. Accad. Naz. Lincei 6 (1927) 5.
[21] L.H. Thomas, The calculation of atomic fields, in: Math. Proc. Cambridge Philos. Soc., Cambridge University Press, 1927: pp. 542–548.
[22] P. Hohenberg, W. Kohn, Inhomogeneous electron gas, Phys. Rev. 136 (1964) B864.
[23] R.G. Parr, R.G. Pearson, Absolute hardness: companion parameter to absolute electronegativity, J. Am. Chem. Soc. 105 (1983) 7512–7516.
[24] P. Geerlings, E. Chamorro, P.K. Chattaraj, F. De Proft, J.L. Gázquez, S. Liu, C. Morell, A. Toro-Labbé, A. Vela, P. Ayers, Conceptual density functional theory: status, prospects, issues, Theor. Chem. Acc. 139 (2020) 36.
[25] R.G. Parr, R.A. Donnelly, M. Levy, W.E. Palke, Electronegativity: the density functional viewpoint, J. Chem. Phys. 68 (1978) 3801–3807.
[26] R.G. Parr, L. v Szentpály, S. Liu, Electrophilicity index, J. Am. Chem. Soc. 121 (1999) 1922–1924.
[27] A.T. Maynard, M. Huang, W.G. Rice, D.G. Covell, Reactivity of the HIV-1 nucleocapsid protein p7 zinc finger domains from the perspective of density-functional theory, Proc. Natl. Acad. Sci. 95 (1998) 11578–11583.
[28] L.R. Domingo, P. Pérez, The nucleophilicity N index in organic chemistry, Org. Biomol. Chem. 9 (2011) 7168–7175.
[29] P. Pérez, A. Aizman, R. Contreras, Comparison between experimental and theoretical scales of electrophilicity based on reactivity indexes, J. Phys. Chem. A 106 (2002) 3964–3966.
[30] L.S. Wong, Bioelectrochemical engineering of the cytochrome P-450 (cam) system, University of California, Los Angeles, 1994.
[31] N. Wazzan, Z. Safi, DFT calculations of the tautomerization and NLO properties of 5-amino-7-(pyrrolidin-1-yl)-2, 4, 4-trimethyl-1, 4-dihydro-1, 6-naphthyridine-8-carbonitrile (APNC), J. Mol. Struct. 1143 (2017) 397–404.
[32] M.J. Frisch, G.W. Trucks, H.B. Schlegel, G.E. Scuseria, M.A. Robb, J.R. Cheeseman, G. Scalmani, V. Barone, G.A. Petersson, H. Nakatsuji, Gaussian 09, Revision A. 02, Gaussian, Inc., Wallingford CT, 2016 Search PubMed;(b) J. Chaia and M. Head-Gordon, Phys. Chem. Chem. Phys 10 (2008) 6615–6620.
[33] R.F. Fink, J. Pfister, H.M. Zhao, B. Engels, Assessment of quantum chemical methods and basis sets for excitation energy transfer, Chem. Phys. 346 (2008) 275–285.
[34] H. Behzadi, N.L. Hadipour, M. Mousavi-khoshdel, Study of CO⋯ HN Hydrogen bond interactions in amyloid beta (Aβ): A DFT study of the electric field gradient and CS tensors and NBO analysis, Comput. Theor. Chem. 965 (2011) 137–145.

[35] J. Guan, Y. Hu, M. Xie, E.R. Bernstein, Weak carbonyl-methyl intermolecular interactions in acetone clusters explored by IR plus VUV spectroscopy, Chem. Phys. 405 (2012) 117–123.
[36] A. Gratien, Spectroscopie ultraviolet-visible et infrarouge de molécules clés atmosphériques, (2008).
[37] C. Daher, Analyse par spectroscopies Raman et infrarouge de matériaux naturels organiques issus d'objets du patrimoine: méthodologies et applications, (2012).
[38] M. Larget, Contribution à l'évaluation de la dégradation du béton: Thermographie infrarouge et couplage de techniques, (2011).
[39] H. Okamoto, M. Tasumi, Picosecond transient infrared spectroscopy of electronically excited 4-dimethylamino-4′-nitrostilbene in the fingerprint region (1640-940 cm− 1), Chem. Phys. Lett. 256 (1996) 502–508.
[40] H. Okamoto, M. Tasumi, Picosecond Transient Infrared Spectroscopy of 4-Dimethylamino-4′-Nitrostilbene in the Fingerprint Region, Laser Chem. 19 (1999) 363–366.
[41] Ş. Çakmak, S. Kansiz, M. Azam, A. Veyisoglu, H. Yakan, K. Min, Synthesis, Spectroscopic Characterization, Single-Crystal Structure, Hirshfeld Surface Analysis, and Antimicrobial Studies of 3-Acetoxy-2-methylbenzoic Anhydride, ACS Omega (2022). https://doi.org/10.1021/acsomega.2c00879.
[42] J.J. McKinnon, M.A. Spackman, A.S. Mitchell, Novel tools for visualizing and exploring intermolecular interactions in molecular crystals, 2004. https://doi.org/10.1107/S0108768104020300.
[43] J.J. McKinnon, D. Jayatilaka, M.A. Spackman, Towards quantitative analysis of intermolecular interactions with Hirshfeld surfaces, Chem. Commun. (2007) 3814–3816.
[44] W. Maalej, R. Jaballi, A. Ben Rached, P. Guionneau, N. Daro, Z. Elaoud, Supramolecular architectures of mononuclear nickel(II) and homobinuclear copper(II) complexes with the 5,5′-dimethyl-2,2′-bipyridine ligand: Syntheses, crystal structures and Hirshfeld surface analyses, J. Mol. Struct. 1250 (2022). https://doi.org/10.1016/j.molstruc.2021.131728.
[45] S. Selvanandan, H. Anil kumar, H.T. Srinivasa, B.S. Palakshamurthy, Crystal structure and Hirshfeld surface analysis of 3-({4-[(4-cyanophenoxy)carbonyl]phenoxy}carbonyl)phenyl 4-(benzyloxy)-3-chlorobenzoate, Acta Crystallogr. Sect. E Crystallogr. Commun. 78 (2022) 989–992. https://doi.org/10.1107/s2056989022008441.
[46] W. ZEMAMOUCHE, Elaboration et caractérisation des produits organiques à intérêt biologique substitués par des méthyles et des halogènes ., 2021.
[47] M. MEDJANI, Structure et spectroscopie (IR , Raman et neutron) des molécules aromatiques encagées dans des dérivés de triazines Structure et spectroscopie (IR , Raman et neutron) des molécules aromatiques encagées dans des dérivés de triazines, UNIVERSITÉ FRÈRES MENTOURI-CONSTANTINE 1 FACULTÉ DES SCIENCES EXACTES, 2018.
[48] A. Favier, Le stress oxydant: Intérêt conceptuel et expérimental dans la compréhension des mécanismes des maladies et potentiel thérapeutique, Actual. Chim. (2003) 108–115.
[49] J. Anastassopoulou, M. Kyriakidou, S. Kyriazis, A.F. Mavrogenis, V. Mamareli, I. Mamarelis, M. Petra, E. Malesiou, C. Kotoulas, P. Kolovou, E. Koutoulakis, A. Markouizou, T. Theophanides, Oxidative stress in ageing and disease development studied

by FT-IR spectroscopy, Mech. Ageing Dev. 172 (2018) 107–114. https://doi.org/10.1016/j.mad.2017.11.009.

[50] N. Turan, K. Buldurun, Synthesis, characterization and antioxidant activity of Schiff base and its metal complexes with Fe (II), Mn (II), Zn (II), and Ru (II) ions: Catalytic activity of ruthenium (II) complex, Eur. J. Chem. 9 (2018) 22–29.

[51] C. Migdal, M. Serres, Espèces réactives de l'oxygène et stress oxydant, Médecine/Sciences 27 (2011) 405–412. https://doi.org/10.1051/medsci/2011274405.

[52] L. Jagannathan, S. Cuddapah, M. Costa, Oxidative Stress Under Ambient and Physiological Oxygen Tension in Tissue Culture, Curr. Pharmacol. Reports 2 (2016) 64–72. https://doi.org/10.1007/s40495-016-0050-5.

[53] G. Pizzino, N. Irrera, M. Cucinotta, G. Pallio, F. Mannino, V. Arcoraci, F. Squadrito, D. Altavilla, A. Bitto, Oxidative Stress: Harms and Benefits for Human Health, Oxid. Med. Cell. Longev. 2017 (2017). https://doi.org/10.1155/2017/8416763.

[54] R. Patel, L. Rinker, J. Peng, W.M. Chilian, Reactive Oxygen Species: The Good and the Bad, React. Oxyg. Species Living Cells (2018). https://doi.org/10.5772/intechopen.71547.

[55] M. Khan, A. Alam, K.M. Khan, U. Salar, S. Chigurupati, A. Wadood, F. Ali, J.I. Mohammad, M. Riaz, S. Perveen, Flurbiprofen derivatives as novel α-amylase inhibitors: Biology-oriented drug synthesis (BIODS), in vitro, and in silico evaluation, Bioorg. Chem. 81 (2018) 157–167. https://doi.org/10.1016/j.bioorg.2018.07.038.

[56] J. Espinosa, J.M. Pérez, J.R. López-Olvera, A. Ráez-Bravo, F.J. Cano-Manuel, P. Fandos, R.C. Soriguer, J.E. Granados, D. Romero, Evaluation of oxidant/antioxidant balance in Iberian ibex (Capra pyrenaica) experimentally infested with Sarcoptes scabiei, Vet. Parasitol. 242 (2017) 63–70. https://doi.org/10.1016/j.vetpar.2017.05.027.

[57] V.I. Lushchak, Free radicals, reactive oxygen species, oxidative stress and its classification, Chem. Biol. Interact. 224 (2014) 164–175. https://doi.org/10.1016/j.cbi.2014.10.016.

[58] H.N. Siti, Y. Kamisah, J. Kamsiah, The role of oxidative stress, antioxidants and vascular inflammation in cardiovascular disease (a review), Vascul. Pharmacol. 71 (2015) 40–56. https://doi.org/10.1016/j.vph.2015.03.005.

[59] A. Galano, Free Radicals Induced Oxidative Stress at a Molecular Level: The Current Status, Challenges and Perspectives of Computational Chemistry Based Protocols, J. Mex. Chem. Soc. 59 (2017) 231–262. https://doi.org/10.29356/jmcs.v59i4.81.

[60] L.J. López-giraldo, P. Villeneuve, Outils d ' évaluation in vitro de la capacité antioxydante, 14 (2007).

[61] I. Diallo, Potentiels anti-oxydants et anti-inflammatoires de sporophores de Lentinula edodes (Shiitake) sous différentes conditions de culture, Université Montpellier, 2020.

[62] T. Islam, K. Ganesan, B.B. Xu, New insight into mycochemical profiles and antioxidant potential of edible and medicinal mushrooms: A review, Int. J. Med. Mushrooms 21 (2019).

[63] J. Delattre, J.-L. Beaudeux, D. Bonnefont-Rousselot, Radicaux libres et stress oxydant: aspects biologiques et pathologiques, Editions Tec & Doc, 2005.

[64] O.M. Ighodaro, O.A. Akinloye, First line defence antioxidants-superoxide dismutase (SOD), catalase (CAT) and glutathione peroxidase (GPX): Their fundamental role in the

entire antioxidant defence grid, Alexandria J. Med. 54 (2018) 287–293. https://doi.org/10.1016/j.ajme.2017.09.001.

[65] C. Sánchez, Reactive oxygen species and antioxidant properties from mushrooms, Synth. Syst. Biotechnol. 2 (2017) 13–22. https://doi.org/10.1016/j.synbio.2016.12.001.

[66] S.J. Forrester, D.S. Kikuchi, M.S. Hernandes, Q. Xu, K.K. Griendling, Reactive oxygen species in metabolic and inflammatory signaling, Circ. Res. 122 (2018) 877–902. https://doi.org/10.1161/CIRCRESAHA.117.311401.

[67] E. Avcı, G. Alp Avcı, D. Ali Kose, Determination of Antioxidant and Antimicrobial Activities of Medically Important Mushrooms Using Different Solvents and Chemical Composition via GC/MS Analyses, J. Food Nutr. Res. 2 (2014) 429–434. https://doi.org/10.12691/jfnr-2-8-1.

[68] T. Rahman, M. Choudhury, Shiitake Mushroom: A Tool of Medicine, Bangladesh J. Med. Biochem. 5 (2013) 24–32. https://doi.org/10.3329/bjmb.v5i1.13428.

[69] W.A. Yehye, N.A. Rahman, A. Ariffin, S.B. Abd Hamid, A.A. Alhadi, F.A. Kadir, M. Yaeghoobi, Understanding the chemistry behind the antioxidant activities of butylated hydroxytoluene (BHT): A review, Eur. J. Med. Chem. 101 (2015) 295–312. https://doi.org/10.1016/j.ejmech.2015.06.026.

[70] M.S. Fouzia, Synthèse, Caractérisation et activités biologiques d'un ligand chélateur des ions métalliques, UNIVERSITE FERHAT ABBAS SETIF-1 FACULTE DE TECHNOLOGIE, 2018.

[71] A.M. Pisoschi, A. Pop, The role of antioxidants in the chemistry of oxidative stress: A review, Eur. J. Med. Chem. 97 (2015) 55–74. https://doi.org/10.1016/j.ejmech.2015.04.040.

[72] R. Belaich, S. Boujraf, Facteurs inflammatoires et stress oxydant chez les hémodialysés : effets et stratégies thérapeutiques, Med. Des Mal. Metab. 10 (2016) 38–42. https://doi.org/10.1016/S1957-2557(16)30009-8.

[73] G. M., K. S., A study of free radical chemistry: Their role and pathophysiological significance, Acta Biochim. Pol. 60 (2013) 1–16. http://www.actabp.pl/pdf/1_2013/1.pdf%5Cnhttp://ovidsp.ovid.com/ovidweb.cgi?T=JS&PAGE=reference&D=emed11&NEWS=N&AN=23513192.

[74] Y. Zhou, H. Yan, M. Guo, J. Zhu, Q. Xiao, L. Zhang, Reactive oxygen species in vascular formation and development, Oxid. Med. Cell. Longev. 2013 (2013). https://doi.org/10.1155/2013/374963.

[75] F. De Marco, Oxidative stress and HPV carcinogenesis, Viruses 5 (2013) 708–731. https://doi.org/10.3390/v5020708.

[76] D. Guyane, Activité anti-oxydante , et caractérisation phénolique du fruit de palmier amazonien Oenocarpus bataua (patawa) Sous la direction de Bernard Fils-Lycaon, Free Radic. Biol. Med. 52 (2012) 1075–1085.

[77] P. Poprac, K. Jomova, M. Simunkova, V. Kollar, C.J. Rhodes, M. Valko, Targeting Free Radicals in Oxidative Stress-Related Human Diseases, Trends Pharmacol. Sci. 38 (2017) 592–607. https://doi.org/10.1016/j.tips.2017.04.005.

[78] E. BOUCHOUKA, Extraction des polyphénols et étude des activités antioxydante et antibactérienne de quelques plantes Sahariennes, BADJI MOKHTAR- ANNABA UNIVERSITY UNIVERSITE BADJI MOKHTAR –ANNABA, 2016.

[79] P. Shah, H.A. Modi, Comparative Study of DPPH, ABTS and FRAP Assays for Determination of Antioxidant Activity, Int. J. Res. Pap. Publ. 3 (2015) 636–641. https://www.researchgate.net/publication/307464470.

[80] S. Rahman Sajon, S. Sana, S. Rana, S. Mushiur Rahman, Z. Mostarin Nishi, S.R. Sajon, Mushrooms: Natural factory of anti-oxidant, anti- inflammatory, analgesic and nutrition, J. Pharmacogn. Phytochem. JPP 464 (2018) 464–475.

[81] A. Favier, Stress oxydant et pathologies humaines, Ann. Pharm. Françaises 64 (2006) 390–396. https://doi.org/10.1016/s0003-4509(06)75334-2.

[82] M.-E. Cuvelier, M.-N. Maillard, Stability of edible oils during storage | Stabilité des huiles alimentaires au cours de leur stockage, OCL - Ol. Corps Gras Lipides 19 (2012) 125–132. https://doi.org/10.1684/ocl.2012.0440.

[83] L.H. Abdel-Rahman, N.M. Ismail, M. Ismael, A.M. Abu-Dief, E.A.-H. Ahmed, Synthesis, characterization, DFT calculations and biological studies of Mn (II), Fe (II), Co (II) and Cd (II) complexes based on a tetradentate ONNO donor Schiff base ligand, J. Mol. Struct. 1134 (2017) 851–862.

[84] S. Kasmi-Mir, M. ElKebich, Z. Dembahri, A. Haouzi, G. Kirsch, Synthesis of new Schiff bases as materials for the design of photovoltaics cells, J. Fundam. Appl. Sci. 8 (2016) 569–583.

[85] A.A. Osowole, R. Kempe, R. Schobert, S.A. Balogun, Synthesis, characterisation and in-vitro biological activities of some metal (II) complexes of 3-(-1-(4-methyl-6-chloro)-2-pyrimidinylimino) methyl-2-napthol, Can. J. Pure Appl. Sci. 4 (2010) 1169–1178.

[86] J. Saranya, S.S. Lakshmi, In vitro antioxidant, antimicrobial and larvicidal studies of schiff base transition metal complexes, J. Chem. Pharm. Res. 7 (2015) 180–186.

[87] J.S. N'DRI, A. TIMOTOU, Z.O.N. Doumade, D. BALLO, A.L.C. KABLAN, N. GUESSAND, C.G. KODJO, Evaluation of the antibacterial activities of two new Schiff bases derived from dapsone, Moroccan J. Heterocycl. Chem. 20 (2021) 20–23.

[88] S. Tetteh, D.K. Dodoo, R. Appiah-Opong, I. Tuffour, Spectroscopic characterization, in vitro cytotoxicity, and antioxidant activity of mixed ligand palladium (II) chloride complexes bearing nucleobases, J. Inorg. Chem. 2014 (2014).

[89] M. Mesbah, T. Douadi, F. Sahli, S. Issaadi, S. Boukazoula, S. Chafaa, Synthesis, characterization, spectroscopic studies and antimicrobial activity of three new Schiff bases derived from Heterocyclic moiety, J. Mol. Struct. 1151 (2018) 41–48. https://doi.org/10.1016/j.molstruc.2017.08.098.

[90] Ö. Altun, M.Ö. Koçer, Pt (II) complex of Schiff base derived from L-phenylalanine and furfuraldehyde in the presence of 8-hydroxyquinoline: Structural analysis, composition of complex and biological activity, Comptes Rendus. Chim. 23 (2020) 127–142.

[91] I.B. Amali, M.P. Kesavan, V. Vijayakumar, N.I. Gandhi, J. Rajesh, G. Rajagopal, Structural analysis, antimicrobial and cytotoxic studies on new metal (II) complexes containing N2O2 donor Schiff base ligand, J. Mol. Struct. 1183 (2019) 342–350.

[92] M. Memišević, A. Zahirović, A. Višnjevac, A. Osmanović, D. Žilić, M. Kralj, S. Muratović, I. Martin-Kleiner, D. Završnik, E. Kahrović, Copper (II) salicylideneimine complexes revisited: From a novel derivative and extended characterization of two homologues to interaction with BSA and antiproliferative activity, Inorganica Chim. Acta 525

(2021) 120460.
[93] G.A. Krishna, T.M. Dhanya, A.A. Shanty, K.G. Raghu, P. V Mohanan, Transition metal complexes of imidazole derived Schiff bases: Antioxidant/anti-inflammatory/antimicrobial/enzyme inhibition and cytotoxicity properties, J. Mol. Struct. 1274 (2023) 134384.
[94] S. Bahçeli, E.K. Sarıkaya, Ö. Dereli, 5-Bromosalicylaldehyde: Theoretical, Experimental and Spectroscopic (FT-IR, Raman, H1 and C13- NMR, UV- Vis) Studies and Their Photovoltaic Parameters, ChemistrySelect 9 (2024) e202400054.
[95] M.S. Meenukutty, A.P. Mohan, V.G. Vidya, V.G.V. Kumar, Synthesis, characterization, DFT analysis and docking studies of a novel Schiff base using 5-bromo salicylaldehyde and β-alanine, Heliyon 8 (2022).
[96] C.G. Priya, B.R. Venkatraman, S. Sowrirajan, N. Elangovan, N. Arumugam, A.I. Almansour, S.M. Mahalingam, Fluorescence property and solvent effect on m-bromosalicylaldehyde derivative; insights from synthesis, characterization, antimicrobial activity and computational studies, Chem. Phys. Impact 7 (2023) 100323.
[97] J. Mesplède, J. Randon, 100 manipulations de chimie générale et analytique, Editions Bréal, 2004.
[98] A.-S. Bernard, S. Clède, M. Émond, H. Monin-Soyer, J. Quérard, Techniques expérimentales en chimie, Dunod, 2014.
[99] J. McMurry, E. Simanek, Chimie organique: les grands principes: cours et exercices corrigés, Dunod, 2000.
[100] C. Chiter, A. Bouchama, T.N. Mouas, H. Allal, M. Yahiaoui, I. Warad, A. Zarrouk, A. Djedouani, Synthesis, crystal structure, spectroscopic and hirshfeld surface analysis, NCI-RDG, DFT computations and antibacterial activity of new asymmetrical azines, J. Mol. Struct. 1217 (2020) 128376.
[101] L.J. Farrugia, WinGX and ORTEP for Windows: an update, J. Appl. Crystallogr. 45 (2012) 849–854.
[102] S. Lifa, C. Boudaren, Synthèse, caractérisation et étude structurale par DRX de l'oxalate mixte de cuivre et de sodium Na2Cu (C2O4) 2.2 H2O et de l'acide oxalique, (n.d.).
[103] L. Masci, Cristallochimie du fer dans les chlorites métamorphiques: approche analytique multiéchelle, expérimentale, et implications pétrologiques, (2019).
[104] C. Jelsch, M.M. Teeter, V. Lamzin, V. Pichon-Pesme, R.H. Blessing, C. Lecomte, Accurate protein crystallography at ultra-high resolution: valence electron distribution in crambin, Proc. Natl. Acad. Sci. 97 (2000) 3171–3176.
[105] J.-J. Rousseau, A. Gibaud, Cristallographie géométrique et radiocristallographie, Dunod Paris, 2007.
[106] J. Barek, A.G. Fogg, A. Muck, J. Zima, Crit. Rev. Anal. Chem. 31, (2001).
[107] M. Lacombe, Méthodes électrochimiques pour l'analyse in situ de composés bioactifs en milieu océanique, (2007).
[108] S. Chevion, M.A. Roberts, M. Chevion, The use of cyclic voltammetry for the evaluation of antioxidant capacity, Free Radic. Biol. Med. 28 (2000) 860–870.
[109] J.E.B. Randles, A cathode ray polarograph. Part II.—The current-voltage curves, Trans. Faraday Soc. 44 (1948) 327–338.

[110] P. Delahay, New instrumental methods in electrochemistry, (1954).
[111] F. Shahidi, Y. Zhong, Measurement of antioxidant activity, J. Funct. Foods 18 (2015) 757–781.
[112] M. Touat, T. Sourisseau, N. Dorvault, R.M. Chabanon, M. Garrido, D. Morel, D.B. Krastev, L. Bigot, J. Adam, J.R. Frankum, DNA repair deficiency sensitizes lung cancer cells to NAD+ biosynthesis blockade, J. Clin. Invest. 128 (2018) 1671–1687.

Chapter II

Synthesis, characterization and biological study of 2,2'-((1E , E')-((2-hydroxypropane-1,3-diyl)bis(azanylylidene))bis(methanylylidene)bis(bis(4-bromophenol) (H2L1)

And its transition metal complexes Cu(II), Mn(II), Co(II) and Zn(II).

II.1. INTRODUCTION

In this chapter we describe the synthesis and characterization of the symmetric tetradentate Schiff ligand 2,2'-((1E, E') -((2-hydroxypropane-1,3-diyl) bis(azanylylidene)) bis (methany lylidene)) bis(bis(4-bromophenol) (H2L1) as well as these transition metal complexes Copper (II), Manganese (II), Cobalt (III) and Zinc (II). The classical spectroscopic methods used to identify the synthesized products are: infrared spectroscopy (FT-IR), ultraviolet-visible spectrophotometry (UV-Vis), nuclear magnetic resonance spectroscopy (1H NMR). The proposed structures were confirmed by elementary analysis. The purity of the prepared products was checked by thin layer chromatography, on silica gel plates and with an appropriate eluent for each compound. Then, an electrochemical study by cyclic voltammetry was made to predict the redox couples of the synthesized compounds and calculations of the theory of the functional density "DFT", are also reported in this part.

With regard to elucidating the synthetic species' antioxidant potential, we have gathered many techniques for every molecule by examining their percentage of inhibition on various cations and active detrimental wanted radicals.

PART I: SYNTHESIS AND CHARACTERIZATION

II.2. Synthesis of ligand 2,2'-((1E,E')-((2-hydroxypropane-1,3-diyl)bis(azanylylidene)) bis(methany lylidene))bis(bis(4-bromophenol) (H2L1)

The Schiff base ligand (H2L1) is synthesized according to the classical method described in the literature [1,2]. The reaction pattern of the synthesis is represented by the following reaction:

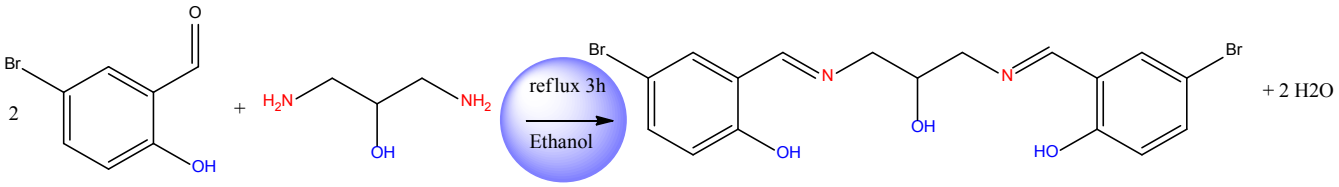

Scheme II.1. Reaction pattern of ligand formation (H2L1).

5-Bromo-2-hydroxybenzaldehyde (0.2 g; 0.99 mmol) is dissolved in 10 ml of ethanol in a 50 ml Bicol flask over high heat with nitrogen and magnetic agitation. After the mixture is well homogenized, add 0.05 g; 0.49 mmol of 1,3-diaminopropan-2-ol dissolved in 10 ml of ethanol

drop by drop. When the solution turns yellow, the reaction mixture is allowed to reflux for three hours. The precipitate is recovered using vacuum filtration, and it is then vacuum-dried for a whole night after being rinsed two or three times with cold methanol and then diethyl ether. Thin-layer chromatography (TLC) employing ethyl acetate/petroleum ether (2/1) as the eluent and a silica gel plate as the stationary phase regulates the ligand's purity. Seventy-one percent was the response yield.

The condensation process of 1,3-diaminopropan-2-ol, with 5-Bromo-2-hydroxybenzaldehyde takes place according to the following reaction mechanism (Scheme II.2).

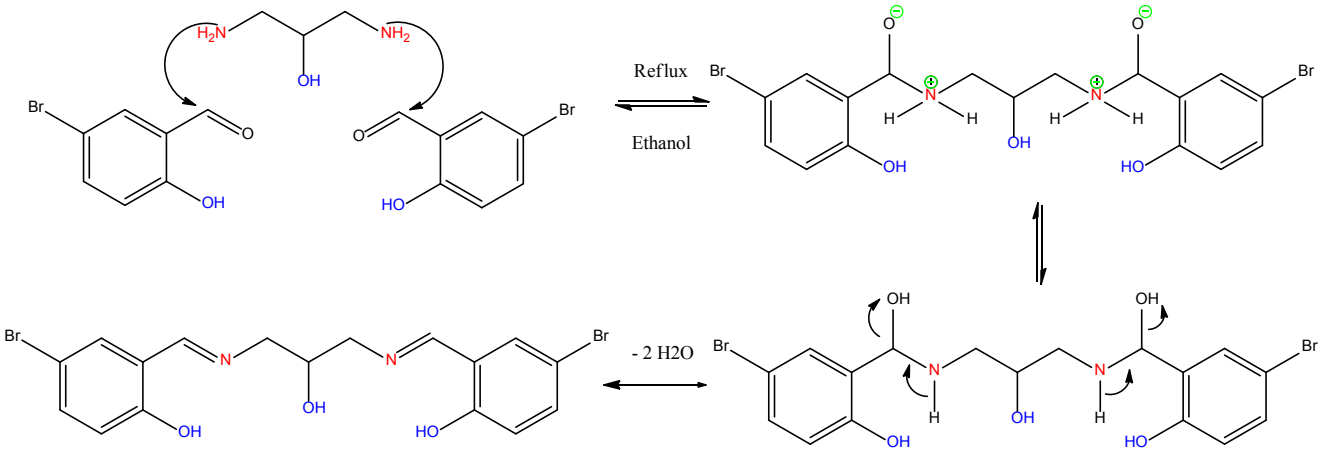

Scheme II.2. Basic Schiff (H2L1) synthesis reaction mechanism.

At optimal conditions, the formation of the ligand (H2L1) was carried out by a nuclear attack of the amine group on the carbonyl fraction of the aldehyde compound forms a double bond between two atoms N and C followed by a release of the water molecule

II.3. Synthesis of Mn(III), Cu(II), Co(III) and Zn(II) complexes with ligand (H2L1)

By following the procedure of Das, K. et al. [3] (Scheme (II.3)), complexes from the ligand (H2L1) were synthesized. In order to do this, a millimolar solution of the metal salt is added drop by drop in the following forms: cobalt CoCl2 chloride, manganese acetate (0.1g; 0.43 mmol), zinc acetate (0.09g; 0.43 mmol), copper acetate (Cu(OAc)2.H2O) (0.08g; 0.43 mmol), and other metal salts. 10 ml of ethanol was used to dissolve 6H2O (0.1g; 0.43 mmol) into a solution of 10 ml ethanoic ligand (H2L1) (0.2g; 0.43 mmol). For four to five hours, the mixture is stirred and kept under reflux. The precipitates are filtered to separate them, and then they are

cleaned with cold ethanol and diethyl ether. The corresponding yields are 71.42%, 60%, 86.81%, and 73.1%.

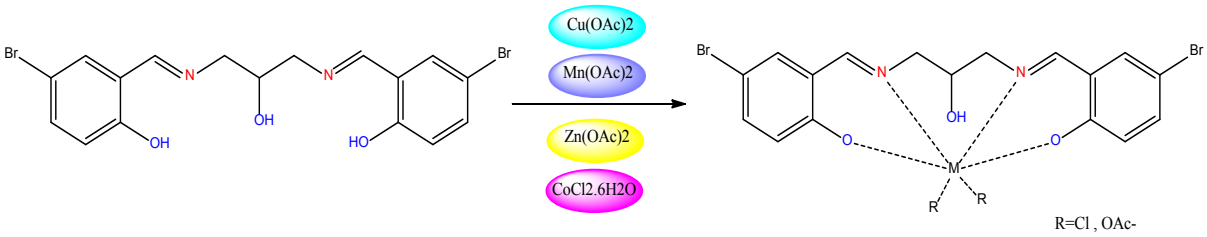

Scheme II.3. General ligand complexation reaction (H2L1)

II.4. Physical and analytical properties of ligand (H2L1) and these complexes

The synthesized ligand (H2L1) and its metal complexes are colored solids and not hygroscopic. They are stable to air and room temperature. Their purity was controlled by thin-layer chromatography (TLC), using ethyl acetate/petroleum ether (2/1) as eluent. Their melting points are acute above 250°C indicating their purity.

Solubility tests on these complexes reveal that they are insoluble in water, partially soluble in ethanol but soluble in DMF, DMSO.

The yields of the ligand synthesis and its complexes are very significant, they are of the order of 73%. All these physicochemical characteristics of the ligands and the transition metal complexes are summarized in Table II.1.

Table II.1. Physicochemical characteristics of prepared compounds.

Compound	Color of the compound	Rdt (%)	melting point °C	Solvent Solubility	R_f (%)
(H_2L1)	Yellow	**71**	**Tf=180**	Ethanol	65
Mn(II) L1	Brown	**60**	**Tf >260**	DMF	48
Cu(II) L1	Olive green	**71.42**	**Tf >260**	DMF	60
Zn(II) L1	Light yellow	**86.81**	**Tf >260**	DMSO	47
Co(II)L1	Dark green	**73.1**	**Tf >260**	DMF	53

II. 5. Spectroscopic characterizations of ligand (H2L1) and its complexes

II.5.1. UV-Visible absorption spectrophotometry analysis

The electron spectra of the ligand (H2L1) and its complexes were performed between 250 and 800 nm, at room temperature, in the DMF for the ligand ,Mn (II) L1,Cu(II) L1 and Co(II)L1 and in the DMSO for Zn(II) L1. Table II.2 below groups the wavelengths and electronic transitions that have occurred.

Table II.2. UV-Vis ligand (H2L1) absorption bands and its complexes.

Compound	λmax (nm)	[ε] (l.mol-1 cm-1)	transition
(H_2L1)	328 424	15000 1000	π→π* n→π*
Mn(II) L1	290 376 619	11600 10500 300	π→π* n→π* TCLM
Cu(II) L1	289 376 615	11700 10500 200	π→π* n→π* TCLM
Zn(II) L1	370	11000	π→π*
Co(II)L1	342 394 669	5000 4000 300	π→π* n→π* TCLM

The ligand (H2L1) has two absorption bands in its UV-visible spectrum, one of which is intense and located at 328 nm in the ultraviolet domain. It is thought that this band corresponds to the aromatic cycle transitions π π*, and the other band is located at 424 nm in the visible domain and is caused by the azomethine group C=N [4–6].

The Mn(II)L1 manganese complex (Figure II.1) exhibits three absorption bands at 290, 376, and 619 nm in its UV-vis absorption spectra. While the third, powerful band is during the d-d transition [7,8], the first two bands correlate to the ligand-metal charge transfer (TCLM) [7–9].

In the solvent DMF, a bathochrome shift is seen for the compound in respect to its ligand. The complexation of (H2L1) with the Mn(II) ion is confirmed by these findings.

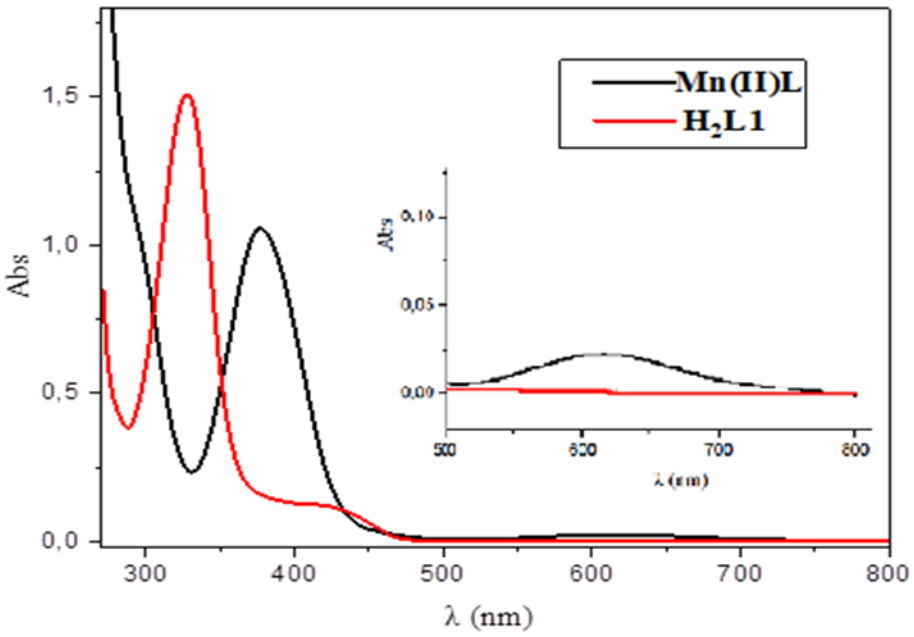

Figure II.1. UV-Visible spectrum of (H2L1) and Mn(II)L1 in DMF.

The Cu(II)L1 complex exhibits three absorption bands in its UV-visible spectrum (Figure II.2). These absorptions were detected at wavelengths of 289, 376, and 615 nm, in that order. The ligand-metal charge transfer transition is responsible for the first two absorption bands (TCLM). Manganese's d-d transition is characterized by the third absorption band [9].

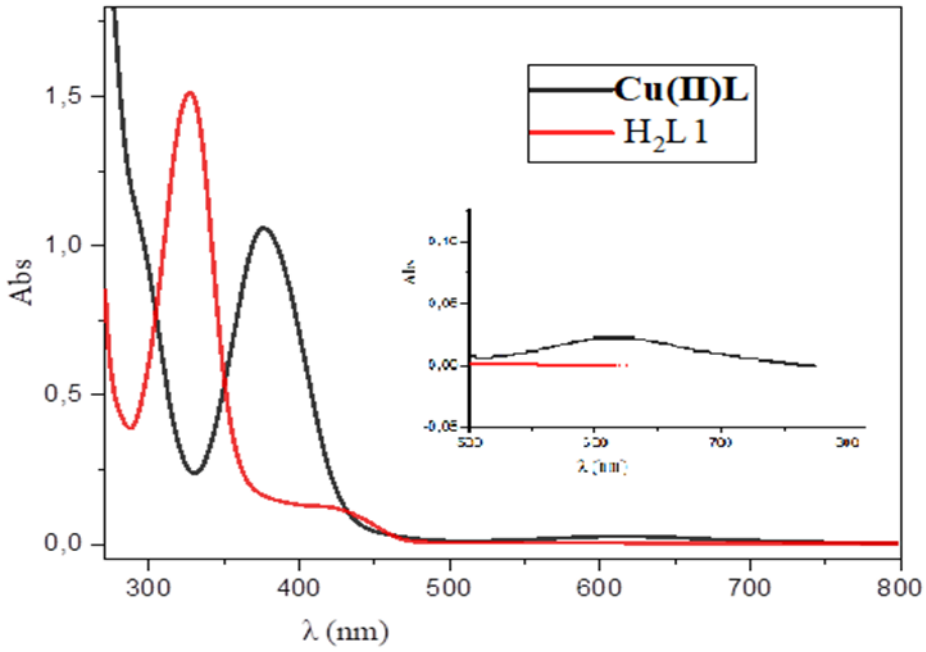

Figure II.2. UV-Visible spectrum of (H2L1) and Cu(II)L1 in DMF.

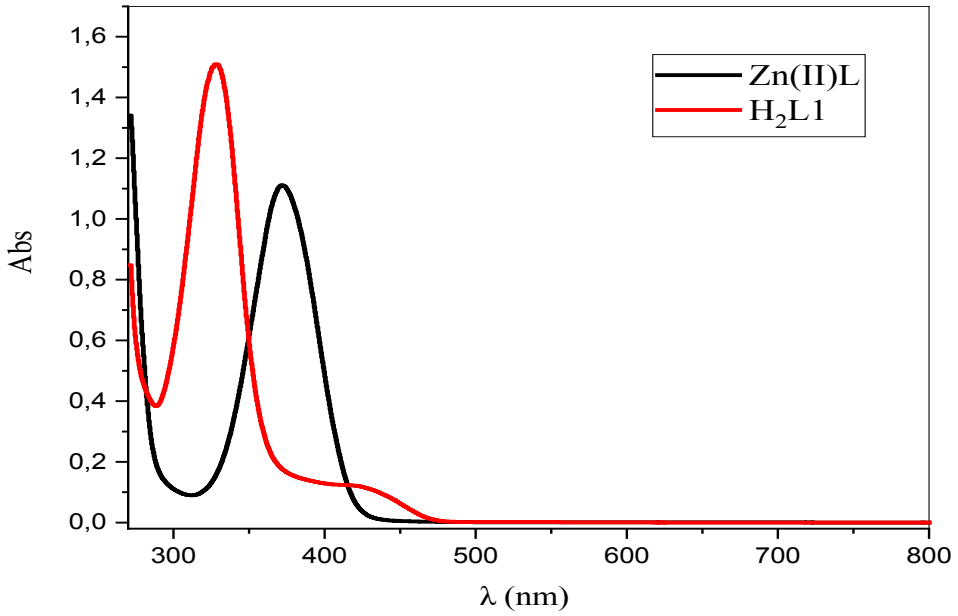

Figure II.3. UV-Visible (H2L1) and Zn(II)L1 spectra in the DMSO.

For Zn(II)L1, a single absorption band recorded at 370 nm which is attributed to the ligand-metal charge transfer transition (TCLM) as shown in Figure(II .3) [10]. The Co(II)L1 complex's UV-visible spectrum is distinguished by two strong transitions at 342 and 394 nm, which are linked to load transfers [10–12], as well as two further transition bands that are d-d less intense at 606 and 663 nm [10,12] (Figure (II.4)).

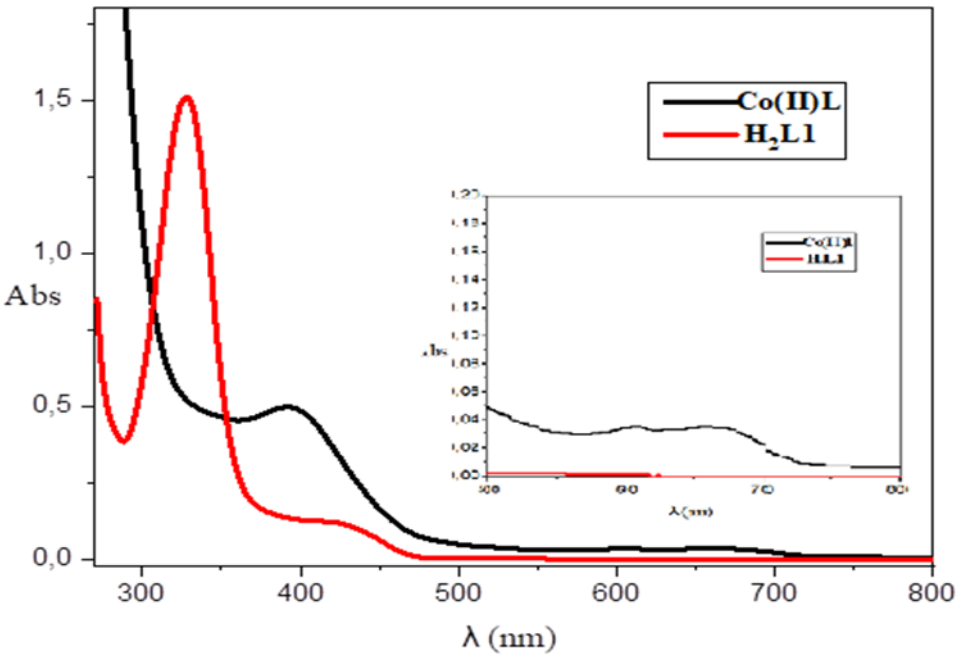

Figure II.4. UV-Visible spectrum of (H2L1) and Co(II)L1 in DMF.

There is a bathochrome displacement for the complexes with respect to the ligand in the solvents DMF and DMSO on all of the complex electron spectra. This verifies the complexation.

II.5.2. Infrared (IR) absorption spectrophotometry analysis

Using infrared absorption spectroscopy, it was possible to first describe the ligand (H2L1) and the complexes it formed, as well as confirm the identity of the inserted species. In fact, if a complexation occurs, specific bands will shift. The production of metal complexes was demonstrated by comparing the IR spectra of these complexes with those of the corresponding ligands. Table II.3 groups the principal infrared absorption bands (cm-1) of the produced products ((H2L1), Cu(II)L1, Mn(II)L1, Co(II)L1, and Zn(II)L1).

Table II.3. Major bands of ligand (H2L1) IR vibration and its complexes.

Compound	Infrared ν (cm-1)							
	ν(O-H)	ν(C=N)	ν(C=C)	ν(C-O)	ν(C-N)	ν(C-Br)	ν(M-O)	ν(M-N)
(H_2L1)	3423	1632	1476	1015	1272	682	/	/
Cu(II)L1	3324	1619	1453	1062	1180	671	537	460
Mn(II)L1	3403	1625	1462	1174	1292	674	560	455
Co(II)L1	3396	1618	1465	1045	1178	651	560	480
Zn(II)L1	3369	1625	1462	1063	1177	574	545	470

The examination of the ligand spectra (H2L1) reveals the emergence of a broad band with an average intensity of approximately 3423 cm-1, as depicted in Figure (II.5) below. This is caused by the intramolecular hydrogen bonding between hydroxyl groups (O-H) and vibrations of the hydroxyl group [13,14].

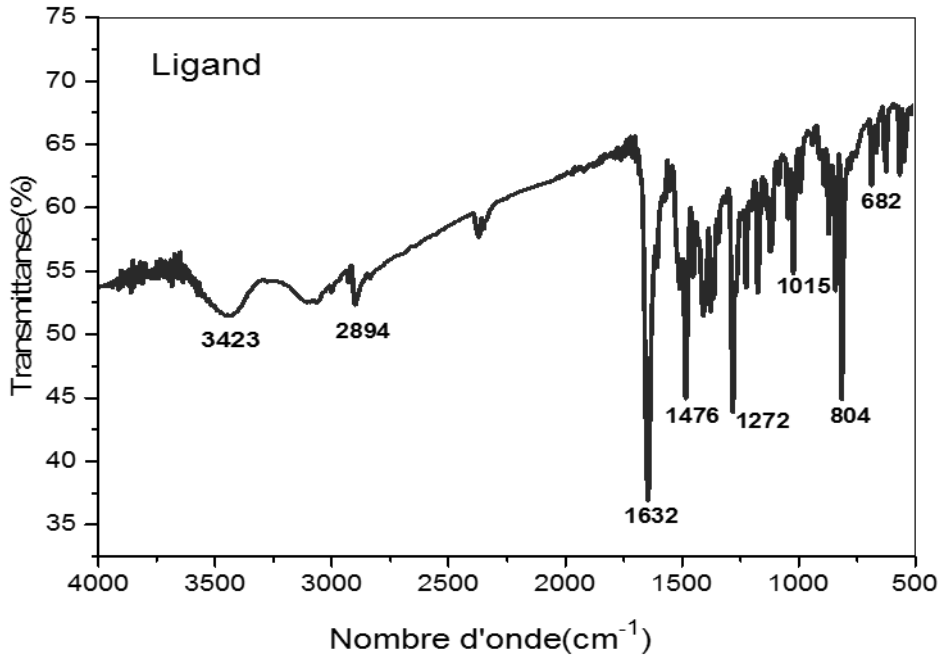

Figure II.5. IR spectrum in KBr of (H2L1).

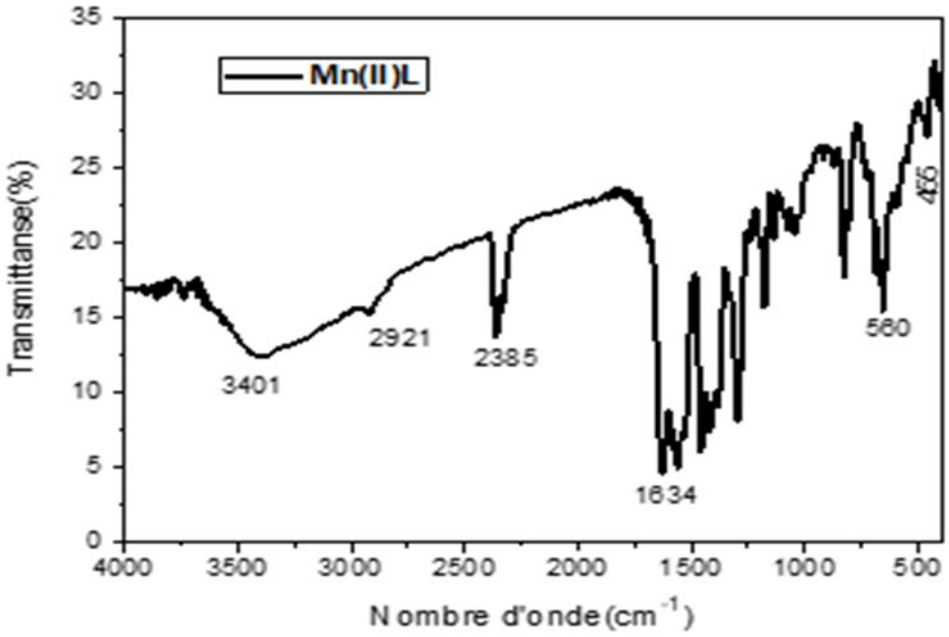

Figure II.6. IR spectrum in Mn (II)L1 KBr.

These bands, which are in the 3324-3423 cm-1 zone of the spectra of manganese (figure II.6), copper, zinc and cobalt, are related to the existence of the O-H group[15].

In the ligand spectra (H2L1), the azomethine band C=N is seen at around 1632 cm-1. The spectra of the Mn(II)L1, Cu(II)L1, Zn(II)L1, Co(II)L1, and 1618 complexes will show a decrease

in this value around 1625, 1619, 1625, and 1618, respectively (Figure II.7). This indicates the bathochrome displacement of this band, which is consistent with the literature and unambiguously indicates the coordination of ligand to metal ions [16,17].

The valence vibration of the double bonds C=C of the hydrocarbon skeleton is responsible for the band that appears in the area of 1476,1462,1453,1462, and 1465 cm-1 for the ligand and the complexes of Mn(II)L1, Cu(II)L1, Zn(II)L1, and Co(II)L1, respectively[18].

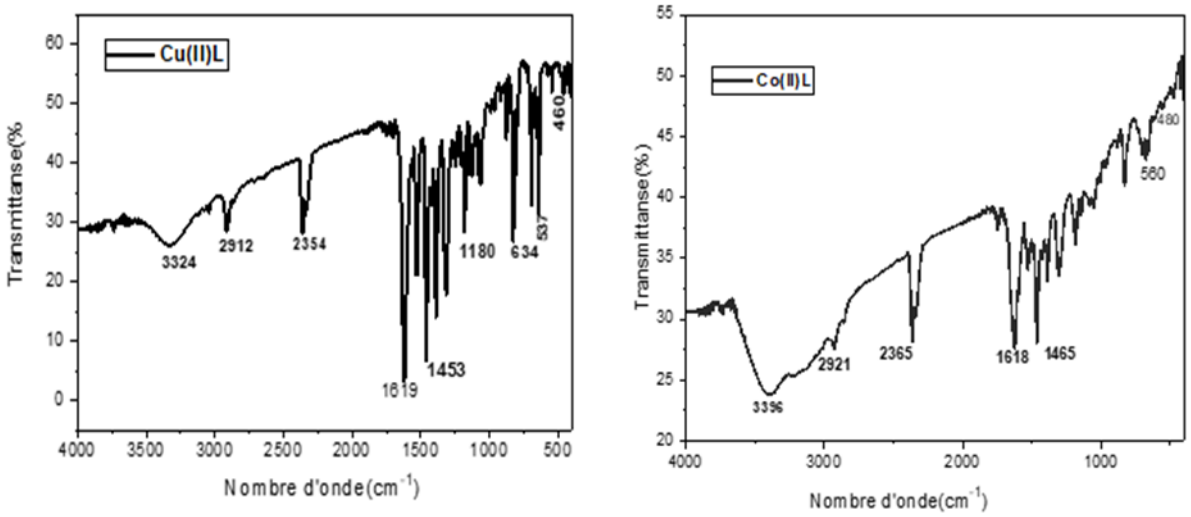

Figure II.7. IR spectrum in KBr of Cu(II)L1 and Co(II)L1.

For the ligand (H2L1) and its complexes, the elongation vibration band of phenolic C-N and C-O was detected in the intervals [1292-1177cm-1] and [1174 - 1045 cm-1], respectively. A hypochromic shift is seen for complexes, indicating that the phenolic group contributed to the complex's formation [2].

The complexes' infrared spectra include novel bands that emerge between 480 and 455 cm-1 and between 560 and 537 cm-1, respectively. These bands are ascribed to vibrations ν (M-O) [19] and ν (M-N) [20] (Figure II.8). Thus, the ligand's co-ordination with the metal ions has been confirmed. In the 682cm-1 areas, the C Br connection is also seen to vibrate [19].

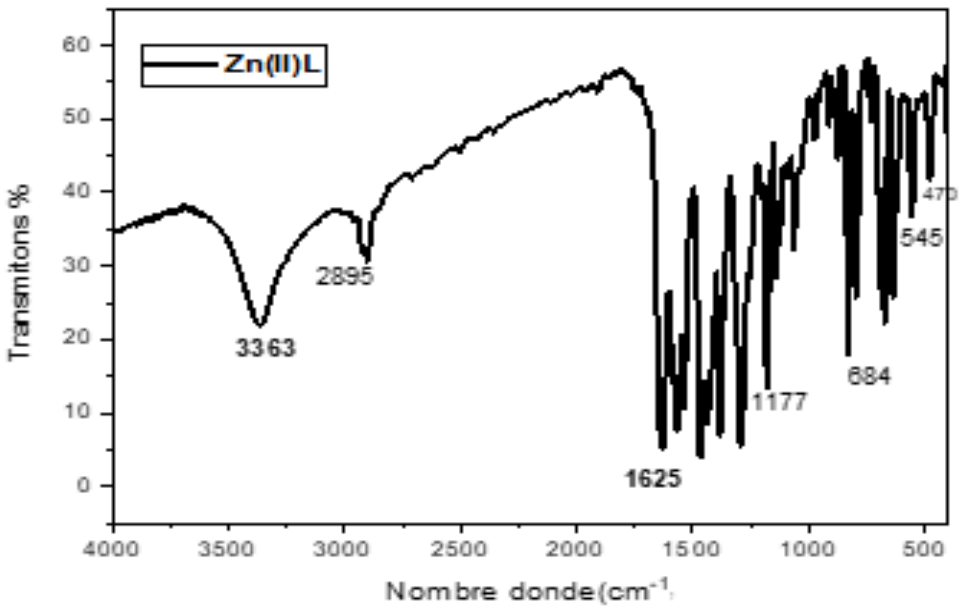

Figure II.8. IR spectrum of Zn(II)L1 in KBr.

II.5.3. Proton (^{1}H NMR) and Carbon (^{13}C NMR) Nuclear Magnetic Resonance Spectroscopy

II.5.3.1.Analysis by ^{1}H-NMR

To identify the structure of our diamagnetic ligand (H2L1), a nuclear magnetic resonance analysis of the proton and carbon was performed using a Bruker AV 300P spectrometer. using TMS as the internal reference and CDCL3 as the solvent.

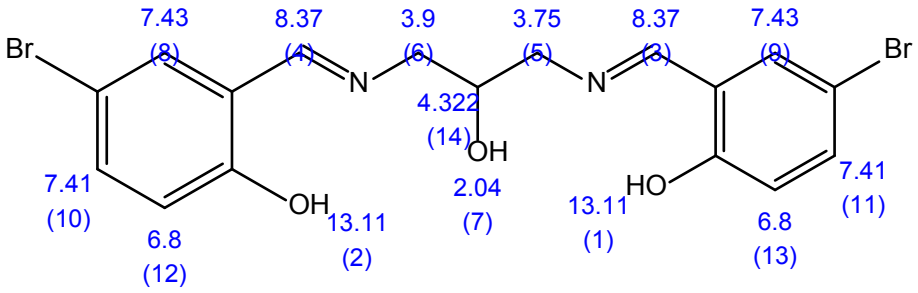

The RMN1H spectrum of the ligand (H2L1) (Figure II.9) shows the different values of the chemical de-placement. The phenolic protons H(1) and H(2) are strongly deblinded, their chemical displacements appear as singlets at the value of δ = 13.11 ppm [1]. The azomethine protons H(3) and H(4), also unblinded, also appear as singlets at the value of δ = 8.37 ppm [1]. the

signals of the aromatic protons appear as two doublets H(10),H(11),H(12),H(13) respectively at values δ=7.41 and 6.8 ppm, and singlets H(8),H(9) to δ= 7.43 ppm [1,21]

The multiplet appearing in the form of a double doublet (dd) at δ = 4.32 ppm is granted to the proton (H14) [22]. the signal of the hydroxyle O H proton which belongs to the aliphatic part is seen at δ=2.04 ppm in the form of singlet [22]. The remaining CH2 protons form a multiplet between 3.72-3.78 ppm H(5) and 3.89-3.94 ppm H(6), respectively [21,22]. The integral curves are almost in agreement with the number of protons in this structure, which of course confirms the proposed structure of the synthesized compound (H2L1)

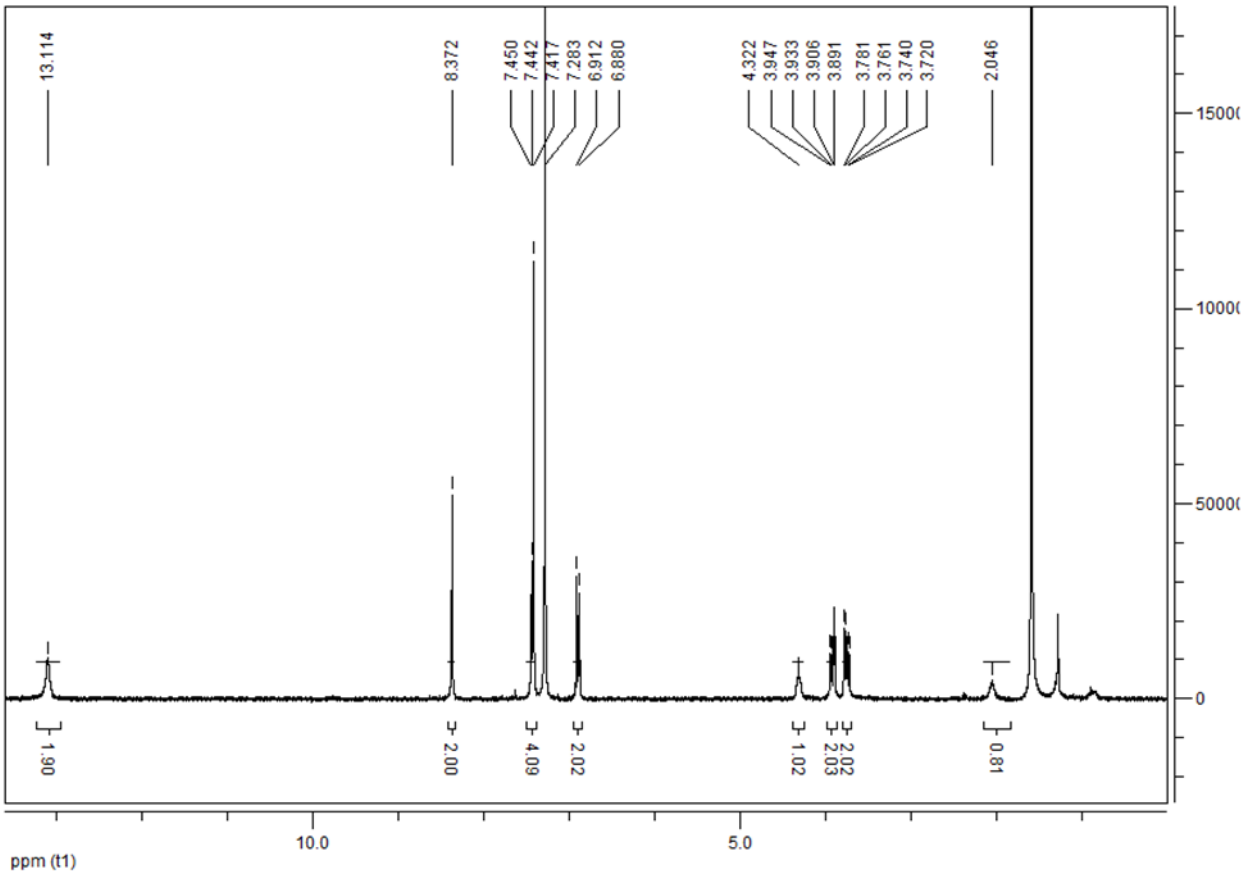

Figure II.9. ^{1}H-NMR spectrum of (H2L1) in CDCl3.

II.5.3.2.Analysis by ^{13}C-NMR

Figure III.10 depicts the ligand's (H2L1) ^{13}C NMR spectrum. It indicates a signal at 70.3 ppm that corresponds to C(1)(C-OH) of the aliphatic portion.

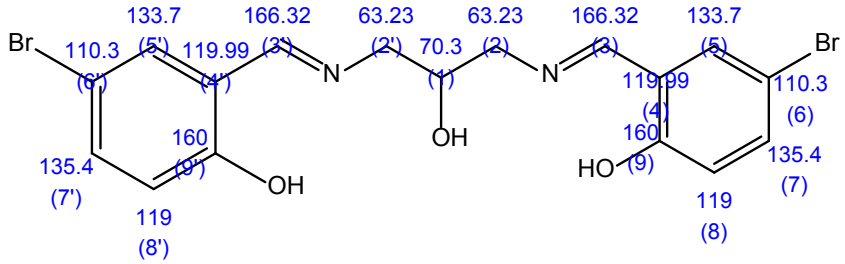

The two carbons of the azomethine group C(3), C(3') are observed at 166.32 ppm , the carbons of the benzene cycle C(4),C(4'),C(5'),C(5'),C(6),C(6'),C(7),C(7'),C(8),C(8')andC(9'),C(9'), respectively at 119.99 , 133.7 , 110.3 ,135.4 , 119.160 ppm. While carbon C(2),C(2') of (CH2) is located at 63.23 ppm [1].

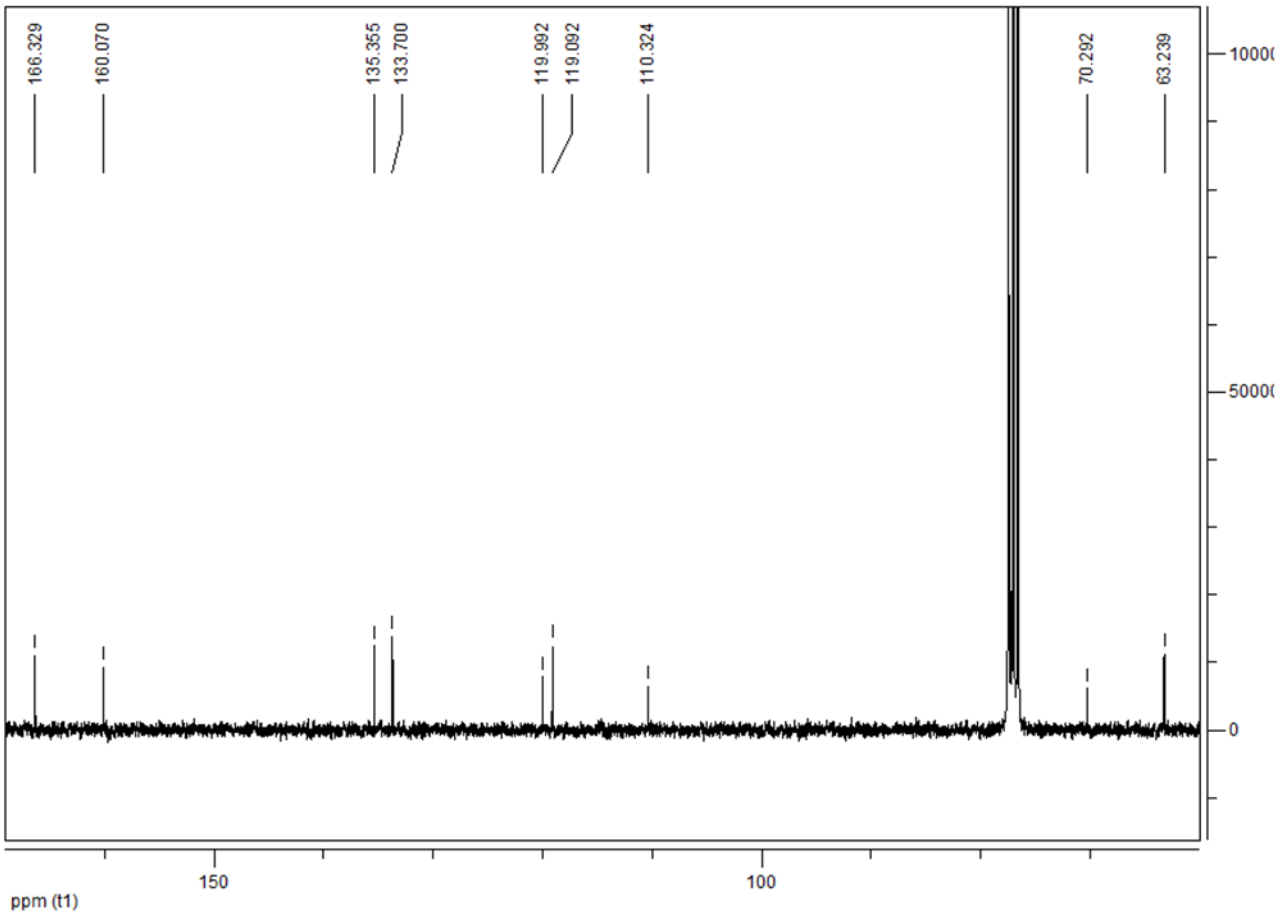

Figure II.10. ^{13}C NMR Spectrum of (H2L1) in CDCl3.

II.6. Study of electrochemical behaviour by cyclic voltammetry of ligand (H2L1) and its metal complexes

The electro-chemical behavior of the synthesized Schiff base ligand (H2L1) and its metal complexes is presented in this section of the study effort (Table II.4). Using a vitreous carbon electrode in dimethyfor-mamide (DMF) with tetrabutylammonium perchlorate (TBAP) 0.1 M, the investigation is conducted using cyclic voltammetry across a potential range of +1600 to -1600 mV/ECS at a scanning speed of 100 mV/s. Potentials are monitored with respect to an auxiliary electrode made of platinum in relation to a saturated calomel reference electrode (ECS). It should be noted that in the potential domain under study, the TBAP support electrolyte in the DMF exhibits no redox activity.

Table II.4. The electrochemical properties of ligand (H2L1) and its complexes were investigated by cyclic voltammetry in DMF

Compound	Electrochemical parameters	
	Epc (V)	Epa (V)
H2L1	-1.319	+1.303
Mn(II)L1	-0.481	/
	-1.288	/
Cu(II)L1	-1.311	+0.659
	-1.559	+1.187
Co(II)L1	-0.574	+1.279

II.6.1. Ligand electrochemical behaviour (H2L1)

Figure (II.11) shows the cyclic voltammogram of the ligand (H2L1) at a concentration of 10-3 M in an atmosphere of nitrogen. During the forward scan, a peak of reduction was observed at Epc = -1.319 V/ECS which is due to the reduction of the azometin group C=N [26–28]. On anodic scanning a peak at Epa= +1.303V/ECS is observed which is attributed to the oxidation of the phenolic group (OH) [24-25].

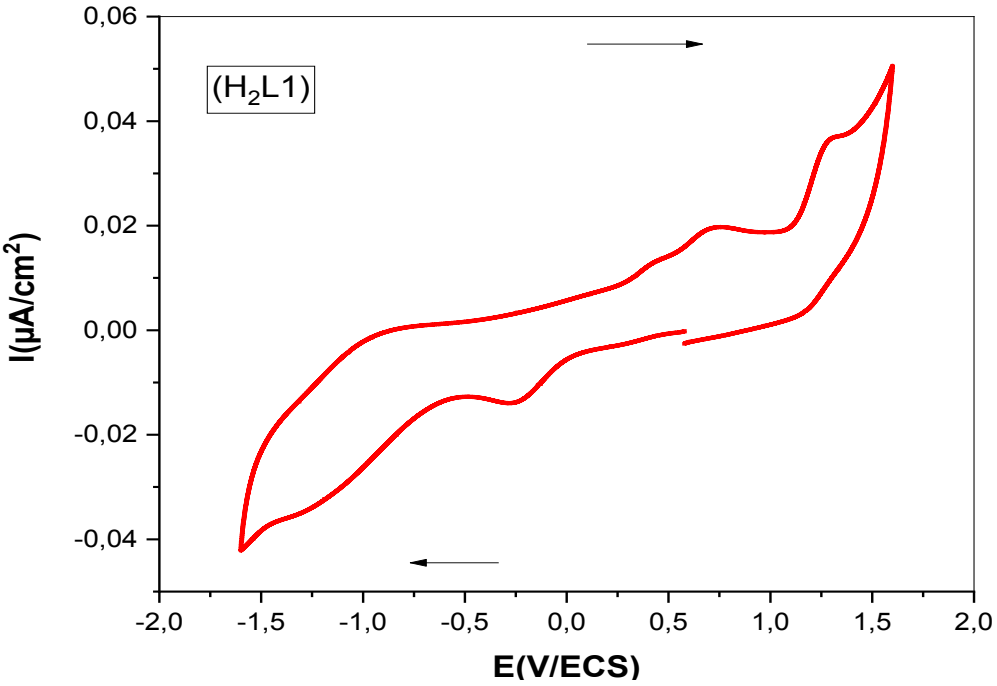

Figure II.11. Cyclic Ligand Voltammetry (H2L1)(10-3M) in DMF+TBAP (10-1M) under nitrogen atmosphere at a scanning speed of 100 mV/s.

II.6.2. Electrochemical behavior of Schiff metal-base complexes (H2L1)

II.6.2.1. Manganese complex

The electrochemical behavior of the Mn(II)L1 complex is presented by the voltammetry of Figure II.12 below.

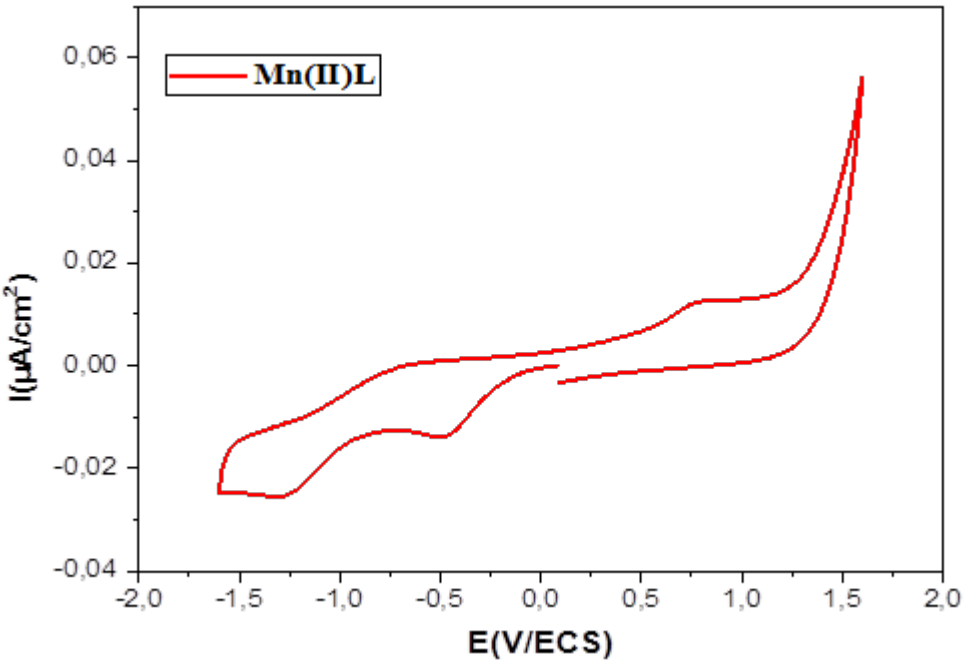

Figure II.12. Mn (II)L1(10-3M) cyclic voltammetry in FMD+TBAP (10-1M) under nitrogen atmosphere at a scanning speed of 100 mV/s.

Two cathode peaks can be seen in the voltammogram at Epc1 = -0.481 and Epc2 = -1.288V/ECS. The transition of Mn(II) ions to Mn(I) [Mn(II) + e- Mn(I)] is responsible for the first peak, whereas the reduction of the azometin group is responsible for the second peak [29–31].

II.6.2.2. Copper complex

Figure III.13 illustrates the copper (II) complex's electrochemical behavior. Two reduction peaks show up at Epc1 = -1.311 V/ECS and Epc2 = -1.559 V/ECS when scanning forward. The reduction of Cu(II) into Cu(I) is responsible for the first peak [34,35], while the reduction of the azometin group [20] is responsible for the second peak, which speeds up the transfer of electrons to the metal [36].

Two oxidation peaks are seen during the return scan at Epa1 = +0.659 V/ECS and Epc = +1.187 V/ECS. The oxidation of the ligand entity is responsible for the second peak, while the oxidation of Cu(II) ions into Cu(III) is responsible for the first peak [24–33].

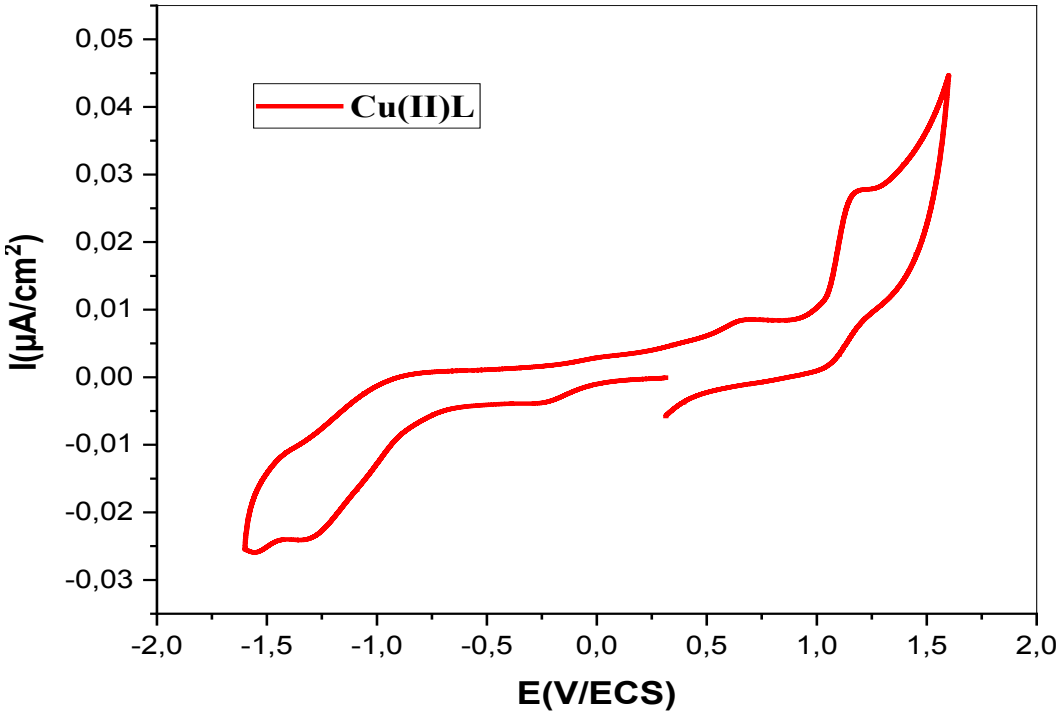

Figure II.13. Cu (II)L1(10-3M) cyclic voltammetry in FMD+TBAP (10-1M) under nitrogen atmosphere at a scanning speed of 100 mV/s.

II.6.2.3. Cobalt Complex

Figure III.14 shows the Cobalt complex's cyclic voltammogram, with a peak at -0.574V/ECS resulting from the reduction of Co(II) to Co(I)[37–39]. The oxidation of the ligand entity is responsible for the peak that is seen at Epa = +1.279 V/ECS when the scanning direction is reversed [24–25].

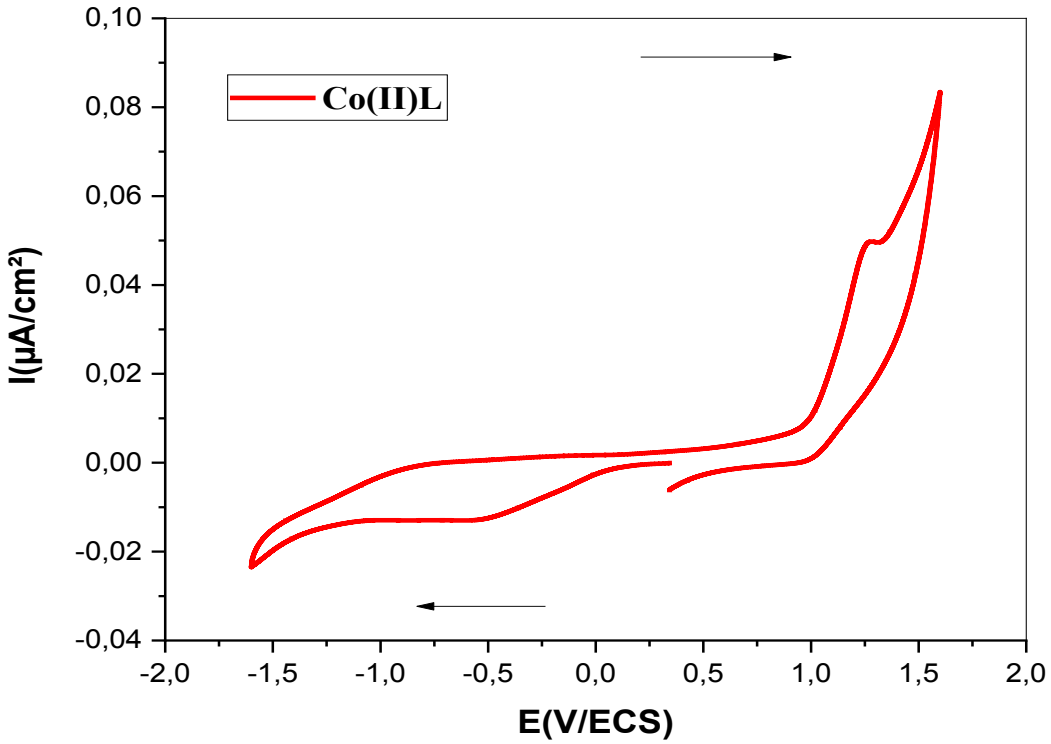

Figure II.14. Cyclic Voltammetry of Co (II)L1(10-3M) in FMD+TBAP (10-1M) under nitrogen atmosphere at a scanning speed of 100 mV/s.

PART II: STRUCTURAL STUDY BY THEORETICAL CALCULATION

II.7.1. Quantum chemistry calculations by DFT

The structural and electrical characteristics of the Schiff base ligand (H2L1) were theoretically studied in this section. Through the use of the Gaussian 9 [42] program, the Beck three-parameter hybrid exchange function [43], the Lee-Yang-Parr correlation function (B3LYP), and the 6-31G (d, p) function [44], complete geometry optimization was carried out by DFT.

In order to forecast additional qualities like chemical reactivity, this investigation enabled us to compare the theoretical findings produced using the B3LYP calculation functional with the basic vector 6-31G (d, p) and those experimenting-rates. As a result, a comparison between molecular orbital calculations (OMF) and molecular electrostatic potential (PEM) was examined. The optimized molecular structure of the ligand complex (H2L1) is depicted in the figure (II.15) below.

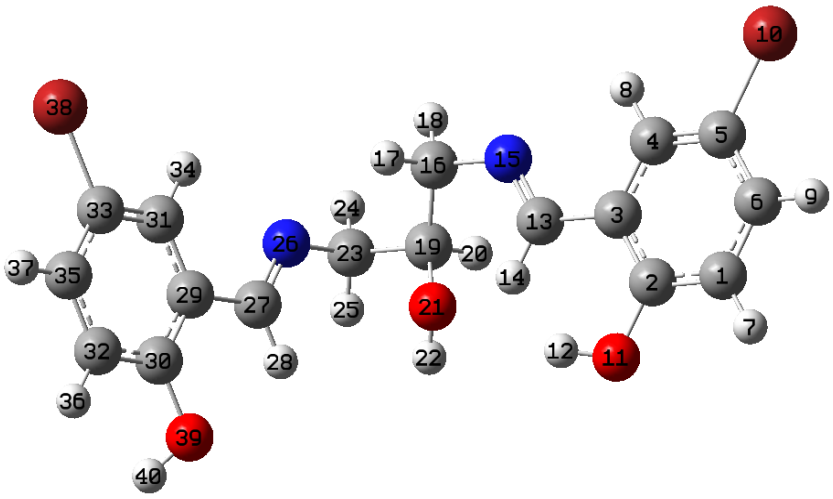

Figure II.15. Optimal molecular structure of the ligand (H2L1).

II.7.2. Frontier molecular orbitals (OMF)

The names "donor" and "acceptor" of electron transfer are more closely related to the molecular orbitals "HOMO" and "LUMO." They enable us to describe the characteristics of molecular reactivity. The absolute energy difference between the EHOMO and ELUMO energies defines the EGAP energy gap. The strong reactivity of the molecules is reflected by the lowest EGAP. Figure (II.16) shows the boundary molecular orbitals (HOMO, HOMO-1, HOMO-2, LUMO, LUMO+1et LUMO+2) of the ligand (H2L1) studied. It can be seen that :

- The LUMO energy distribution of the ligand is distributed over the entire molecule with the exception of the two Bromine atoms and one of the hydroxy groups. On the other hand, LUMO+2 contains only half of the molecule.
- The HOMO energy level covers both aromatic cycles with their substituents one of the amine parts.

The energy values of the boundary orbitals of the ligand (H2L1) are summarized in the following table.

Table II.5. Values of the HOMO, LUMO, HOMO-1, HOMO-2, LUMO+1, LU-MO+2 and the energy difference (ΔEGAP) of the ligand (H2L1).

Energy (eV)	H2L1
E (Homo)	-7.69
E (Homo-1)	-7.7
E (Homo-2)	-8.11
E (Lumo)	-5.32
E (Lumo+1)	-5.26
E (Lumo+2)	-3.73
E (gap) (HOMO → LUMO)	2.37
E (gap) (HOMO -1 → LUMO+1)	2.44
E (gap) (HOMO -2 → LUMO+2)	4.38

We find that the first oxidation/reduction of the ligand occurs on HOMO/LUMO which has ΔEGAP1 equal to 2.37 eV then on HOMO-1/LUMO+1 which has ΔEGAP2 equal to 2.44 eV after on HOMO-2/LUMO+2 which at ΔEGAP3 equal to 4.38 eV.

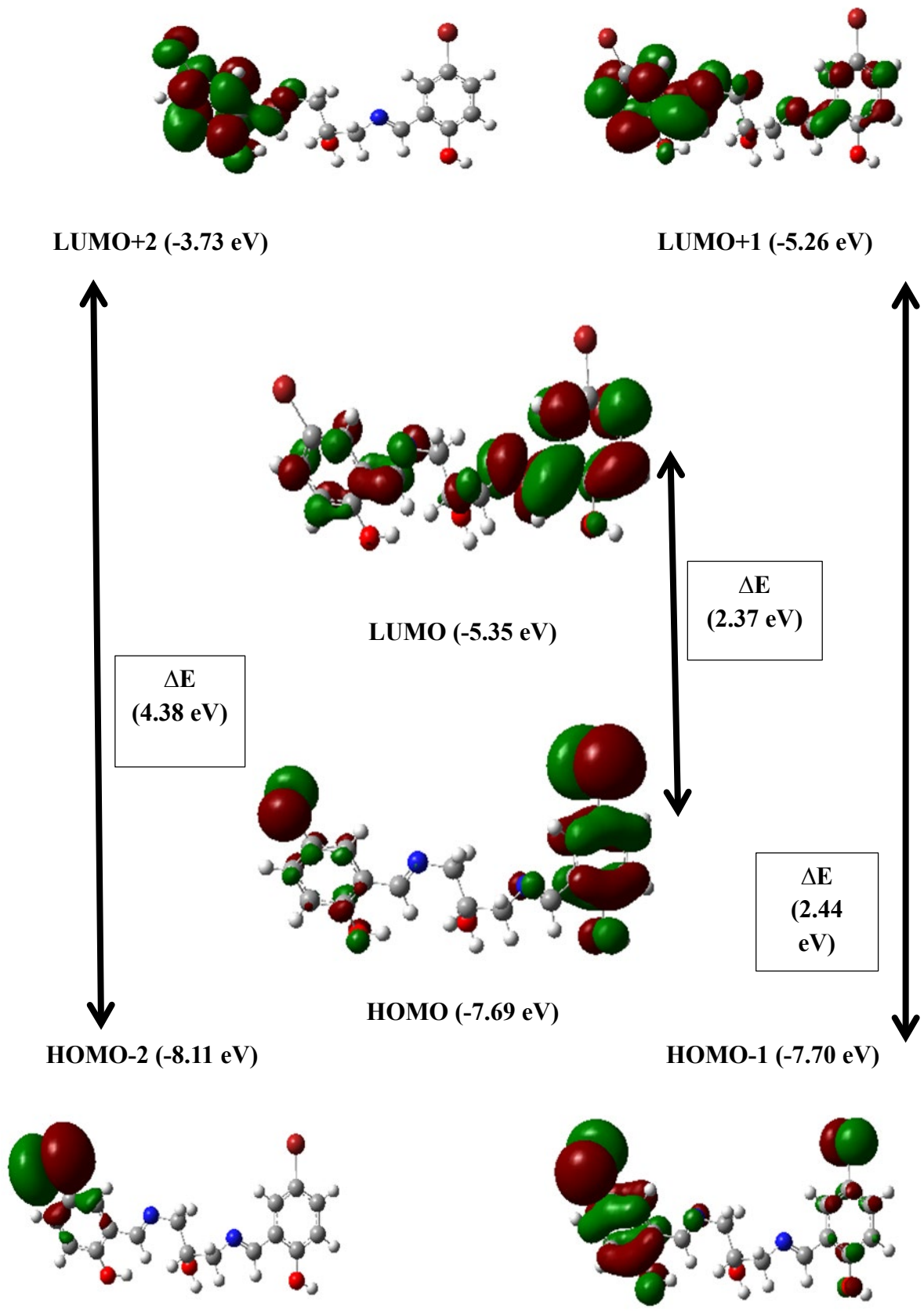

Figure II.16. Frontier molecular orbitals (OMF) of H2L1 ligand.

We can calculate the values of the chemical potential μ = (E HOMO + E LUMO) /2, which is a negative value, and the chemical hardness η = (E HOMO - E LUMO) /2 for these molecules using the estimated energies of HOMO and LUMO by the methods DFT/6-311G (d, p) [45]. The ligand's (H2L1) various molecular quantum properties are grouped in the table below.

Table II.6. Quantum parameters for ligand (H2L1).

Quantum parameters (eV)	Ligand (H_2L1)
Ionization energy I	**7.69**
Electronic affinity A	**5.32**
Chemical potential μ	**-6.5**
Hardness η	**1.18**
Electrophilicity ω	**17.9**
Softness σ	**0.84**
Electronegativity χ	**6.5**

II.7.3. Mulliken atomic charges

The atomic charges of Mulliken of the Schiff base studied was also calculated by optimization of neutral geometric structure in the gaseous state. The results are summarized in Table II.7. Mulliken charge measures the electronic structure's charge under atomic displacement and is closely correlated with the molecule's vibrational characteristics. The connected protons are the most positive atoms, whereas oxygen and nitrogen are the most negative atoms [46,47]. The findings also demonstrate that the highest positive atomic charge is found in C30 atoms. Their attachment to the hydroxy group's oxygen atom is the cause of this [32].

Based on the data analyzed and shown in Table II.7, the O11, O39, O21, N15, and N26 atoms are the strongest. The latter are these compounds' active foci of reactivity.

Table II.7. Ligand Mulliken Atomic Charges (H2L1).

Atoms	Mulliken charges	Atoms	Mulliken charges
C1	-0.466	O21	-0.765
C2	0.548	H22	0.507
C3	-0.150	C23	-0.600
C4	-0.413	H24	0.374
C5	-0.359	H25	0.352
C6	-0.397	N26	-0.607
H7	0.367	C27	0.150
H8	0.350	H28	0.322
H9	0.365	C29	-0.177
Br10	0.381	C30	0.560
O11	-0.763	C31	-0.408
H12	0.508	C32	-0.462
C13	0.137	C33	-0.362
H14	0.309	H34	0.360
N15	-0.629	C35	-0.398
C16	-0.567	H36	0.368
H17	0.377	H37	0.366
H18	0.374	Br38	0.384
C19	-0.012	O39	-0.756
H20	0.332	H40	0.510

II.7.4. Molecular Electrostatic Potential (MEP)

A relationship exists between the electron density and the molecular electrostatic potential (MEP). Utilizing the molecular electrostatic potential as a helpful descriptor, we were able to identify the active regions accountable for both nucleophilic and electrophilic assaults. The examined compounds' MEP is shown in Figure II.17.

In order to do this, we examined reactive sites for electrophilic and nucleophilic assaults and determined MEP areas using the optimal geometry of the molecules under study. A closer look

at the colors of the presentations in Figure II.17 reveals that blue denotes positive sections connected to nucleophilic reactivity, whereas red and yellow represent negative parts of the MEP associated to electrophilic reactivity.

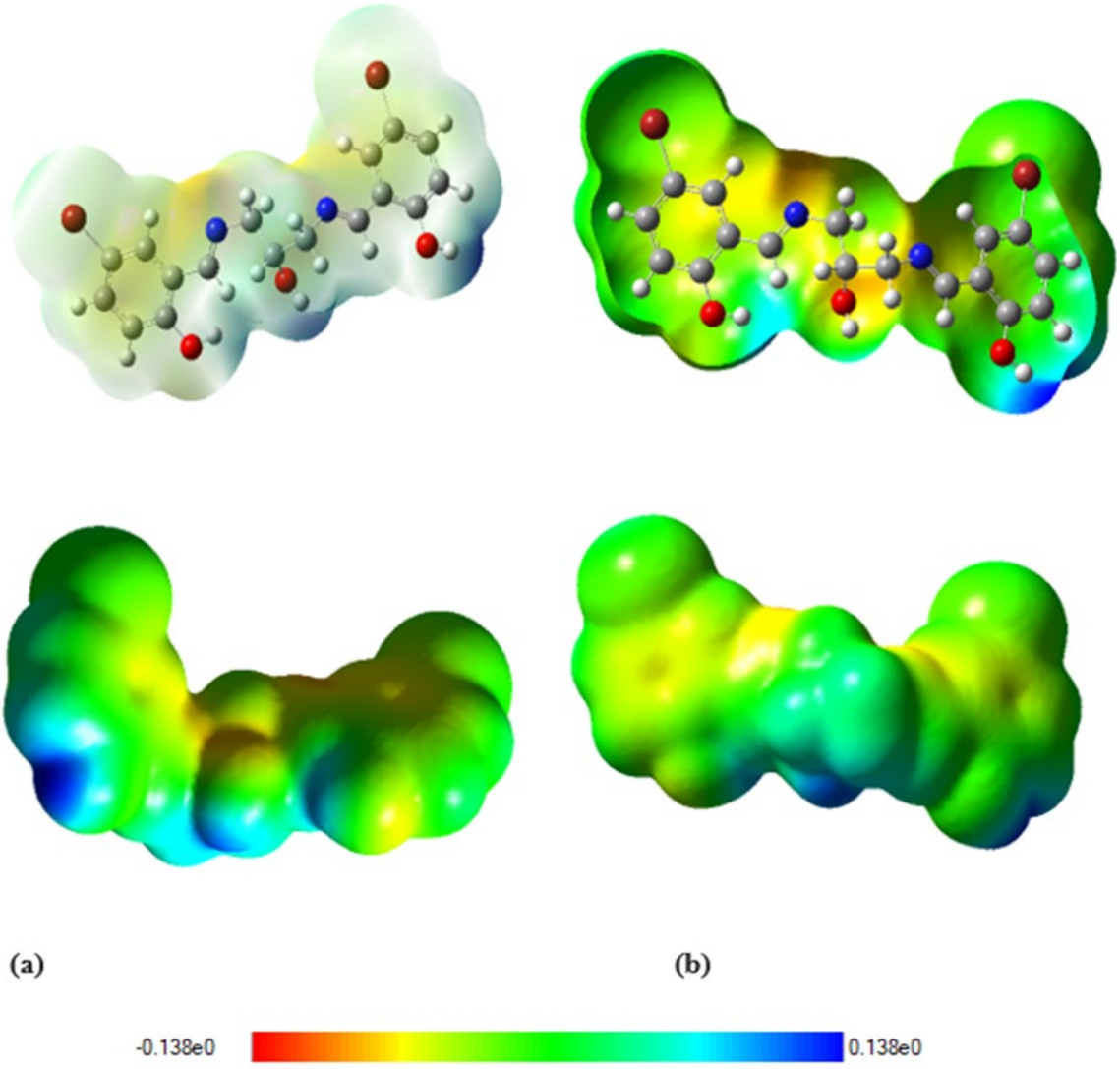

Figure II.17. Cartographer of the molecular electrostatic potential of ligands H2L1 drawn on surfaces of total density (a): Front view and (b) Rear view.

Five potential electrophilic attack sites—O11, O21, O39, N15, and N28—are present in the investigated H2L1 ligand, as shown in Figure II.17. As a result, the two phenyl cycles are a negative area and represent another potential site for electrophilic assault. It is evident from the computed MEP zones that the potential positive sites that might result in nucleophilic assaults are found near hydrogen atoms, whereas the negative sites of potentials are found on electronegative atoms (nitrogen and oxygen) and double conjugated bonds [42,43].

PART III: BIOLOGICAL STUDY, ANTIOXIDANT PROPERTIES

There are two main ways that antioxidants can trap radicals: through hydrogen transfer (TAH) or electron transfer (TES). Methods based on (TAH) are very quick (typically taking only a few seconds to complete) and assess the antioxidant's traditional capacity to eliminate free radicals by giving one atom of hydrogen. However, techniques based on (TES) are sluggish and take a long time to complete; they identify the antioxidant potential's capacity to transfer an electron to decrease an oxidizing substance [48]. The study's findings demonstrate that the examined compounds have a medium range of free radicals that they can trap.

Using several in vitro techniques, we examined the antioxidant capabilities of Schiff's base ligand and its metal complexes in order to evaluate the outcomes and determine the structure-activity connections for each technique [49]. It has been established that these compounds' imine or azo-methine groups are necessary for their biological functions. Furthermore, the biological characteristics of Schiff bases can be linked to several groups found in their structures, including hydroxyl, methoxyl, halogens, and certain heteroatoms like nitrogen, oxygen, and sulfur that make up the cyclic portions of the molecules [50]. In order to compare the anti-radical activity of Schiff and its metal complexes with that of other antioxidants like BHT, various base concentrations of Schiff were used.

Table II.8. Antioxidant activity of ligand (H2L1) and its complexes by different methods.

	DPPH IC50 (µg/ml)	**ABTS IC50 (µg/ml)**
Ligand (H2L1)	713.776	202.217
Mn(II) L1	458.832	1607.150
Cu(II) L1	900.312	1011.549
Co(II) L1	546.839	903.604
Zn(II)L1	1160.861	533.198
BHA	6.14±0.41	1.81±0.10
BHT	12.99±0.41	1.29±0.30

II.8.1. DPPH radical test

When FR (Free Radicals) sensors are present, the violet-colored DPPH radical (2,2'-diphenyl-1-picrylhydrazyl) becomes yellow and reduces to 2,2'-diphenyl-1-picrylhydrazine, which is the product of this spectrophotometric method [51]. The DPPH radical is frequently employed as a gauge to determine if a compound has antioxidant activity by giving off a hydrogen atom [52].

Using spectrophotometry, the antioxidant activity of several produced compounds (H2L1, Cu(II)L1, Zn(II)L1) against the radical DPPH was assessed by tracking the radical's decrease. All compounds have very little to no radical control action, according to the data. Using the standards BHA and BHT, Figure II.18 shows the percentage of inhibition in the concentration of the ligand (H2L1) and its metal complexes Cu(II)L1 and Zn(II)L1.

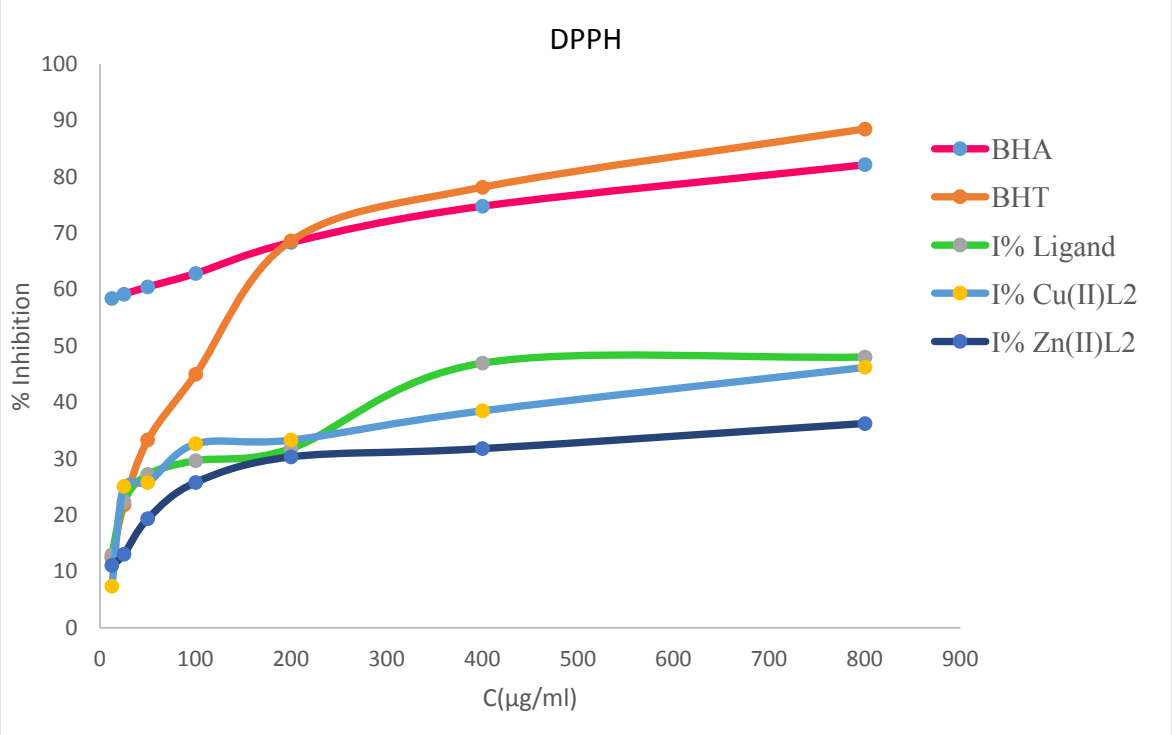

Figure II.18. Kinetics of anti-radical activity of (H2L1), Mn(II)L1 , Cu(II)L1, Co(II)L1 and Zn(II)L1 with BHA and BHT standards.

Lower IC50 values indicate a higher capacity of the test compound to act as a DPPH sensor, while higher values indicate a lower trapping activity of the scavengers. The ligand H2L1 and its complexes Cu(II)L1 and Zn(II) had values of 713,776, 900,311 and 1160,681 (µg/ml) which are practically non-significant by standard intake used BHA and BHT which were around 6.14 and 12.99 (µg/ml) respectively.

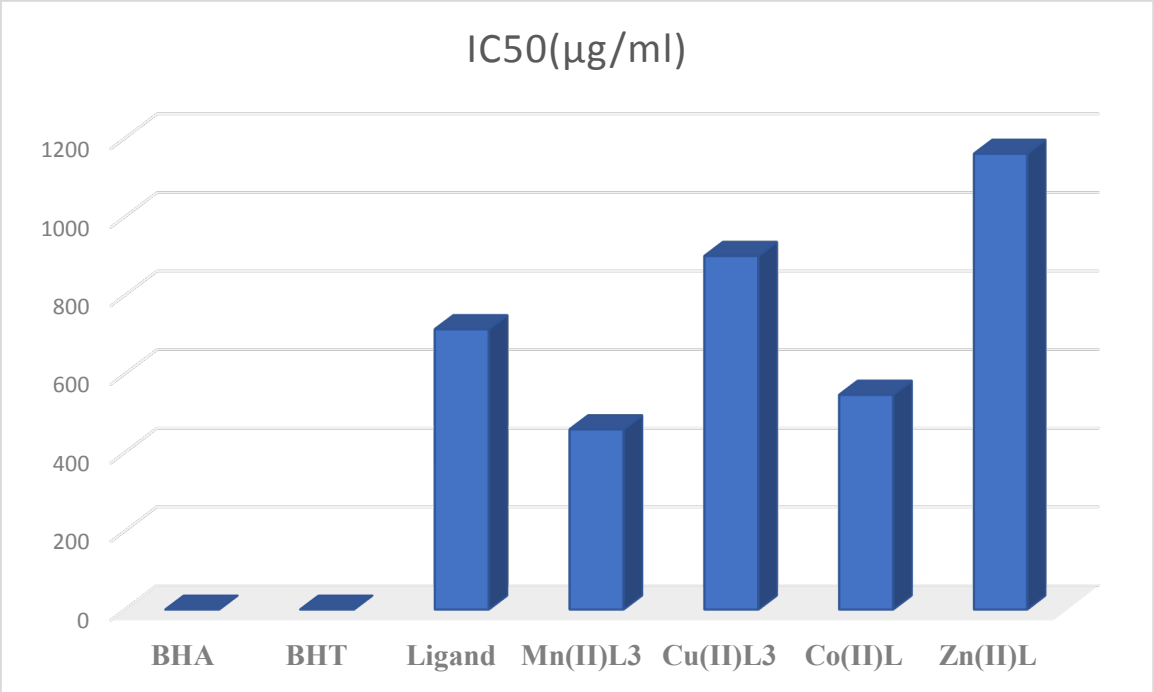

Figure II.19. IC50 inhibitory concentration values in (µg/ml). Ligand (H2L1), complexes Mn(II)L1, Cu(II)L1, Co(II)L1, Z(II)L1 and standard BHA and BHT.

The IC50 value is inversely proportional to the antioxidant capacity of a compound, because it expresses the amount of antioxidant required to decrease the free radical concentration by 50%. The smaller the IC50 value, the greater the antioxidant activity of a compound.

Thus, the antioxidant activity of the studied compounds can be classified in the following descending order:

BHA> BHT> ligand>Cu(II)L1>Zn(II)L1

The antioxidant activity of the ligand (H2L1) and its complexes was expressed in IC50 (figure II.23). The molecules presented in this chapter had inhibitory concentrations of 50% of free radicals much higher than those hydroxyanisole butyls and butylhydroxytoluene (BHA and BHT, positive control). This suggests that the radical-trapping activity of these molecules is due to an electron donor mechanism and not a hydrogen donor mechanism since there are no hydrogen atoms to donate.

II.8.2. Anti-radical activity of ABTS+•

The free radical ABTS is frequently employed to examine the anti-radical activity of extracts or isolated compounds due to its ease of use and rapidity. The reduced form of ABTS and

darkening of the solution at 734 nm occur when it comes into touch with a hydrogen donor. Each extract's anti-radical activity profile against the ABTS•+ radical is displayed in Figure II.20. These graphs show that the anti-radical power is proportional to the product concentration. These data were used to calculate the IC50 effective concentration. The findings are shown in Table II.8. Recall that IC50 is the quantity of reagents needed to inhibit half of the initial concentration of free radicals in the system.

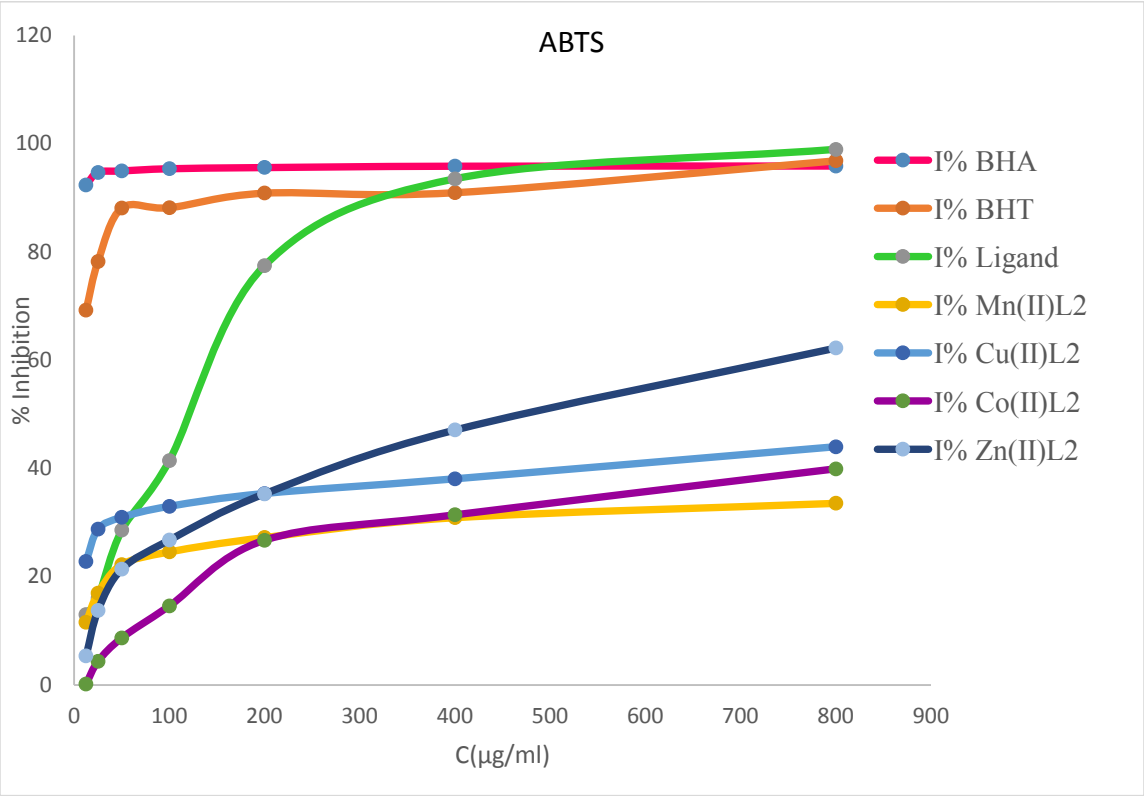

Figure II.20. Trapping effect of ABTS+ radical of H2L1, Mn(II)L1, Cu(II)L1 , Co(II)L , Zn(II)L1 and BHT and BHA standards.

Narrow trapping of the ABTS radical (202.217, 533.198 (µg/ml)) was seen with ligand (H2L1), Zn(II)L1, and the combination exhibited the best antioxidant capacity corresponding to the lowest IC50 value. It is noteworthy that although these values are better than those of the other complexes, Mn(II)L1, Cu(II)L1, and Co(II)L (1607.150, 1011.549, and 903.600(µg/ml)) correspondingly, they are still below the standard, which is BHT (1.29 µg/ml) and BHA (1.81 µg/ml). Figure II.2 shows the antioxidant capacity of our compounds vis-à-vis ABTS, whose results are expressed in IC50.

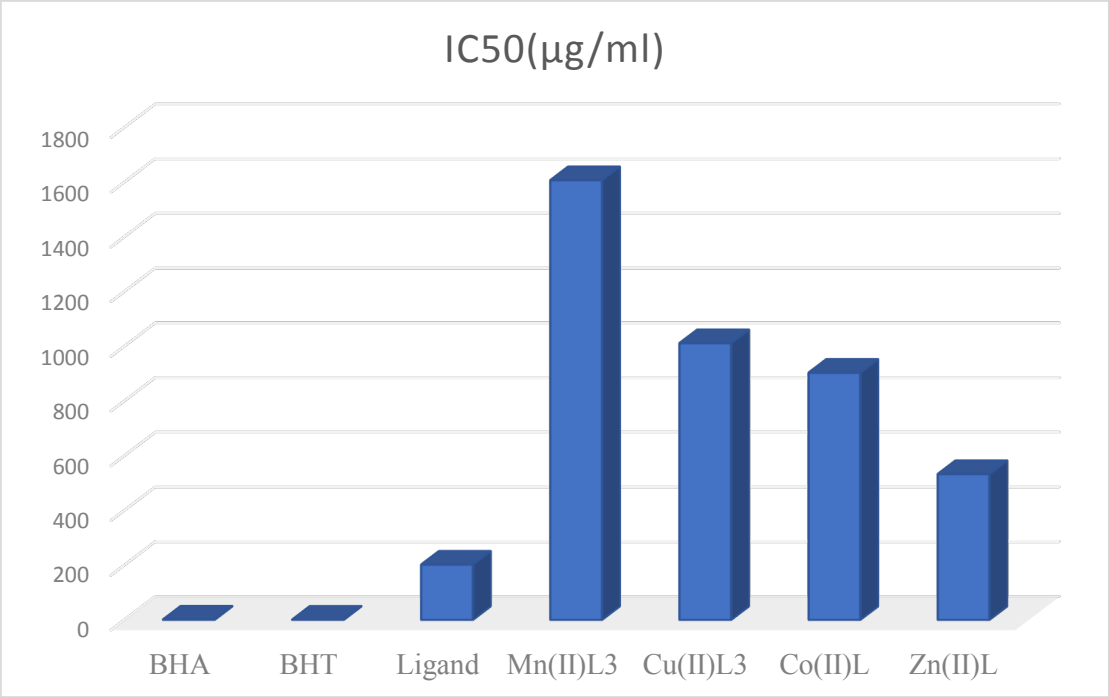

Figure II.21. IC50 inhibitory concentration values in (µg/ml). From (H2L1), Mn(II)L1, Cu(II)L1, Co(II)L1, Zn(II)L1 and standard BHA and BHT towards ABTS.

The highest antioxidant capacity corresponding to the lowest IC50 value was recorded with the ligand (H2L1) followed by the Zn(II)L1 and showed a narrow trapping effect of the radical ABTS (202.217, 533.198 (µg/ml) respectively. It should be noted that these values are better than those of the other complexes Mn(II)L1, Cu(II)L1 , Co(II)L (1607.150, 1011.549, 903.600(µg/ml)) respectively but still lower than that of the standard used: BHT (1.29 µg/ml) and BHA (1.81 µg/ml).

The IC50 of the antioxidant activity of the studied compounds can be classified in the following descending order:

BHT>BHA>Ligand>Zn(II)L1>Co(II)L1

II.9. Conclusion

Ligand 2,2'-((1E,E')-(bis(azanylylidene)bis(methanylylidene)bis(bis(4-bromophenol)(2-hydroxypropane-1,3 diyl) (H2L1) and the synthetic Cu(II), Mn(II), Co(II), and Zn(II) metallic complexes were produced. The synthetic products have good purity and respectable yields. Through spectral investigations (IR, UV/Vis, and 1H-NMR), we were able to identify and describe every structure. The various spectra's interpretations agree with the suggested structures. Synthetic compounds are by no means potent antioxidants, as demonstrated by biological studies of their antioxidant capacity against DPPH and ABTS.

References

[1] B. Biswas, M. Mitra, J. Adhikary, G. Rama Krishna, P.P. Bag, C.M. Reddy, N. Aliaga-Alcalde, T. Chattopadhyay, D. Das, R. Ghosh, Synthesis, X-ray structural and magnetic characterizations, and epoxidation activity of a new bis(μ-acetato)(μ-alkoxo)dinuclear iron(III) complex, Polyhedron 53 (2013) 264–268. https://doi.org/10.1016/j.poly.2012.12.040.

[2] B. Biswas, A. Pal, G.R. Krishna, C.M. Reddy, F. Tuna, R. Ghosh, An antiferromagnetically coupled dimeric Ni (II) complex anion and its counter cationic monomeric Ni (II) complex, and some other mononuclear transition metal compounds using some neutral ligands, Polyhedron 30 (2011) 2032–2037.

[3] K. Das, C. Massera, E. Garribba, A. Frontera, A. Datta, Synthesis, structural and DFT interpretation of a Schiff base assisted Mn(III) derivative, J. Mol. Struct. 1199 (2020) 126985. https://doi.org/10.1016/j.molstruc.2019.126985.

[4] M. Maiti, D. Sadhukhan, S. Thakurta, E. Zangrando, G. Pilet, A. Bauzá, A. Frontera, B. Dede, S. Mitra, Synthesis, structural characterization, theoretical calculations and catecholase mimetic activity of manganese-Schiff base complexes, Polyhedron 75 (2014) 40–49. https://doi.org/10.1016/j.poly.2014.03.005.

[5] S. Sen, P. Talukder, S.K. Dey, S. Mitra, G. Rosair, D.L. Hughes, G.P.A. Yap, G. Pilet, V. Gramlich, T. Matsushita, Ligating properties of a potentially tetradentate Schiff base [(CH 3) 2 NCH 2 CH 2 N [double bond, length as m-dash] CHC 6 H 3 (OH)(OMe)] with zinc (ii), cadmium (ii), cobalt (ii), cobalt (iii) and manganese (iii) ions: synthesis and structural studies, Dalt. Trans. (2006) 1758–1767.

[6] K. Das, A. Datta, B.B. Beyene, C. Massera, E. Garribba, C. Sinha, T. Akitsu, S. Tanka, A zig-zag end-to-end azido bridged MnIII 1-D coordination polymer: Spectral elucidation, magnetism, redox study and biological activity, Polyhedron 127 (2017) 315–322.

[7] M. Usharani, E. Akila, R. Rajavel, Mixed ligand Schiff base complexes: synthesis, spectral characterization and antimicrobial activity, J. Chem. Pharm. Res 4 (2012) 726–731.

[8] O. Diouf, D.G. Sall, M.L. Gaye, A.S. Sall, Synthèse et étude des propriétés spectroscopiques, magnétiques et électrochimiques des complexes de cuivre (II) et de nickel (II), Comptes Rendus. Chim. 10 (2007) 473–481.

[9] A.H. Kianfar, S. Ramazani, R.H. Fath, M. Roushani, Synthesis, spectroscopy, electrochemistry and thermogravimetry of copper (II) tridentate Schiff base complexes, theoretical study of the structures of compounds and kinetic study of the tautomerism reactions by ab initio calculations, Spectrochim. Acta Part A Mol. Biomol. Spectrosc. 105 (2013) 374–382.

[10] G. Ceyhan, M. Köse, V. McKee, S. Uruş, A. Gölcü, M. Tümer, Tetradentate Schiff base ligands and their complexes: synthesis, structural characterization, thermal, electrochemical and alkane oxidation, Spectrochim. Acta Part A Mol. Biomol. Spectrosc. 95 (2012) 382–398.

[11] A. Pui, C. Policar, J.-P. Mahy, Electronic and steric effects in cobalt Schiff bases complexes: Synthesis, characterization and catalytic activity of some cobalt (II) tetra-halogens-dimethyl salen complexes, Inorganica Chim. Acta 360 (2007) 2139–2144.

[12] M. V Rodić, V.M. Leovac, L.S. Jovanović, L.S. Vojinović-Ješić, V. Divjaković, V.I. Češljević, Transition metal complexes with thiosemicarbazide-based ligands: Part 59.

Synthesis, structures and electrochemical properties of cobalt (III) complexes with 2-acetylpyridine S-methylisothiosemicarbazone, Polyhedron 46 (2012) 124–132.

[13] O.E. Sherif, N.S. Abdel-Kader, DFT calculations, spectroscopic studies, thermal analysis and biological activity of supramolecular Schiff base complexes, Arab. J. Chem. 11 (2018) 700–713.

[14] O.E. Sherif, N.S. Abdel-Kader, Spectroscopic and biological activities studies of bivalent transition metal complexes of Schiff bases derived from condensation of 1, 4-phenylenediamine and benzopyrone derivatives, Spectrochim. Acta Part A Mol. Biomol. Spectrosc. 117 (2014) 519–526.

[15] I. V Korendovych, E. V Rybak-Akimova, Chloro {2, 2′-[(1S, 2S)-1, 2-diphenyl-1, 2-ethanediylbis (nitrilomethylidyne)] diphenolato-κ4O, N, N′, O′}(ethanol-κO) manganese (III), Acta Crystallogr. Sect. C Cryst. Struct. Commun. 60 (2004) m82–m84.

[16] A. Rambabu, M.P. Kumar, S. Tejaswi, N. Vamsikrishna, DNA interaction, antimicrobial studies of newly synthesized copper (II) complexes with 2-amino-6-(trifluoromethoxy) benzothiazole Schiff base ligands, J. Photochem. Photobiol. B Biol. 165 (2016) 147–156.

[17] M. Merzougui, K. Ouari, J. Weiss, Ultrasound assisted synthesis, characterization and electrochemical study of a tetradentate oxovanadium diazomethine complex, J. Mol. Struct. 1120 (2016) 239–244.

[18] K. Mohammadi, M. Niad, A. Irandoost, Synthesis, spectral, thermal and thermodynamic studies of oxovanadium (IV) complexes of Schiff bases derived from 3, 4-diaminobenzoic acid with salicylaldehyde derivatives, Spectrochim. Acta Part A Mol. Biomol. Spectrosc. 107 (2013) 145–150.

[19] S. Dekar, K. Ouari, S. Bendia, D. Hannachi, J. Weiss, Mononuclear oxovanadium (IV) Schiff base complex: Synthesis, spectroscopy, electrochemistry, DFT calculation and catalytic activity, J. Organomet. Chem. 866 (2018) 165–176.

[20] M. Sarigul, S.E. Kariper, P. Deveci, H. Atabey, D. Karakas, M. Kurtoglu, Multi-properties of a new azo-Schiff base and its binuclear copper (II) chelate: Preparation, spectral characterization, electrochemical, potentiometric and modeling studies, J. Mol. Struct. 1149 (2017) 520–529.

[21] B. Wafa, Les complexes de métaux de transition. Synthèse chimique, caractérisation spectroscopique et électrochimique. Application antibactérienne, UNIVERSITÉ FERHAT ABBAS - SETIF1- FACULTÉ DE TECHNOLOGIE, 2021. http://dspace.univ-setif.dz:8888/jspui/handle/123456789/3746.

[22] L.D. Popov, S.A. Borodkin, Y. V. Revinskii, I.N. Shcherbakov, V.G. Vlasenko, S.I. Levchenkov, Synthesis and Selected Properties of Novel Metal Complexes with Bis-Azomethine Based on 7-Hydroxy-4-methyl-8-formylcoumarin and 1,3-Diaminopropan-2-ol, Russ. J. Gen. Chem. 89 (2019) 1800–1807. https://doi.org/10.1134/S1070363219090123.

[23] A. Adenier, M.M. Chehimi, I. Gallardo, J. Pinson, N. Vila, Electrochemical oxidation of aliphatic amines and their attachment to carbon and metal surfaces, Langmuir 20 (2004) 8243–8253.

[24] R. Benramdane, F. Benghanem, A. Ourari, S. Keraghel, G. Bouet, Synthesis and char-

acterization of a new Schiff base derived from 2,3-diaminopyridine and 5-methoxysalicylaldehyde and its Ni(II), Cu(II) and Zn(II) complexes. Electrochemical and electrocatalytical studies, J. Coord. Chem. 68 (2015) 560–572. https://doi.org/10.1080/00958972.2014.994514.

[25] A. Ourari, K. Ouari, M.A. Khan, G. Bouet, Dioxygen activation with a cytochrome P450 model. Characterization and electrochemical study of new unsymmetrical tetradentate Schiff-base complexes with iron (III) and cobalt (II), J. Coord. Chem. 61 (2008) 3846–3859.

[26] S. Zolezzi, E. Spodine, A. Decinti, Electrochemical studies of copper (II) complexes with Schiff-base ligands, Polyhedron 21 (2002) 55–59.

[27] S. Kumar, A. Hansda, A. Chandra, A. Kumar, M. Kumar, M. Sithambaresan, M.S.H. Faizi, V. Kumar, R.P. John, Co(II), Ni(II), Cu(II) and Zn(II) complexes of acenaphthoquinone 3-(4-benzylpiperidyl)thiosemicarbazone: Synthesis, structural, electrochemical and antibacterial studies, Polyhedron 134 (2017) 11–21. https://doi.org/10.1016/j.poly.2017.05.055.

[28] D. Hannachi, N. Ouddai, H. Chermette, A quantum chemistry investigation on the structure of lanthanide triflates Ln (OTf) 3 where Ln= La, Ce, Nd, Eu, Gd, Er, Yb and Lu, Dalt. Trans. 39 (2010) 3673–3680.

[29] N.E. Eltayeb, Manganese(III) complexes with tetradentate schiff base ligands: Ir, uv/vis, electrochemistry and fluorescence properties, Indones. J. Chem. 20 (2020) 451–457. https://doi.org/10.22146/ijc.46395.

[30] I. Kuźniarska-Biernacka, O. Rodrigues, M.A. Carvalho, P. Parpot, K. Biernacki, A.L. Magalhães, A.M. Fonseca, I.C. Neves, Electrochemical and catalytic studies of a manganese (III) complex with a tetradentate Schiff-base ligand en capsulated in NaY zeolite, Eur. J. Inorg. Chem. 2013 (2013) 2768–2776.

[31] M.H. Habibi, E. Askari, Synthesis, structural characterization, thermal, and electrochemical investigations of a square pyramid manganese(III) complex with a Schiff base ligand acting as N2O2 tetradentate in equatorial and as O monodendate in axial positions: Application as a pr, Synth. React. Inorganic, Met. Nano-Metal Chem. 43 (2013) 406–411. https://doi.org/10.1080/15533174.2012.740741.

[32] R.A.A. Ammar, A.N.M.A. Alaghaz, A.A. Elhenawy, DFT, characterization and investigation of vibrational spectroscopy of 4-(4-hydroxy)-3-(2-pyrazine-2-carbonyl)hydrazonomethylphenyl-diazen-yl- benzenesulfonamide and its copper(II) complex, J. Mol. Struct. 1067 (2014) 94–103. https://doi.org/10.1016/j.molstruc.2014.02.051.

[33] D.F. V Lewis, C. Ioannides, D. V Parke, Interaction of a series of nitriles with the alcohol-inducible isoform of P450: Computer analysis of structure—activity relationships, Xenobiotica 24 (1994) 401–408.

[34] M.H. Habibi, R. Mokhtari, M. Mikhak, M. Amirnasr, A. Amiri, Synthesis, spectral and electrochemical studies of Cu(II) and Ni(II) complexes with new N 2O 2 ligands: A new precursor capable of depositing copper nanoparticles using thermal reduction, Spectrochim. Acta - Part A Mol. Biomol. Spectrosc. 79 (2011) 1524–1527. https://doi.org/10.1016/j.saa.2011.05.010.

[35] M. Kuate, E.M. Ngandung, F.A.N. Kamga, A.G. Paboudam, C.A. Mariam, C.N. Pecheu,

T.K. Ignas, P.T. Ndifon, Cobalt (II), Nickel (II) and Copper (II) complexes of Tetradentate Schiff base ligands derived from 4-Nitro-O-phenylenediamine: Synthesis, Characterization, cyclic voltammetry and biological studies, Egypt. J. Chem. 65 (2022) 477–495. https://doi.org/10.21608/EJCHEM.2022.82313.4087.

[36] S.A. Hosseini-Yazdi, A. Mirzaahmadi, P. Samadzadeh-Aghdam, A.A. Khandar, G. Mahmoudi, W. Scott Kassel, W.G. Dougherty, Synthesis, characterization, X-ray structure, spectroscopic and electrochemical studies of copper and zinc complexes with two new polydentate ligands, Inorganica Chim. Acta 414 (2014) 115–120. https://doi.org/10.1016/j.ica.2014.01.039.

[37] A.H. Sarvestani, A. Salimi, S. Mohebbi, R. Hallaj, Synthesis, spectroscopy and electrochemistry of cobalt(III) Schiff base complexes, J. Chem. Res. (2005) 190–193. https://doi.org/10.3184/0308234054213708.

[38] M. Salehi, M. Amirnasr, S. Meghdadi, K. Mereiter, H.R. Bijanzadeh, A. Khaleghian, Synthesis, characterization, and X-ray crystal structure of cobalt (III) complexes with a N2O2-donor Schiff base and ancillary ligands. Spectral, antibacterial activity, and electrochemical studies, Polyhedron 81 (2014) 90–97.

[39] A.H. Kianfar, S. Zargari, Synthesis, spectroscopy and electrochemical study of cobalt(III) N2O2 Schiff-base complexes, J. Coord. Chem. 61 (2008) 341–352. https://doi.org/10.1080/00958970701329217.

[40] S.T. Lutta, S.M. Kagwanja, Synthesis and electrochemical studies of heterobinuclear zinc and molybdenum mononitrosyl complexes linked by Schiff base ligands, Transit. Met. Chem. 26 (2001) 523–527.

[41] K. Ouari, S. Bendia, J. Weiss, C. Bailly, Spectroscopic, crystal structural and electrochemical studies of zinc(II)-Schiff base complex obtained from 2,3-diaminobenzene and 2-hydroxy naphthaldehyde, Spectrochim. Acta - Part A Mol. Biomol. Spectrosc. 135 (2015) 624–631. https://doi.org/10.1016/j.saa.2014.07.034.

[42] M. Ben Jomaa, H. Chebbi, N.F. Bourguiba, M.F. Zid, Structure cristalline, caractérisation spectroscopique, calcul DFT et analyse de surface Hirshfeld du perchlorate de p-toluidinium, Acta Crystallogr. Sect. E Crystallogr. Commun. 74 (2018) 91–97. https://doi.org/10.1107/S2056989017018096.

[43] M. Ashfaq, M.N. Tahir, S. Muhammad, K.S. Munawar, A. Ali, G. Bogdanov, S.S. Alarfaji, Single-Crystal Investigation, Hirshfeld Surface Analysis, and DFT Study of Third-Order NLO Properties of Unsymmetrical Acyl Thiourea Derivatives, ACS Omega 6 (2021) 31211–31225. https://doi.org/10.1021/acsomega.1c04884.

[44] W. ZEMAMOUCHE, Elaboration et caractérisation des produits organiques à intérêt biologique substitués par des méthyles et des halogènes ., 2021.

[45] R. Shahidha, S. Muthu, M. Raja, R.R. Muhamed, B. Narayana, P.S. Nayak, B.K. Sarojini, Spectroscopic (FT-IR, FT-Raman), first order hyperpolarizabilities, NBO, Fukui function and molecular docking study of N-(4-Chloro-3-methylphenyl)-2-phenylacetamide, Optik (Stuttg). 140 (2017) 1127–1142. https://doi.org/10.1016/j.ijleo.2017.03.120.

[46] H.P. Ebrahimi, J.S. Hadi, Z.A. Abdulnabi, Z. Bolandnazar, Spectroscopic, thermal analysis and DFT computational studies of salen-type Schiff base complexes, Spectrochim. Acta - Part A Mol. Biomol. Spectrosc. 117 (2014) 485–492.

https://doi.org/10.1016/j.saa.2013.08.044.

[47] L.H. Abdel-Rahman, N.M. Ismail, M. Ismael, A.M. Abu-Dief, E.A.H. Ahmed, Synthesis, characterization, DFT calculations and biological studies of Mn(II), Fe(II), Co(II) and Cd(II) complexes based on a tetradentate ONNO donor Schiff base ligand, J. Mol. Struct. 1134 (2017) 851–862. https://doi.org/10.1016/j.molstruc.2017.01.036.

[48] R.L. Prior, X. Wu, K. Schaich, Standardized methods for the determination of antioxidant capacity and phenolics in foods and dietary supplements, J. Agric. Food Chem. 53 (2005) 4290–4302.

[49] A. Baghiani, S. Boumerfeg, F. Belkhiri, S. Khennouf, N. Charef, D. Harzallah, L. Arrar, M.A.A. Wahhab, Antioxidant and radical scavenging properties of Carthamus caeruleus L extracts grow wild in Algeria flora, Comun. Sci. 1 (2010) 128.

[50] S. Kumar, D.N. Dhar, P.N. Saxena, Applications of metal complexes of Schiff bases-A review, (2009).

[51] H. TRABSA, Activité antioxydante et anti-inflammatoire des fractions des plantes médicinales : Sedum sediforme et Lycium arabicum Devant, Université Ferhat Abbas Sétif 1, 2015.

[52] B. Tepe, D. Daferera, A. Sokmen, M. Sokmen, M. Polissiou, Antimicrobial and antioxidant activities of the essential oil and various extracts of Salvia tomentosa Miller (Lamiaceae), Food Chem. 90 (2005) 333–340.

Chapter III

Synthesis, characterization, biological and optical study of 2,2'-((1E,11E)-5,8-dioxa-2,11-diazadodeca-1,12-diyl)bis(4-bromophenol) (H2L2)

And its transition metal complexes Cu(II), Mn(II), Co(II) and Zn(II).

III.1. Introduction

This chapter focuses on the establishment of the different findings related to the synthesis, characterization, and investigation of the physicochemical characteristics of the symmetric tetradentate Schiff (H2L2) ligand base and its copper (II), manganese (II), zinc(II), and cobalt(II) complexes.

A low electronic density metal center acceptor may be easily coordinated thanks to the strong nucleophilic nature of the Schiff tetradentate base ligand (H2L2), which is characterized by two free electronic doublets carried by each of the two nitrogen atoms. By combining one primary diamine equivalent with two aldehyde equivalents, one can generate the N2O2-type Schiff tetradentate (H2L2). Following the amine's nucleophilic assault on the brominated salicylaldehyde's carbonyl function and the transposition of a hydrogen atom from nitrogen, condensation is performed. After then, this middleman lets go of a water molecule.

PART I: synthesis and characterization

III.2. Synthesis of ligand 2,2'-((1E,11E)-5,8-dioxa- 2,11-diazadodeca-1,12-diyl)bis(4-bromophenol) (H2L2)

The reaction path of obtaining the base ligand Schiff (H2L2) is shown below, it was synthesized according to the classical method described in the literature with a small change [1]

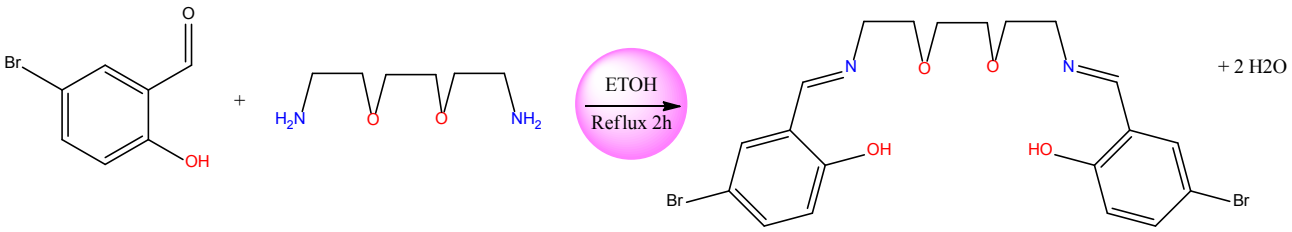

Scheme III.1. Reaction scheme of ligand formation (H2L2).

under a 50 ml Bicol flask under a nitrogen environment, a solution of 5-bromo salicylaldehyde (0.2 g; 0.994 mmol) that had previously been dissolved in a minimum of 100% ethanol is added (0.073 g; 0.497 mmol) by 2,2'-(ethane-1,2-diylbis(oxy))diethanamine. This solution is prone to reflux under constant agitation [2,3]. A yellow precipitate is seen after ten minutes, and the reaction is kept going for two hours. After filtering, the reaction crude is twice cleaned with ethanol and three times with diethyl ether. Thin-layer chromatography (TLC) using silica gel

as the stationary phase and ethyl acetate/petroleum ether (2/1) as the eluent regulates the purity of the reaction result. A 78% estimate for the reaction yield was made.

The condensation process of 1,3-diaminopropan-2-ol, with 5-Bromo-2-hydroxybenzaldehyde takes place according to the following reaction mechanism (Scheme III.2)

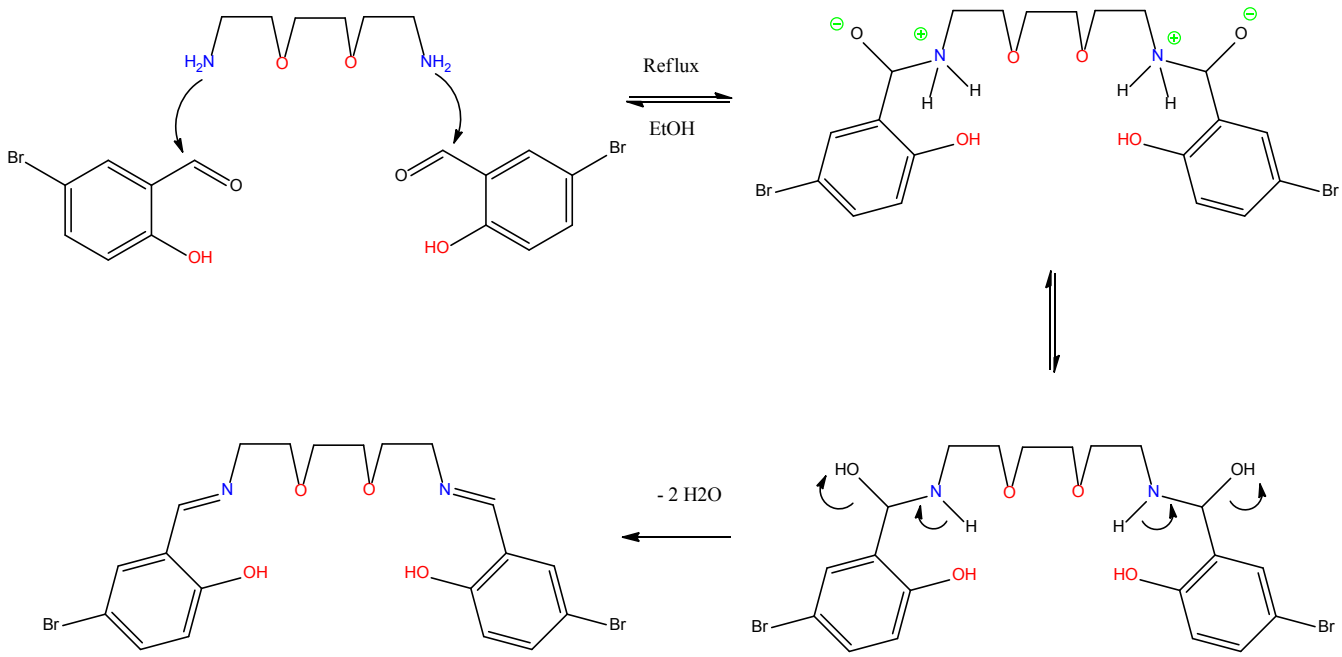

Scheme III.2. Basic Schiff (H2L2) synthesis reaction mechanism.

III.3. Synthesis of Mn(III), Cu(II), Co(II) and Zn(II) complexes with ligand (H2L2)

For the synthesis of ligand-derived metal complexes (H2L2), we followed the classical method. The synthesis is done according to the reaction scheme below

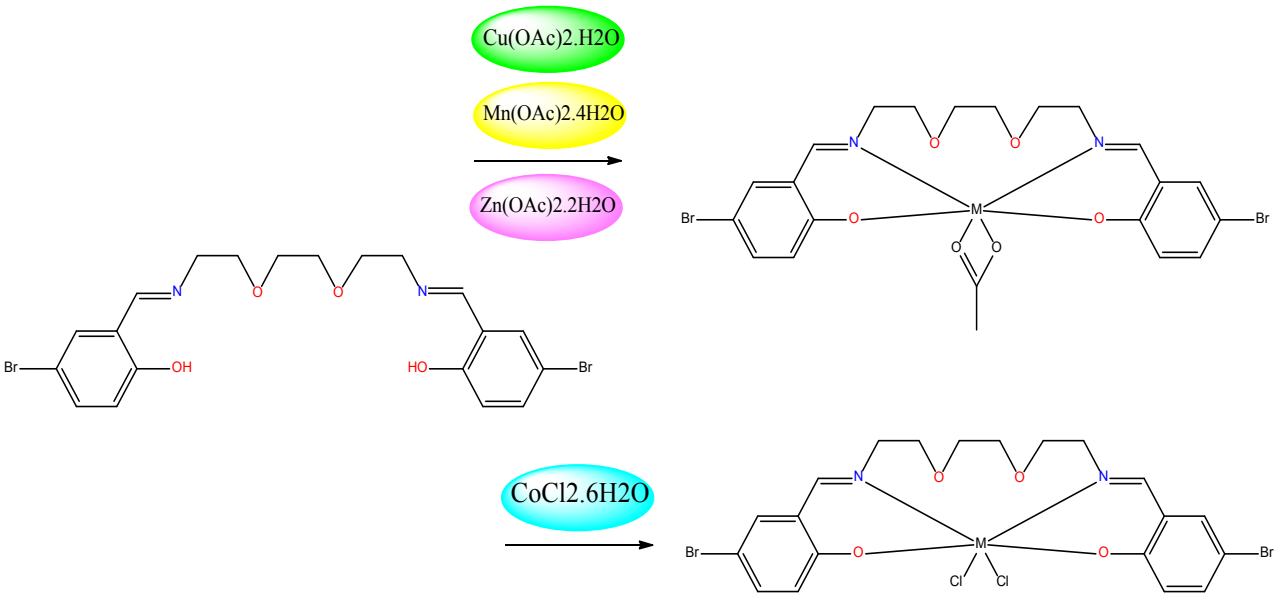

Scheme III.3. General ligand complexation reaction (H2L2)

III. 3. 1. Manganese complex synthesis

In a 50 ml flask with a refrigerant on top that contained 10 ml of 100% ethanol and 0.1 g (0.194 mmol) of ligand (H2L2) dissolved in it, Tetrahydrate manganese acetate (II) (0.05 g; 0.194 mmol) [4] is added drop by drop to a methanoic solution after homogenization. The combination is allowed to reflux for three hours after the solution's coloration instantly becomes brown. After filtering the raw material, diethyl ether is used to wash the solid that was left behind. There is a 76% response yield.

III. 3. 2. Synthesis of the Cuivric complex

The process is the same as for the product Mn(II)L: in a tricol balloon, 0.1 g (0.194 mmol) of Schiff (H2L2) ligand base is dissolved in 10 ml of 100% ethanol, and a 0.04 g (0.194 mmol) solution of hydrated copper acetate is added to taste [5]. The flask is heated in an oil bath while being stirred and connected to a reflux refrigerant. The reaction mixture is refluxed in ethanol at 75°C for 24 hours while being exposed to a nitrogen environment. After forming a light green precipitate, which was recovered after filtering, cold 100% ethanol was used as a wash. This reaction has a yield of 78.85%.

III . 3.3. Zinc complex synthesis

Put (0.04g; 0.194 mmol) bihydrate metal salt Zn(OAc)2.2H2O dissolved in 10 ml methanol into a 50 ml flask topped with a refrigerant that contains (0.1 g; 0.194 mmol) ligand (H2L2) dissolved fully in 10 ml methanol [5,6]. For 24 hours, the mixture is swirled to reflux at 75°C. Next, a pale yellow precipitate is seen. It is recovered by filtering and repeatedly cleaned with cold methanol. It has a yield of 65.21%.

III. 3. 4. Synthesis of Cobalt Complex

A ligand (H2L2) solution (0.1 g; 0.195 mmol) was mixed with an ethanoic solution of hexahydrate cobalt chloride (0.05 g; 0.195 mmol). For a whole day, the mixture is heated and kept under reflux agitation. Diethyl ether has been used to filter and wash the unprocessed chemical. CCM used petroleum ethyl ether acetate (2/1) solvents to manage the compound's purity. 56.35% is the reaction yield.

III.4. Physical and analytical properties of ligand (H2L2) and its complexes

All of the synthetic metal complexes, together with their ligand (H2L2), are powders that are colored and solid. With the exception of ligand, which is soluble in methanol, they are insoluble in organic solvents such as ethanol, methanol, and dichloromethane both at room temperature and under heat. Nonetheless, they dissolve in dimethylformamide (DMF) and dimethylsulfoxide (DMSO). Table III.1 lists the yields as well as the physical and analytical characteristics of every synthesized molecule.

Table III.1. Physical and chemical characteristics of ligand (H2L2) and its complexes.

Compound	Color of the compound	Rdt (%)	Fusion point °C	Solvent Solubility	R_f (%)
(H_2L2)	Jaune	78	132	Ethanol Methanol	66
Mn(II) L2	Marron	76	256	DMF	80
Cu(II) L2	Vert	78.35	224	DMSO	60
Zn(II) L2	Jaune claire	65.21	Tf >260	DMSO	55
Co(II)L2	Vert foncé	56.35	232	DMF	62

III. 5. Spectroscopic characterizations of ligand (H2L2) and its complexes

III.5.1. UV-Visible Absorption Spectrophotometry Analysis

Since these complexes are insoluble in other organic solvents, the electronic spectra of the different produced compounds were recorded between 800 and 200 nm, at ambient temperature, and in the 10-3M DMF solvent concentration. The synthesized compounds' electron spectra are displayed in Figures III.1, III.2, III.3, III.4, and III.5. Table III.2 below provides a summary of the absorption bands.

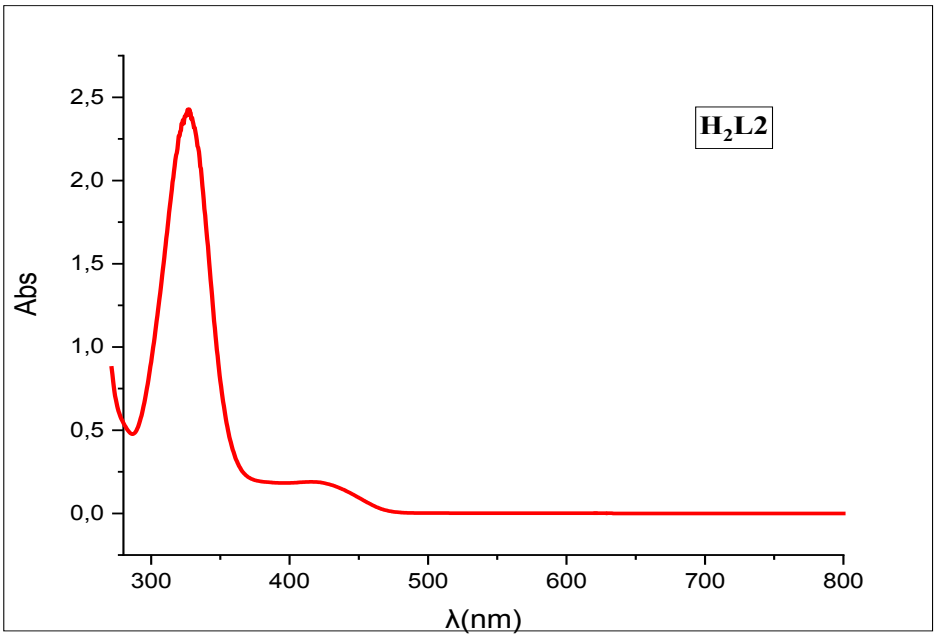

Figure III.1. Ligand (H2L2) UV-Visible spectrum in DMF.

The UV-Vis spectrum of the ligand is characterized by the presence of an absorption band whose wavelength is 327 nm which is due to the transition π→ π∗ of the aromatic cycles and a wide band of low intensity at 420 nm which had been linked to the transition and n→π* of the group azomethine [4].

A bathochrome shift is observed for the two complexes Mn(II)L2 and Zn(II)L2 compared to their ligand in the solvent DMF. The bands, at 368 and 376 nm respectively, are attributable to the π→π* transitions. It should be noted that the electronic transition n→π* is not observed in the manganese and zinc complex electron spectrum for the concentration studied [4,7,8].

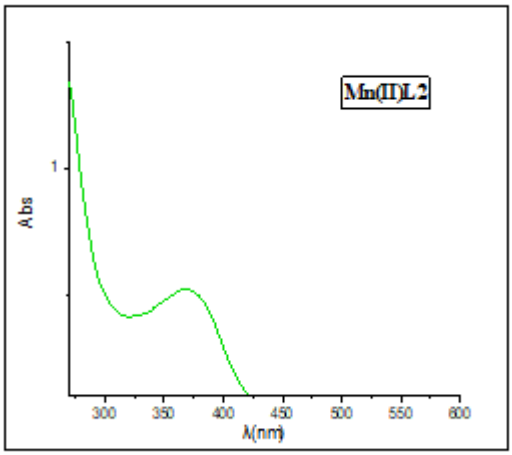

Figure III.2.
UV-Visible Spectrum of Mn(II) L2 in DMF

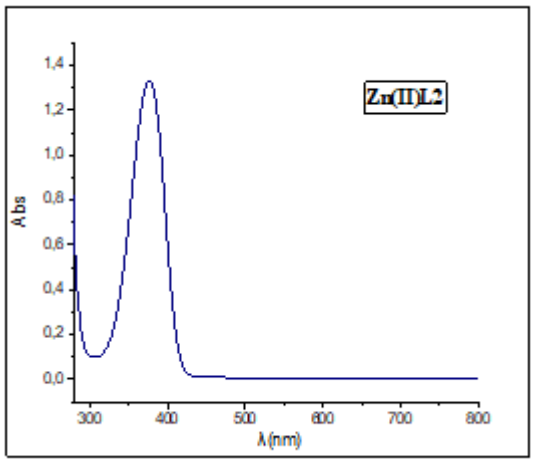

Figure III.3.
UV-Visible Spectrum of Zn(II) L2 in DMF

The π → π* transitions of azomethine chromophores are responsible for the two absorption bands observed in the ultraviolet domain at 297 and 298 nm, respectively, in the absorption spectra of the copper (II) and cobalt (II) complexes. The two complexes' less strong bands, which emerge at 376 and 378 nm, respectively, are linked to n → π* transitions [5]. It is noteworthy that, at the concentration under investigation, the nickel complex electronic spectrum does not exhibit the d-d electronic transition.

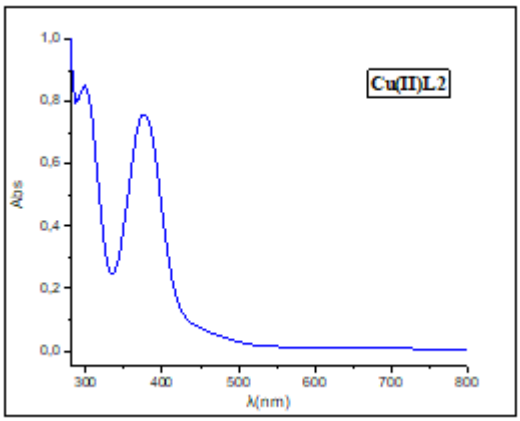

Figure III.4.
UV-Visible Spectrum of Cu(II) L2 in DMF.

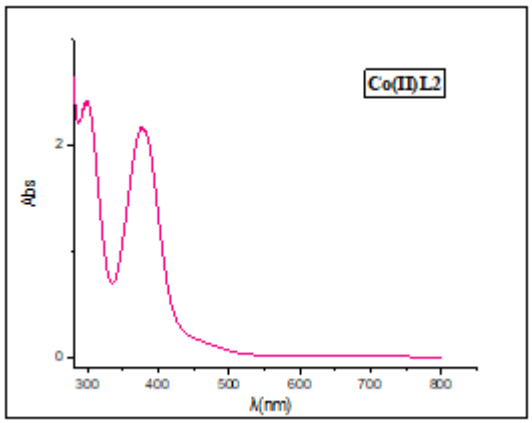

Figure III.5.
UV-Visible Spectrum of Cu(II) L2 in DMF

Table III.2. UV-Vis ligand (H2L2) absorption bands and its complexes.

Compound	λmax (nm)	Transition
(H_2L2)	327 420	π → π* n → π*
Mn(II) L2	368	π → π*
Cu(II) L2	297 376	π → π* n → π*
Zn(II) L2	376	π → π*
Co(II)L2	298 378	π → π* n → π*

III.5.2. Infrared absorption spectrophotometry (IR) analysis

Table (III.3) below displays the principal vibration bands of the various chromophores inside the structures. The most significant vibrations selected in this table are those resulting from the elongation of the functional groups found in the produced molecules.

A broad average band appears in the ligand spectrum analysis (H2L2) at about 3435 cm-1; this is caused by the hydroxyl group's (O-H) elongation vibrations [9]. These bands, which show up in the 3700–3400 cm-1 range for complexes of manganese, copper, cobalt, and zinc, are associated with the existence of coordination or hydration water molecules. The literature claims that this band is practically visible in every compound in this class [10].

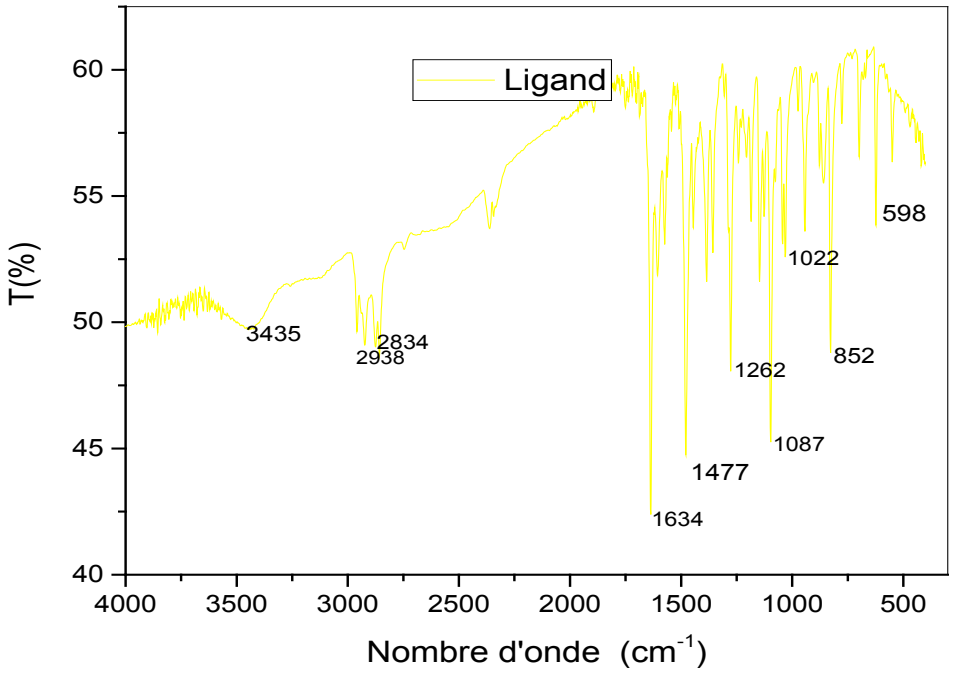

Figure III.6. IR ligand (H2L2) spectrum in KBr.

For the absorption bands of imine groups (C=N) [11] and (C-O) [12] are in the vicinity of 1634 cm-1 and 1087 for ligand and 1634, 1605, 1617, 1629 cm-1 and 1103 , 1118 , 1155 ,1118 cm-1 for metal complexes Mn(II)L2 ,Cu(II)L2 , Zn(II)L2 and Co(II)L2 respectively, where the two heteroatoms are the metal-bound groups, there is bathochromic displacement of the C=N band for all complexes [13] , and hypsochromic displacement of C-O relative to the ligand [14] , this explains the fragility of the first band by the decrease of its constant stiffness and the reinforcement of this constant for the band C-O which receives an additional electronic density through the metal which explains the coordination of the ligand by the metals used .

In addition to these two absorptions, the vibrations in the plane, corresponding to the aromatic C=C groups, are characterized by relatively intense and acute bands between 1440 and 1480 cm-1, and the vibration band of C-O of the ether group which is in the vicinity of 1260 and 1305 cm-1.

The presence of additional bands in the 400-600 cm-1 area of the metal complexes spectra, assigned to ν (M-O) and ν (M-N), confirms the nature of the metal-ligand bond [15].

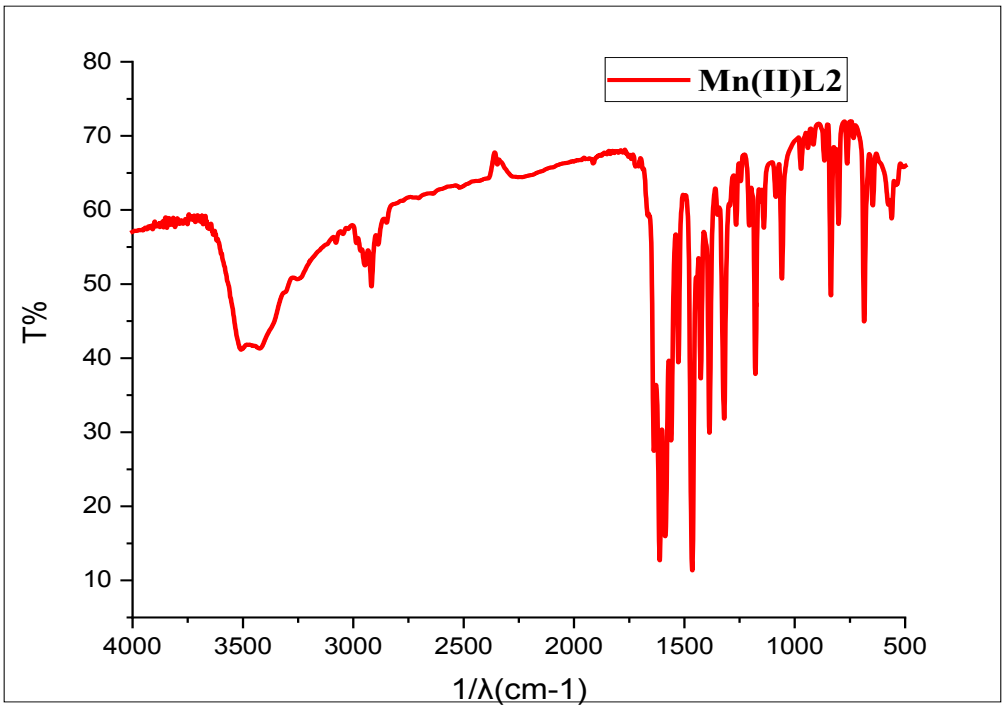

Figure III.7. Mn (II)L2 IR spectrum in KBr.

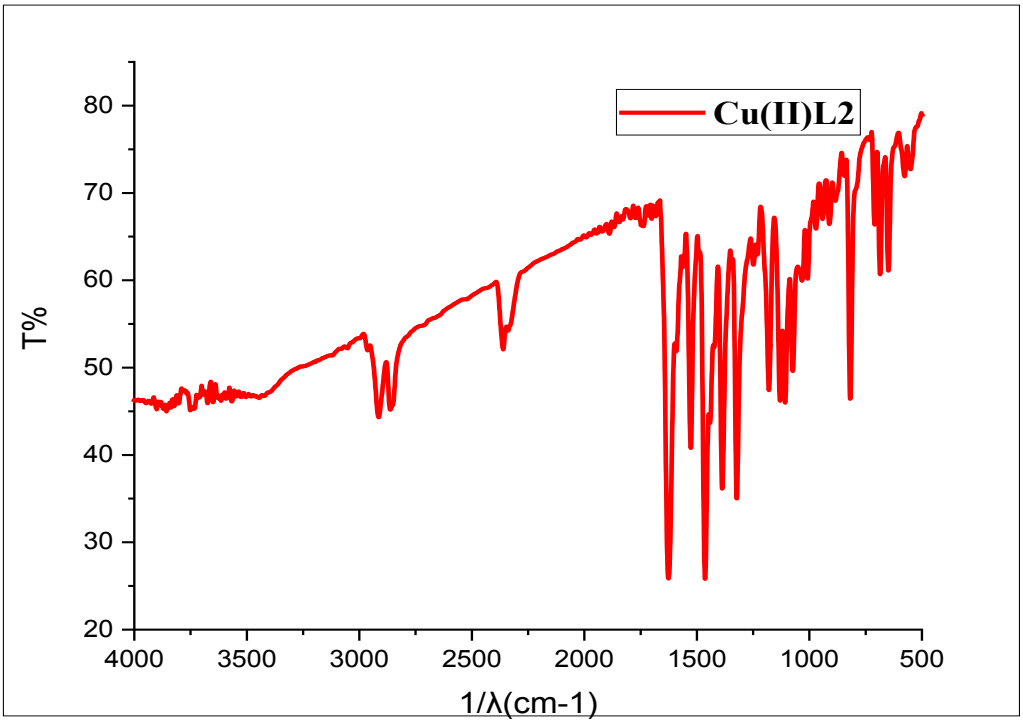

Figure III.8. Cu (II)L2 IR spectrum in KBr.

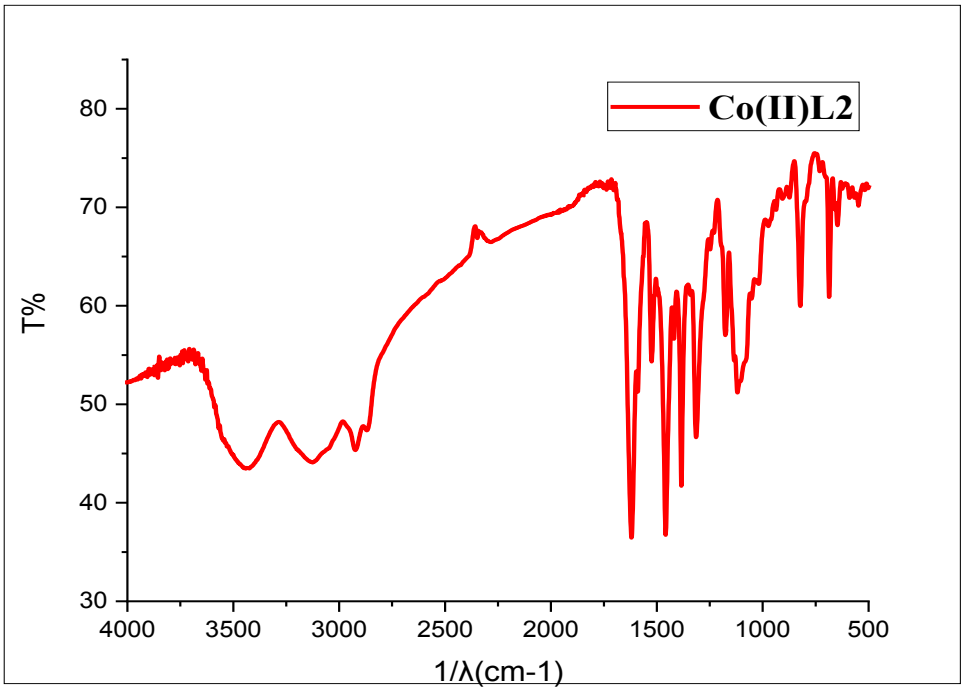

Figure III.9. Co(II)L2 IR Spectrum in KBr

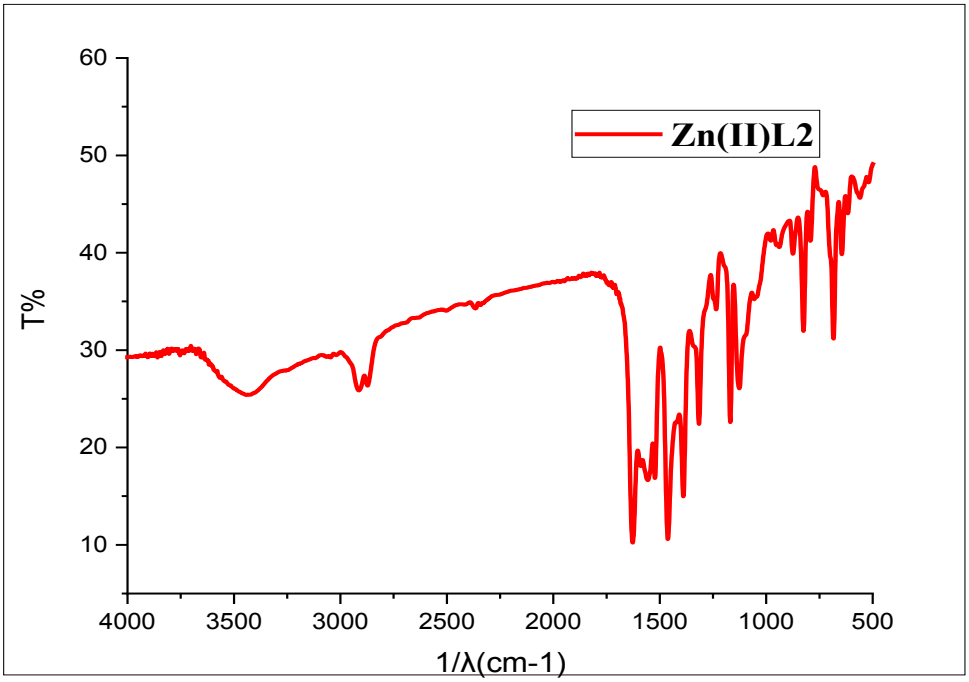

Figure III.10. Zn(II)L2 IR spectrum in KBr.

Table III.3. Major bands of ligand (H2L2) IR vibration and its complexes.

Compound	Infrared ν (cm-1)						
	ν(O-H)	ν(C=N)	ν(C=C)	$\nu(C\text{-}O)_{ether}$	$\nu(C\text{-}O)_{O\text{-}H}$	ν(M-O)	ν(M-N)
(H_2L2)	3435	1634	1477	1262	1087	/	/
Cu(II)L2	3677	1605	1442	1305	1118	643	456
Mn(II)L2	3435	1634	1461	1287	1103	676	410
Co(II)L2	3427	1629	1455	1305	1118	643	419
Zn(II)L2	3440	1617	1455	1305	1155	631	456

III.5.3. Proton (^{1}H NMR) and Carbon (^{13}C NMR) Nuclear Magnetic Resonance Spectroscopy

III.5.3.1.Analysis by ^{1}H-NMR

To confirm the structure of the synthesized ligand, a structural analysis was conducted by nuclear magnetic resonance of proton and carbon 13 on a Bruker AV 300P MHz spectrometer to confirm the structure, in the deuterated CDCL3 using the TMS as the internal reference.

The synthesized ligand structure is given below, with proton numbering:

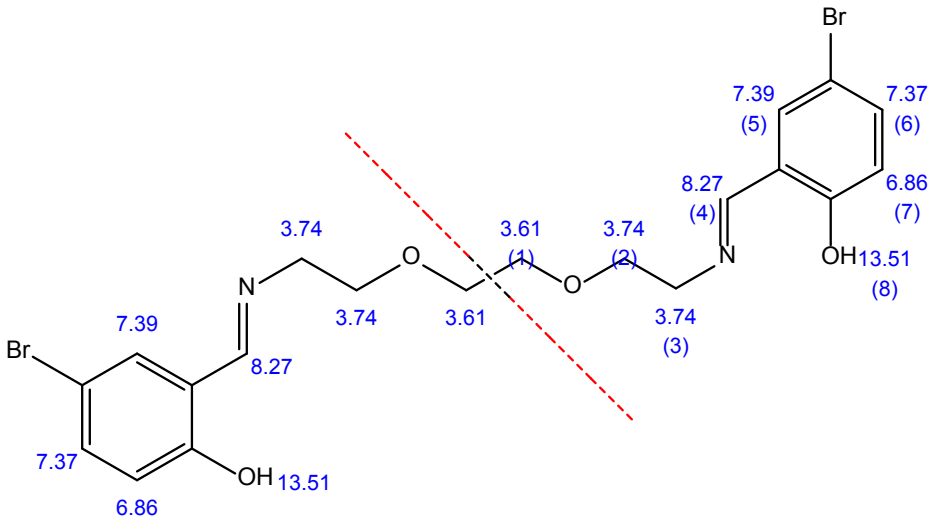

In the ligand's (1H) NMR spectra, the two protons of the phenolic O-H group are represented by a singlet at 13.51 ppm (H2L2). This indicates that the imine function has formed since the protons of the azomethine group (CH=N) are singlets at 8.27 ppm [16–18]. As doublets between 6.86 and 7.37 ppm [18] and as a singlet at 7.39 ppm, the aromatic protons are released and

separated. Four ethylene protons (CH2) are responsible for the multiplets at 3.61 ppm in the spectrum, whereas eight protons from the ligand's aliphatic habitat correlate to 3.74 ppm [19].

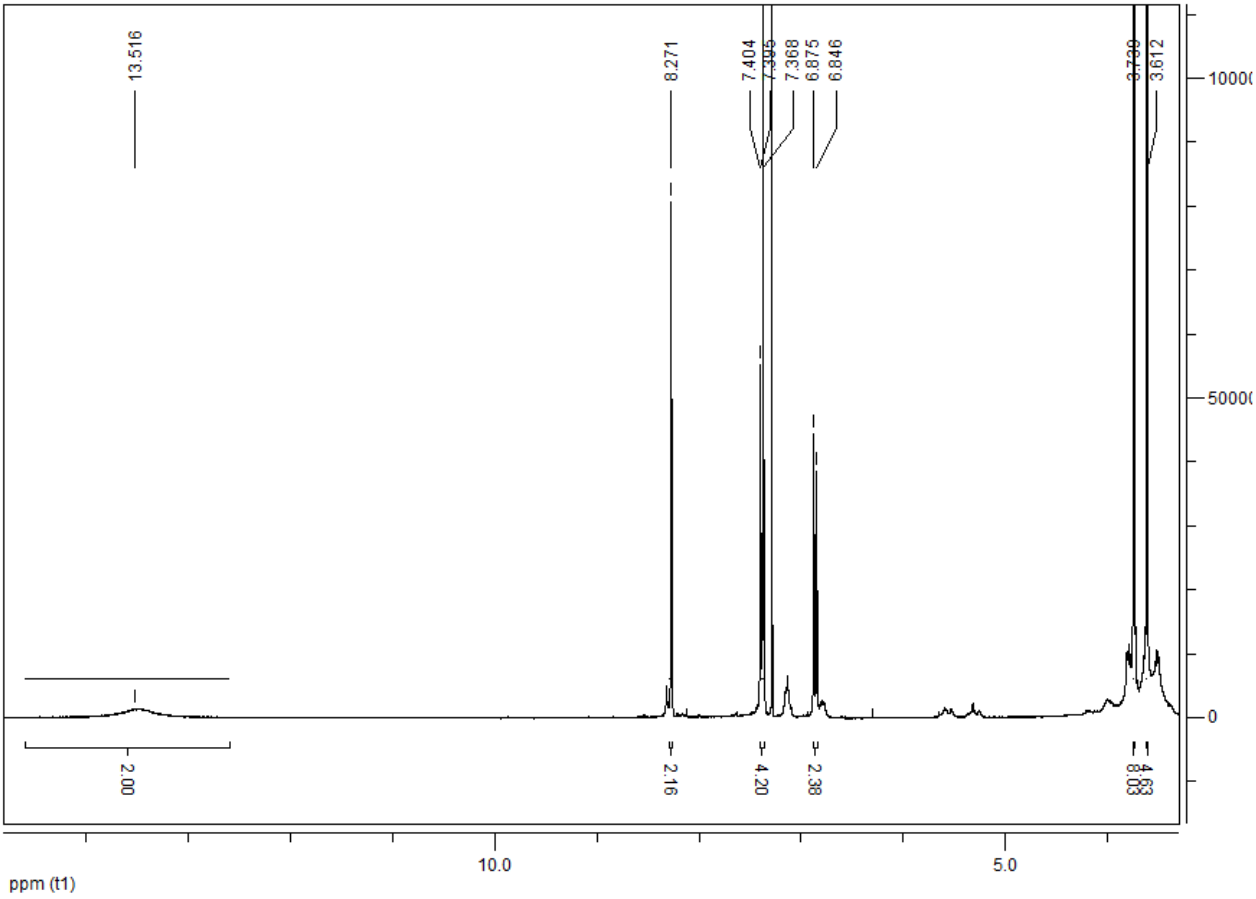

Figure III.11. ^{1}H-NMR spectrum in CDCl3 of (H2L2).

III.5.3.2.Analysis by ^{13}C-NMR

NMR-13C was also used to elucidate the Schiff base's structure. The figure below shows the signals corresponding to the various carbons as well as the chemical displacements, δ in ppm. The carbon atom imine C5 is considered to be the cause of the peak, which is detected at 165.2 ppm [20]. The ligand's aromatic carbons (H2L2) are measured in the range of 120.15, 160.4, 119.1, 134.9, 109.9, and 133.4 ppm [21]. However, the ethylene (CH2) component's carbon, C2, C3, and C4 are found at 70.6, 70.2, and 58.8 ppm, respectively [22].

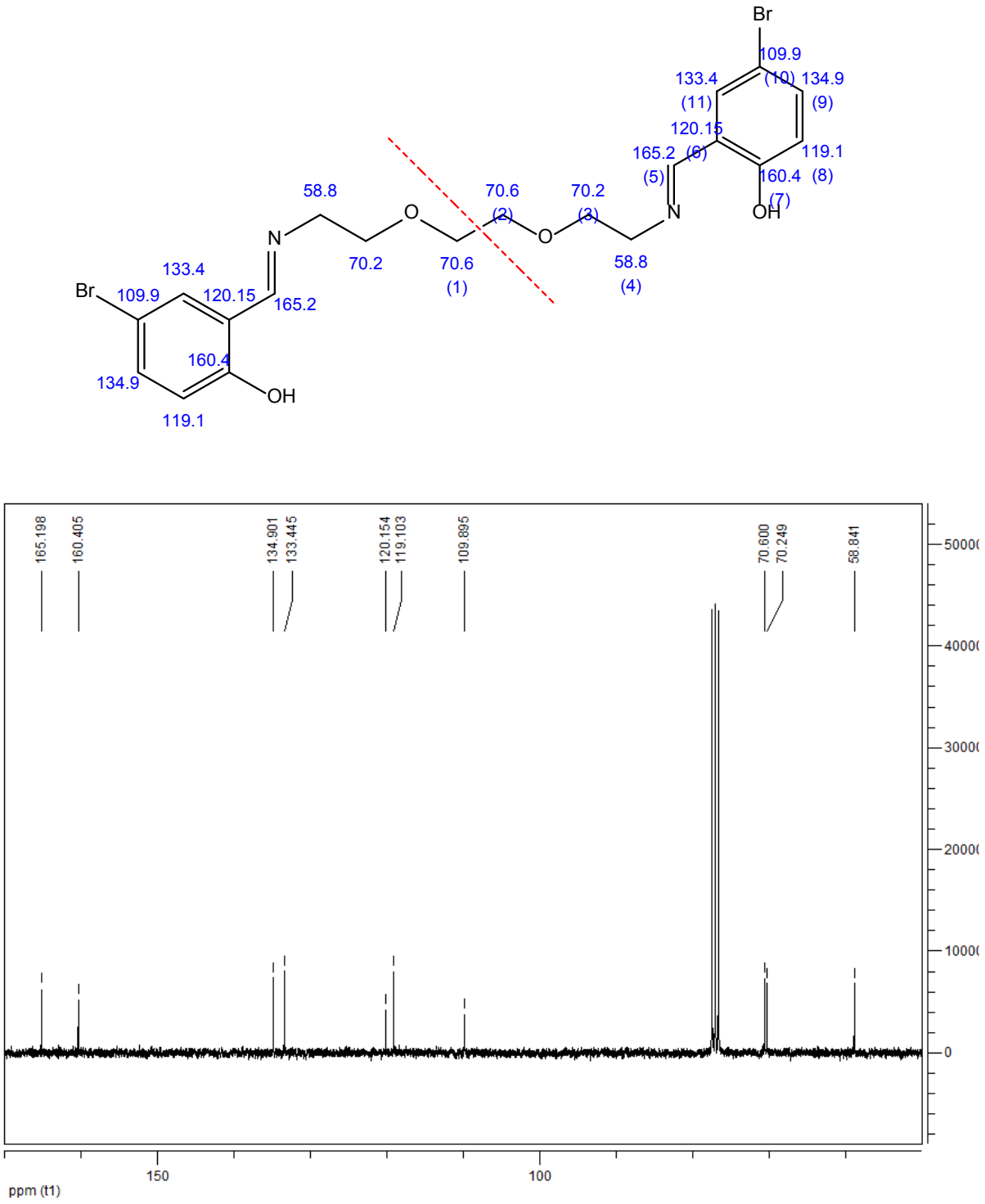

Figure III.12. ^{13}C NMR spectrum in CDCl3 of (H2L2).

III.6. Study of electrochemical behavior by cyclic voltammetry of ligand (H2L2) and its metal complexes

The electrochemical behavior of the produced Schiff base ligand (H2L2) and its metal complexes is shown in this section of the study effort. Using a vitreous carbon electrode in dimethylformamide medium (DMF) with tetrabutylammonium perchlorate (TBAP 0.1M) present, the investigation is conducted using cyclic voltammetry with a scanning speed of 100 mV/s and a potential range of +1600 to -1600 mV/ECS. Potentials are monitored with respect to an auxiliary electrode made of platinum in relation to a saturated calomel reference electrode (ECS).

Table III.4. The electrochemical properties of ligand (H2L2) and its complexes were investigated by cyclic voltammetry in DMF

Compound	Electrochemical parameters	
	Epc (V)	Epa (V)
H2L2	-0.431	+1.273
	-1.089	
Mn(II)L2	-0.641	+0.711
	-1.391	
Cu(II)L2	-0.465	+0.638
	-1.112	+1.205
Co(II)L2	-0.621	+0.715
Zn(II)L2	-0.549	/
	-1.374	/

III.6.1. Ligand (H2L2) electrochemical behavior

According to the ligand voltammogram (H2L2) shown in figure (IV.13) and plotted at 100 mV/s, it is noted that during the forward scan, two cathode peaks located at Epc1= -0.431 V/ECS and Epc2 = -1.089 V/ECS. The second peak is attributed to the reduction of the azomethin group [10].

As for the observed peak in the return scan, the potential is Ep = +1.273 V/ECS, which is due to the oxidation of the O-H group [23,24].

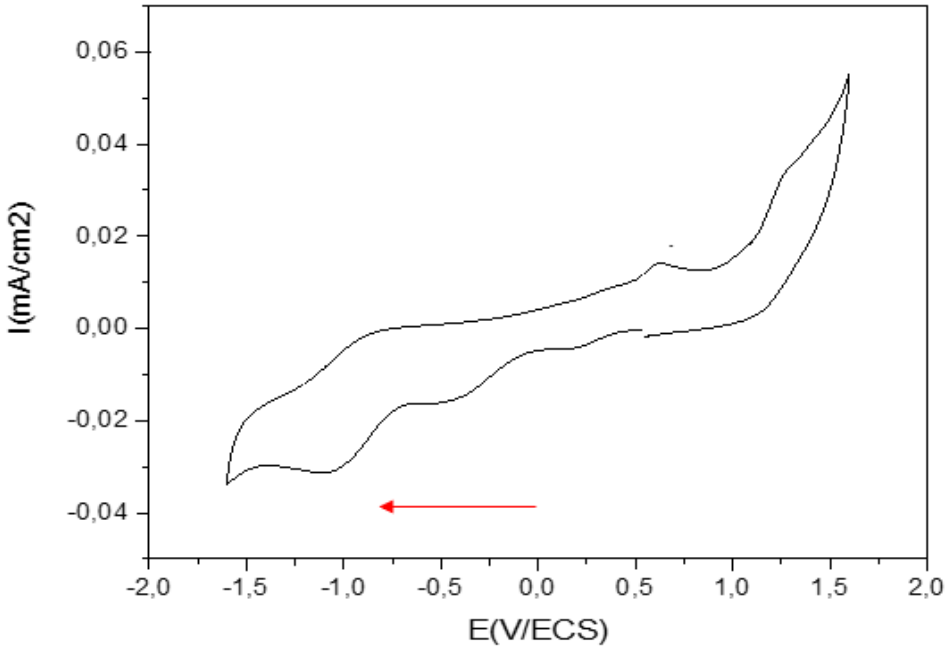

Figure III.13. Cyclic Ligand Voltammetry (H2L2)(10^{-3}M) in DMF+TBAP (10^{-1}M) under nitrogen atmosphere at a scanning speed of 100 mV/s

III.6.2. Electrochemical behavior of Schiff metal-base complexes (H2L2)

III.6.2.1. Manganese complex

The study of the electrochemical properties of the Mn(II)L2 complex in DMF medium was carried out on the potential range from -2000 to +2000 mV/ (ECS) with a scanning speed equal to 100 mV/s as shown in Figure IV.14.

The voltammogram obtained shows the appearance of a single anode peak and two cathode peaks. The anode peak of Mn(II)L2 complex is located at Epa = +0.711V/ECS which is due to the passage of Mn(II) into Mn(III) [Mn(II) Mn(III) + e -] [10,25].

On the cathode side, the two peaks are located at Epc1 = -0.641 V/ECS, Epc2= -1.391 V/ECS. The first peak is attributed to the reduction of Mn(II) species to Mn(I)[25,26], while the second one is due to the reduction of the azometin group [27,28].

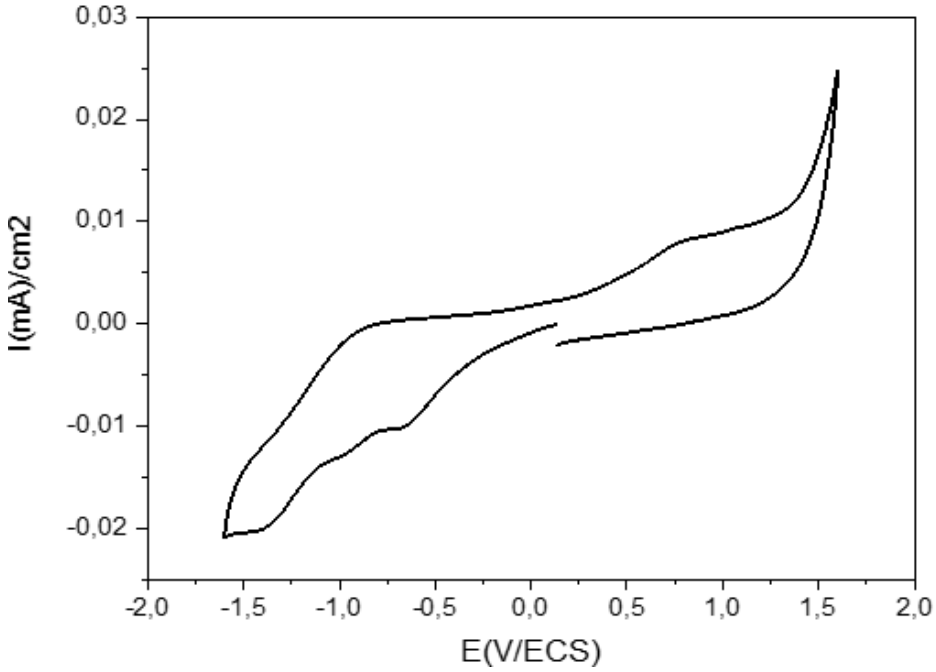

Figure III.14. Mn (II)L2(10-3M) cyclic voltammetry in FMD+TBAP (10-1M) under nitrogen atmosphere at a scanning speed of 100 mV/s.

III.6.2.2. Copper complex

The electrochemical behavior of the copper complex is shown in Figure IV.15. During the forward scan, two reduction peaks appear at Epc1 = -0.465, Epc2 = -1.112V/ECS where the first peak is attributed to the passage of Cu(II) into Cu(I) [21,30], and the second peak is due to the reduction of the azomethine group [21,27,31].

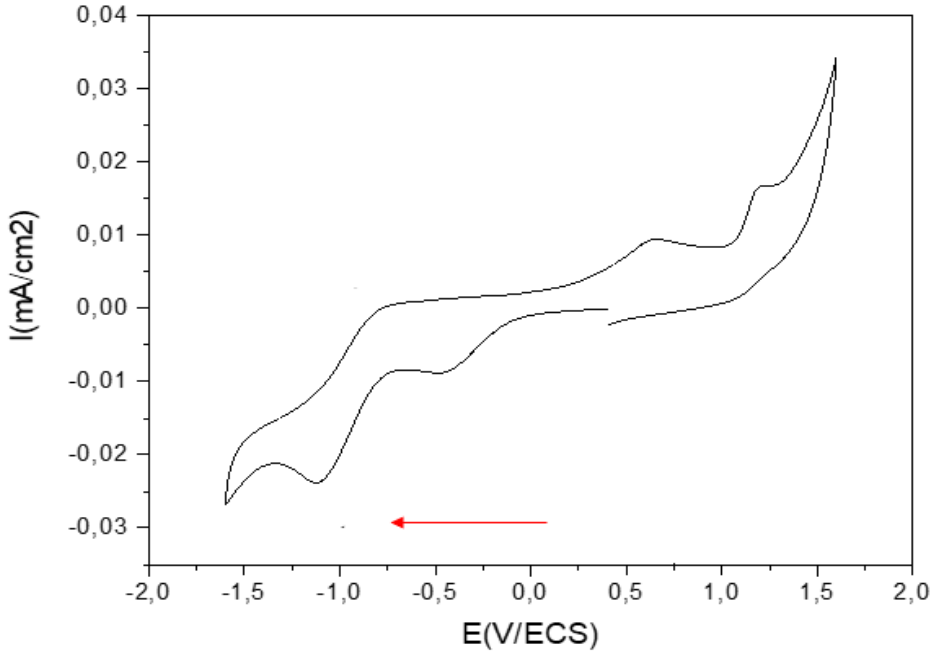

Figure III.15. Cu(II)L2(10-3M) cyclic voltammetry in FMD+TBAP (10-1M) under nitrogen atmosphere at a scanning speed of 100 mV/s.

There are two oxidation peaks located at Epa1 = +0.638, Epa2 = +1.205 V/ECS where the first peak is attributed to the reduction of the redox system Cu(II) / Cu(III) [29,30] while the second peak is attributed to the oxidation of the ligand entity [23,24].

III.6.2.3. Cobalt Complex

Figure IV.19 displays the Cobalt complex's cyclic voltammogram. The reduction of Co(II) to Co(I) is shown by a reduction peak at -0.621 V/ECS[32,33], which is caused by the reaction Co(II)+e-→Co(I). The Co(II) complex is oxidized to Co(III) at a relatively high potential of +0.715 V/ECS when the scanning direction is reversed [5,32].

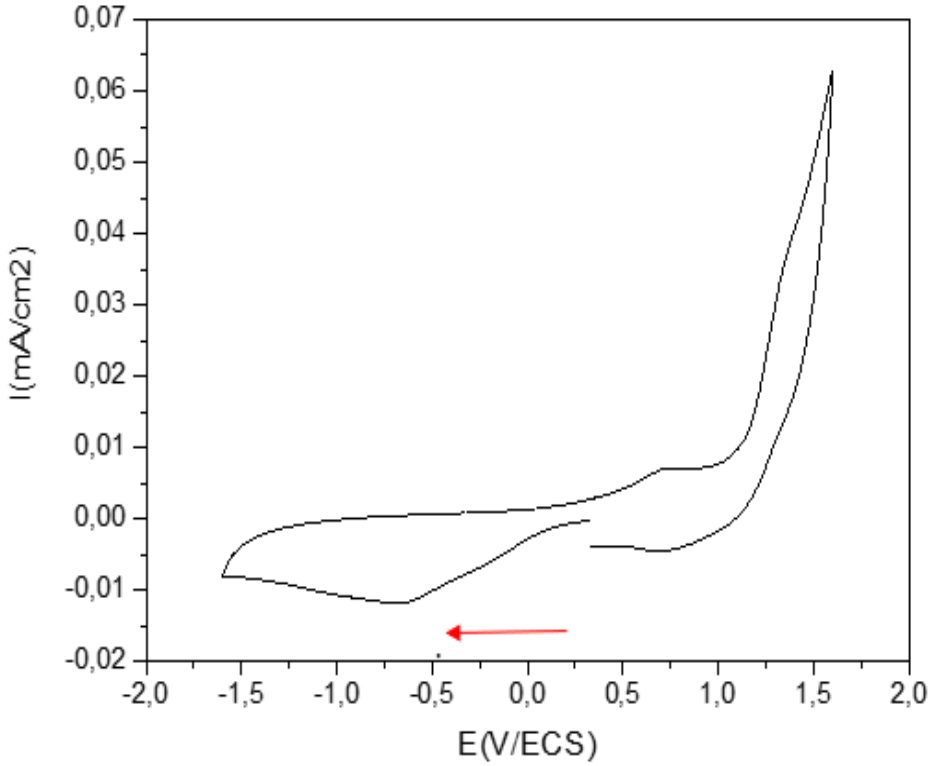

Figure III.16. Co(II)L2(10-3M) cyclic voltammetry in FMD+TBAP (10-1M) under nitrogen atmosphere at a scanning speed of 100 mV/s.

III.6.2.4. Zinc Complex

The study of the electrochemical properties of the Zn(II)L2 complex are presented in the following figure III.17.

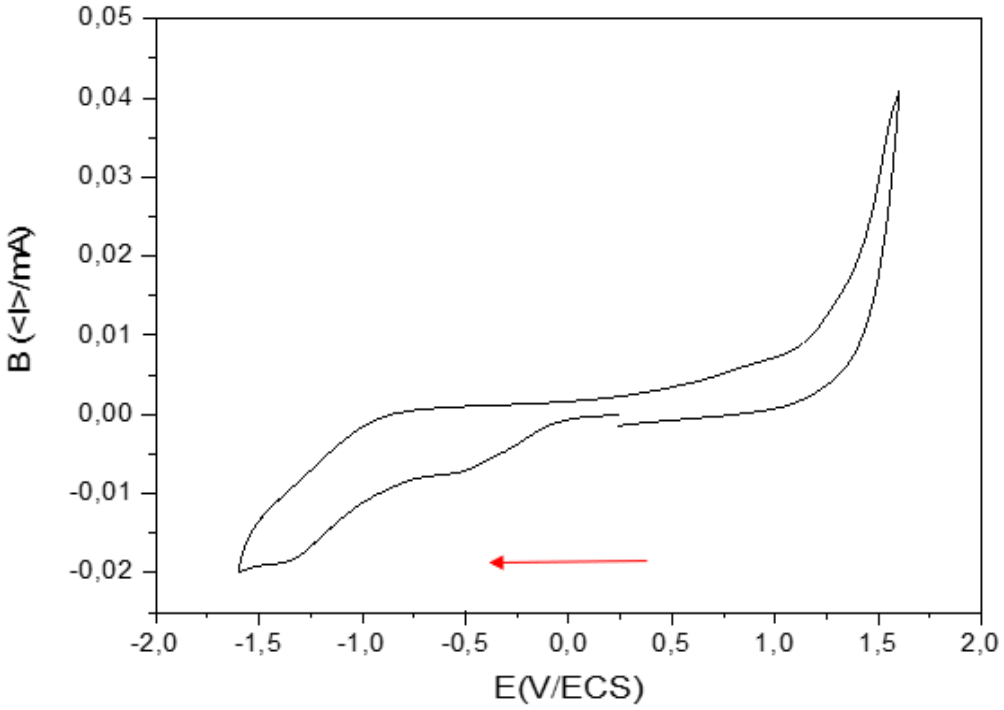

Figure III.17. Zn(II)L2(10-3M) cyclic voltammetry in FMD+TBAP (10-1M) under nitrogen atmosphere at a scanning speed of 100 mV/s.

The voltamogram obtained shows the appearance of only two cathode peaks where the first one located at Epc1 = -0.549 V/ECS is attributed to the passage of Zn(II) into Zn(0) [34], and the second one assigned to Epc2= -1.374 V/ECS is due to the reduction of the azometin group [34-36].

III.7. CRYSTALLOGRAPHIC STUDY OF SINGLE CRYSTALS

In addition to the identification of the structure of the various organic and complex ligands by the classical analysis methods already mentioned, we proceeded to elucidate the structure by X-ray diffraction, especially for the compound Cu(II)L2.

III.7.1. Preparation and selection of single crystals

The produced compound Cu(II)L2 was formed as a single crystal by slowly evaporating the solvent DMF at room temperature. Under polarized light, the resultant crystal is examined under a microscope. Due to their extreme sensitivity, one must take extremely little measures,

such as isolating the one that will probably be kept for installation on the diffractometer's goniometer and often applying paraffin oil. to prevent overlaps and lessen the effects of absorption (macles).

Excellent single crystals appropriate for X-ray diffraction investigation were produced for the synthesized copper complex.

III.7.2. Recording of intensities

Using Mo-Kα monochromatic graphite radiation (λ = 0.71073 Å), a single crystal of the produced compound was chosen and put on a Bruker D8-VENTURE diffractometer fitted with a Photon II CCD zone detector. APEX-III software was used to gather data at 298 (2) K. The data were then merged using SAINT and adjusted for absorption using a multi-scan technique (SADABS). After a thorough refining of all observed reflections using least squares, the final cell constants were found. Crystallographic information is displayed in Table III.5.

III.7.3. Resolution and refinement of crystal structure

For solution and structural refinement, the generated hkl set was employed. To find all non-H atoms, the structure was solved using direct techniques with SIR 2002 [37]. Anisotropic refinement of the structure was done with SHELXL-2014 [38] using complete matrix least squares on the F2 process in the WINGX software package [39], which was utilized to prepare the material for publishing. The reliability factors for R and RW, which are not weighted, are:

$$R = \{\Sigma[w(|F0| - |Fc|)]/ \Sigma\, w(|F0|)\},\ Rw = \{\Sigma[w(|F0| - |Fc|)^2]/\Sigma\, w(|F0|^2)\}^{1/2},$$

$$wR2 = \{\Sigma[w(F0^2 - Fc^2)^2]/ \Sigma\, w(F0^2)\}^{1/2}$$

$$w = 1/[\sigma^2 (Fo^2) + (0.0336P)^2 + 0.2893P] \text{ where } P = (Fo^2 + 2Fc^2)/3$$

H atoms were added using a conduct model to the determined and improved places. Structural figures were generated using the Windows application Mercury 3.8 [40]. Table III.5 summarizes information on crystal data, data collecting, and structural refining.

Table III.5. Crystallographic data of the copper complex and details of structural refinement.

Molecular formula	C22 H23 Br2 Cu N2 O6
Molecular weight	634.78 g mol^{-1}
Temperature (K)	298(2)
Radiation λ (Å)	0.71073
Crystal system	Orthorhombic
Space group	*Pbca*
a/Å	9.1888(3)
b/ Å	21.3139(5)
c/ Å	25.0582(6)
α/ °	90
β/ °	90
γ/ °	90
V/$Å^3$	4907.6(2)
Z	8
Calculated density (mg cm^{-3})	1.718
Absorption coefficient (mm^{-1})	4.186
F(0 0 0)	2528
Reflections measured/independent	74644 / 7489 [R(int) = 0.0925]
Range/indices (h, k, l)	h= −13→13, k = −30→29, l = −33→35
Theta range for data collection (°)	2.509 to 30.517
Completeness to theta = 25.242	99.9 %
Refinement method	Full-matrix least-squares on F^2
Data / restraints / parameters	7489 / 0 / 299
Goodness of fit on F^2	1.020
Final R indices [I>2sigma(I)]	R1 = 0.0824, wR2 = 0.2362
Extinction coefficient	n/a
Largest diff. peak and hole (e.A-3)	1.368 and -2.293

III.7.4. Description of the structure

Figure III.18 shows an asymmetric unit view of the Cu(II)L2 molecule examined, based on the Schiff base ligand (H2L2) with the selective atom numbering system. Crystallization of the

complex occurs in the orthorhombic space group (α = β = γ = 90°) Pbca, as revealed by the determination of its structure. There are eight complicated molecules in the mesh, with a volume of 4907.6 Å3/mesh. Note that the existence of X-ray-absorbing bromine atoms accounts for the high absorption coefficient (μ = 4.186 mm^{-1}).

The Schiff base ligand functions as a tetradentate of N2O2 through the unfolded hydroxyl groups O(3) and O(7) and the iminated nitrogen atoms N(1) and N(2), as seen in the picture below. The acetic acid molecule and a Schiff base ligand (H2L2) are coupled with the metal ion..

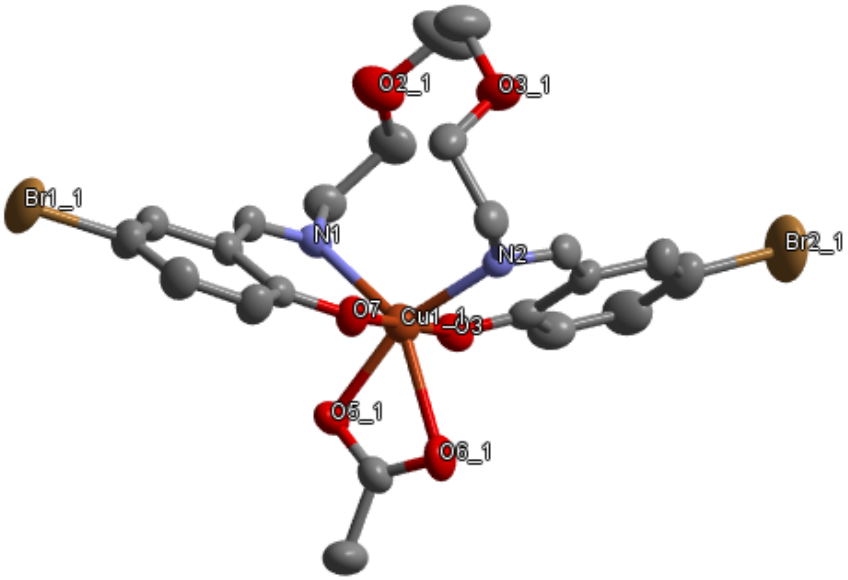

Figure III.18. Representation of the Cu(II)L2 complex molecule.

III.7.5. Connections and angles

The lengths and binding angles match those of other research using comparable Schiff base ligands [41,42]. Table III.7 shows that the acquired angles deviate somewhat from the ideal values, which are 120° for sp2 hybridization and 109.5 for sp3 hybridization. The Cu(II)L2 complex's bonds and atom-to-atom angles are arranged in Tables III.6 and III.7 below.

Figure III.19 shows that copper is coordinated with two oxygen atoms of two hydroxyl groups (O3 and O7) and two nitrogen atoms of the imine function (N1 and N2) of the Schiff base ligand. The distances between the nitrogen atoms and the coordinated oxygen atoms and the metal Cu-O3, Cu-N1, Cu-O7 and Cu-N2 are respectively 1.870 (4), 2.057 (4), 1.852 (4) and 2.160 Å. The chelation angles O7-Cu-N1, O3-Cu-N2, O7- Cu-N2N2 et N1-Cu-N2 have the following respective values 89.82 (13), 89.99 (14), 89.03 (14) et 109.89 (15) °.

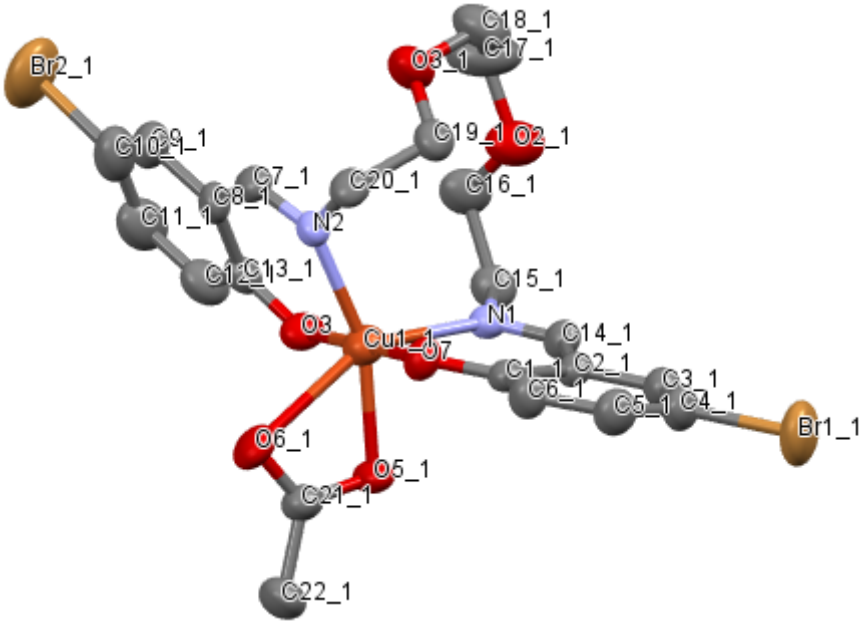

Figure III. 19. Representation of the Cu(II)L2 complex molecule with atom numbering.

Table III.6. Bond lengths in the Cu(II)L2 complex.

bond lengths (Å)			
Br1—C4	1.900 (4)	O3-C18	1.420(9)
Br2-C10	1.895(7)	O4-C13	1.302(7)
Cu1-O1	1.852(4)	O5-C21	1.285(7)
Cu1-O4	1.870(4)	O6-C21	1.241(7)
Cu1-O5	2.031(4)	C1-C6	1.391(8)
Cu1-N1	2.057(4)	C1-C2	1.429(7)
Cu1-N2	2.160(4)	C2-C3	1.409(8)
Cu1-O6	2.400(5)	C2-C14	1.439(7)
O1-C1	1.325(6)	C3-C4	1.359(8)
N1-C7	1.279(7)	C4-C5	1.386(9)
N1-C20	1.489(7)	C5-C6	1.393(8)
O21-C16	1.400(8)	C7-C8	1.441(8)
N2-C14	1.284(7)	C8-C9	1.398(9)
N2-C15	1.460(7)	C8-C13	1.425(8)
O2-C17	1.423(10)	C9-C10	1.346(10)
O3-C19	1.409(8)	C11-C12	1.374(10)
C12-C13	1.415(8)	C15-C16	1.513(9)
C17-C18	1.489(11)		

Table III.7. Angles (°) in the Cu(II)L2 complex

Angles (°)			
C11—O1—C12	117.58(11)	C9-C10-C11	119.5(7)
O1-Cu1-O4	178.27(18)	C1-O1-Cu1	131.8(3)
O1-Cu1-O5	90.88(18)	C7-N1-C20	114.8(4)
O4-Cu1-O5	89.51(18)	C7-N1-Cu1	125.2(4)
O1-Cu1-N1	89.02(17)	C20-N1-Cu1	119.8(3)
O4-Cu1-N1	90.01(17)	O1-C1-C6	118.6(5)
O5-Cu1-N1	158.78(17)	O1-C1-C21	122.9(5)
O1-Cu1-N2	89.84(17)	C6-C1-C2	118.4(5)
O4-Cu1-N2	91.84(18)	C16-O2-C17	111.1(7)
O5-Cu1-N2	91.32(16)	C14-N2-C15	115.7(5)
O5-Cu1-N2	91.32(16)	C14-N2-Cu1	122.0(4)
N1-Cu1-N2	109.90(17)	C15-N2-Cu1	122.3(4)
O1-Cu1-O6	89.28(18)	C3-C2-C1	118.9(5)
O4-Cu1-O6	89.49(18)	C3-C2-C14	116.8(5)
O5-Cu1-O6	58.09(14)	C1-C2-C14	124.1(5)
N1-Cu1-O6	100.70(15)	C19-O3-C18	115.9(6)
N2-Cu1-O6	149.37(15)	C4-C3-C2	120.9(5)
C9-C10-Br2	121.6(6)	C13-O4-Cu1	131.9(4)
C11-C10-Br2	118.9(5)	C3-C4-C5	120.9(5)
C12-C11-C10	120.1(7)	C3-C4-Br1	118.6(5)
C11-12-C131	121.8(7)	C5-C4-Br1	120.5(5)
O4-C13-C12	119.3(5)	C21-O5-Cu1	99.5(3)
O4-C13-C8	124.2(5)	C4-C5-C6	119.6(6)
C12-C13-C8	116.5(6)	C21-O6-Cu1	83.6(4)
N2-C14-C2	126.4(5)	C1-C6-C5	121.3(5)
N2-C15-C16	110.5(5)	N1-C7-C8	126.2(5)
O2-C16-C15	109.5(6)	C9-C8-C13	120.2(6)
O2-C17-C18	109.8(7)	C91-C8-C7	117.9(5)
O3-C18-C17	111.6(7)	C13-C8-C7	121.8(5)
O3-C19-C20	107.5(5)	C10-C9-C8	121.9(7)
N1-C20-C19	109.3(4)	C9-C10-C11	119.5(7)
O6-C21-O5	118.9(5)		

III.7.6. Elementary Cell

Here is an illustration of the Cu(II)L2 complex's elementary cell, found in Figure (III.20). This compound's elementary cell is made up of eight asymmetric units whose stacking (Z = 8, Z: number of patterns per cell) along the three directions results in a three-dimensional structure rich in hydrogen bonds (a = 9.1888 (3) Å, b = 21.3139 (5) Å, c = 25.0582 (6) Å). Type O—H… N, C—H… Br, and type C—H…… π hydrogen bonds and interactions bind the molecules in the crystal.

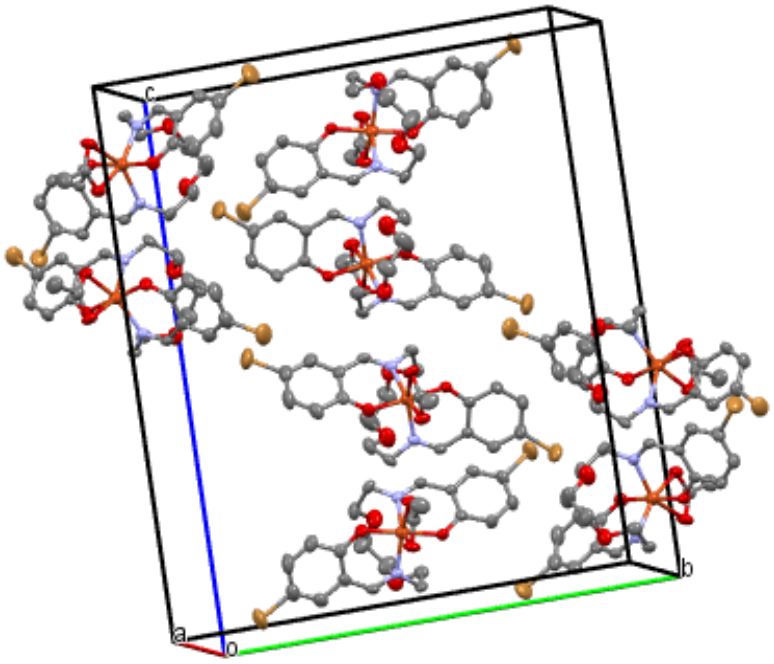

Figure III.20. Representation of the mesh with axes a, b and c of the Cu(II)L2 complex.

The unit cell being not centrosymmetric, characterized by an inversion point in the center O at [0, 0, 0],with three screw axis 2 times in the direction [1, 0, 0], [0, 1, 0] and [0, 0, 1] to (x, ¼,0), (0, y, ¼) and (¼, 0, z) with the screw components [½,0, 0], [0, ½, 0], [0.0 , ½] respectively and three sliding planes perpendicular to the planes [1, 0, 0] [0, 1, 0] and [0, 0, 0, 1] with the sliding components [0, ½ ,0],[0, 0, ½] and [½,0, 0] respectively.

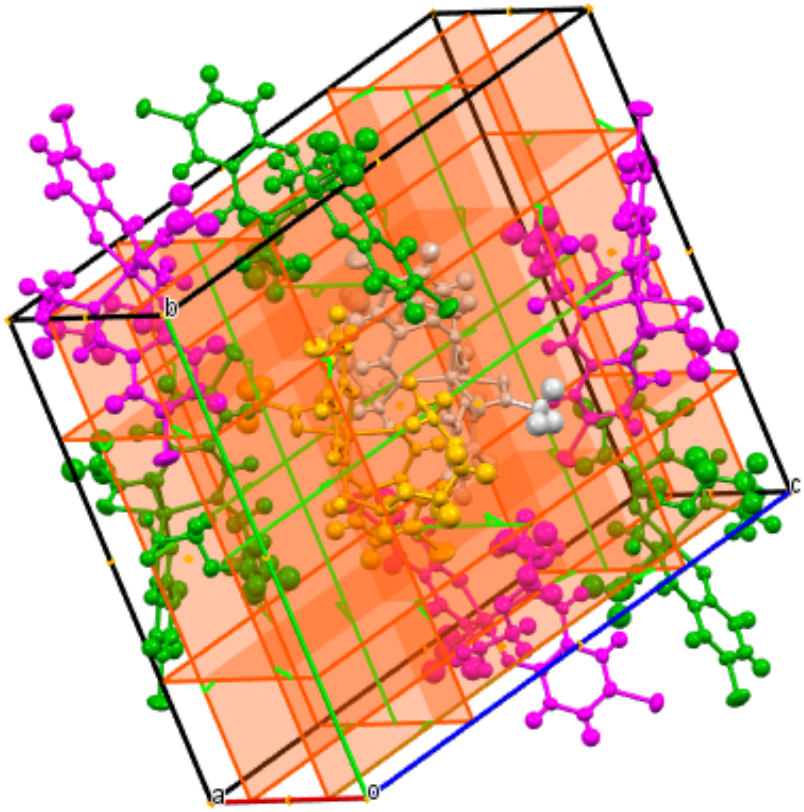

Figure III.21.

Mesh in the plane a, b c of the complex Cu (II)L2 with symmetry elements .

III.7.7. Crystal lattice

The Cu(II)L2 complex's crystalline lattice is shown in Figure III.2**2** based on the three principal planes, a, b, and c. In plan a, the lattice takes on an undulating, zigzag-like pattern, whereas in plan b, a parallel form alternates by forming tunnels within the network. Additionally, the plane shows a type of parallel diagonals of molecules.

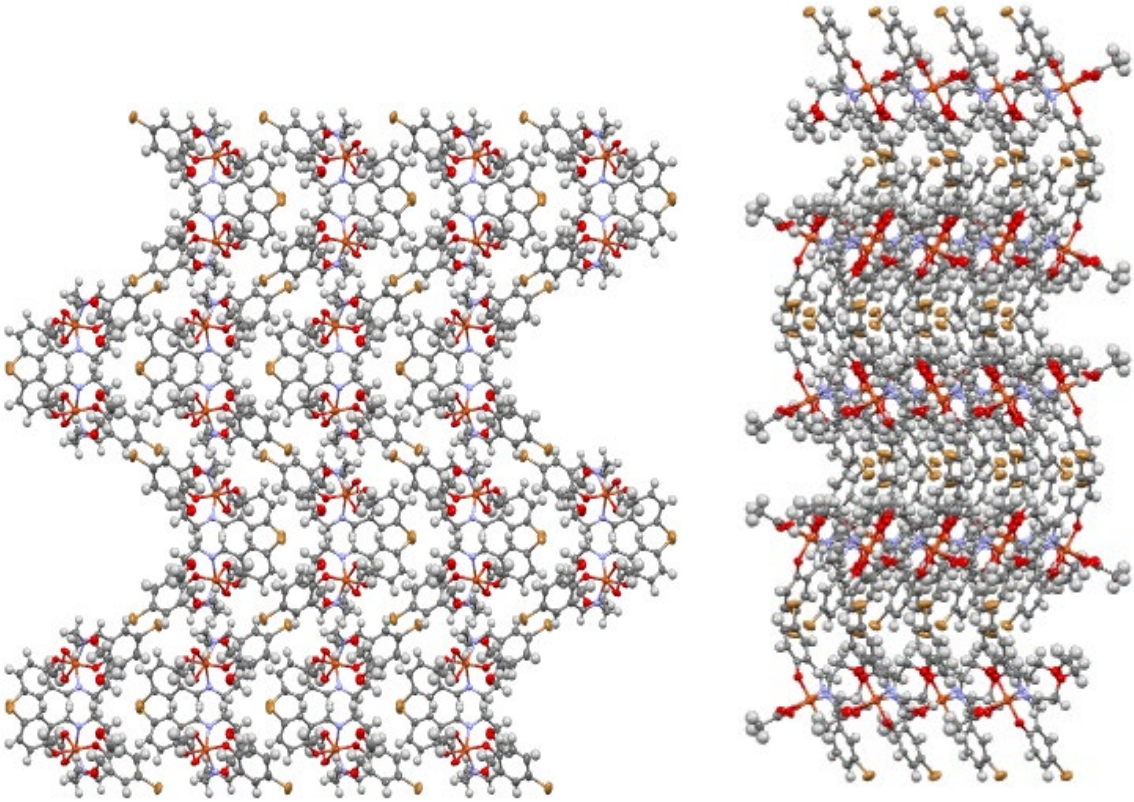

Plan a (100)

Plan c (001)

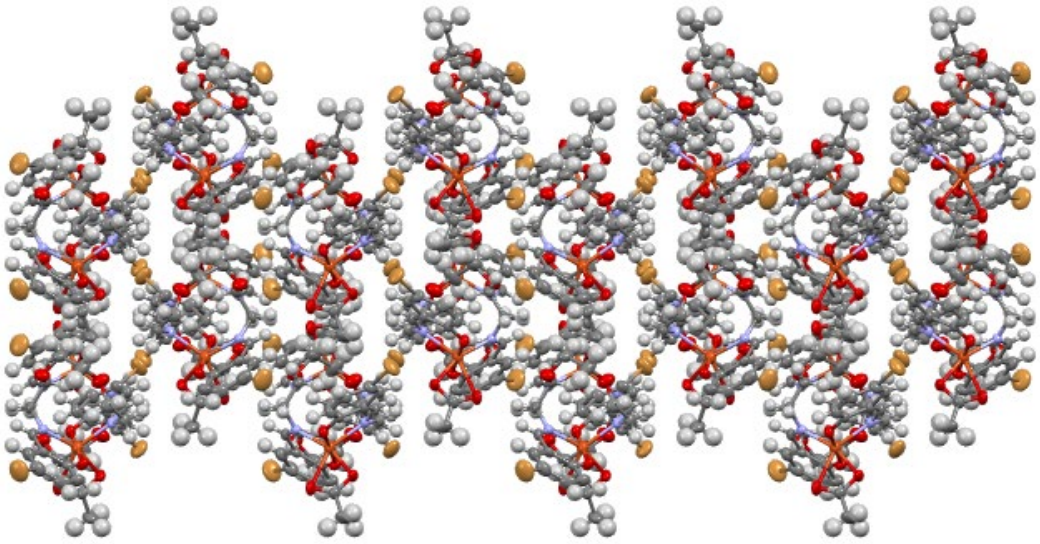

Plan b (010)

Figure III.22. Crystalline molecular stacking of Cu(II)L2 in three crystallographic planes:(a) [100], (b) [010] and (c) [001].

Figure III.23 shows a perspective projection of the Cu(II)L2 lattice, observing that the atoms are ordered so as to form parallel lines for each group of identical atoms

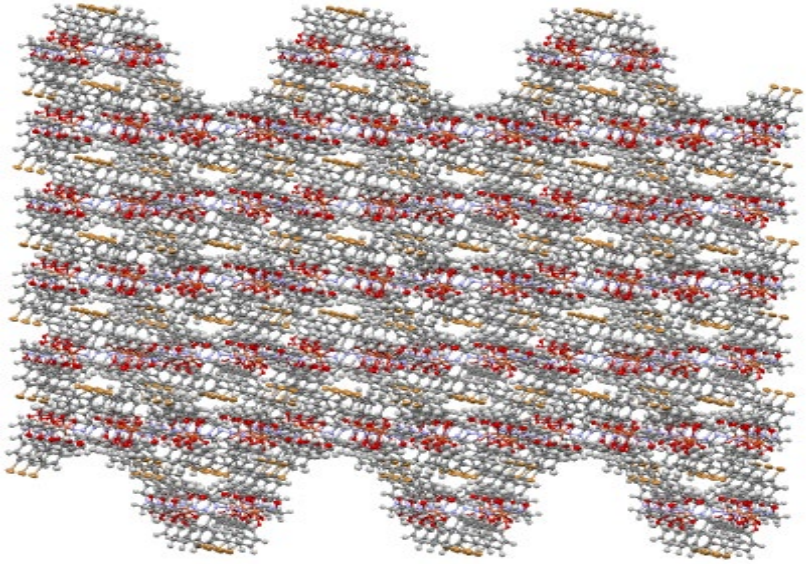

Figure III.23. Perspective view of the crystal lattice.

Type C—H…. intermolecular hydrogen bonds, which have an angle of 59.04 (5) °, stabilize the three-dimensional lattice. The associated acceptor-donor lengths are 3.154 Å, donor-hydrogen 2.314 Å, and acceptor-hydrogen 2.542 Å. On the other hand, every molecule in a formal unit cell is a member of a unique chiral helical chain, which forms the three-dimensional lattice of the grid-shaped complex.

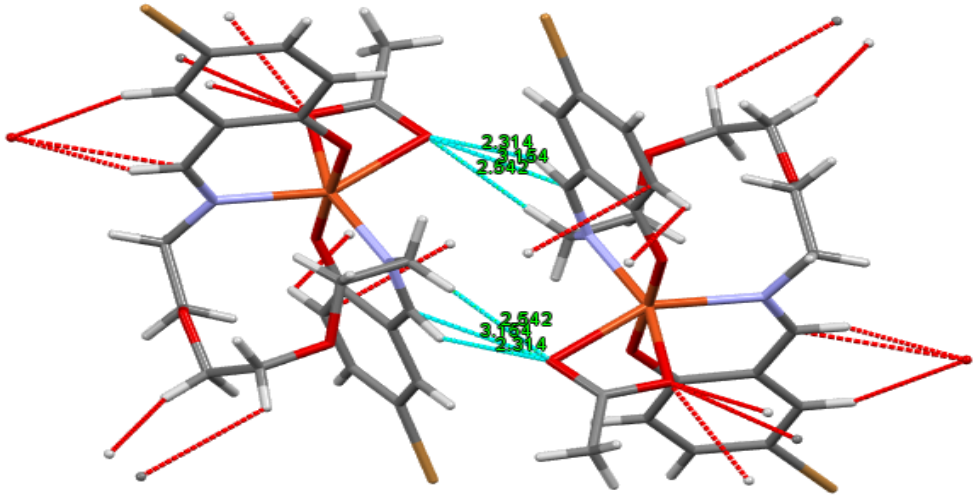

Figure III.24. Perspective projection visualizing the intermolecular interaction by hydrogen bond (C— H…X) presents between two neighbors molecules.

III.8. Hirshfeld surface analysis

To identify all intermolecular interactions within the complex Cu(II)L2's crystal structure as well as the types of atoms involved in their production, an investigation of the compound's Hirshfeld surface was carried out [43,44].

For every molecule that is a part of a crystalline structure, the Hirshfeld surface indicates one of its unique properties. There are several surfaces for a single molecule depending on the crystal structure it belongs to since HS is dependent on the molecular environment.

Using the Crystal Explorer 3.1[45–47] software, Hirshfeld surfaces are produced with a normalized contact distance (dnorm), which is based on two types of distances: the exterior distance (de) and the internal distance (di), spanning ranges from -0.718 (red) to 1.383 (blue). Near the oxygen atoms O2, O3, O5, O6, and O7, "hot" red patches are associated with the hydrogen bond O-H-O, short-distance contacts O-H-C, and Br type interactions Br… H/H… Br.

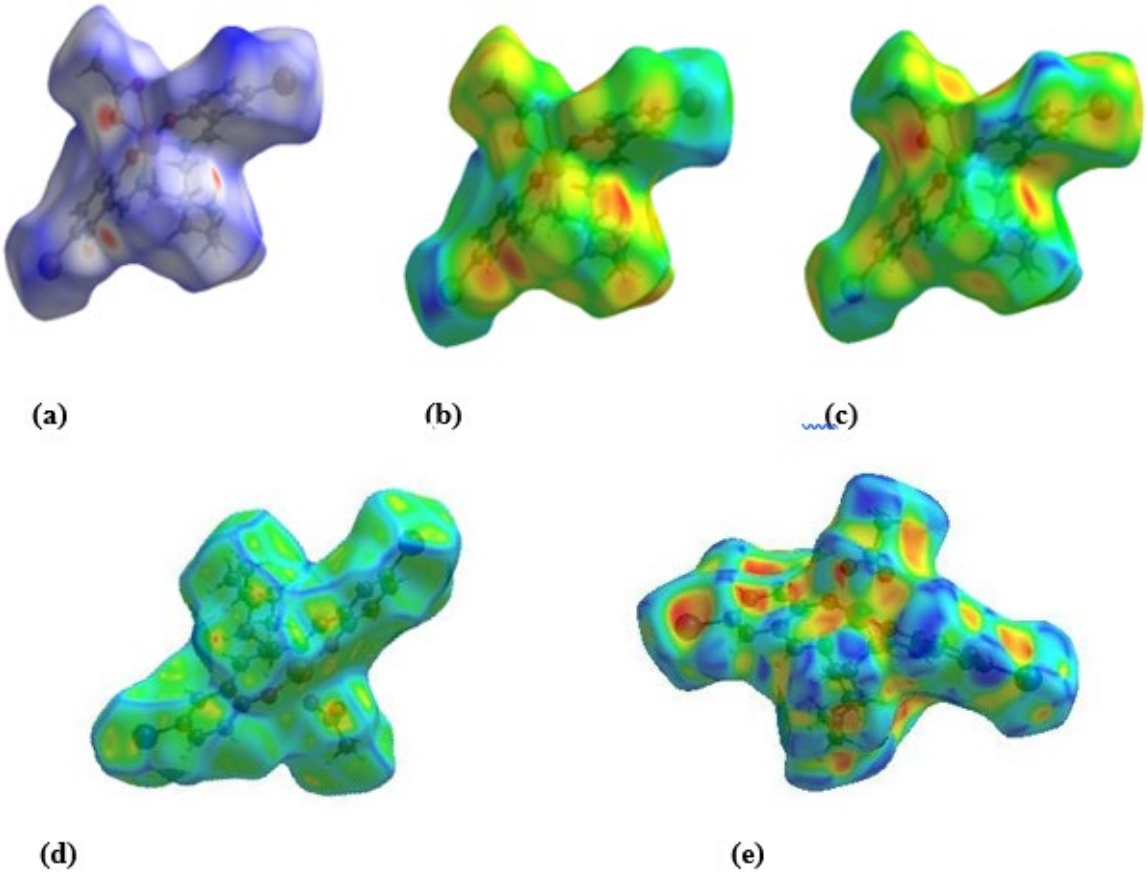

Figure III.25. Hirshfeld surface of Cu(II)L2 plotted on (a) = dnorm , (b) = di , (c) = de , (d) = curvedness , (e) = shape index .

At a rate of 43.6%, H… H type interactions (Figure II.26) in the molecular structure make the biggest contribution in the interaction surface. These contributions have two points that are

pointed in the direction of the origin, di +de ~ 1 Å. These interactions are normal and occur in the white portions of the surface, as shown by the comparison of the distance di +de with the total of the Van der Waals rays of the atoms involved in the bond (rVdW (H) + rVdW (H) =0.5+0.5 = 2.4 Å).

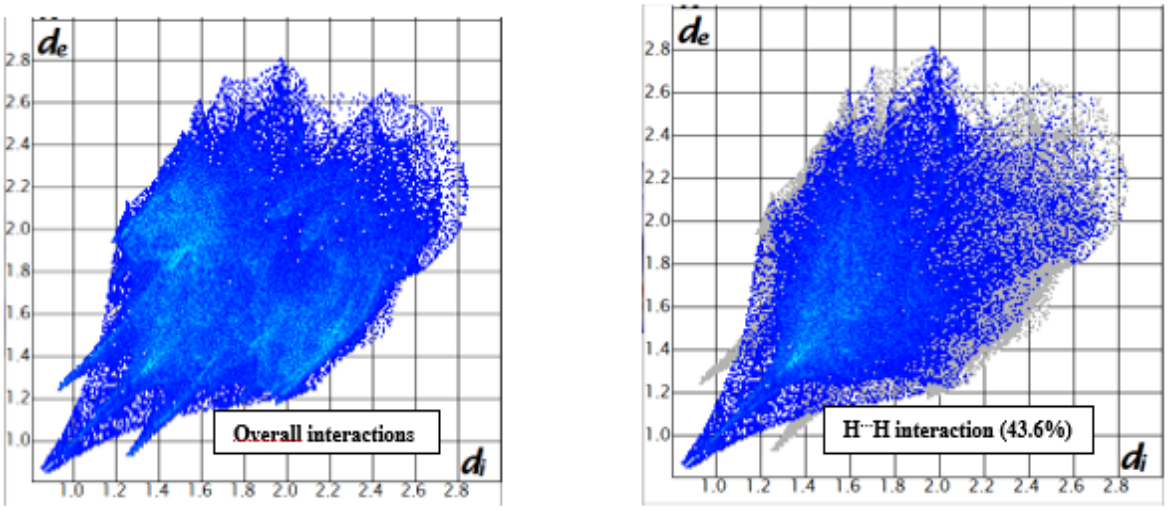

Figure III.26. The Cu(II)L2 structure two-dimensional fingerprint type H…H.

With the highest involvement, contact type Br... H accounts for one third of all intermolecular connections, or 22.5% (Figure III.27). Since each fingerprint point is situated at a distance (de, di) that is either larger than or equal to its van der Waals distance (de = di = 2.83 Å), this interval of intermolecular interactions (Br...H) is formed by a zero percentage.

Type H–C/C–H contacts (Figure III.27) comprise 17.4% of all contacts and are distinguished by two peaks with rounded, short, and symmetrical tops. Based on a comparison between di+de and the total of the Van der Waals rays of the atoms involved in the bond with di+ de ~ 2,78 Å, this interaction is thought to be the strongest interaction in the crystal. The Van der Waals radius of the atoms is 2.9 Å, which makes these connections significant. They are seen in the vicinity of light red dots, which suggest that short-distance interactions C-H... C are more prevalent.

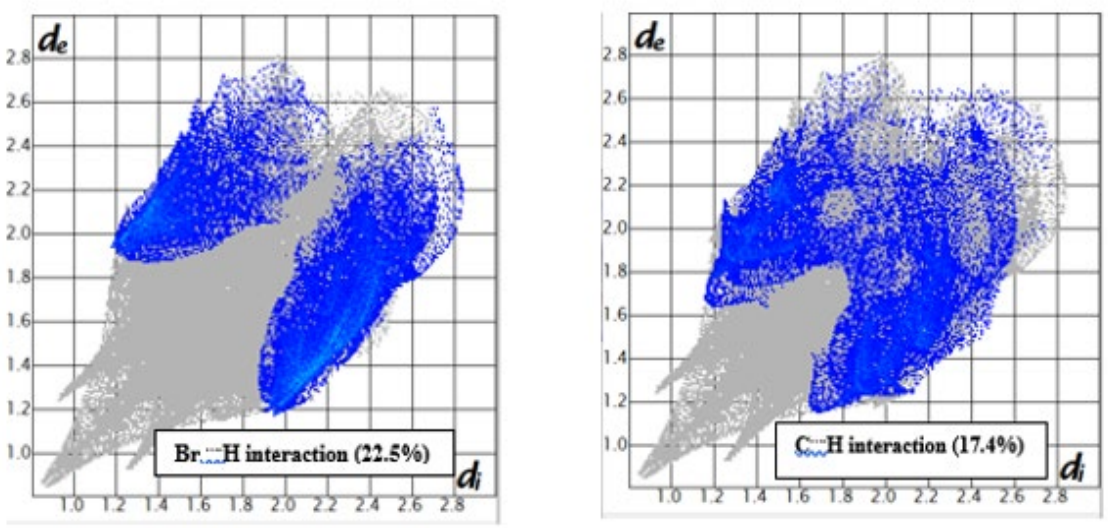

Figure III.27. Br… H/H… Br and C…H/H… C two-dimensional fingerprints of the Cu(II)L2 structure.

Two lengthy symmetrical peaks with di + de ~ 2.7 Å in Figure III.28, which depicts the Cu(II)L2 Hirshfeld surface fingerprint trace in two dimensions, indicate that type contacts H…O/O… H exhibit a 12.2% yield. The hydrogen interactions are represented by short distances, O-H...O and O-H…C, and are marked by bright red spots.

Br… C/C… Br contacts are about 3.2%, with di+ de ~ 3.8 Å which slightly exceeds the value of Van der Waals radii (rVdW= 3.6 Å). This contact is represented as a white spot near the Brome atom.

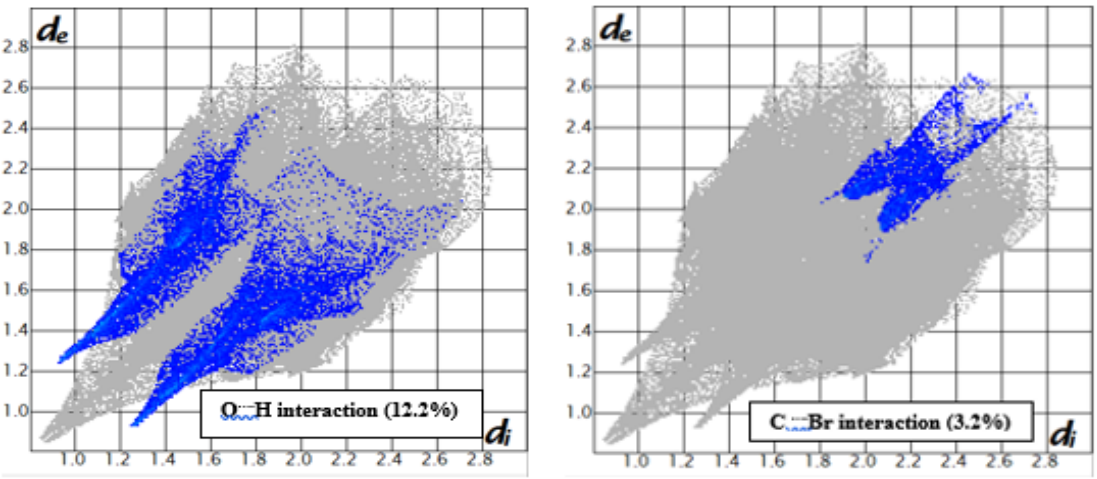

Figure III.28. Two-dimensional fingerprints type O…H/H…O and C…Br/Br…C of the Cu(II)L2 structure.

In addition, contacts N… C/C… N represent 0.3% of the structural contribution (Figure III.32). They represent interactions of type π-π.

As shown in figure III.29, the absence of this interaction in the molecular stack is justified because it contributes only 0.4% of N... H/H… N contacts of all the interatomic contacts within its crystalline structure around the (de, di) distances slightly larger than their Van der Waals rays, (di+ de) Å corresponds to the links π..... π. For the whole structure, Table III.8 compiles the relative contributions of the various contacts to the Hirshfeld surfaces.

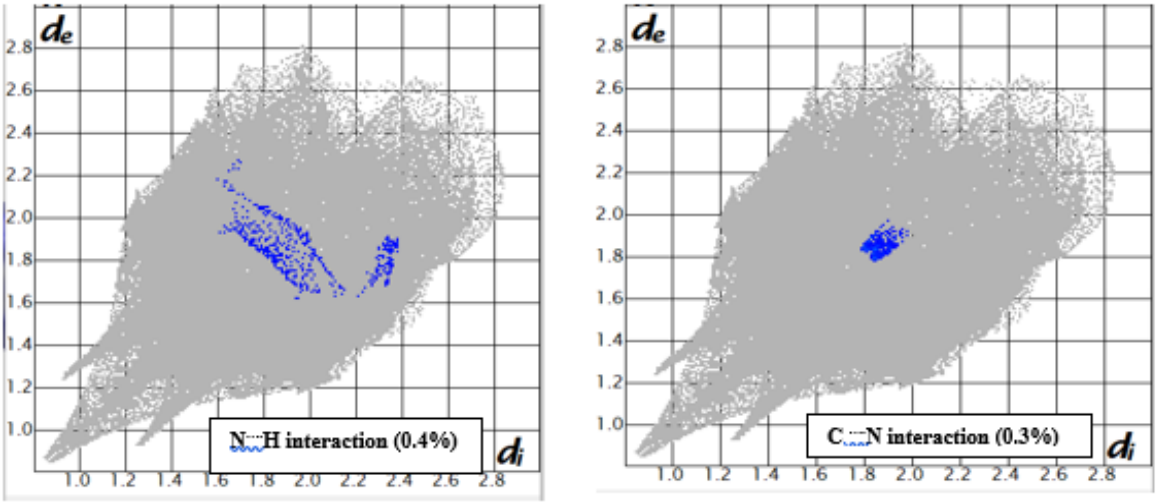

Figure III.29. Two-dimensional fingerprints of type N…H/H…N and C…N/N…C of the Cu(II)L2 structure.

Table III.8. Percentage contribution of different intermolecular interactions to the surface of Hirshfeld de Cu(II)L2.

Contacts	Contribution	Contacts	Contribution
O…H/H…O	12.2 %	N…H/H…N	0.4 %
C…H/H…C	17.4 %	Br…H/H…Br	22.5%
Br…O/O…Br	0.1 %	Br…C/C…Br	3.2%
N…C/C…N	0.3 %	H…H	43.6 %

Figure III.30 displays the Hirshfeld surface created around the asymmetric unit overlaid on dnorm, illustrating interactions with adjacent relatives and relations

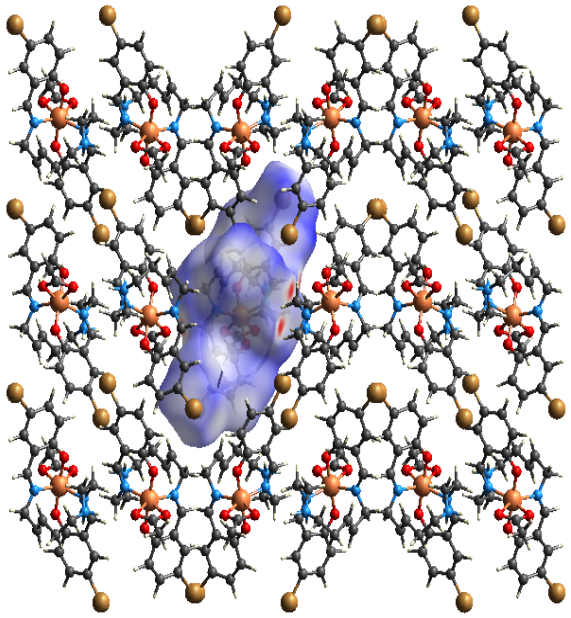

According to a

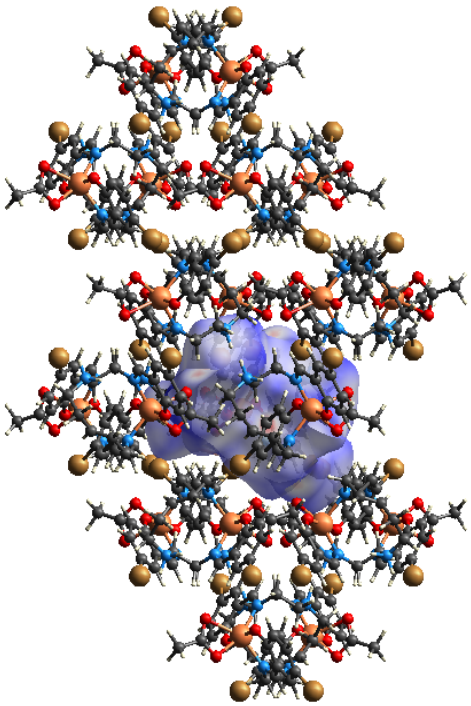

According to b

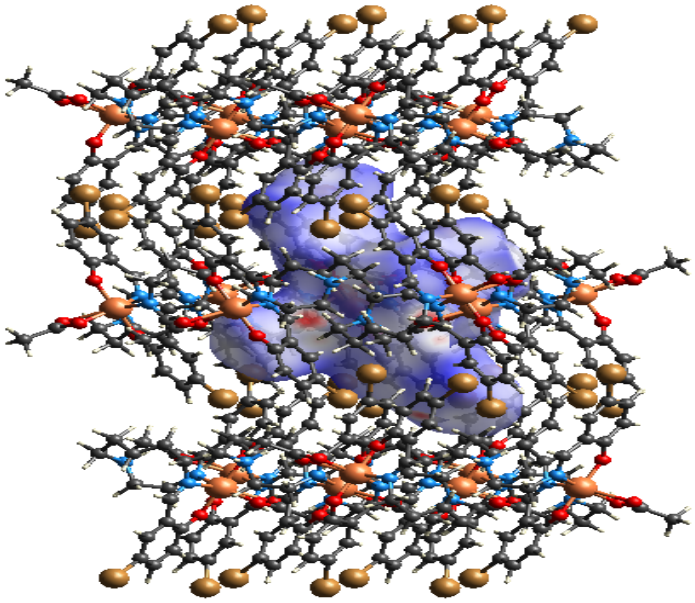

According to c

Figure III.30. The Hirshfeld surface of Cu(II)L mapped to dnorm showing interactions with nearby neighbors in three directions (x,y,z) at a distance of 3.8 Ao.

PART II: STRUCTURAL STUDY BY THEORETICAL CALCULATION

III.9. Quantum chemistry calculations by DFT

Quantum chemistry and in particular theoretical calculations by the method of functional density theory (DFT), recently used in the field of organic chemistry, provide information on the reactivity of organic compounds.

Thus, the goal of the current work is to investigate the Schiff base ligand's (H2L2) molecular and electrical structure. Using the DFT approach, the examined molecule's shape was entirely optimized at the B3LYP level, with the base 6-31G (d,p). [48,49]. quantum hints Using the GAUSSIAN 09 program, the highest and lowest occupied molecular orbitals (HOMO and LUMO), dipole moment (μ), absolute electronegativity (χ), absolute hardness (η), softness (σ), and Mulliken charge densities were computed. The figure below shows the optimized molecular structure of the ligand (H2L2).

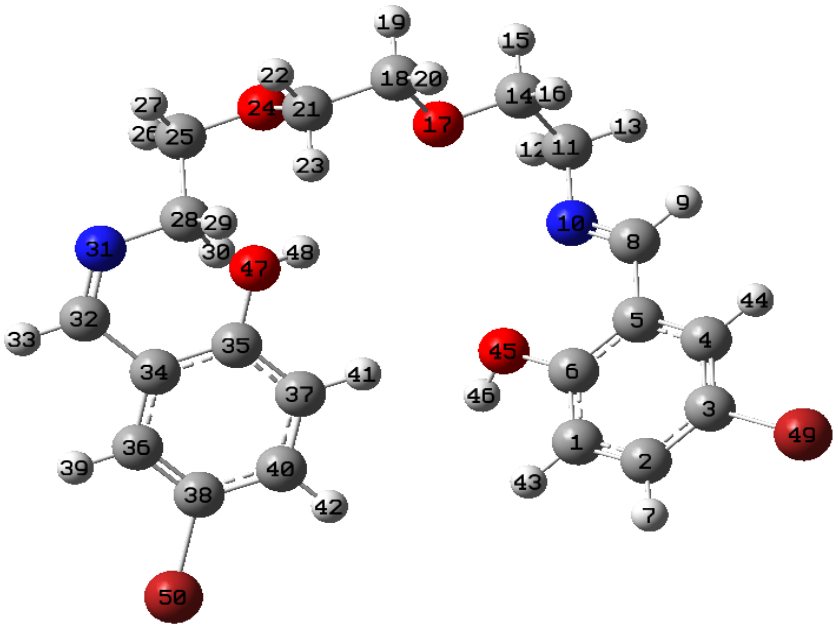

Figure III.31. Optimal molecular structure of the ligand (H2L2).

III.9.1. Frontier molecular orbitals (OMF)

In general, the highest occupied molecular orbital (HOMO) and the lowest unoccupied molecular orbital (LUMO) of Schiff bases are connected to their border molecular orbitals and their reactivity. A molecule with a high energy of the highest occupied molecular orbital (EHOMO) donates electrons to a low energy empty orbital (ELUMO) acceptor that is suitable [50]. The molecule has a stronger electron acceptor power when its EHOMO value is higher, indicating

that it is also a good electron donor when its ELUMO value is low [50–52]. When the produced molecules exhibit a modest energy gap (ΔEGAP) and all of the EHOMO and ELUMO values are negative, it is indicative of their stability [50].

A molecule's minimal energy needed to excite an electron is expressed by the difference, ΔEGAP = ELUMO – EHOMO, which is known as the energy gap. With a decrease in the gap value, the molecule becomes more reactive. We have calculated theoretically that the latter is stable for our chemical.

With regard to the ligand (H2L2), the two atoms N8 and N31 of the imine groups are the sites of condensation of the high occupied molecular orbital (HOMO) on the aromatic cycles and their substituents. An aromatic cycle and its substituents alone are the focus of an unoccupied orbital, or LUMO. The compound exhibits high stability as indicated by the HOMO-LUMO energy gap (ΔE = 2.4 eV).

Quantum parameters for the ligand (H2L2), such as EHOMO, ELUMO, and EGAP, have been computed and are compiled in Table III.9. The distribution of electronic densities of frontier molecular orbitals is shown in Figure III.32.

Table III.9. Energy of frontier orbitals (eV) for the ligand (H2L2)

Energy (eV)	H2L2
E (Homo)	-7.684
E (Lumo)	-5.284
E (gap) (HOMO → LUMO)	2.4
E (gap) (HOMO -1 → LUMO+1)	2.65
E (gap) (HOMO -2 → LUMO+2)	4.32

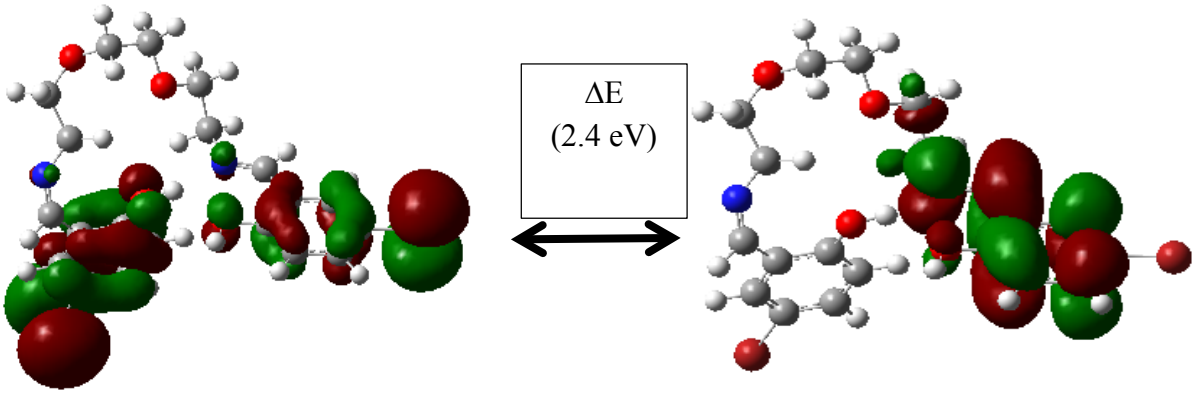

HOMO (-7.684 eV) **LUMO (-5.284 eV)**

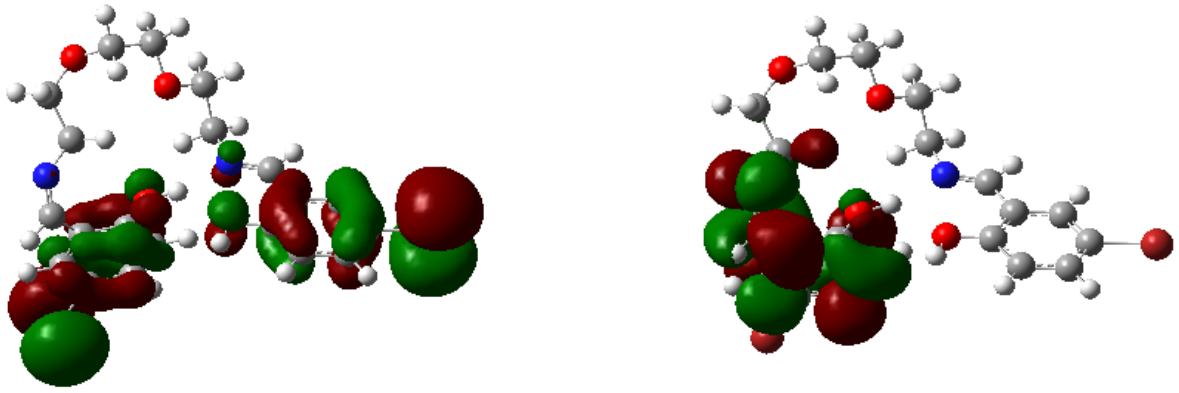

HOMO-1(-7.689 eV) **LUMO+1 (-5.03 eV)**

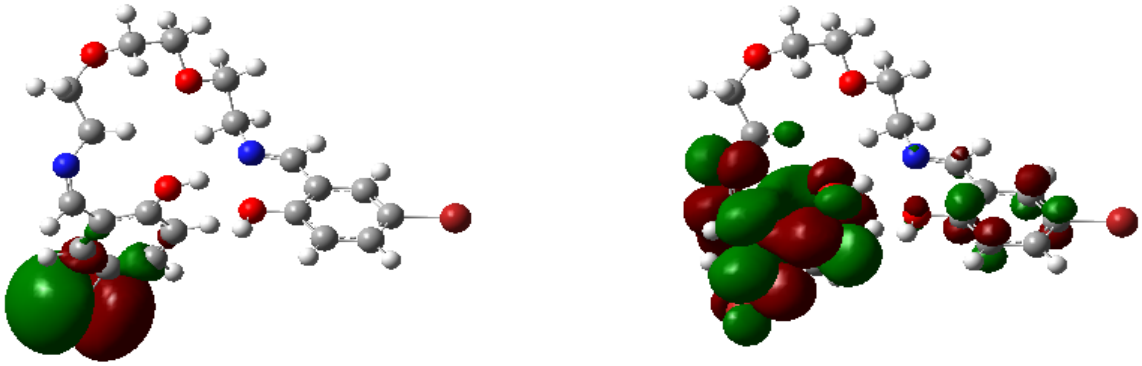

HOMO-2 (-8.12 eV) **LUMO+2 (-3.80 eV)**

Figure III.32. Frontier molecular orbitals (FMOs) of H2L2 ligands.

Chemical system stability and reactivity are related to chemical hardness (η). Chemical hardness is defined as the difference between the highest occupied and lowest vacant molecular orbital based on frontier molecular orbitals. A molecule is said to be more stable or less reactive the larger the HOMO-LUMO energy gap [49,53]. Table III.10 lists the chemical parameter values in groups.

Table III.10. Quantum parameters for ligand (H2L2).

Quantum parameters (eV)	Ligand (H_2L2)
Ionization energy I	7.68
Electronic affinity A	5.28
Chemical potential μ	-6.48
Hardness η	1.2
Electrophilicity ω	17.49
Softness	0.83
Electronegativity χ	6.48

The electron chemical potential (μ) is defined as the negative of the electronegativity of a molecule [54], according to Table III.10, the trend in the electron chemical potential of the ligand (H2L2) is considered high.

The electrophilicity index (ω) is a measure of energy stabilization after one system accepts an additional electronic charge of another species [53,54], the electrophilicity value for ligand (H2L2) is large , describes this system as a Lewis acid.

III.9.2. Mulliken atomic charges

Mulliken atomic charge calculations are crucial for understanding molecular systems because they determine the dipole moment, molecule polarizability, and other electronic characteristics. The creation of donor-acceptor pairs involving charge transfer in the molecule is suggested by the charge distributions on the atoms. Mulliken atomic charges for ligand (H2L2) is listed in the table below.

Table III.11. Mulliken atomic charges calculated for the ligand (H2L2).

atoms	Mulliken charges	atoms	Mulliken charges
C1	-0.468	C25	-0.370
C2	-0.399	H26	0.341
C3	-0.378	H27	0.331
C4	-0.461	C28	-0.639
C5	-0.157	H29	0.360
C6	-0.584	H30	0.367
H7	0.366	N31	-0.589
C8	0.185	C32	0.099
H9	0.327	H33	0.341
N10	-0.592	C34	-0.153
C11	-0.630	C35	0.563
H12	0.369	C36	-0.405
H13	0.360	C37	-0.469
C14	-0.368	C38	-0.367
H15	0.329	H39	0.359
H16	0.324	C40	-0.415
O17	-0.561	H41	0.367
C18	-0.367	H42	0.366
H19	0.328	H43	0.368
H20	0.327	H44	0.358
C21	-0.389	O45	-0.749
H22	0.340	H46	0.510
H23	0.336	O47	-0.774
O24	-0.553	H48	0.461
Br50	0.381	Br49	0.389

The atomic charges of Mulliken show that the most negative atoms are oxygen and nitrogen and that the atom H46 bound to O45 has the most positive atomic charge.

The distribution of Mulliken charges also shows that the nitrogen atom O47 of the hydroxy group is more negative compared to other atoms and it is interesting to mention that the most

negative atoms are: O45, O47, O24, O17, N10 and N31. The latter are active centers in the reactivity of these molecules.

III.9.3. Molecular Electrostatic Potential (MEP)

The electrostatic potential is shown on the constant electron density surface, or MEP. In addition, it is highly helpful for studying hydrogen binding interactions and the link between physiochemical properties and molecular structure [50,51]. At any given position r (x, y, z), the electrostatic potential V(r) is defined as the energy of interaction between the electric charge produced by the molecule's electrons, its nuclei, and its protons at r.

In the current investigation, three-dimensional (3D) plots of the molecular electrostatic potential (MEP) of the ligand H2L2 were created (Figure III.33). The maximum negative region, shown in red, preferred the site for signs of an electrophilic attack, while the maximum positive region, shown in blue, preferred the site for symptoms of a nucleophilic attack. Potential rises in the following order: red < green < blue, with red displaying the most repulsion and blue the strongest attraction.

The regions with negative potential are on the electronegative atoms which are O17, O24 , O15 , O17, N31 and N 8, while the regions with positive potential are on the hydrogen atoms.

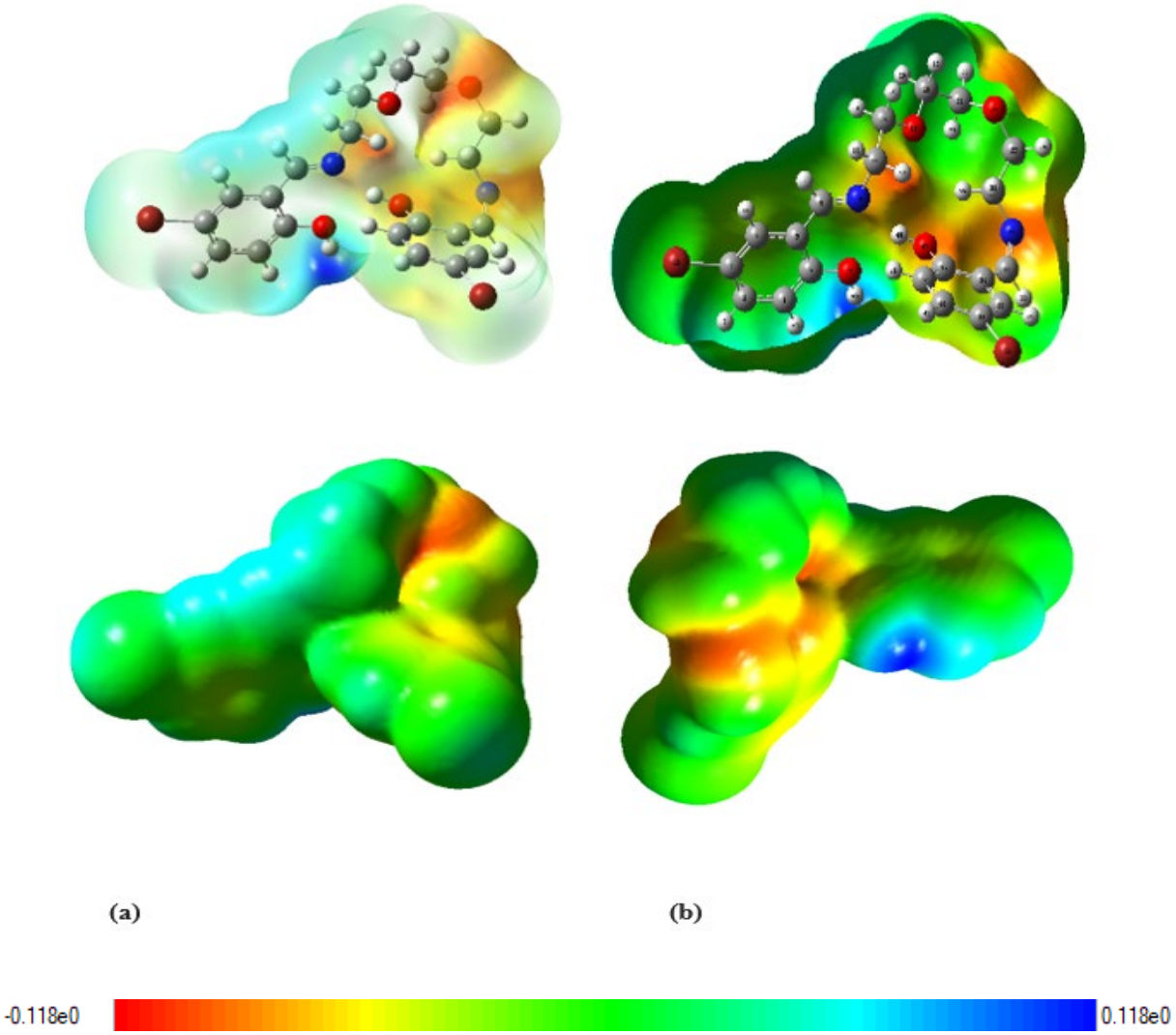

Figure III.33. Cartograph of the molecular electrostatic potential of ligands H2L2 drawn on surfaces of total density (a): Front view and (b) Rear view

III.10. Nonlinear optical properties (NLO)

Several kinds of active materials in ONL have been created recently due to their many uses in photonics and optoelectronics [55,56]. The sophisticated laser methods make advantage of these materials [57]. Of them, organic and organometallic compounds [58] are gaining increasing attention because to their comparatively simple and costly synthesis. Here, we unleash the full potential of the ligand's non-linear optics (H2L2).

We find that the polarity of solvents plays a major role in determining their effects on the hyperpolarizability of H2L. Specifically, the values of β_0 and β_{HRS} for H2L2 in solvents are around double those of gaseous solvents.

In terms of the depolarization ratio ($DR^{\omega=0}$), we note that the NLO response of the ligand (H2L2) exhibits a dominating dipole symmetry. The ligand's (H2L2) computed non-linear optical characteristics are grouped in Table (III.12).

Table III.12. Non-linear optical properties (NLO) of the ligand (H2L2).

	Gas	Benzene	Chloroform	1-Hexanol	Ethanol	DMF	Water
μ	1.010	1.152	1	0.814	1.155	1.153	0.798
α **(0;0)**	296	334	355	367	371	373	374
Δα **(0;0)**	220	233	216	193	242	243	192
$\boldsymbol{\rho^0}$	43	50	53	54	55	55	55
Q_0	259	406	458	459	588	600	489
Q_{vec}	259	406	458	459	588	600	489
Q_{HRS}	124	175	192	194	239	243	205
DR	3.435	4.397	4.791	4.661	5.309	5.359	4.762
α **(-ω;ω)**	298	336	333	331	327	331	325
Δα **(-ω;ω)**	222	236	218	199	236	236	198
$\boldsymbol{\rho^\omega}$	44	50	49	49	49	49	48
Q_{EOPE}	263	412	399	362	443	455	354
Q^ω_{SHG}	274	428	385	333	400	412	314
Q^ω_{HRS}	132	186	166	148	170	175	140
DR^m	3.383	4.267	4.355	4.065	4.568	4.621	4.008

The second generation of harmonics (β_{SHG}), hyper-Rayleigh scattering (β_{HRS}), and electro-optical Pockels effect (β_{EOPE}) of H2L revealed an increase of β_{SHG} 0,0239 and β_{HRS} 0,0239 indifferent environment in the following order:

gas < water <1-Hexanol < Chloroform < Ethanol < DMF < Benzene.

In the case of a frequency-dependent effect (ω= 0.0239 au). The compound's second-order NLO responses in the solvents under study show that benzene has somewhat higher SHG0.0239 and HRS 0.0239 values than the other solvents.

It is noted that our results on the ligand (H2L2) was published in the journal ChemistrySelect - WILEY (DOI: 10.1002/slct.202302953).

PART III: BIOLOGICAL STUDY, ANTIOXIDANT PROPERTIES

Antioxidant activity cannot be precisely and uniquely quantified quantitatively due to the complexity of oxidation processes and the various nature of antioxidants, which include both hydrophilic and hydrophobic components. Therefore, there is no one universal approach that can be used to evaluate antioxidant activity.

In fact, in order to assess a molecule's overall antioxidant impact, it is sometimes required to integrate the results of many complimentary tests in order to obtain a fairly accurate estimate of the sample's antioxidant capacity [59] . We choose to use the DPPH, ABTS technique in this investigation.

Table III.13. Antioxidant activity of ligand (H2L1) and its complexes by different methods.

	DPPH IC50 (µg/ml)	ABTS IC50 (µg/ml)
Ligand (H2L2)	457.362	389.607
Mn(II) L2	1394.941	252.065
Cu(II) L	1018.727	1027.982
Co(II) L2	1877.934	830.608
Zn(II)L2	248964.5	1390.506
BHA	6.14±0.41	1.81±0.10
BHT	12.99±0.41	1.29±0.30

III.11.1. DPPH radical test

Figure III.37 below illustrates the percentage inhibition of the ligand (H2L2), its complexes, and the standard antioxidant. The produced molecules exhibit extremely low to almost non-existent inhibition of the employed free radical (DPPH), displaying values of 457.362, 1394.941, 1018.727, 1877.934, and 248964.5 (µg/ml) for H2L2, Mn(II)L2, Cu(II)L2, Co(II)L2, and Zn(II)L2, in that order.

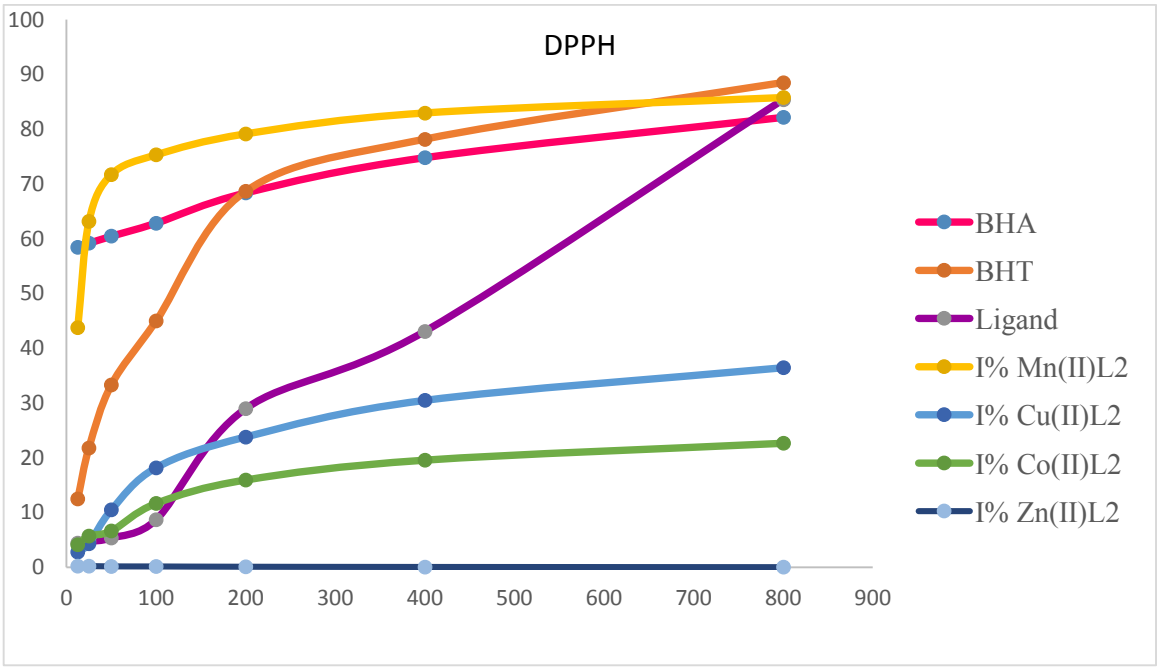

Figure III.34. DPPH free radical scavenging activity of standard BHA, BHT and synthesized compounds

The antiradical effectiveness metric known as IC50 is used. It conveys the quantity of antioxidants needed to reduce DPPH concentration by half. The relationship between a compound's antioxidant capability and its IC50 (antiradical capabilities) is inverse. Figure III.35 shows the various IC50s, which are derived from the equations of the curves indicating the inhibition percentages in relation to the compound concentrations.

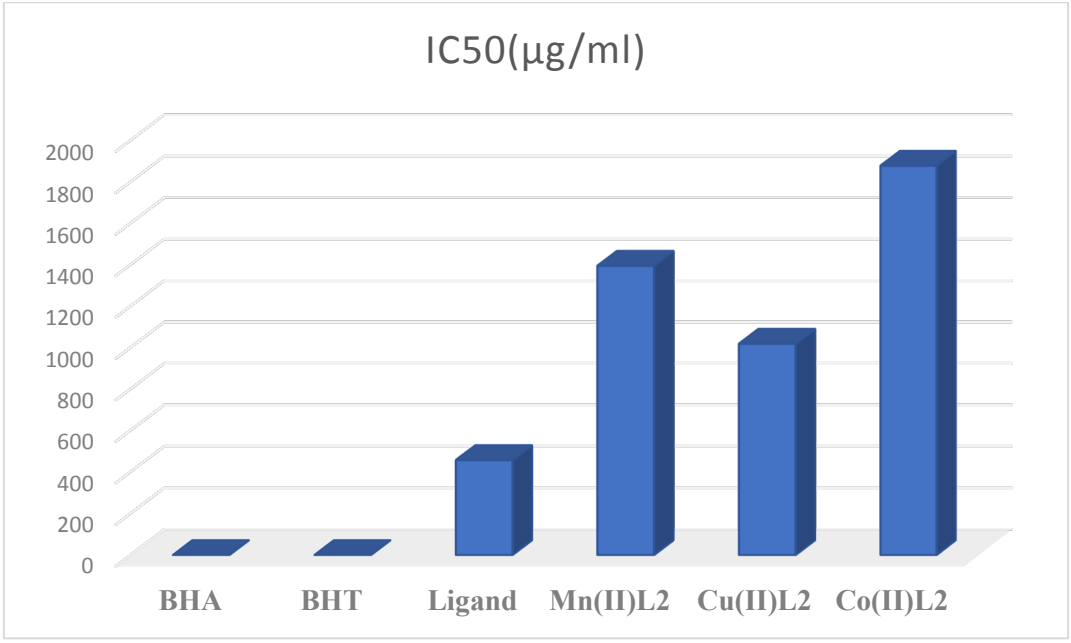

Figure III.35. IC50 inhibitory concentration values expressed in (µg/ml). Ligand (H2L2), Mn(II)L2, Cu(II)L2, Co(II)L2, Zn(II)L2 complexes and BHA and BHT standards

Antioxidant potencies obtained by DPPH testing of molecules are classified (in descending order) as follows:

Zn(II)L2 < Co(II)L2 < Mn(II)L2 < Cu(II)L2 < H2L2 < BHT < BHA

III.11.2. ABTS radical test

The results obtained by the ABTS+ test clearly show that the synthesized molecules, have a very low potential of the radical ABTS+, of which among the five molecules the complex Mn(II) L2 and the ligand (H2L2) represent the lowest IC50 values (IC50=252.065 µg/ml and 389.607 (µg/ml) respectively) and therefore the highest anti-radical activity in this series and which still remains shabby by contribution to the standard used . On the other hand, the remaining complexes inhibit low to zero or IC50 values corresponding to 1027.982, 830.608 , 1390.506 (µg/ml).

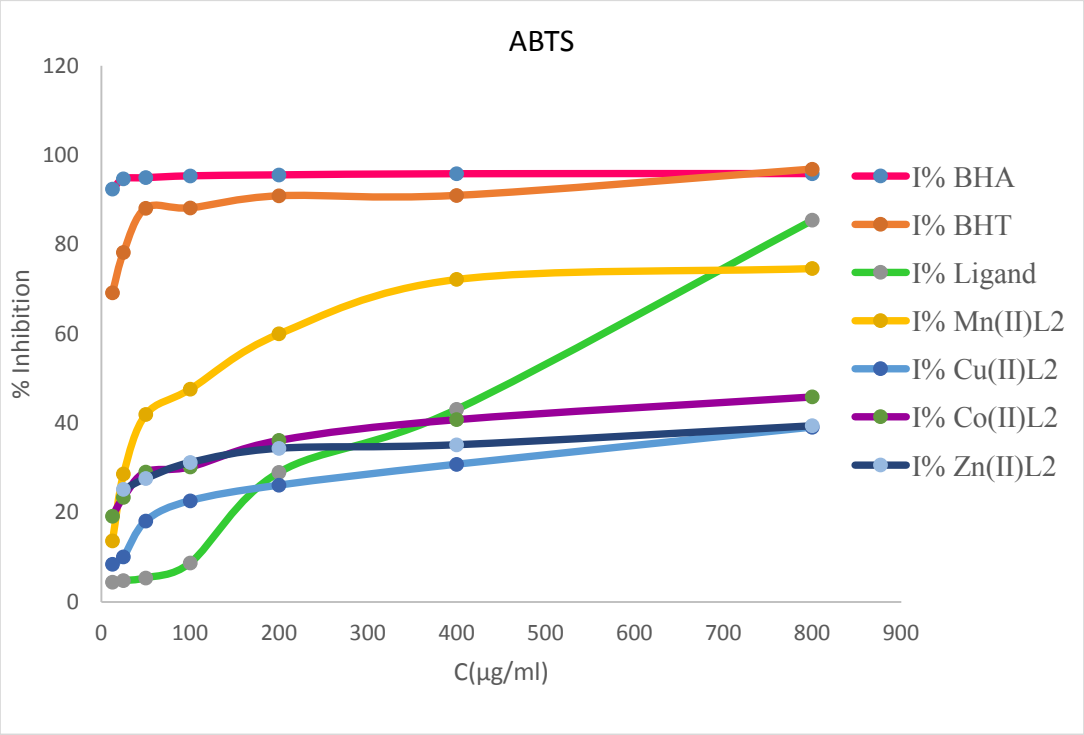

Figure III.36. ABTS anti-radical activity of synthesized molecules (H2L2), Mn(II)L2 , Cu(II)L2, Co(II)L2, Zn(II)L2 and BHA , BHT standards.

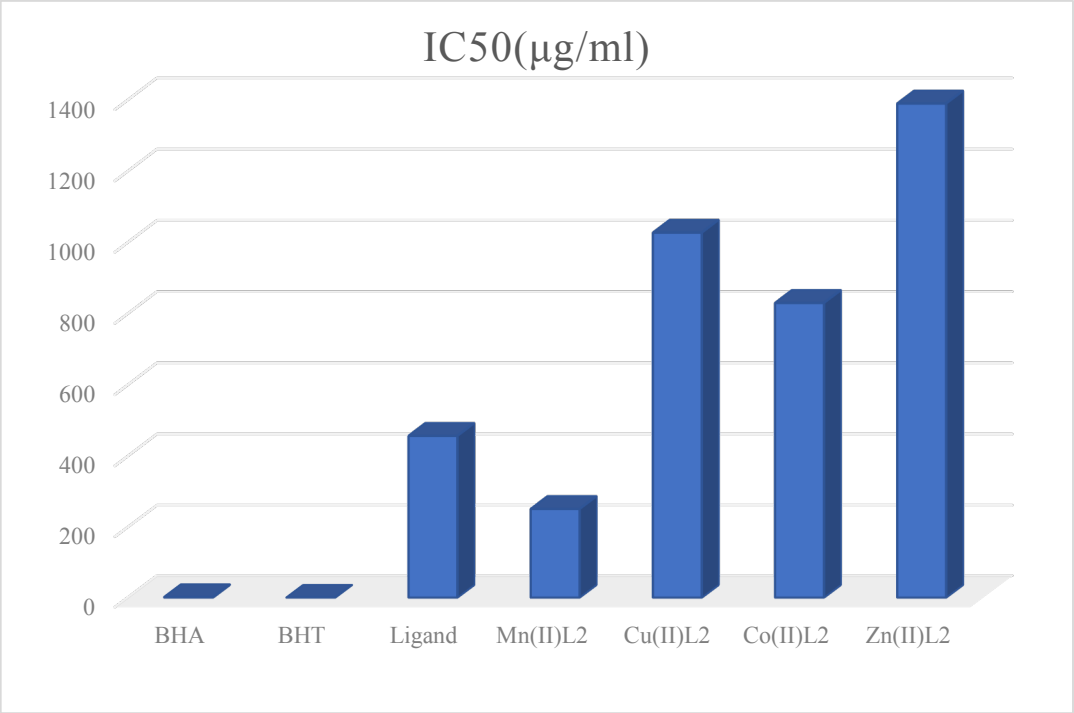

Figure III.37. IC50 inhibitory concentration values in (µg/ml). Du (H2L2), Mn(II)L2, Cu(II)L2, Co(II)L2, Zn(II)L2 and BHA , BHT standards towards ABTS.

Through a comparative analysis of the antioxidant activities of the investigated compounds using two different radical scavenging methods (DPPH• and ABTS+), it is evident that the studied Schiff ligand exhibits a moderate level of antioxidant activity, while the complexes of Mn(II)L2, Cu(II)L2, Co(II)L2, and Zn(II)L2 have nearly negligible antioxidant activity. In conclusion, even with the strong impact of electroattractor groups, none of these compounds exhibit appreciable antioxidant action.

III.12. Conclusion

Ligand 2,2'-((1E,11E)-5,8-dioxa-2,11-diazadodeca-1,12-diyl) bis(4-bromophenol) (H2L2) and its metal complexes Cu(II)L2, Mn(II)L2, Co(II)L2 and Zn(II)L2 were produced. The yields are tolerable, and the synthesized goods have outstanding purity. Through spectral investigations (IR, UV/Vis, and 1H-NMR), we were able to identify and describe every structure. The various spectra's interpretations agree with the suggested structures Cu(II)L2 mononuclear complex is a single product that is formed as a single crystal and has undergone a thorough structural analysis that provides solid evidence for the structure of the suggested compound.

The most significant contribution to the interaction surface is represented by H... H type contacts, according to a thorough analysis of the Hirshfeld surface of the molecular structure. H2L2, the ligand under investigation, is a promising option for a non-linear optical material. Several techniques were used to assess the antioxidant capacity of items that were produced in vitro. The results indicated that DPPH• and ABTS•+ have modest antioxidant activity.

References

[1] J. Devi, S. Devi, A. Kumar, Synthesis, antibacterial evaluation and QSAR analysis of Schiff base complexes derived from [2,2′-(ethylenedioxy)bis(ethylamine)] and aromatic aldehydes, Medchemcomm 7 (2016) 932–947. https://doi.org/10.1039/c5md00554j.

[2] N. Papri, A. Sarker, M.L. Hossain, K.S. Hossain, M.A.B. Siddique, A.K.M.L. Rahman, Synthesis, characterization and biological applications of Mo(VI) and V(IV) complexes of 2-[2-(2-aminoethoxy) ethoxy]ethanamine dithiocarbamate, Chiang Mai J. Sci. 48 (2021) 196–206.

[3] B.K. Vernekar, P.S. Sawant, Interaction of metal ions with Schiff bases having N2O2 donor sites: Perspectives on synthesis, structural features, and applications, Results Chem. 6 (2023) 101039. https://doi.org/10.1016/j.rechem.2023.101039.

[4] Y.M. Ahmed, G.G. Mohamed, Synthesis, spectral characterization, antimicrobial evaluation and molecular docking studies on new metal complexes of novel Schiff base derived from 4,6-dihydroxy-1,3-phenylenediethanone, J. Mol. Struct. 1256 (2022). https://doi.org/10.1016/j.molstruc.2022.132496.

[5] A.A. Alothman, E.S. Al-Farraj, W.A. Al-Onazi, Z.M. Almarhoon, A.M. Al-Mohaimeed, Spectral characterization, electrochemical, antimicrobial and cytotoxic studies on new metal(II) complexes containing N2O4 donor hexadentate Schiff base ligand, Arab. J. Chem. 13 (2020) 3889–3902. https://doi.org/10.1016/j.arabjc.2019.02.003.

[6] H. Kargar, M. Fallah-Mehrjardi, K.S. Munawar, Metal complexes incorporating tridentate ONO pyridyl hydrazone Schiff base ligands: Crystal structure, characterization and applications, Coord. Chem. Rev. 501 (2024) 215587. https://doi.org/10.1016/j.ccr.2023.215587.

[7] M.N.A. Al-Jibouri, S.A.H. Al-Ameri, W.M. Al-Jibouri, M.A.K. Al-Souz, Spectroscopic study of the effect of a new metal chelate on the stability of PVC, J. Assoc. Arab Univ. Basic Appl. Sci. 14 (2013) 67–74. https://doi.org/10.1016/j.jaubas.2012.11.003.

[8] F.Y. Waddai, E.K. Kareem, S.A. Hussain, Synthesis, spectral characterization and antimicrobial activity of some transition metal complexes with new schiff base ligand (BDABI), Orient. J. Chem. 34 (2018) 434–443. https://doi.org/10.13005/ojc/340147.

[9] M. Yadav, N. Mishra, N. Sharma, S. Chandra, D. Kumar, Microwave assisted synthesis, characterization and biocidal activities of some new chelates of carbazole derived Schiff bases of cadmium and tin metals, Spectrochim. Acta - Part A Mol. Biomol. Spectrosc. 132 (2014) 733–742. https://doi.org/10.1016/j.saa.2014.04.185.

[10] S. Dekar, K. Ouari, S. Bendia, D. Hannachi, J. Weiss, Mononuclear oxovanadium(IV) Schiff base complex: Synthesis, spectroscopy, electrochemistry, DFT calculation and catalytic activity, J. Organomet. Chem. 866 (2018) 165–176. https://doi.org/10.1016/j.jorganchem.2018.04.015.

[11] W.H. Mahmoud, M.M. Omar, Y.M. Ahmed, G.G. Mohamed, Transition metal complexes of Schiff base ligand based on 4,6-diacetyl resorcinol, Appl. Organomet. Chem. 34 (2020) 1–20. https://doi.org/10.1002/aoc.5528.

[12] M.R. Buchner, M. Müller, Beryllium Crown Ether Complexes Reinvestigated, Zeitschrift Fur Anorg. Und Allg. Chemie 644 (2018) 1186–1189. https://doi.org/10.1002/zaac.201800334.

[13] Y.M. Ahmed, M.M. Omar, G.G. Mohamed, Synthesis, spectroscopic characterization,

and thermal studies of novel Schiff base complexes: theoretical simulation studies on coronavirus (COVID-19) using molecular docking, J. Iran. Chem. Soc. 19 (2022) 901–919. https://doi.org/10.1007/s13738-021-02359-w.

[14] T.I. Kashar, A.H. El-Sehli, Synthesis, characterization, antimicrobial and anticancer activity of Zn(II), Pd(II) and Ru(III) complexes of dehydroacetic acid hydrazone, J. Chem. Pharm. Res. 5 (2013) 474–483.

[15] M.M. Abd-Elzaher, A.A. Labib, H.A. Mousa, S.A. Moustafa, M.M. Ali, A.A. El-Rashedy, Synthesis, anticancer activity and molecular docking study of Schiff base complexes containing thiazole moiety, Beni-Suef Univ. J. Basic Appl. Sci. 5 (2016) 85–96. https://doi.org/10.1016/j.bjbas.2016.01.001.

[16] I. Jirjees, S.A. Ali, H.A. Mahdi, Synthesis, Characterization of Schiff Base and its Complexes Derived from 4-Aminoantipyrine and using in Extraction of Nickel (II) Ion, Int. J. Sci. Eng. Res 6 (2015) 735–743.

[17] A.E. Şabik, M. Karabörk, G. Ceyhan, M. Tümer, M. Dığrak, Polydentate Schiff base ligands and their La (III) complexes: Synthesis, characterization, antibacterial, thermal, and electrochemical properties, Int. J. Inorg. Chem. 2012 (2012).

[18] A. Bhowmick, M. Islam, R. Bhowmick, M. Sarkar, A. Shibly, E. Hossain, Synthesis and Structure Determination of Some Schiff Base Metal Complexes with Investigating Antibacterial Activity, Am. J. Chem. 2019 (2019) 21–25. https://doi.org/10.5923/j.chemistry.20190901.03.

[19] R.V. Palaniswamy, M. Dhandapani, J. Suyambulingam, C. Subramanian, Synthesis, characterization, thermal, theoretical and antimicrobial studies of Schiff base ligand and its Co(II) and Cu(II) complexes, J. Serbian Chem. Soc. 85 (2020) 215–225. https://doi.org/10.2298/JSC181128049V.

[20] C. Enol, Z. Hayvali, H. Dal, T. Hökelek, Syntheses, characterizations and structures of NO donor Schiff base ligands and nickel(II) and copper(II) complexes, J. Mol. Struct. 997 (2011) 53–59. https://doi.org/10.1016/j.molstruc.2011.04.037.

[21] M. Sarigul, S.E. Kariper, P. Deveci, H. Atabey, D. Karakas, M. Kurtoglu, Multi-properties of a new azo-Schiff base and its binuclear copper (II) chelate: Preparation, spectral characterization, electrochemical, potentiometric and modeling studies, J. Mol. Struct. 1149 (2017) 520–529.

[22] T. Eren, M. Kose, K. Sayin, V. McKee, M. Kurtoglu, A novel azo-aldehyde and its Ni(II) chelate; Synthesis, characterization, crystal structure and computational studies of 2-hydroxy-5-{(E)-[4-(propan-2-yl) phenyl]diazenyl}benzaldehyde, J. Mol. Struct. 1065–1066 (2014) 191–198. https://doi.org/10.1016/j.molstruc.2014.02.052.

[23] Souad DEKAR Ep ABID, Synthèse chimique et propriétés spectroscopiques de complexes de métaux de transition symétriques et asymétriques. Réactivité électrochimique en milieu organique en présence du dioxygène : Approche biomimétique, UNIVERSITE FERHAT ABBAS-SETIF-1 FACULTE DES SCIENCES, 2019. http://dspace.univ-setif.dz:8888/jspui/handle/123456789/3514.

[24] R. Benramdane, F. Benghanem, A. Ourari, S. Keraghel, G. Bouet, Synthesis and characterization of a new Schiff base derived from 2,3-diaminopyridine and 5-methoxysalicylaldehyde and its Ni(II), Cu(II) and Zn(II) complexes. Electrochemical and electrocatalytical studies, J. Coord. Chem. 68 (2015) 560–572.

https://doi.org/10.1080/00958972.2014.994514.

[25] S. Chahmana, S. Keraghel, F. Benghanem, R. Ruíz-Rosas, A. Ourari, E. Morallón, Synthesis, spectroscopic characterization, electrochemical properties and biological activity of 1-[(4Hydroxyanilino)-methylidene] naphthalen-2(1H)-one and its Mn (III) complex, Int. J. Electrochem. Sci. 13 (2018) 175–195. https://doi.org/10.20964/2018.01.27.

[26] K. Das, S. Goswami, B.B. Beyene, A.W. Yibeltal, C. Massera, E. Garribba, A. Frontera, Z. Cantürk, T. Askun, A. Datta, Spectral, electrochemical and DFT studies of a trimetallic CuII Derivative: Antimycobacterial and cytotoxic activity, Inorganica Chim. Acta 490 (2019) 155–162. https://doi.org/10.1016/j.ica.2019.03.014.

[27] M. Sarigul, P. Deveci, M. Kose, U. Arslan, H. Türk Dagi, M. Kurtoglu, New tridentate azo-azomethines and their copper(II) complexes: Synthesis, solvent effect on tautomerism, electrochemical and biological studies, J. Mol. Struct. 1096 (2015) 64–73. https://doi.org/10.1016/j.molstruc.2015.04.043.

[28] M. Merzougui, K. Ouari, J. Weiss, Ultrasound assisted synthesis, characterization and electrochemical study of a tetradentate oxovanadium diazomethine complex, J. Mol. Struct. 1120 (2016) 239–244. https://doi.org/10.1016/j.molstruc.2016.05.046.

[29] S. Zolezzi, E. Spodine, A. Decinti, Electrochemical studies of copper(II) complexes with Schiff-base ligands, Polyhedron 21 (2002) 55–59. https://doi.org/10.1016/S0277-5387(01)00960-3.

[30] A.H. Kianfar, S. Ramazani, R.H. Fath, M. Roushani, Synthesis, spectroscopy, electrochemistry and thermogravimetry of copper(II) tridentate Schiff base complexes, theoretical study of the structures of compounds and kinetic study of the tautomerism reactions by ab initio calculations, Spectrochim. Acta - Part A Mol. Biomol. Spectrosc. 105 (2013) 374–382. https://doi.org/10.1016/j.saa.2012.12.010.

[31] G. Saha, K.K. Sarkar, T.K. Mondal, C. Sinha, Synthesis, spectra, structure, redox properties and DFT computation of copper(I)-triphenylphosphine-pyridyl Schiff bases, Inorganica Chim. Acta 387 (2012) 240–247. https://doi.org/10.1016/j.ica.2012.01.030.

[32] A. Ourari, A. Alouache, D. Aggoun, R. Ruiz-Rosas, E. Morallon, Electrocatalytical reduction of bromocyclopentane and iodobenzene using Cobalt(III) and Nickel(II) Tris- and Bis-bidentates Schiff Bases Complexes, Int. J. Electrochem. Sci. 13 (2018) 5589–5602. https://doi.org/10.20964/2018.06.39.

[33] S. Kumar, A. Hansda, A. Chandra, A. Kumar, M. Kumar, M. Sithambaresan, M.S.H. Faizi, V. Kumar, R.P. John, Co(II), Ni(II), Cu(II) and Zn(II) complexes of acenaphthoquinone 3-(4-benzylpiperidyl)thiosemicarbazone: Synthesis, structural, electrochemical and antibacterial studies, Polyhedron 134 (2017) 11–21. https://doi.org/10.1016/j.poly.2017.05.055.

[1] M. Mesbah, T. Douadi, F. Sahli, S. Issaadi, S. Boukazoula, S. Chafaa, Synthesis, characterization, spectroscopic studies and antimicrobial activity of three new Schiff bases derived from Heterocyclic moiety, J. Mol. Struct. 1151 (2018) 41–48. https://doi.org/10.1016/j.molstruc.2017.08.098.

[35] S.A. Hosseini-Yazdi, A. Mirzaahmadi, P. Samadzadeh-Aghdam, A.A. Khandar, G. Mahmoudi, W. Scott Kassel, W.G. Dougherty, Synthesis, characterization, X-ray structure, spectroscopic and electrochemical studies of copper and zinc complexes with two new polydentate ligands, Inorganica Chim. Acta 414 (2014) 115–120. https://doi.org/10.1016/j.ica.2014.01.039.

[36] M. Montazerozohori, M. Sedighipoor, Synthesis, spectral identification, electrochemical behavior and theoretical investigation of new zinc complexes of bis((E) 3-(2-nitrophenyl)-2- propenal)propane-1,2-diimine, Spectrochim. Acta - Part A Mol. Biomol. Spectrosc. 96 (2012) 70–76. https://doi.org/10.1016/j.saa.2012.05.011.

[37] H. Bouraoui, A. Boudjada, N. Hamdouni, Y. Mechehoud, J. Meinnel, Crystal structure of 1,1'-[selanediylbis(4,1-phenylene)]bis(2-chloroethan-1-one), Acta Crystallogr. Sect. E Crystallogr. Commun. 71 (2015) o935–o936. https://doi.org/10.1107/S2056989015019969.

[38] M.C. Burla, R. Caliandro, B. Carrozzini, G.L. Cascarano, L. De Caro, C. Giacovazzo, G. Polidori, D. Siliqi, The revenge of the Patterson methods. I. Protein ab initio phasing, J. Appl. Crystallogr. 39 (2006) 527–535. https://doi.org/10.1107/S0021889806017894.

[39] L.J. Farrugia, WinGX and ORTEP for Windows: An update, J. Appl. Crystallogr. 45 (2012) 849–854. https://doi.org/10.1107/S0021889812029111.

[40] C.F. Macrae, I.J. Bruno, J.A. Chisholm, P.R. Edgington, P. McCabe, E. Pidcock, L. Rodriguez-Monge, R. Taylor, J. Van De Streek, P.A. Wood, Mercury CSD 2.0 - New features for the visualization and investigation of crystal structures, J. Appl. Crystallogr. 41 (2008) 466–470. https://doi.org/10.1107/S0021889807067908.

[41] L. Liu, D.Z. Jia, K.B. Yu, Synthesis, structure and photochromic properties of 4-acyl pyrazolone derivants, J. Photochem. Photobiol. A Chem. 154 (2003) 117–122. https://doi.org/10.1016/S1010-6030(02)00321-0.

[42] C. Arici, C. Ariel, M.N. Tahm, R.I.K. J, O.R.H. Atakol, 4-Chloro-2-(4-oxopent-2-en-2-ylamino)phenol, Acta CJ3"stallographica Sect. C 55 (1999) 1691–1692. https://doi.org/10.1107/S0108270199008501.

[43] M.A. Spackman, D. Jayatilaka, Hirshfeld surface analysis, CrystEngComm 11 (2009) 19–32. https://doi.org/10.1039/b818330a.

[44] S. Selvanandan, H. Anil kumar, H.T. Srinivasa, B.S. Palakshamurthy, Crystal structure and Hirshfeld surface analysis of 3-({4-[(4-cyanophenoxy)carbonyl]phenoxy}carbonyl)phenyl 4-(benzyloxy)-3-chlorobenzoate, Acta Crystallogr. Sect. E Crystallogr. Commun. 78 (2022) 989–992. https://doi.org/10.1107/s2056989022008441.

[45] M. Hanif, A. Noor, M. Muhammad, F. Ullah, M.N. Tahir, G.S. Khan, E. Khan, Complexes of 2-Amino-3-methylpyridine and 2-Amino-4-methylbenzothiazole with Ag(I) and Cu(II): Structure and Biological Applications, Inorganics 11 (2023). https://doi.org/10.3390/inorganics11040152.

[46] W. Maalej, R. Jaballi, A. Ben Rached, P. Guionneau, N. Daro, Z. Elaoud, Supramolecular architectures of mononuclear nickel(II) and homobinuclear copper(II) complexes with the 5,5′-dimethyl-2,2′-bipyridine ligand: Syntheses, crystal structures and Hirshfeld surface analyses, J. Mol. Struct. 1250 (2022). https://doi.org/10.1016/j.molstruc.2021.131728.

[47] U. Sathya, J.S. Nirmalram, S. Gomathi, D. Dhivya, S. Jegan Jennifer, I. Abdul Razak,

V. Jancik, A study of the crystal structures, supramolecular patterns and Hirshfeld surfaces of bromide salts of hypoxanthine and xanthine, Acta Crystallogr. Sect. E Crystallogr. Commun. 78 (2022) 652–659. https://doi.org/10.1107/S2056989022005278.

[48] M.J. Frisch, G.W. Trucks, H.B. Schlegel, G.E. Scuseria, M.A. Robb, J.R. Cheeseman, G. Scalmani, V. Barone, B. Mennucci, G.A. Petersson, Uranyl extraction by N, N-dialkylamide ligands studied by static and dynamic DFT simulations, Gaussian 9 (2009) 227.

[49] P. Geerlings, F. De Proft, W. Langenaeker, Conceptual density functional theory, Chem. Rev. 103 (2003) 1793–1873. https://doi.org/10.1021/cr990029p.

[50] T.A. Yousef, O.K. Alduaij, S.F. Ahmed, G.M. Abu El-Reash, O.A. El-Gammal, Semi- and thiosemicarbazide Mn(II) complexes: Characterization, DFT and biological studies, J. Mol. Struct. 1119 (2016) 351–364. https://doi.org/10.1016/j.molstruc.2016.04.033.

[51] R.A.A. Ammar, A.N.M.A. Alaghaz, A.A. Elhenawy, DFT, characterization and investigation of vibrational spectroscopy of 4-(4-hydroxy)-3-(2-pyrazine-2-carbonyl)hydrazonomethylphenyl-diazen-yl- benzenesulfonamide and its copper(II) complex, J. Mol. Struct. 1067 (2014) 94–103. https://doi.org/10.1016/j.molstruc.2014.02.051.

[52] N. Acar, C. Selçuki, E. Coşkun, DFT and TDDFT investigation of the Schiff base formed by tacrine and saccharin, J. Mol. Model. 23 (2017) 1–12.

[53] A. Chandrasekar, T.K. Ghanty, C.V.S. Brahmmananda Rao, M. Sundararajan, N. Sivaraman, Strong influence of weak hydrogen bonding on actinide-phosphonate complexation: Accurate predictions from DFT followed by experimental validation, Phys. Chem. Chem. Phys. 21 (2019) 5566–5577. https://doi.org/10.1039/c9cp00479c.

[54] A.V. Christophe Morell1 , José L. Gázquez2, 3, F. Guégan1, A. Henry, Chermette1, ., Revisiting Electroaccepting and Electrodonating Powers: proposals for Local electrophilicity and Local nucleophilicity descriptors, Am. Chem. Soc. (1999).

[55] N.N. Ma, G.C. Yang, S.L. Sun, C.G. Liu, Y.Q. Qiu, Computational study on second-order nonlinear optical (NLO) properties of a novel class of two-dimensional Λ-and W-shaped sandwich metallocarborane-containing chromophores, J. Organomet. Chem. 696 (2011) 2380–2387.

[56] R.M. El-Shishtawy, F. Borbone, Z.M. Al-Amshany, A. Tuzi, A. Barsella, A.M. Asiri, A. Roviello, Thiazole azo dyes with lateral donor branch: Synthesis, structure and second order NLO properties, Dye. Pigment. 96 (2013) 45–51.

[57] E. Yalçın, S. Achelle, Y. Bayrak, N. Seferoğlu, A. Barsella, Z. Seferoğlu, Styryl-based NLO chromophores: synthesis, spectroscopic properties, and theoretical calculations, Tetrahedron Lett. 56 (2015) 2586–2589.

[58] K. Hatua, P.K. Nandi, Theoretical study of electronic structure and third-order optical properties of beryllium–hydrocarbon complexes, Comput. Theor. Chem. 996 (2012) 82–90.

[59] A.T. Maynard, M. Huang, W.G. Rice, D.G. Covell, Reactivity of the HIV-1 nucleocapsid protein p7 zinc finger domains from the perspective of density-functional theory, Proc. Natl. Acad. Sci. 95 (1998) 11578–11583.

Chapter IV

Synthesis, characterization and biological study of E-4-((5-bromo-2-hydroxyhybenzylidene)amino)butanoic acid (H2L3)

And its transition metal complexes Cu(II), Mn(II).

Cu(II), Mn(II), Co(II) and Zn(II).

IV.1. INTRODUCTION

This chapter is dedicated to the non-symmetric bidented Schiff ligand E-4-((5-bromo-2-hydroxyhybenzylidene)amino)butanoic acid (H2L3) and the transition metal complexes that it binds to. To access the complexes of the relevant transition metals, copper (II) and manganese (II), we will first discuss the synthesis strategy of the non-symmetrical Schiff bases ligand (H2L3). Conventional spectroscopy techniques described in the Presidents Chapters were used to identify the synthesized products. A research on the biological assessment of the antioxidant capacity of synthetic compounds has been conducted.

PART I: SYNTHESIS AND CHARACTERIZATION

IV.2. Synthesis of E-4-((5-bromo-2-hydroxyhybenzylidene)amino)butanoic acid (H2L3)

The traditional procedure outlined in the literature [1] was used to manufacture the Schiff base ligand (H2L3). The following reaction represents the synthesis's reaction pattern:

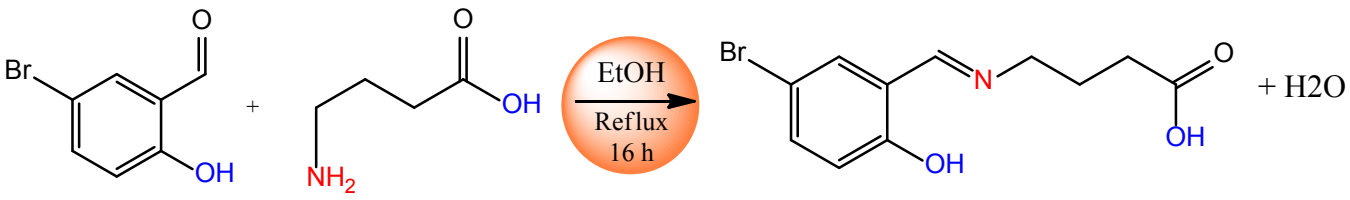

Scheme IV.1. Reaction pattern of ligand formation (H2L3).

Under nitrogen and magnetic agitation, 5-bromo-2-hydroxybenzaldehyde (0.2g; 1.31 mmol) is dissolved in 10 ml ethanol in a 50 ml Bicol flask. Once the mixture is well homogenized, a dropwise addition of 4-aminobutanoic acid (0.13g; 1.29 mmol) is made, and the mixture is refluxed for 24 hours. Thick layer chromatography (TLC) is used to monitor the reaction; ethyl acetate/petroleum ether (2/1) is the eluent, and a silica gel plate serves as the stationary phase. Yellow needles with Rdt=58.1% are produced when the reaction is finished, after the yellow solution is cooled and the residue is filtered and recrystallized in methanol. As seen below, the Schiff base ligand's whole synthesis process is represented:

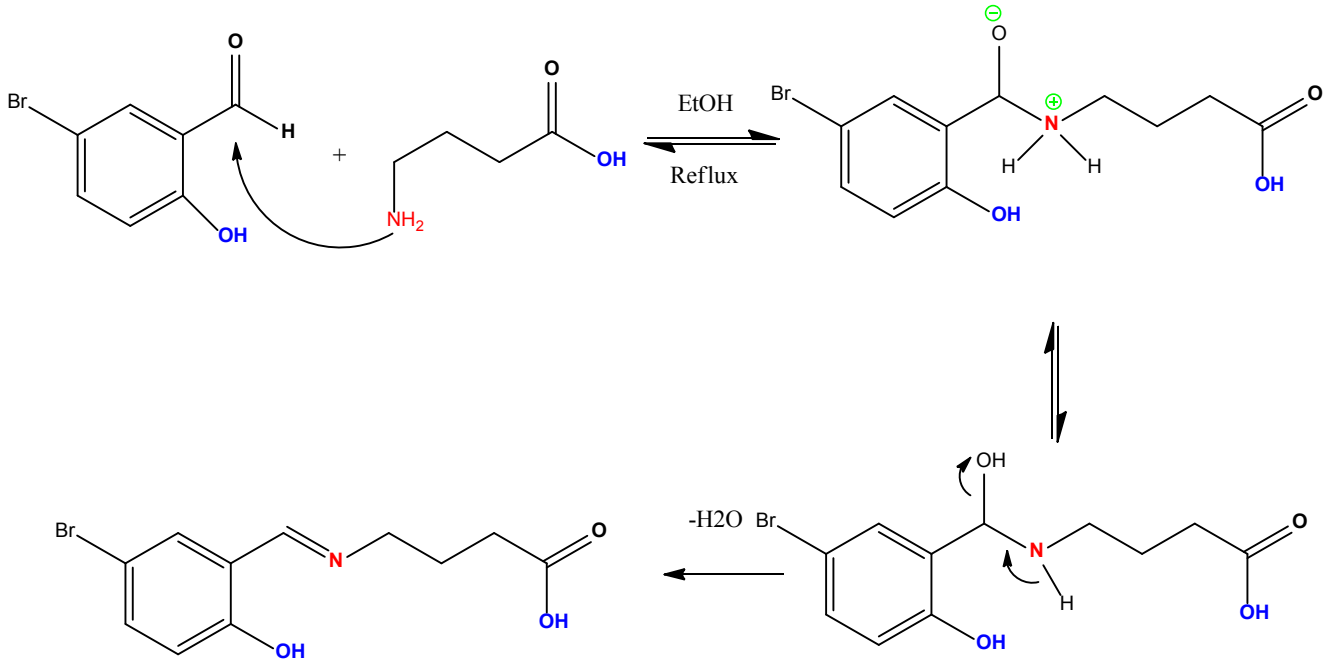

Scheme IV.2. Basic Schiff Synthesis Reaction Mechanism (H2L3).

IV.3. Synthesis of Mn(III) and Cu(II) complexes with ligand (H2L3)

The main reaction pattern of complex preparation is illustrated by the following reaction:

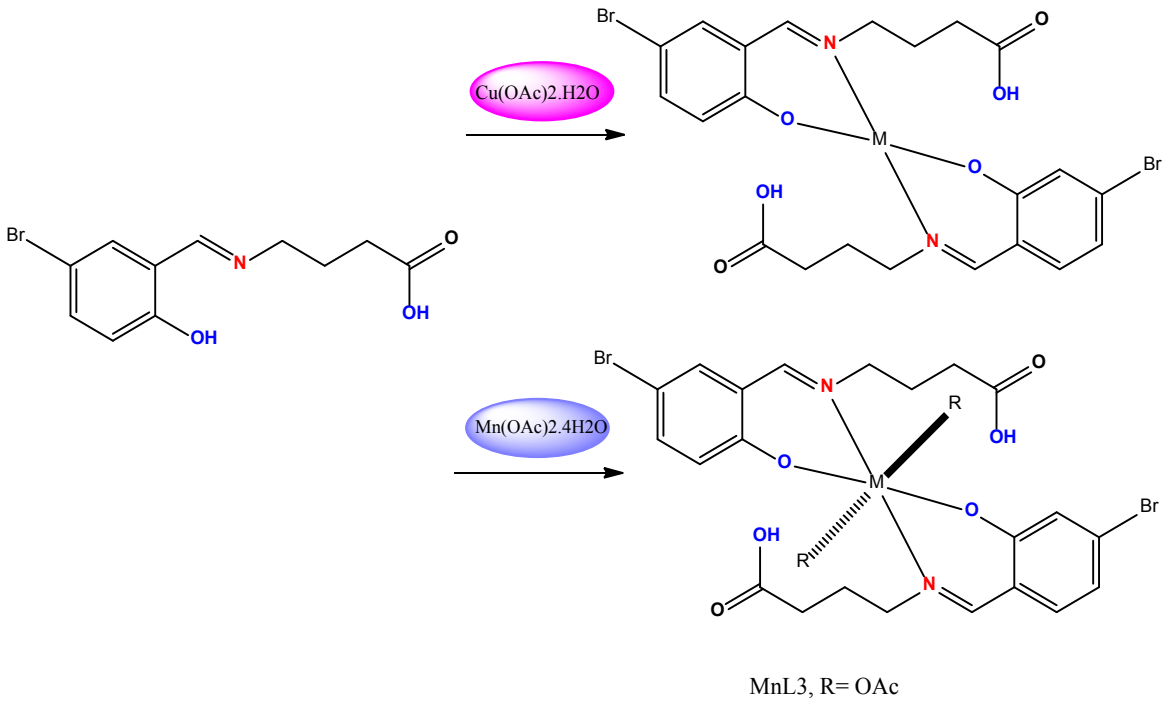

MnL3, R= OAc

Scheme IV.3: General ligand complexation reaction (H2L3).

IV. 3. 1. Manganese complex synthesis

An ethanoic ligand (H2L3) solution (0.2g; 0.842 mmol) is poured to a 50 ml Bicol flask capped with a refrigerant, and then drop by drop a methanoic solution of manganese acetate Mn (OAc)2.4H2O (0.1g; 0.421 mmol) is added [2,3]. Brown coloration quickly replaces the reaction medium's color. After 24 hours of reflux heating, the reaction mixture was cooled to room temperature. After filtering the source material, diethyl ether is used to wash the resulting solid. We were able to confirm the purity of the isolated complex and the reaction sequence by using CCM (SiO2, 1:1 ethyl ether acetate). Rtd is 77%.

IV. 3. 2. Synthesis of the Cuivric complex

A solution (0.084g, 0.421mmol) of the monohydrate metallic salt Cu(OAc)2.H2O is added to a 50 ml flask that already contains (0.2 g; 0.842 mmol) ligand (H2L3). Under agitation and in a nitrogen environment, the mixture is returned for three hours at a temperature of 75°C [1,4,5]. Filtration and diethyl ether washing follow the precipitate's cooling. A dark green powder with a 64.44% yield is the product that is isolated.

IV.4. Physical and analytical properties of ligand (H2L3) and its complexes

Once the ligand (H2L3) and its complexes were purified, their characterizations were carried out. Drying of complexes is carried out under vacuum for one night, are solid compounds, stable to air. The yield, the melting point are listed in Table IV.1.

Table IV.1. Physico-chemical characteristics of the ligand (H2L3) and its complexes.

Compound	**Color of the compound**	**Rdt (%)**	**Fusion point** °C	**Solvent Solubility**	**R_f (%)**
(H_2L3)	Yellow	**58.1**	**Tf=180**	Ethanol Methanol	67
Mn(II) L3	Brown	**77**	**Tf >260**	DMF	56
Cu(II) L3	Dark green	**64.4**	**Tf >260**	DMSO	82

IV. 5. Spectroscopic characterizations of ligand (H2L3) and its complexes

IV.5.1. UV-Visible Absorption Spectrophotometry Analysis

The electron spectra of the Schiff base ligand (H2L3) and its complexes were realized between 200 and 800 nm, at room temperature, in methanol with a concentration of 10-3M. Table IV. 2 below groups the absorption bands of the compounds synthesized in this chapter.

Table IV.2. UV-Vis ligand (H2L3) absorption bands and its complexes.

Compound	λmax (nm)	Transition
(H_2L3)	260	π → π*
	333	π → π*
	418	n → π*
Mn(II) L3	233	π → π*
	275	n → π*
	366	LMCT
Cu(II) L3	234	π → π*
	272	n → π*
	368	LMCT

As seen in Figure (IV.1) below, the ligand spectrum (H2L3) yields three bands at 260, 333, and 418 nm, which correspond to the transition π → π*of the aromatic group and the azomethine function, respectively [2].

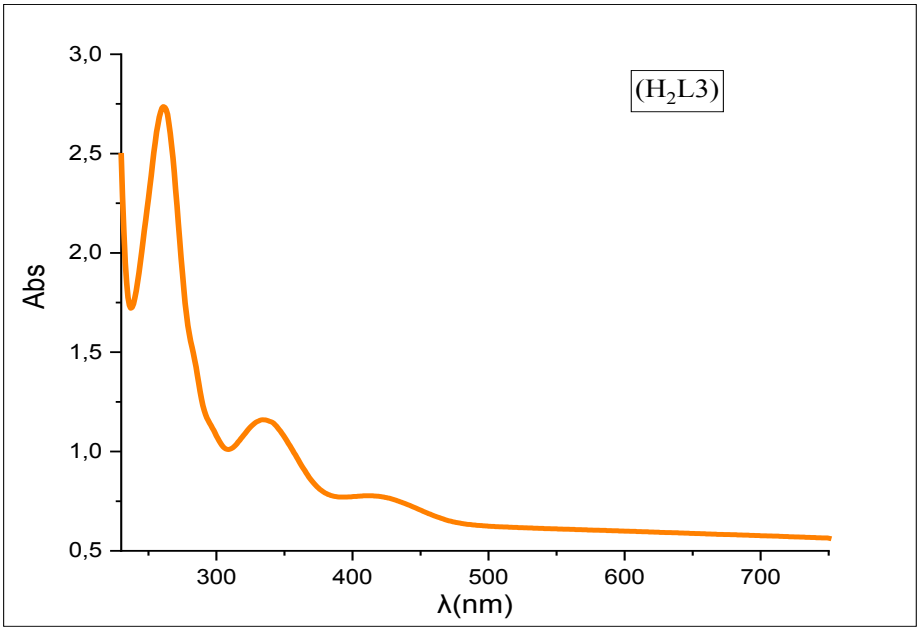

Figure IV.1. UV-Visible Spectrum of ligand (H2L3) in DMF.

Due to their comparable structures, the complexes' electron absorption spectrum data are quite similar. The complexes show a hypsochrome shift with respect to their ligand, which greatly enhances the development of coordination bonds between the ligand and the metal in the complexes. The π→ π* transitions of azomethine (CH═ N) chromophores are responsible for the strong bands at 233 and 234 nm for the Mn(II)L3 and Cu(II)L3 complexes, respectively [1,2].

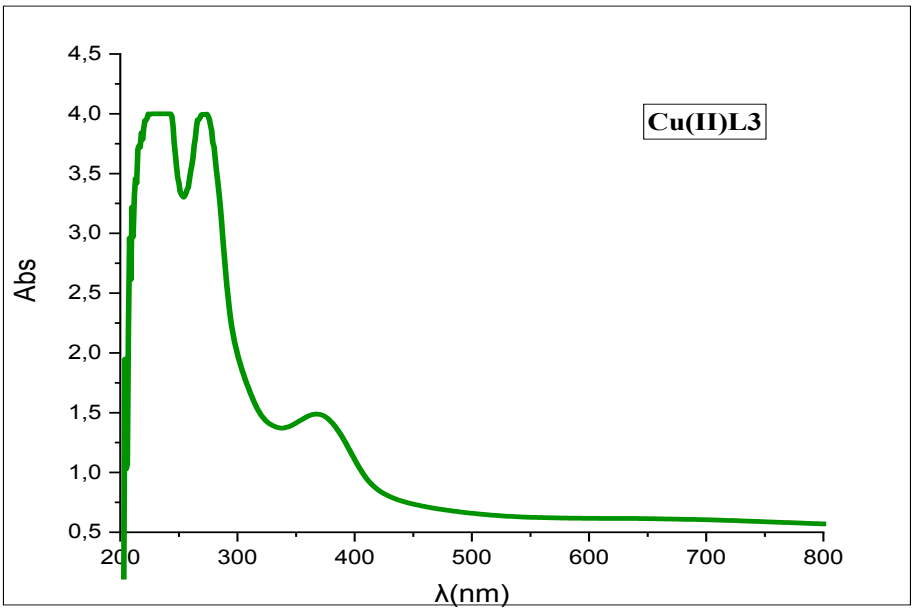

Figure IV.2. UV-Visible Spectrum of Cu(II)L3 in DMF.

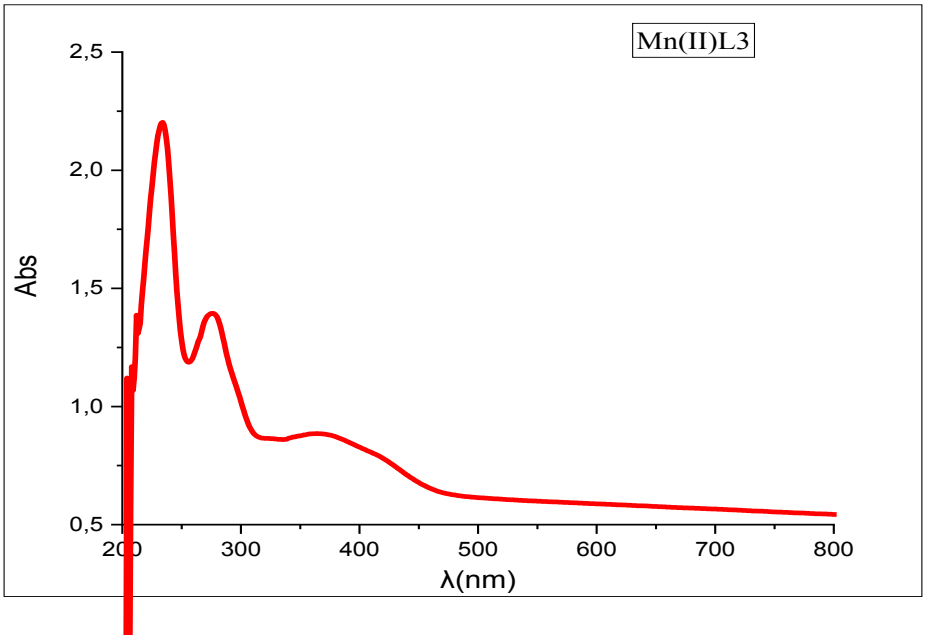

Figure V.3. Mn(II)L3 UV-Visible Spectrum in DMF .

Electronic transitions n→π* are responsible for the bands that arise at 275 and 272 nm, which are more intense than the first ones. The remaining bands at 366 and 368 nm are linked to the O(p)/M(d) metal-ligand charge transfer phenomenon in LMCT [4,6]. d-d transitions were hidden by the intra-ligand charge transfer and transition bands, which prevented their observation.

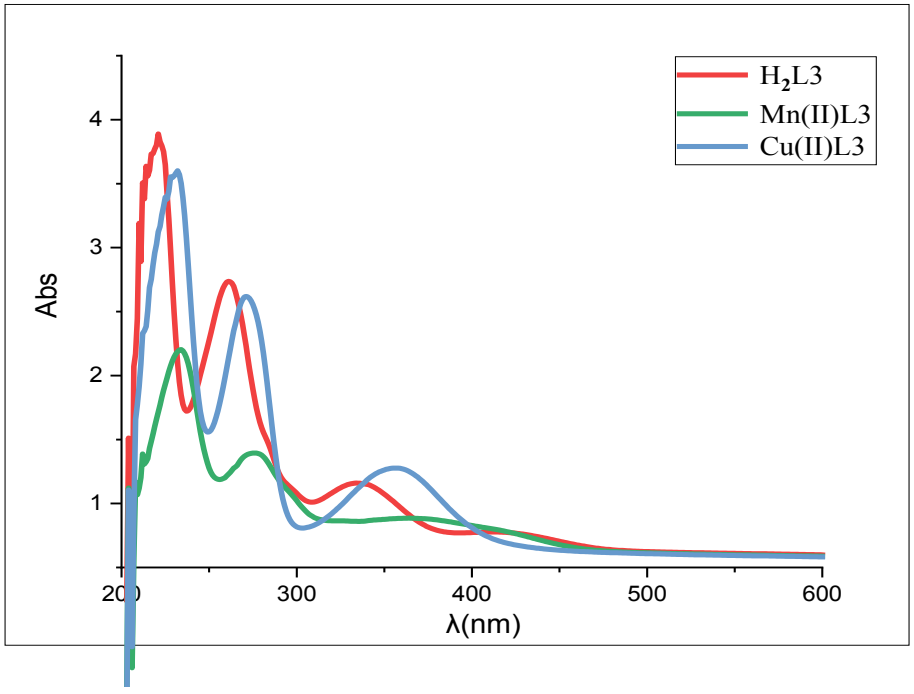

Figure IV.4. UV-Visible Spectrum of (H2L3) and its corresponding complexes in DMF

The electronic spectra give a confirmation as to the modes of coordination of the metals with the NNOO atoms and this for all the complexes.

IV.5.2. Infrared absorption spectrophotometry (IR) analysis

The IR spectra of the complexes are interpreted and compared to this of the corresponding ligand (H2L3). These spectra allowed us to determine the coordination sites. Table IV.3 presents the most important elongation vibrations of the functional groups constituting the molecular structures.

Table IV.3. Main bands of ligand (H2L3) IR vibration and its complexes.

Compound	Infrared ν (cm-1)						
	ν(O-H)	ν(C=N)	ν(C=C)	ν(C-O)	ν(C=O)$_{Acide}$	ν(M-O)	ν(M-N)
(H_2L3)	3424	1645	1503	1191	2929	/	/
Cu(II)L3	3418	1618	1469	1252	2936	743	675
Mn(II)L3	3418	1564	1537	1225	2922	743	661

The bands corresponding to the hydroxyl and azomethine groups are among the most significant ones to notice that define the various Schiff bases (Figure IV.5).

The elongation vibrations of the hydroxyl group and acid O-H are responsible for the broad band in the ligand's infrared spectra that is centered at 3424 cm-1 [7–9]. Cu(II)L3 and Mn(II)L3 exhibit elongation bands of the O-H group of the acid function at 3418 cm-1, respectively, for the complexes [10,11].

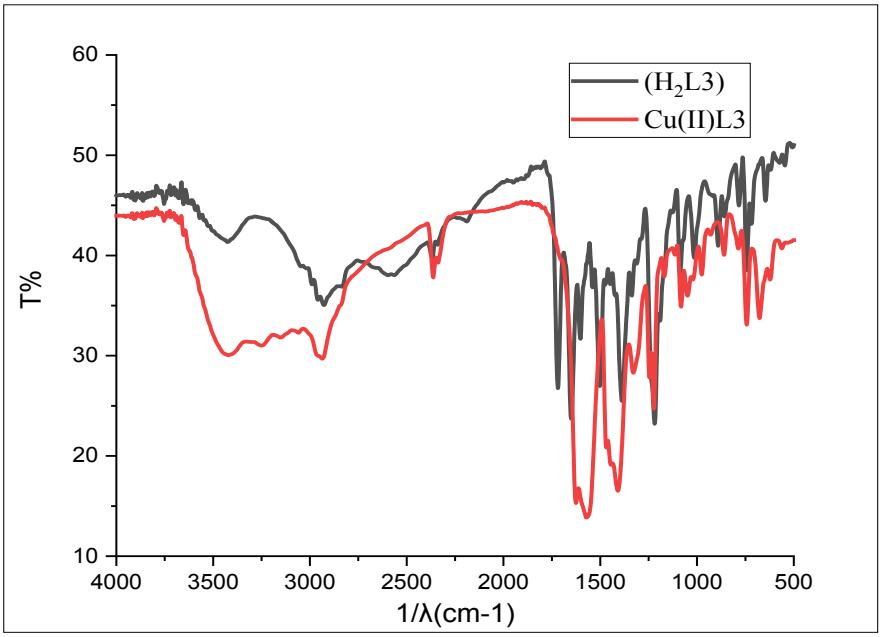

Figure IV.5. IR spectrum of Cu(II)L3 in KBr.

Cu(II)L3 and Mn(II)L3 have sharp and strong bands at 1618 and 1564 cm-1, respectively, that are indicative of the valence vibrations of these imine functions [12]. values are less than the ligand's measured value of 1645 cm-1, a bathochrome displacement is generated, confirming complexation [13,14]

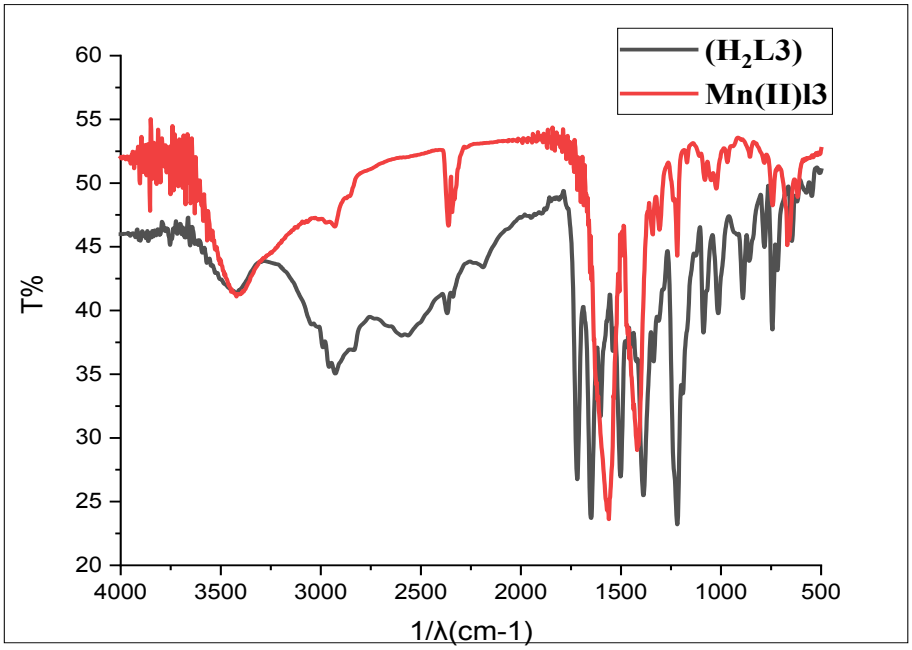

Figure IV.6. IR spectrum OF Mn(II)L3 in KBr.

It was found that the phenolic C─ O elongation vibration band in the ligand (H2L3) was around 1191 cm-1. A shift in hypsochromic equilibrium is seen in the complicated series (in the preceding sequence). As the C─O elongation vibration band of the acid group is not involved in complexation, it is located in the vicinity of 1218 cm-1 for ligand and its complexes. This band appears at a higher frequency of 1252, 1225 cm-1, confirming the participation of the phenolic group in the formation of the complex [15].

The valence vibration of the double bonds C═C of the aromatic cycles is responsible for the band that appears in the ligand and its complexes in the interval of 1400–1570 cm–1 [16].

Acute and strong bands, seen at 1720 cm-1 for the ligand and 1564, 1421 cm-1 for the metal complexes, describe the valence vibrations of the carbonyl C═ O functions of the carboxyl group. Mn(II)L3, Cu(II)L3, and so forth The acid group O–H is responsible for the broad band that appears at 2929 cm-1 for the ligand and 2936, 2922 cm-1 for its complexes.

Furthermore, in the spectra of the metal complexes, additional bands are observed between 641 and 743 cm -1, which are ascribed to the vibrations of the M—O and M—N bonds, respectively [17]. These bands are not present in the spectra of the ligands.

IV.5.3. Proton (^{1}H NMR) Nuclear Magnetic Resonance Spectroscopy

A structural analysis on the ligand (H2L3) was performed by nuclear magnetic resonance of the proton on a Bruker 300P MHz spectrometer, using the deuterated MeOH as solvent, and in the presence of TMS as reference.

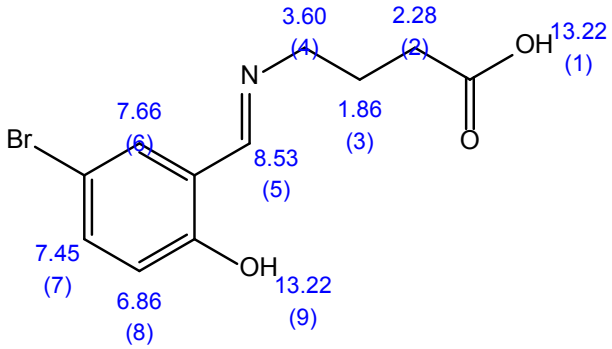

The H1 NMR spectrum of the ligand shows the different values of the chemical displacements. The proton signal of the hydroxyl group O-H(H9) and the acid group (H1) [2] is observed at δ= 13.22 ppm . the signals of the aromatic protons appear as two doubled to δ= 7.45 ppm which corresponds to the proton (H7) and to δ= 6.86ppm which corresponds to the proton (H8) and a singlet at δ= 7.66 ppm which corresponds to the protons (H6)[1].

Hydrogen from the imine group H C N (H5) [4] appears as a singlet at 8.53 ppm and two triplets at 2.28 and 3.60 ppm and a multiplet at 1.86 ppm each corresponding to two protons (H2), (H4), and (H3) respectively [2,6]. The integral curves are in agreement with the number of protons in this structure, which of course confirms the proposed structure of the synthesized compound.

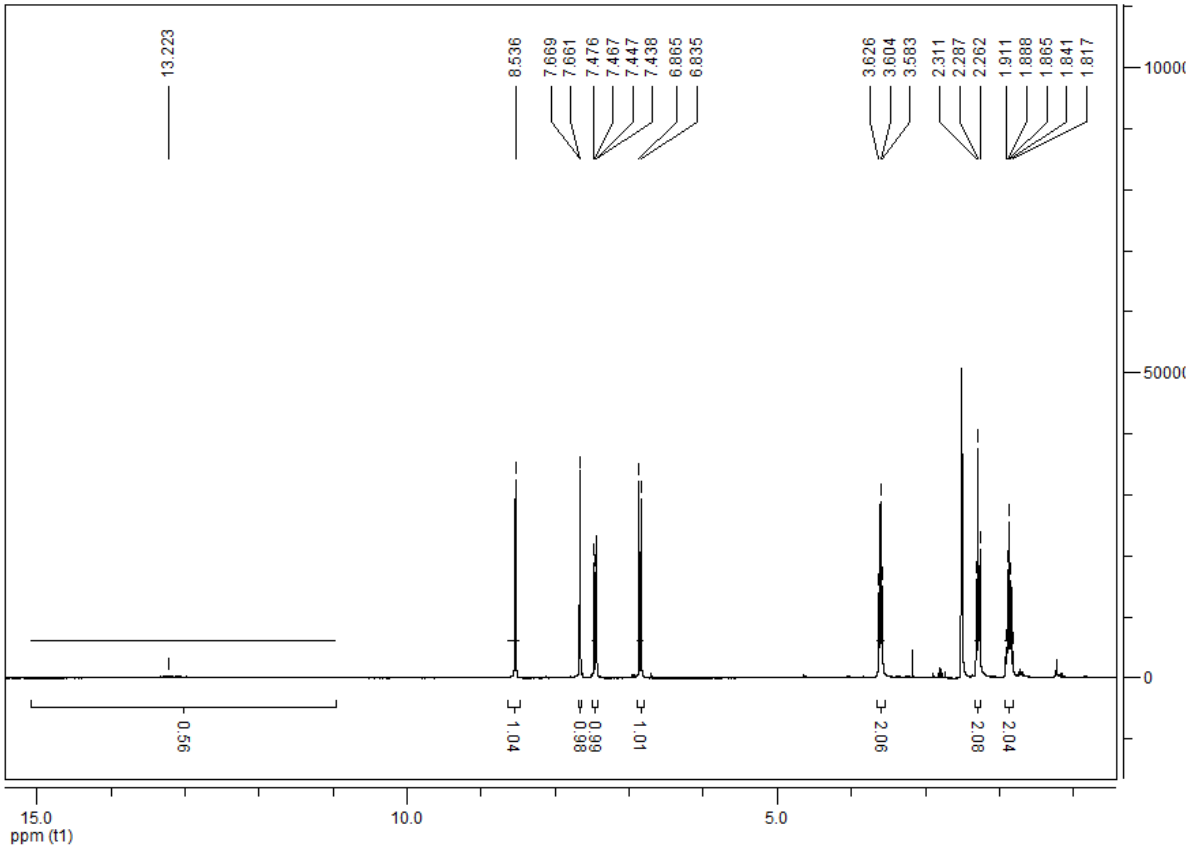

Figure IV.7. ^{1}H-NMR spectrum in MeOH of (H2L3)

IV.6. Study of electrochemical behavior by cyclic voltammetry of ligand (H2L3) and its metal complexes

In this part of the research work, we present the electrochemical behavior of synthesized Schiff base ligand(H2L3) and its metal complexes. The study is carried out by platinum electrode cyclic voltammetry in di methyl sulfoxide (DMSO), in the presence of Tetraethylammoni-umTetrafluoroborate (C2H5)4NBF4 0.1 M over a potential range from +2000 to -2000 mV/ECS with a scanning speed of 100 mV/s. Potentials are measured against a saturated calo-mel reference electrode (ECS) in the presence of a vitreous carbon auxiliary electrode.

Table IV.4. The electrochemical properties of ligand (H2L3) and its complexes were investigated by cyclic voltammetry in DMF

Compound	Electrochemical parameters	
	Epc (V)	Epa (V)
H2L3	-0.820 -1.45	+0.703
Mn(II)L3	-1.263 -1.422	/
Cu(II)L3	-0.752 -1.235	+0.971

IV.6.1. Ligand electrochemical behavior (H2L3)

The cyclic redox voltammogram of a studied Schiff base solution (H2L3) shown in figure (IV.8) shows an anodic peak at Epa1 = +0.709 V/ECS corresponding to oxidation of the phenolic group OH[7].

At the cathode scan, two peaks are observed at Epc= -0.820 and -1.458 V/ECS which are due to reduction to azomethine group reduction [8,13].

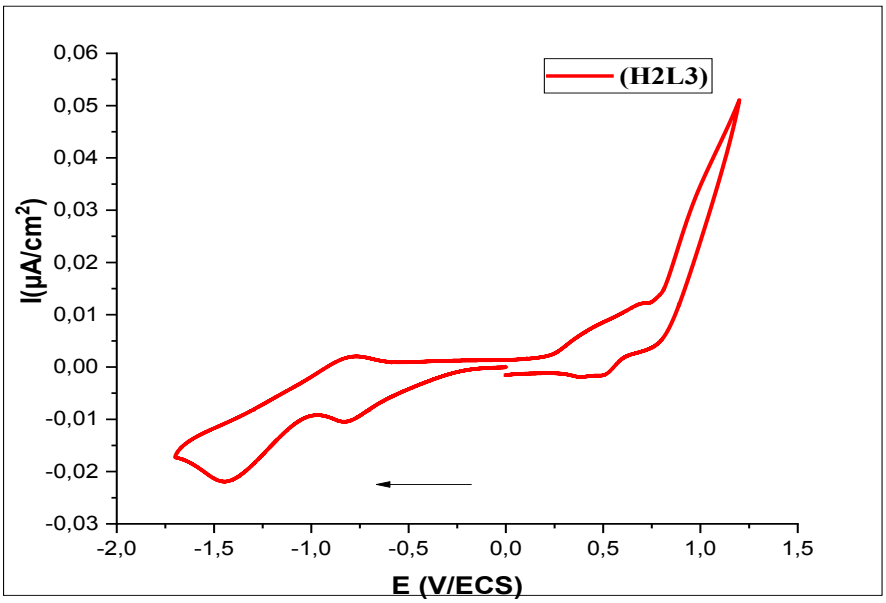

Figure IV.8. Cyclic Ligand Voltammetry (H2L3)(10-2M) in DMSO+(C2H5)4NBF4 (10-1M) under nitrogen atmosphere at a scanning speed of 100 mV/s.

IV.6.2. Electrochemical behavior of Schiff metal-base complexes (H2L3)

IV.6.2.1. Manganese complex

The manganese complex voltammogram, collected at a scanning speed V=100 mV/s between -2000 and +1500 mV/ECS, is displayed in Figure (IV.9). The voltammogram displays two reduction peaks at Epc1 = -1.263 and Epc2 = -1.422 V/ECS. The reduction of Mn(II) to Mn(I) is responsible for the first peak [18–20], while the reduction of the imine function is responsible for the second peak [9].

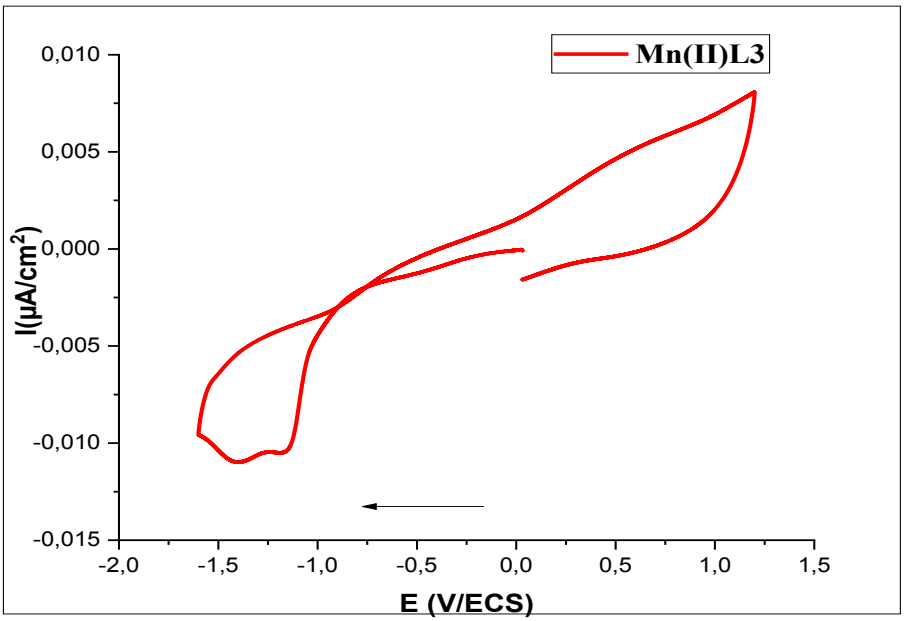

Figure IV.9. Mn (II)L3(10-2M) Cyclic Voltammetry in DMSO+(C2H5)4NBF4 (10-1M) under nitrogen atmosphere at a scanning speed of 100 mV/s.

IV.6.2.2. Copper Complex

The electrochemical behavior of the Cu(II)L3 complex is presented by the voltammetry of figure IV.10 below.

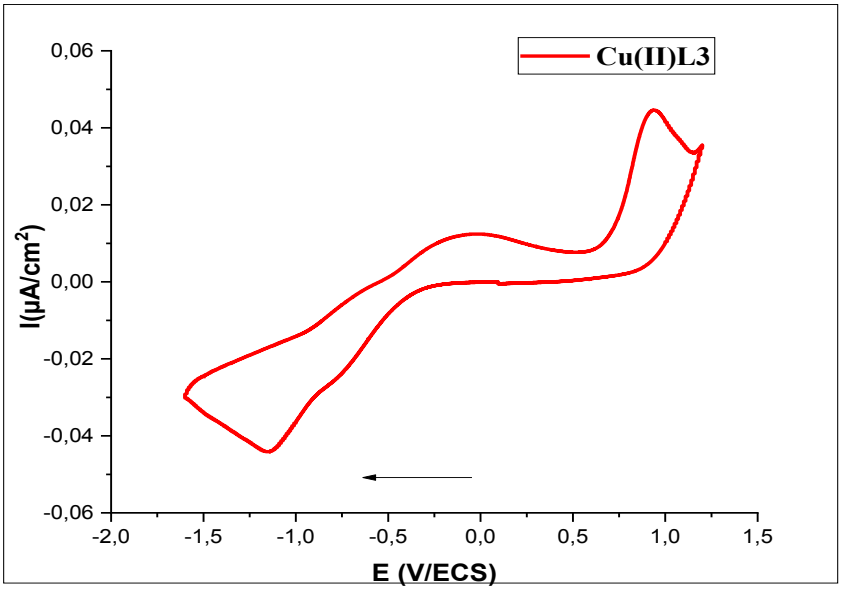

Figure IV.10. Cu(II)L3(10-2M) cyclic voltammogram in DMSO+(C2H5)4NBF4 (10-1M) under nitrogen atmosphere at a scanning speed of 100 mV/s.

The transfer of copper Cu(II) to Cu(III) is linked to a reduction peak at Epc1 = -0.752 V/ECS during acquisition [21], and the reduction of imines functions is responsible for a peak at Epc2 = -1.235 V/ECS [8,9,11]. This complex's cyclic voltammogram likewise exhibits a peak at +0.971 V/ECS of ligand entity oxidation [10].

IV.7. CRYSTALLOGRAPHIC STUDY OF SINGLE CRYSTALS

For certain compounds, we were able to get single crystals out of all the syntheses that were carried out. We were able to determine their molecular structure by X-ray diffraction (XRD) after obtaining a single crystal. This allowed us to determine the geometry of their molecular structures, the configurational isomeria of their Schiff base ligand upon complexation, and the characteristics of the coordinating atoms. In this section, the crystal structures of the copper complex Cu(II)L3 and the ligand H2L3 were examined.

the recording, resolution and refinement of structures are well detailed in the Presiding chapter.

IV.7.1. Crystallographic characterization of ligand (H2L3)

The ligand (H2L3) was crystallized after three days in a test tube by diffusion of diethyl ether in methanol at room temperature. The structure crystallizes in an Orthorhombic Pbcn space group system (α = γ = γ = 90°). The mesh contains 8 ligand molecules that occupy a volume of 2342.09 Å3/mesh. It should be noted that the absorption coefficient, μ = 3.50 mm-1, is high because of the presence of two bromine atoms that absorb X-rays.

X-ray diffraction on the single crystal reveals that the ligand (H2L3) responds to the molecular formula C11H12BrNO3. Table IV.5 presents the main crystalline parameters of the structure. The following figure describes the crystalline structure of the ligand (H2L3)

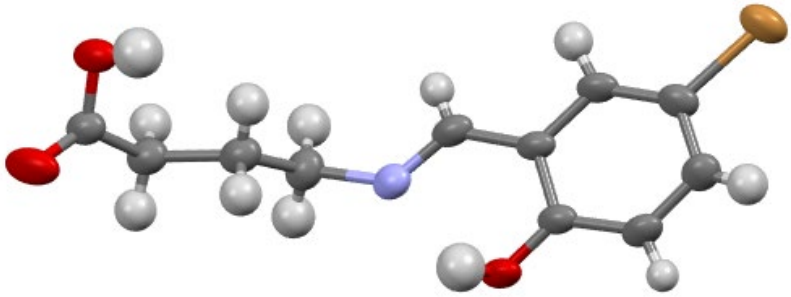

Figure IV.11. Molecule representation (H2L3).

Table IV.5. Ligand Crystallographic Data (H2L3).

Molecular formula	$C_{11}H_{12}BrNO_3$
Molecular weight	286.13
Temperature (K)	298(2)
Radiation λ (Å)	0.71073
Crystal system	Orthorhombic
Space group	*Pbcn*
a/Å	10.9154(2),
b/ Å	13.0463(3)
c/ Å	16.4466(4)
α/ °	90
β/ °	90
γ/ °	90

V/Å^3	2342.09 (9)
Z	8
Calculated density (mg cm^{-3})	1.623
Absorption coefficient (mm^{-1})	3.50
F(0 0 0)	1152
Reflections measured/independent	44375, 4477 [R(int) = 0.0413]
Range/indices (h, k, l)	***h***= −20→20, ***k*** = −16→16, ***l*** = −25→25
Theta range for data collection (°)	2.509 to 30.517
Completeness to theta = 25.242	100 %
Refinement method	Full-matrix least-squares on F^2
Data / restraints / parameters	44375 / 0 / 157
Goodness of fit on F^2	1.065
Final R indices (all data)	R1 = 0.0807, wR2 = 0.1845
Extinction coefficient	n/a
Largest diff. peak and hole (e.A^{-3})	1.066 and -0.802

IV.7.1.1. Links and angles

An asymmetrical view of the studied Schiff base ligand (H2L3) unit with the atom selective numbering scheme is shown in Figure IV.12 Some distances and selected bonding angles are listed in Table IV.6.

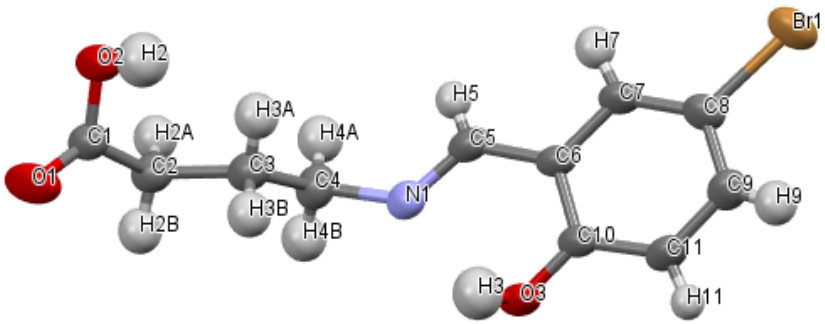

Figure IV.12. Ligand crystal structure (H2L3) with numbering.

Table IV.6. Ligand bond lengths and angles (H2L3).

Distances (Å)		Angles (°)	
C1-C2	1.432(4)	C3-C4-N1	113.9(3)
C2-C3	1.791(5)	N1-C5-C6	133.3(2)
C3-C4	1.429(4)	C7-C6-C5	130.2(2)
C4-N1	1.695(5)	C10-C6-C5	119.2(3)
C5-N1	1.418(5)	C10-C6-C7	110.6(3)
C5-C6	1.652(5)	C6-C7-C8	130.9(2)
C6-C7	1.513(4)	C7-C8-Br1	131.24(18)
C7-C8	1.585(5)	C9-C8-Br1	108.3(3)
C8-C9	1.316(4)	C9-C8-C7	120.4(3)
C9-C11	1.478(5)	C8-C9-C11	109.9(3)
C11-C10	1.657(5)	O3-C10-C11	132.2(2)
C10-C6	1.340(3)	C6-C10-O3	111.0(3)
C10-O3	1.396(4)	C6-C10-C11	116.8(3)
C8-Br1	2.035(3)	C9-C11-C10	131.4(2)
C1-O1	1.141(4)	C3-C4-N1	113.9(3)
C1-O2	1.328(3)	C5 N1 C4	135.3(2)
		O1-C1-O2	124.5(3)
		O1-C1-C2	119.4(3)
		O2-C1-C2	116.0(3)
		C1-C2-C3	111.6(3)
		C4-C3-C2	112.7(3)

IV.7.1.2. Intermolecular interactions

The lengths and angles of the intermolecular hydrogen bonds are collected in Table IV.6 This bond is defined by three variables: Hydrogen donor distance: D- H. The acceptor hydrogen interaction: H…A. The acceptor hydrogen donor angle: D- H… A. There is a relationship between the interaction H…A and the angle D -H… A; the stronger the interaction H…A the stronger the angle D- H… A is large and the lower the hydrogen bond the smaller the angle. These types of hydrogen bonds can be intramolecular when the donor and acceptor are part of the same molecule and intermolecular when they are part of two different molecules.

Table IV.7. Angles (°) of the intermolecular hydrogen bonds of the Cu(II)L3 complex.

D-H…A	D-H(Å)	H...A(Å)	D...A (Å)	D-H...A (°)
C5-H5…O1^{iii}	0.78(4)	2.448	3.077(3)	138.84
C7-H7…O1^{iii}	0.92(4)	2.658	3.488(3)	150.24
C9-H9…O3^{ii}	0.9300	2.561	3.296(3)	136.24
C11-H11…Br1^{i}	0.85(3)	3.005	3.58(3)	126.34
C3-H3B…Cg1^{iv}	0.9700	2.606	3.345(3)	133.12
Symmetry code*: (i) ½+x, ½-y,1-z; (ii) 3/2+x,-1/2+y,z; (iii)) -½+x, -½+y,1/2+z ; (iv) 3/2-x,1/2+y,z*				

IV.7.1.3. Elementary cell

The ligand (H2L3) elementary cell is seen in Figure IV.13 below, with a volume of 2342.09 Å 3/cell. There is one molecule in the asymmetric unit and eight molecules per (Z=8) in the mesh.

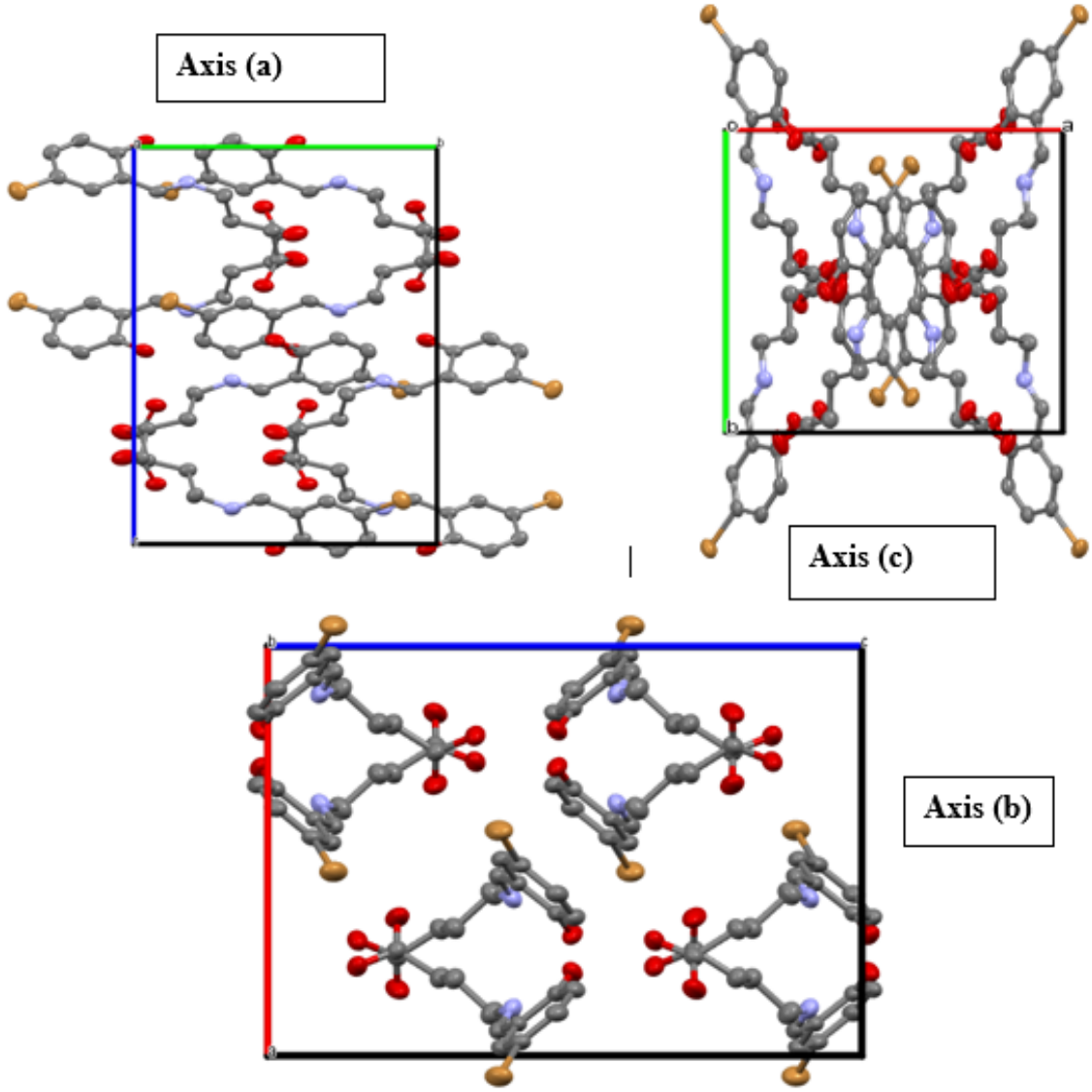

Figure IV.13. Projection of the elementary cell of (H2L3) along the three crystallographic axes a, b and c.

The unit cell being centrosymmetric, characterized by an inversion point in the center O at [0, 0, 0],with three screw axis 2 times in the direction [1, 0, 0], [0, 1, 0] and [0, 0, 1] to (x, ¼,0), (0, y, ¼) and (¼, 0, z) with the screw components [½,0, 0], [0, ½, 0], [0,0 , ½] and three sliding planes perpendicular to planes [1, 0, 0], [0, 1, 0] and [0, 0, 0, 1] with sliding components [0, ½ ,0],[0, 0, ½] and [½,½, 0] respectively.

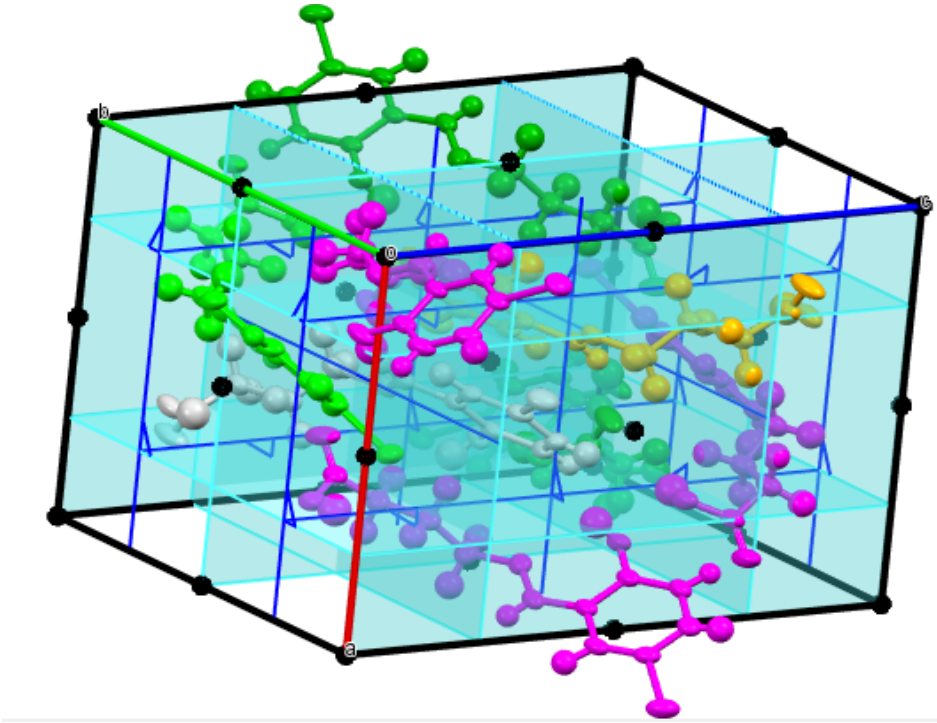

Figure IV.14. Mesh in a plane, b c of ligand (H2L3) with symmetry elements.

IV.7.1.4. Crystal lattice

Figure IV.15 shows a projection of the ligand lattice (H2L3) along the three axes (a), (b) and (c), the atoms are ordered to form parallel lines for each group of identical atoms. The crystalline lattice of this compound shows us that the crystalline system is formed by stacking parallel lines.

In the c plane, the molecules of the crystalline network adopt an alternate parallel shape by creating tunnels inside the network. In the b plane, a form also alternate and ordered. The adjacent molecules adopt in the case of the plane has an alternate zigzag shape

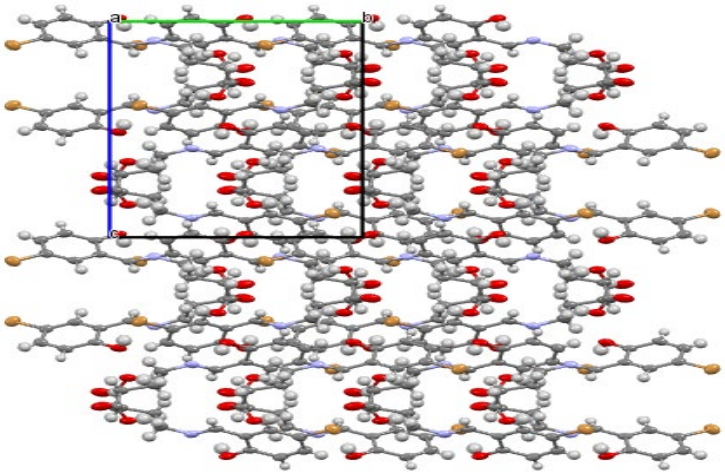

(a) [100]

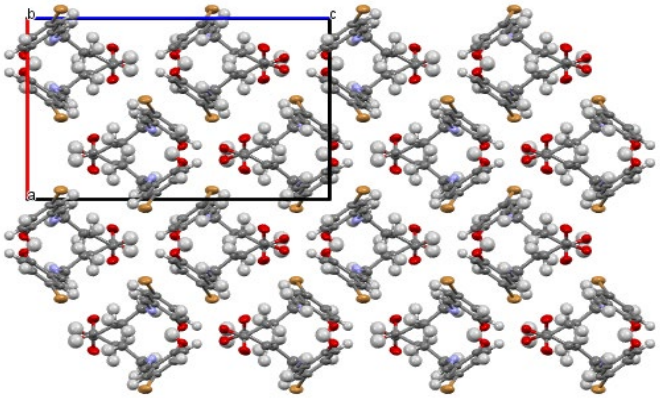

(b) [010]

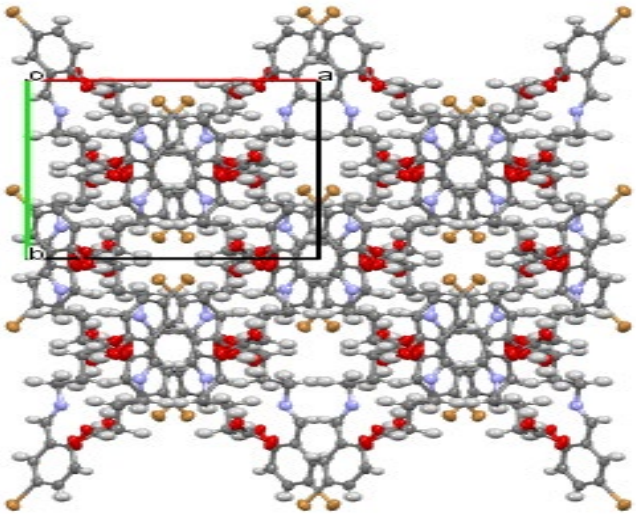

(c) [001]

Figure IV.15. Molecular crystalline stack of (H2L3) in three crystallographic planes: (a) [100], (b) [010] and (c) [001].

IV.7.2. Crystallographic characterization of the Cu(II)L3 complex

The Cu(II)L3 complex crystallizes in a monoclinic system having the space group P21/c or Z = 2 (Z: numer of patterns per mesh) with a structure is centrosymmetric. The mesh parameters are : a =8.2370(6)Å, b =11.960(1) Å , c =11.850(1) Å , $\alpha = \gamma = 90.00°$, β=96.697(3)°. The following figure (IV.16) shows the perspective representation of the Cu(II)L3 mononuclear complex. The main crystalline parameters of the structure are shown in Table IV.8.

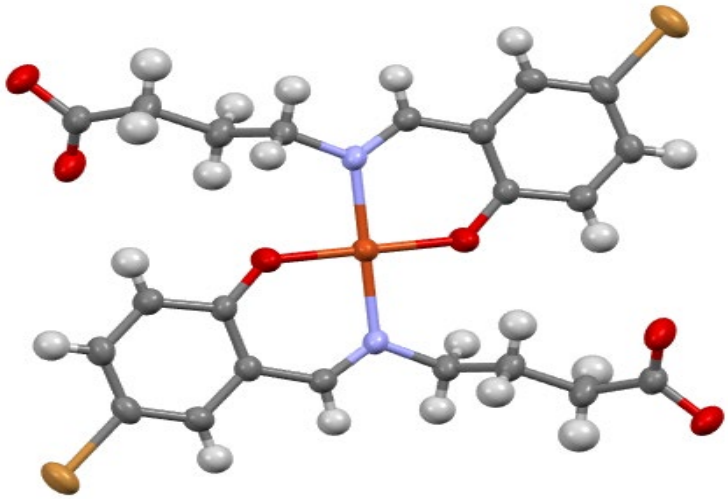

Figure IV.16. Perspective representation of the molecule Cu(II)L3.

Table IV.8. Crystallographic data of the Cu(II)L3 complex.

Molecular formula	$C_{22}H_{20}Br_2CuN_2O_6$
Molecular weight	638.97
Temperature (K)	298(2)
Radiation λ (Å)	0.71073
Crystal system	Monoclinic
Space group	*P21/n*
a/Å	8.2370(6)
b/ Å	11.960(1)
c/ Å	11.850(1)
α/ °	90
β/ °	96.697(3)
γ/ °	90
V/Å^3	1159.47(16)
Z	2
Calculated density (mg cm^{-3})	1.83
Absorption coefficient (mm^{-1})	3.63
F(0 0 0)	637
Reflections measured/independent	44375, 4477 [R(int) = 0.0925]
Range/indices (h, k, l)	$\boldsymbol{h}$= −11→10, $\boldsymbol{k}$ = −17→17, $\boldsymbol{l}$ = −16→16
Theta range for data collection (°)	3.331 to 30.590
Completeness to theta = 25.242	99.1 %
Refinement method	Full-matrix least-squares on F^2
Data / restraints / parameters	3535/ 0 / 151
Goodness of fit on F^2	1.018
Final R indices (all data)	R1 = 0.0740, wR2 = 0.1185
Extinction coefficient	n/a
Largest diff. peak and hole (e.A^{-3})	0.663 and -0.937

IV.7.2.1. Polyhedron of coordination

Table IV.9 summarizes the lengths of the interatomic bonds and the angles surrounding the metallic center Cu. The structure of the Cu(II)L3 complex reveals that copper is tetracoordinated, the coordination of the nickel atom is ensured between the two oxygens (O1 and O2) and

the two azotes (N1 and N2) of the Schiff base (N2O2) in a configuration, these atoms constitute the equatorial plane of the polyhedron, which gives copper a square plane geometry.

Table IV.9. Interatomic distances and Cu(II)L3 complex bond angles.

Distances (Å)		**Angles (°)**	
Cu1-O1	2.397(5)	O1-Cu2-O1^{i}	180.00(10)
Cu1-O2	2.029(4)	O1-Cu2-N1^{i}	89.19(10)
Cu1-O3	1.869(4)	O1^{i} -Cu2-N1	89.19(10)
Cu1-O4	1.855(4)	O1-Cu2-N1	90.81(10)
Cu1-N1	2.161(5)	O1^{i}-Cu2-N1	90.81(10)
Cu1-N2	2.060(4)	N1-Cu2-N1	180.0
Symmetry code: (i)1-x,1-y,1-z			

IV.7.2.2. Intermolecular interactions

Two kinds of intermolecular hydrogen bonding are seen in the Cu(II)L3 complex crystal: C—H….O and C—H….H. Figure IV.17 shows how mild these relationships are. Table IV.10 below provides a summary of the atoms' lengths, angles, and types of bonds involved in these intermolecular interactions.

Table IV.10. Lengths (Å) and angles (°) of Cu(II)L3 intermolecular hydrogen bonds.

D-H…A	**D-H(Å)**	**H...A(Å)**	**D...A (Å)**	**D-H...A (°)**
C7-H7…O2^{ii}	0.9300	2.641	3.55(2)	165.76
C10-H10A^{iii}...*Cg*1	0.9700	3.116	3.55	108.83
Symmetry code*: (ii) -1+x, y, z, (iii) ½+x,1/2-y, ½+z*				

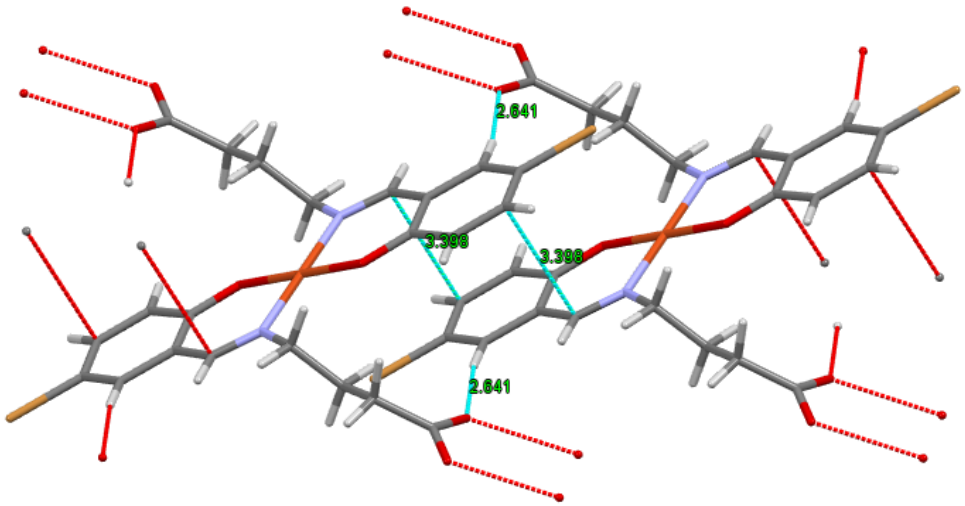

Figure IV.17. Representation of the intermolecular interaction in the Cu(II)L3 crystal.

IV.7.2.3. Elementary cell

Figure IV.18 below shows the elementary cell of the Cu(II)L3 complex occupying a volume of 1159.47Å 3/cell. The asymmetric unit contains a single molecule and the mesh contains two molecules per (Z=2).

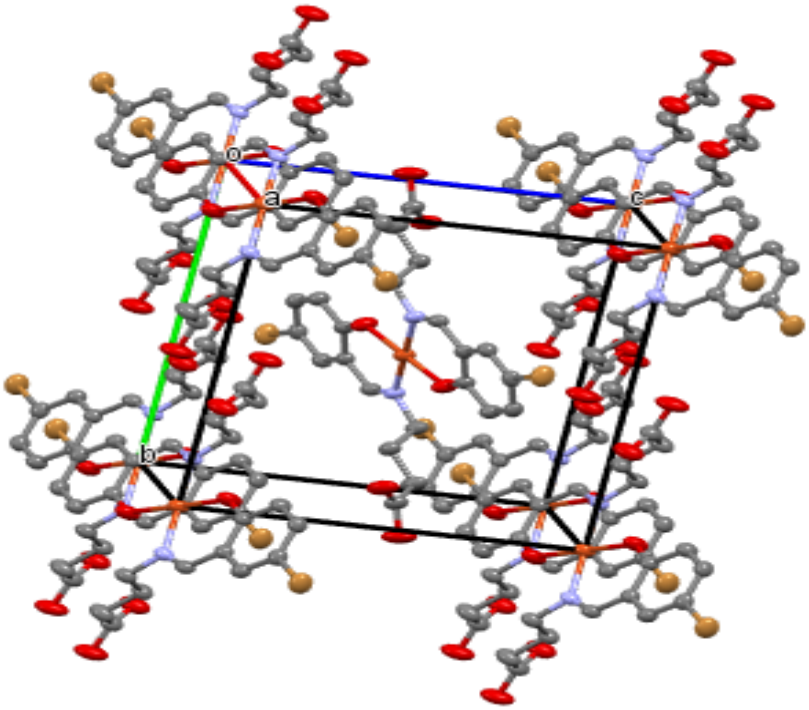

Figure IV.18. Representation of the mesh with axes a, b and c

The unit cell being centrosymmetric, characterized by an inversion point in the center O at [0, 0, 0], screw axis 2 times in the direction [0, 1, 0] at ¼, y, ¼ with screw components [0, ½, 0] and a sliding plane perpendicular to the plane [0 1 0] with sliding components [½, 0, ½] as shown in Figure IV.19 below.

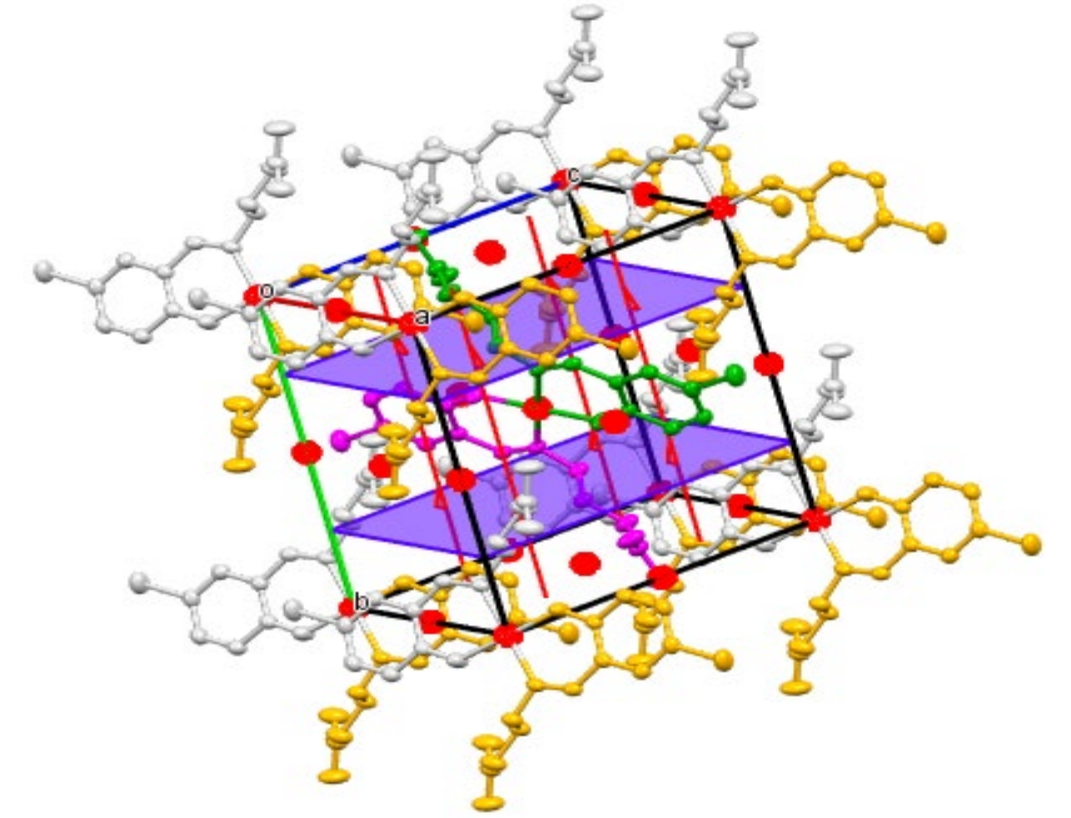

Figure IV.19. Mesh in plane a, b c of Cu (II)L3 complex with symmetry elements.

IV.7.2.4. Crystalline lattice

The crystalline lattice of the Cu(II)L3 complex is shown in Figure IV.20 based on the three principal planes, a, b, and c. The lattice takes on an alternating zigzag pattern in plane a and con, while the two neighboring structures alternate in a parallel form in plane b

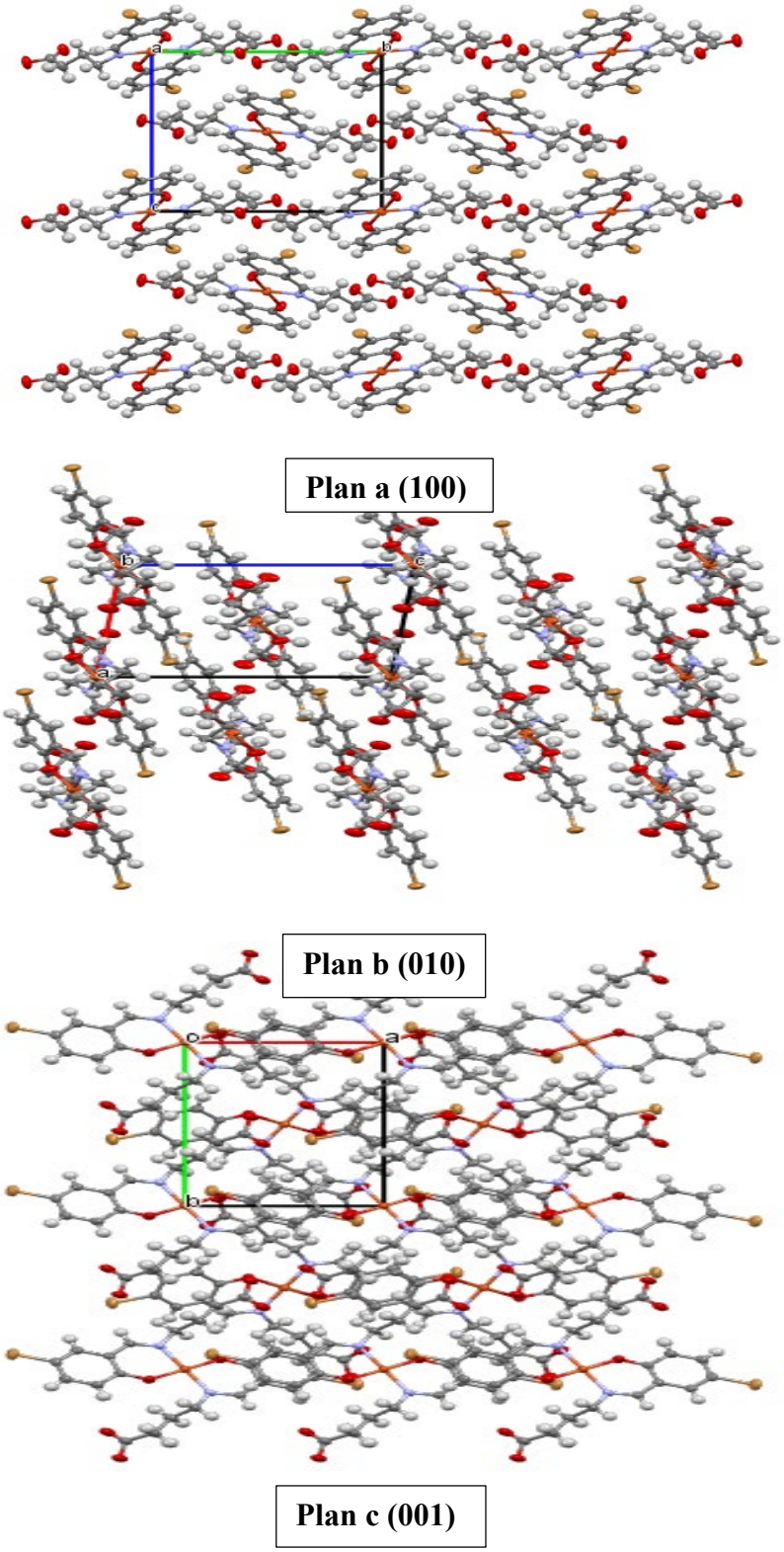

Figure IV.20. Representation of the Cu(II)L3 crystal lattice.

IV.8. Hirshfeld surface analysis

A Hirshfeld surface analysis [22,23] was carried out in order to gain a better understanding of the nature of the stacking in the crystal structures of the Cu(II)L3 copper complex and the ligand (H2L3). This method makes it possible to recognize and examine the intimate relationships that exist between the atoms that make up the crystal. Using Crystal Explorer 3.1, Hirshfeld surfaces are produced with a normalized contact distance (dnorm) that is based on two different types of distances: the exterior distance (de) and the internal distance (di), which span ranges from -0.718 (red) to 1.383 (blue) [22–25].

A close look at the three-dimensional Hirshfeld surface (Figure IV.21) indicates that the O-H hydrogen bond is responsible for the "hot" red spots that are located close to O1, O2, and N1, N2. O, C-H, N, and O-H, C, short-distance connections.

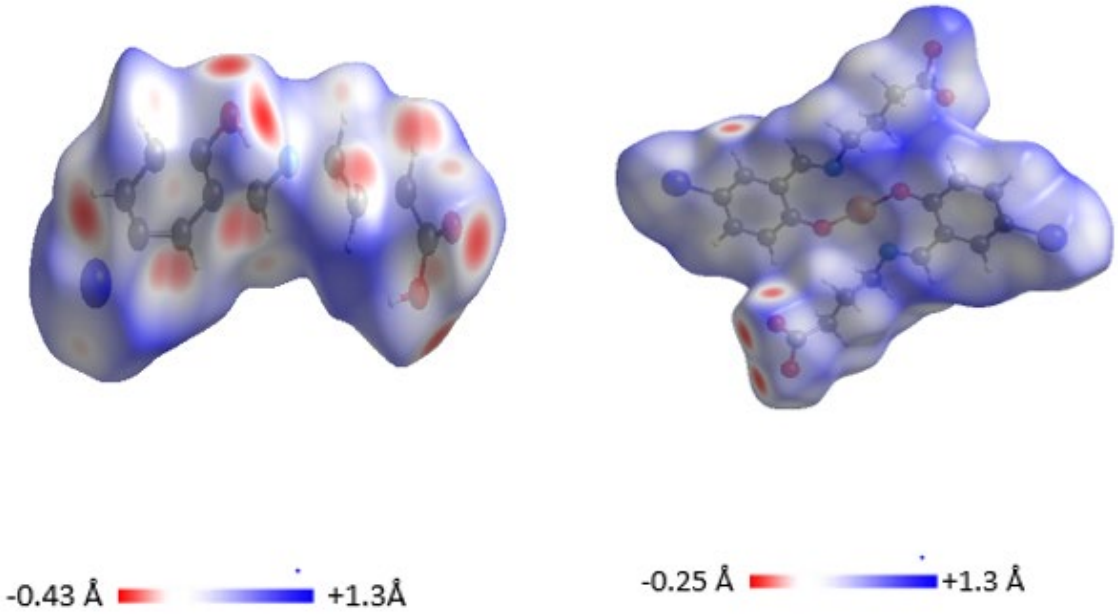

Figure IV.21. Hirshfeld surface of (H2L3) and Cu(II)L3 plotted on dnorm.

With a rate of 36 and 25.3%, respectively, contacts of type H... H (Figure IV.22) in the molecular structure represent the most significant contribution in the surface of interaction of the ligand (H2L3) and Cu(II)L3. An origin-oriented point, with di+de ~ 1.2 Å for H2L3 and ~ 2.4 Å for Cu(II)L3, characterizes these contributions. The normalcy of these contacts is indicated by comparing the distance di +de with the sum of the Van der Waals rays of the bond's atoms (rVdW (H) + rVdW (H) = 1.2+1.2 = 2.4 Å). These interactions are found in the white portions of the surface.

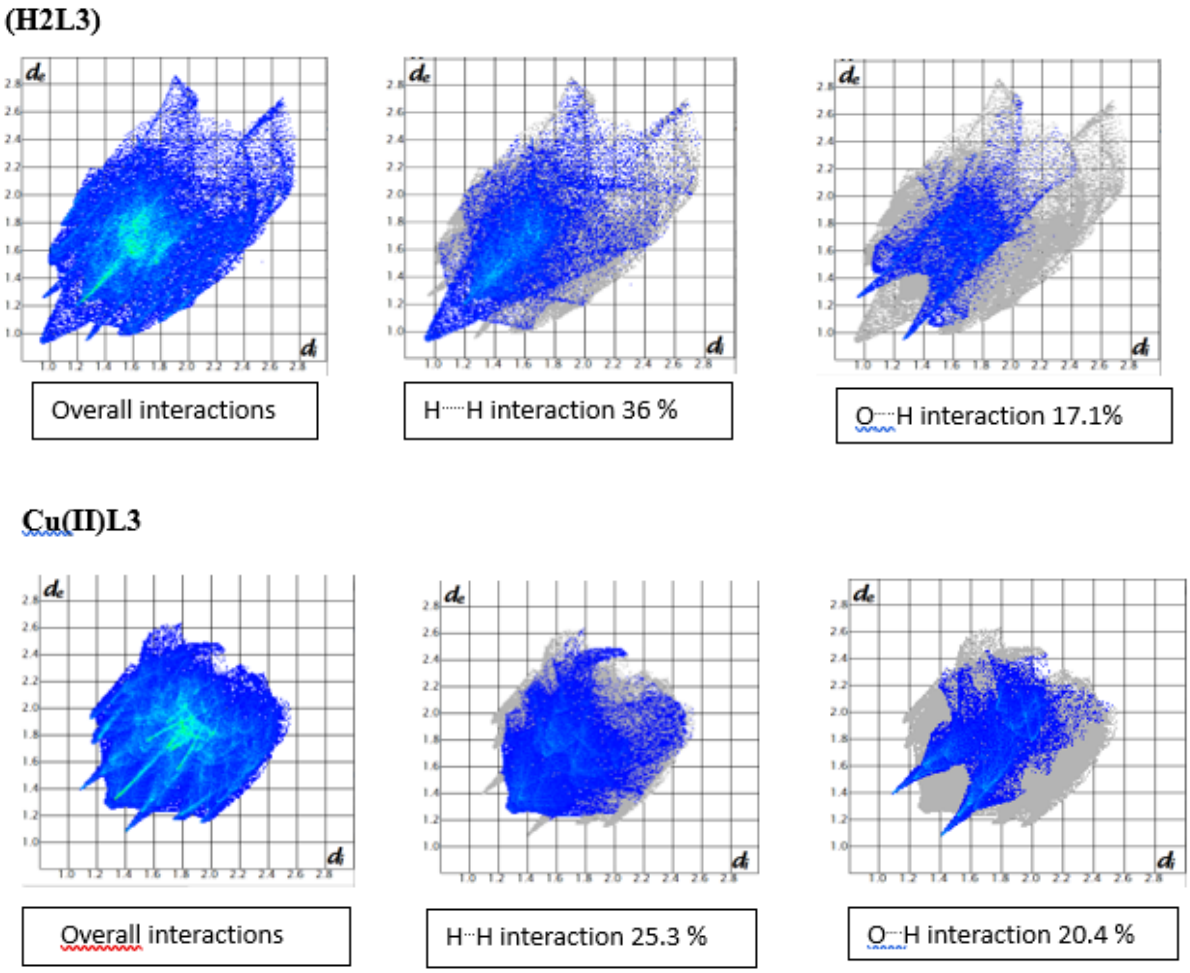

Figure IV.22. Two-dimensional fingerprints of each type of interaction in the structure of (H2L3) and Cu(II)l3.

A two-dimensional fingerprint trace of the Hirshfeld surface of (H2L3) and Cu(II)l3 showed that type contacts H…O/O… H (Figure IV.22) show 17.1% and 20.4% respectively, they are illustrated by two long symmetrical peaks with di+ de ~ 2.4 Å and 2.8 Å for (H2L3) and Cu(II)l3 . This interaction is considered the second strong interaction in the crystal after the interaction of types H…H, this judgment is based on the comparison of di+de with the sum of the Van der Waals rays of the atoms participating in the bond (rVdW (H) + rVdW (O) = 1.2 +1.2 = 2,4 Å et 1.4 +1.4= 2.8 Å). They are indicated by bright red points where the hydrogen interactions O-H… O and O-H… C are located, translated by short distances.

PART II: STRUCTURAL STUDY BY THEORETICAL CALCULATION

IV.9. Quantum chemistry calculations by DFT

A theoretical investigation using the theorem «DFT» and the computation B3LYP/6-311G (d, p) has been added to the practical portion in order to determine certain quantum parameters, such as the partial charge of atoms, the energy of molecular orbitals (HOMO and LUMO), the ion potential, etc. via perhaps identifying the favorable locations that may trigger the response of decreased antioxidant activity. The ligand's ideal molecular structure (H2L3) is depicted in the image below.

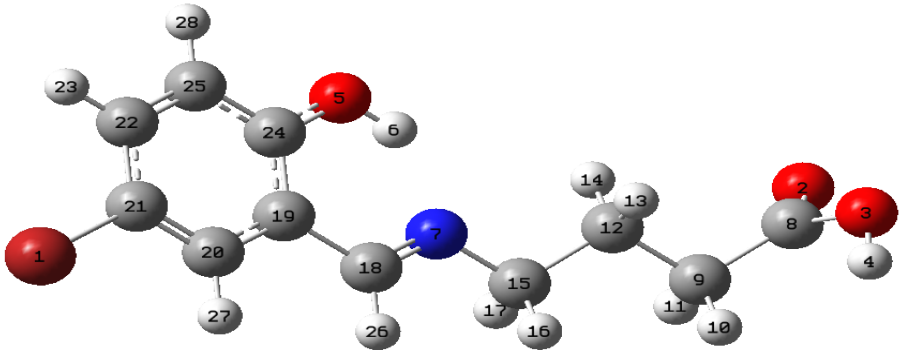

Figure IV.23. Optimal molecular structure of the ligand (H2L3).

IV.9.1. Frontier molecular orbitals (OMF)

It is commonly recognized that HOMO and ionization energy (I) are connected, with the former revealing information about a molecule's locations that are more likely to donate electrons to the right orbital of an acceptor molecule. The electronic affinity (A), on the other hand, which indicates the locations most likely to take electrons from appropriate donor species, is connected to LUMO [26].

The electron distributions computed in the highest occupied molecular orbital (HOMO) and lowest unoccupied molecular orbital (LUMO) are displayed in Figure IV.24. It is evident that the ligand's (H2L3) HOMO energy distribution is mostly dispersed across the aromatic cycle, including the hydroxy group and the brome atom. Conversely, the LUMO includes the whole ligand's aromatic cycle with the imine function.

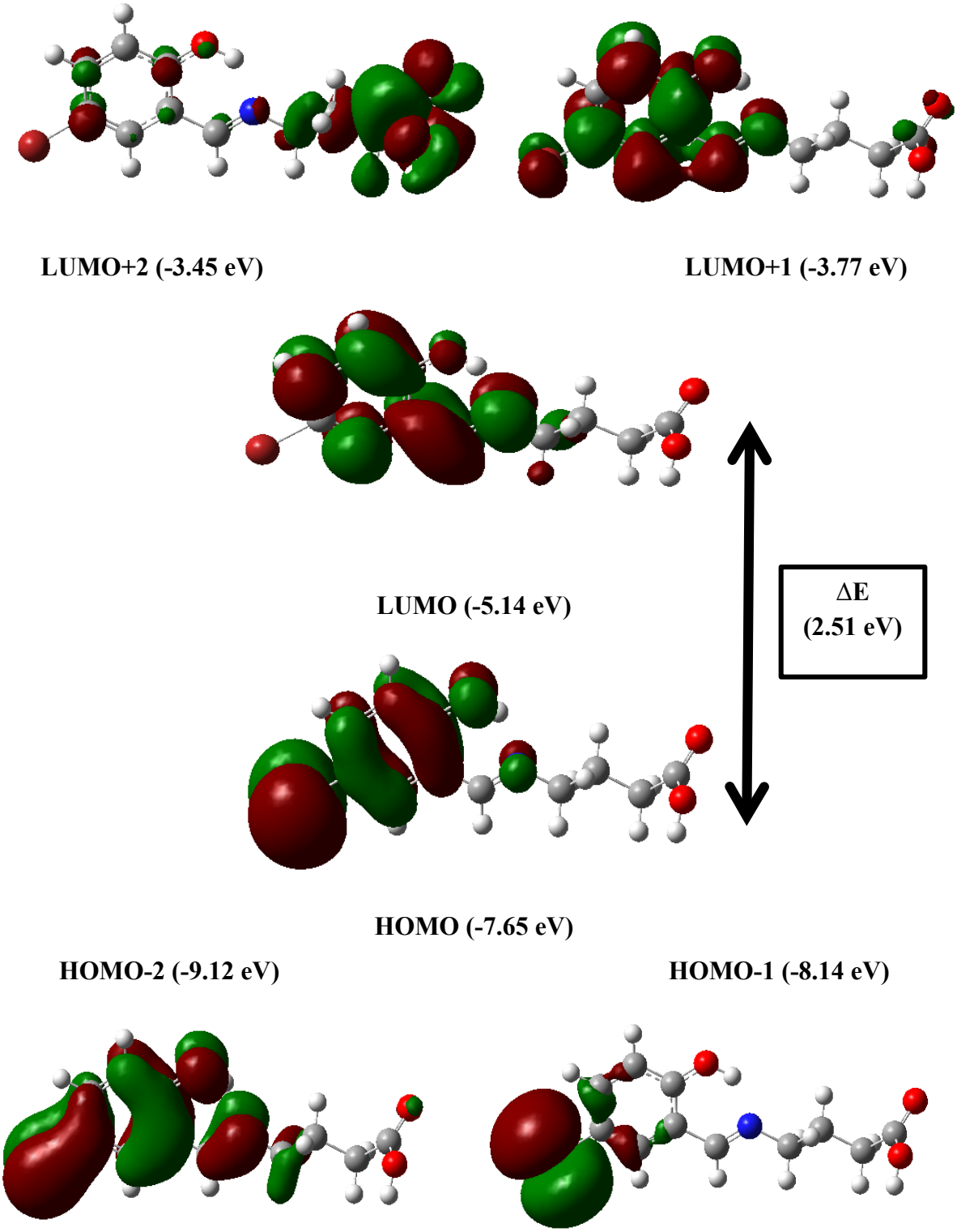

Figure IV.24. HOMO and LUMO molecular orbitals of the H2L3 ligand.

The quantum chemical parameter values calculated for the ligand (H2L3) are collected in Table IV.11.

Table IV.11. Energy of the frontier orbitals (eV) for the ligand (H2L3) at the theoretical level B3LYP/6-311 G.

Energy (eV)	H2L3
E (Homo)	-7.65
E (Lumo)	-5.14
E (gap)	2.51

The results presented in Table IV.11 show that the high value of E(HOMO) (-7.65) shows good efficacy [27].

On the other hand, the low values of E(LUMO)(-5.14) increase the probability that the molecule accepts electrons [28]. The results found from the quantum calculations indicate that the ligand (H2L3) has a low value of the energy difference (ΔE = 2.51 eV). This confirms the reactivity of the studied compound.

Other quantum parameters such as absolute hardness (η) and softness (σ) can influence biological efficiency. The absolute hardness (η) is approximately equal to ΔE/2 and can be defined according to the chemical principle of absolute hardness and softness (HSAB). It provides information on the reactivity of the molecule. A high value of absolute hardness (η) indicates high stability and low reactivity while the high value of softness (σ) shows that the molecule has a high reactivity [29,30].

In addition, the global electrophilic index (ω) is another important parameter that defines the ability of a molecule to accept and/or give electrons, where a high value of (ω) indicates a g ood electrophile (acceptor), while a small value of (ω) suggests a good nucleophilic (donor) [27]. In other words, the ability to acquire electrons to stabilize.

The results show that ligand has a low chemical reactivity. This is in good agreement with the low value of the overall hardness (1.26 eV) and the high value of the global electrophilic index (ω) (16.25) (Table IV.12), which proves that the ligand (H2L3) is a good electrophile. This result corroborates with the literature [29,31].

Table IV.12. Quantum parameters for ligand (H2L1).

Quantum parameters (eV)	Ligand (H_2L3)
Ionization energy I	**7.65**
Electronic affinity A	**5.14**
Chemical potential μ	**-6.40**
Hardness η	**1.26**
Electrophilicity ω	**16.25**
Softness σ	**0.79**
Electronegativity χ	**6.40**

IV.9.2. Mulliken atomic charges

Mulliken charges of atoms is used to determine the distribution of charges in the molecular structure and locate active sites. Table IV.13 groups the Mulliken charges for the ligand (H2L3). Hydrogen atoms and some carbon atoms have positive charges, while nitrogen and oxygen atoms have negative charges. The most negative atoms are: O2, O3, O5 and N7. The latter are active centers in the reactivity of these molecules.

Table IV.13. Mulliken atomic charges calculated for the ligand (H2L3).

Atoms	Mulliken charges	atoms	Mulliken charges
Br 1	**0.425**	**C15**	**-0.546**
O2	**-0.835**	**H16**	**0.366**
O3	**-0.757**	**H17**	**-0.384**
C4	**0.511**	**C18**	**0.184**
O5	**-0.827**	**C19**	**-0.139**
C6	**0.481**	**C20**	**-0.459**
N7	**-0.581**	**C21**	**0.415**
C8	**1.223**	**C22**	**-0.407**
C9	**-0.935**	**H23**	**0.366**
H10	**0.386**	**C24**	**0.600**
H11	**0.392**	**C25**	**-0.467**
C12	**-0.788**	**H26**	**0.331**
H13	**0.387**	**H27**	**0.362**
H14	**0.386**	**H28**	**-0.371**

Table IV.14. Theoretical (B3LPY/ 6-31G (d, p) ligand (H2L3) bond angles.

Liaison	Distance	Liaison	Angle
C1-C2	1.40854	C13-O12-C1	118.71
C1-O12	1.40085	C1-C2-O10	119.20
C2-O10	1.38507	C17-N19-C20	118.97
C13-O12	1.45027	O10-C2-C3	120.33
C17-N19	1.28812	C2-C1-O12	112.93
C20-N19	1.46836	O30-C29-O31	121.70
C29-O30	1.23420	C24-C29-O30	126.99
C29-O31	1.38253	C21-C20-N19	109.73

IV.9.3. Molecular electrostatic potential (MEP)

For molecules, electrostatic potential maps are highly helpful three-dimensional diagrams. They make the molecular characteristics and charge distributions visible. The optimized Gaussian 0.9 geometries' molecular electrostatic potential (MEP) was computed in order to forecast the compounds under study's reactive electrophilic and nucleophilic attack sites. MEP's positive (green) and negative (red and yellow) areas correspond to nucleophilic and electrophilic reactivity, respectively.

Figure IV.28 shows that the oxygen atoms O2, O3, and O5 (shown in red and yellow) are covered in a negative charge. On the remaining ligand atoms (H2L3), however, the positive area was confined. The most reactive component of the complexes is the oxygen atoms' high electronegativity.

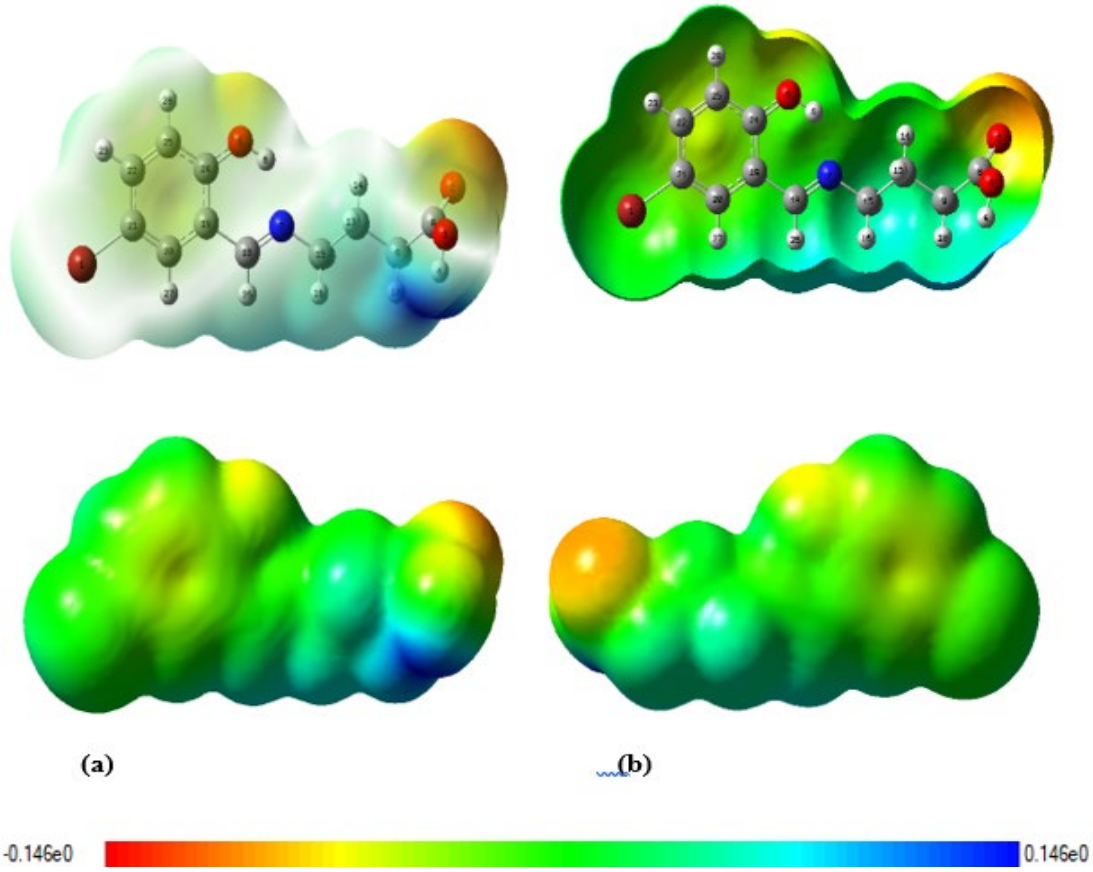

Figure IV.25. Cartograph of the molecular electrostatic potential of ligands H2L3 drawn on surfaces of total density (a): Front view and (b) Rear view.

PART III: BIOLOGICAL STUDY, ANTIOXIDANT PROPERTIES

The creation of novel antioxidant compounds for use in food, medicine, and cosmetics is now of significant interest. Artificially produced compounds possessing anti-oxidant properties can function via many pathways, including as ion reduction, lipid peroxidation suppression, and free radical trapping [32].

Therefore, in order to evaluate this antioxidant activity, several methodologies based on diverse chemical reactions must be used [33].

The DPPH and ABTS assays were employed in this investigation to assess the antioxidant capacity of the ligand (H2L3) and its metal complexes. The findings, which are reported as IC50 (concentrations that trap 50% of free radicals or inhibitory concentrations), are shown in Table IV.15. BHT and BHA were two of the standard compounds employed in the comparison investigation.

Table IV.15. Antioxidant activity of ligand (H2L3) and its two complexes by different methods.

	DPPH IC50 (µg/ml)	ABTS IC50 (µg/ml)
Ligand (H2L3)	316.476	740.747
Mn(II) L3	1348.239	525.651
Cu(II) L3	1914.222	644.606
BHA	6.14±0.41	1.81±0.10
BHT	12.99±0.41	1.29±0.30

IV.10.1. Test du radical DPPH

The percentage of the tested chemicals' trapping effect is displayed in Figure IV.26 together with the BHA and BHT standards'. Ligand (H2L3) has a non-significant capability by contributing to BHA and BHT, and it has a considerable dose-dependent antiradical capacity. It can trap free radicals DPPH• at the micro molar scale.

The ligand (H2L3) rapidly achieves maximum activity at a very low concentration, according to the data, but the two complexes, Mn(II)L3 and Cu(II)L3, take longer to attain maximum activity, but only at low concentrations and with a yield that is regarded as low.

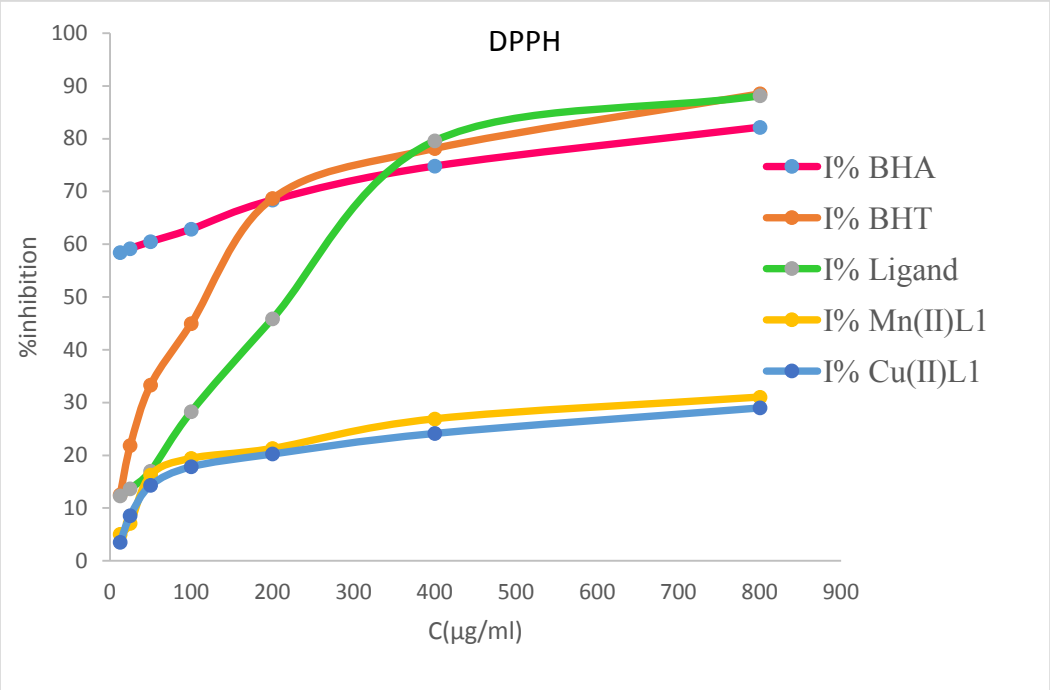

Figure IV.26. Kinetics of the anti-radical activity of the ligand (H2L3) and its metal complexes Mn(II)L3 , Cu(II)L3 with the BHA and BHT standards on the DPPH radical.

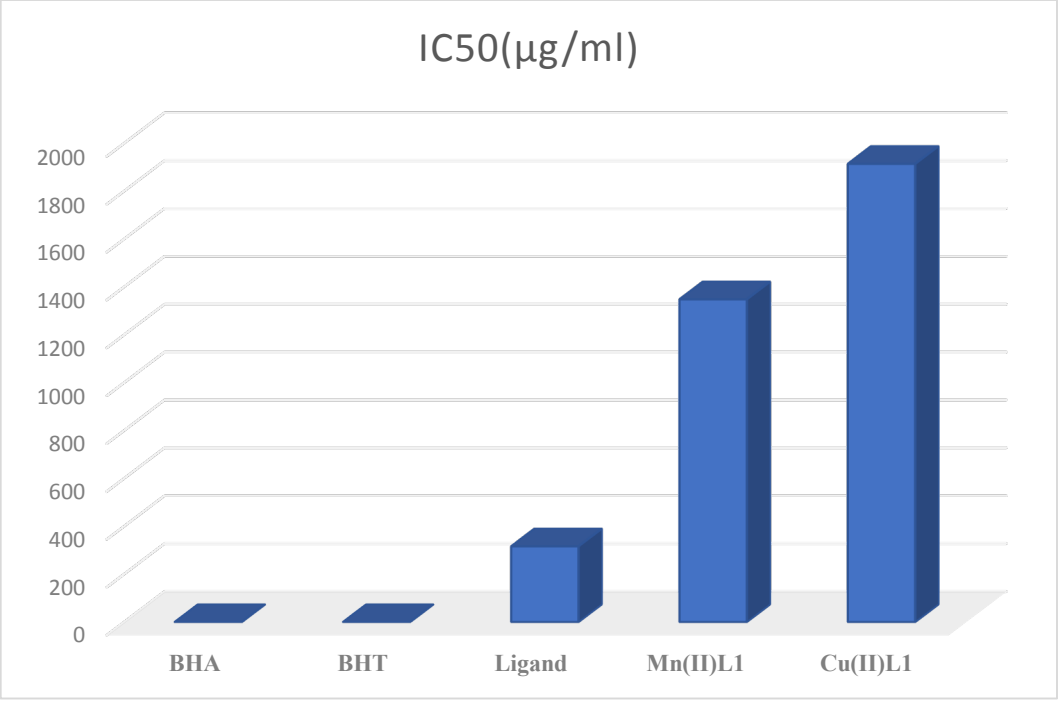

Figure IV.27. IC50 inhibitory concentration values in (µg/ml). Ligand (H2L3), Mn(II)L3 and Cu(II)L3 complexes and BHA and BHT standards.

Based on these findings, it seems that the ligand (H2L3) has a moderate level of antioxidant power, while the complexes of Mn(II)L3 and Cu(II)L3 have much lower levels than those of BHA and BHT, with IC50 values for BHA and BHT being 316.476, 1348.239, 1914.222

(µg/ml), and 6.14, 12.99 (µg/ml), respectively. These findings demonstrate the dose-dependent antioxidant action of the ligand (H2L3). Generally speaking, the chemicals under study's antioxidant activity can be arranged in declining order:

$$Cu(II)L3 < Mn(II)L3 < H2L3 < BHT < BHA$$

The links between structure and activity imply that a molecule's antioxidant capacity is enhanced by a number of structural features. The reducing power of some compounds is dependent on the presence and arrangement of electrodonor and electroattractor groups [34,35]. Our products' ability to trap may be attributed to their O-H (hydroxyl) groups, which have the ability to donate hydrogen to neutralize the DPPH• radical. However, this is not the case for our molecules due to the presence of the aliphatic chain, which breaks the aromaticity of the system and prevents electron mobility. Strong electroattractor groups, such as bromine, fluorine, and nitro, in para position on the phenyl nucleus, will significantly increase the activity of molecules.

IV.10.2. ABTS radical test

The ABTS+ radical was also used to gauge radical activity. The kinetics of (H2L3), Mn(II)L3, and Cu(II)L3, as well as the standards employed to trap this radical, are displayed in Figure IV.31. The ABTS-+ test and the Mn(II)L3 complex show that it has a dose-dependent antioxidant impact; an increase in antioxidant power is shown with an increase in the Mn(II)L3 tested concentrations. Furthermore, even at high concentration values, the Cu(II) complexL3 and its ligand, H2L3, have relatively low power. BHT and BHA had a substantially stronger free radical trapping capacity than the studied compounds, with IC50 values of 740.747, 525.651, and 644.606 (µg/ml) for H2L3, Mn(II)L3, and Cu(II)L3, respectively (Table IV.15).

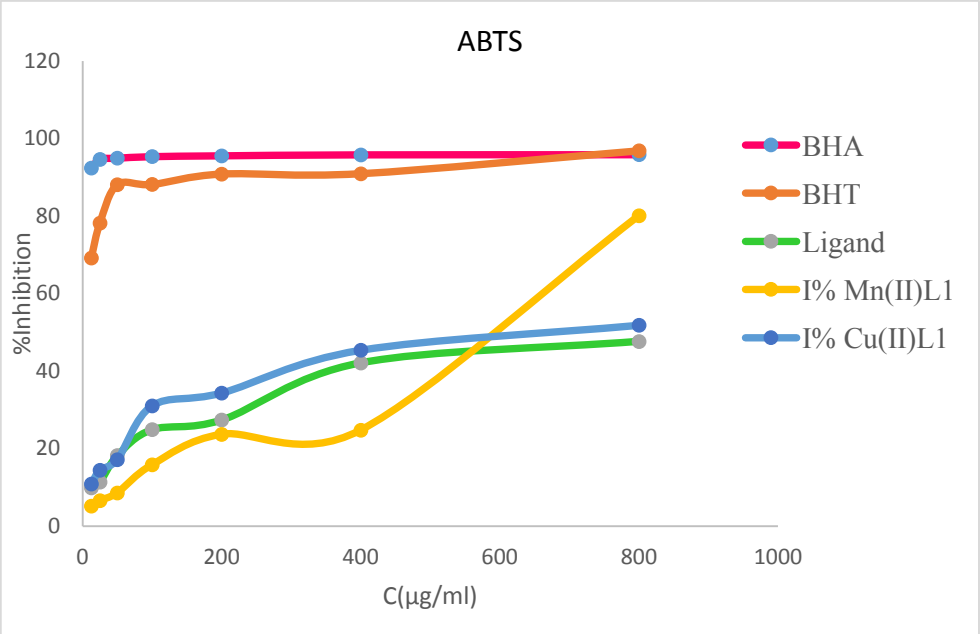

Figure IV.28. Trapping effect of the ABTS+ radical of H2L3, Mn(II)L3, Cu(II)L3 and BHT and BHA standards.

The compound with the highest antioxidant capacity and lowest IC50 value was ligand (H2L3). Its metal complexes, Mn(II)L3, and Cu(II)L3, were next, and they each demonstrated a narrow trapping effect of the radical ABTS (740.747, 525.651, and 644.606 µg/ml) by contribution to the standard BHA and BHT with a large deviation, as seen in figure IV.32 below.

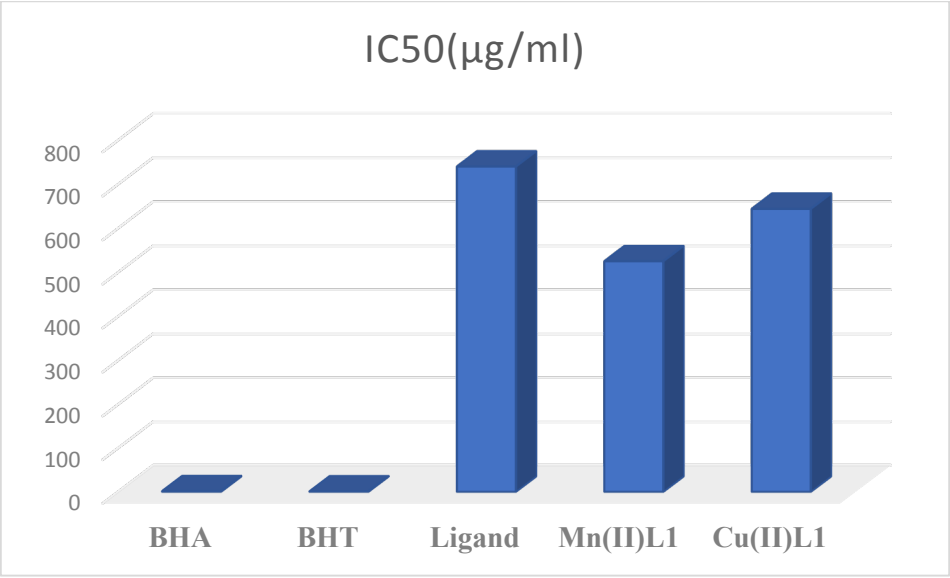

Figure IV.29. IC50 inhibitory concentration values in (µg/ml). Ligand (H2L3), Mn(II)L3 and Cu(II)L3 complexes and BHA and BHT standards towards ABTS.

The two metal complexes, Mn(II)L3 and Cu(II)L3, react better with the radical ABTS+. This is evident when comparing the antioxidant activities of the studied compounds measured by the two methods, DPPH• radical scavenging and ABTS+ radical scavenging. The ligand base of Schiff exerts an antioxidant effect almost in the same order. In conclusion, the electroattractor groups have a strong effect on the non-significant antioxidant activity of all these compounds.

IV.11. Conclusion

The metal complexes Cu(II) and Mn(II) of ligand E-4-((5-bromo-2-hydroxyhybenzylidene)amino)butanoic acid (H2L3) were produced. Both the yields and the quality of the synthesized goods are respectable. We were able to identify and describe every structure using spectral studies (IR, UV/Vis, and 1H-NMR) with cyclic voltammetry. The hypothesized structures are compatible with the interpretation of the various spectra. ligand (H2L3) and the mononuclear complex Cu(II)L3 are produced as single crystals and have undergone extensive structural analysis, which firmly validates the suggested compounds' structures. After a thorough analysis of the molecular structure's Hirshfeld surface, it is evident that the most significant contribution to the interaction surface is made by H... H type interactions.

The potential of antioxidants in vitro has been assessed using several techniques. The results indicated that these compounds have modest antioxidant activity.

References

[1] E. Halevas, A. Hatzidimitriou, B. Mavroidi, M. Sagnou, M. Pelecanou, D. Matiadis, Synthesis and Structural Characterization of (E)-4-[(2-Hydroxy-3-methoxybenzylidene)amino]butanoic Acid and Its Novel Cu(II) Complex, Molbank J. (2021). https://doi.org/https://doi.org/10.3390/1179.

[2] G. Valarmathy, R. Subbalakshmi, Synthesis, characterization and antimicrobial screening of Co(II), Ni(II), Cu(II), Mn(II) and Zn(II) complexes with schiff base derived from 2-sulphanilamidopyridine and 2-Hydroxy-3-methoxybenzaldehyde, Asian J. Chem. 25 (2013) 2077–2079. https://doi.org/10.14233/ajchem.2013.13322

[3] A.N. Al-Hakimi, M.N.R. Alotaibi, N.A. Al-Gabri, J.S. Alnawmasi, Biological evaluation of nano-sized novel Schiff base ligand-based transition metal complexes, Results Chem. 6 (2023) 101107. https://doi.org/10.1016/j.rechem.2023.101107.

[4] P. Deepika, H.M. Vinusha, M. Begum, R. Ramu, P.S. Shirahatti, M.N. Nagendra Prasad, 2-methoxy-4-(((5-nitropyridin-2-yl)imino)methyl)phenol Schiff base ligand and its Cu(II) and Zn(II) complexes: synthesis, characterization and biological investigations, Heliyon 8 (2022) e09648. https://doi.org/10.1016/j.heliyon.2022.e09648.

[5] A.D. Khalaji, S.M. Rad, G. Grivani, D. Das, Nickel(II) and copper(II) complexes with an asymmetric bidentate Schiff-base ligand derived from furfurylamine: Synthesis, spectral, XRD, and thermal studies, J. Therm. Anal. Calorim. 103 (2011) 747–751. https://doi.org/10.1007/s10973-010-1024-1.

[6] I. Bougossa, D. Aggoun, A. Ourari, R. Berenguer, S. Bouacida, E. Morallon, Synthesis and characterization of a novel non-symmetrical bidentate Schiff base ligand and its Ni(II) complex: electrochemical and antioxidant studies, Chem. Pap. 74 (2020) 3825–3837. https://doi.org/10.1007/s11696-020-01200-7.

[7] R. Benramdane, F. Benghanem, A. Ourari, S. Keraghel, G. Bouet, Synthesis and characterization of a new Schiff base derived from 2,3-diaminopyridine and 5-methoxysalicylaldehyde and its Ni(II), Cu(II) and Zn(II) complexes. Electrochemical and electrocatalytical studies, J. Coord. Chem. 68 (2015) 560–572. https://doi.org/10.1080/00958972.2014.994514.

[8] M. Sarigul, S.E. Kariper, P. Deveci, H. Atabey, D. Karakas, M. Kurtoglu, Multi-properties of a new azo-Schiff base and its binuclear copper (II) chelate: Preparation, spectral characterization, electrochemical, potentiometric and modeling studies, J. Mol. Struct. 1149 (2017) 520–529.

[9] M. Sarigul, P. Deveci, M. Kose, U. Arslan, H. Türk Dagi, M. Kurtoglu, New tridentate azo-azomethines and their copper(II) complexes: Synthesis, solvent effect on tautomerism, electrochemical and biological studies, J. Mol. Struct. 1096 (2015) 64–73. https://doi.org/10.1016/j.molstruc.2015.04.043.

[10] G. Saha, K.K. Sarkar, T.K. Mondal, C. Sinha, Synthesis, spectra, structure, redox properties and DFT computation of copper(I)-triphenylphosphine-pyridyl Schiff bases, Inorganica Chim. Acta 387 (2012) 240–247. https://doi.org/10.1016/j.ica.2012.01.030.

[11] A.H. Kianfar, S. Ramazani, R.H. Fath, M. Roushani, Synthesis, spectroscopy, electrochemistry and thermogravimetry of copper(II) tridentate Schiff base complexes, theoretical study of the structures of compounds and kinetic study of the tautomerism reactions

by ab initio calculations, Spectrochim. Acta - Part A Mol. Biomol. Spectrosc. 105 (2013) 374–382. https://doi.org/10.1016/j.saa.2012.12.010.

[12] K. Das, S. Goswami, B.B. Beyene, A.W. Yibeltal, C. Massera, E. Garribba, A. Frontera, Z. Cantürk, T. Askun, A. Datta, Spectral, electrochemical and DFT studies of a trimetallic CuII Derivative: Antimycobacterial and cytotoxic activity, Inorganica Chim. Acta 490 (2019) 155–162. https://doi.org/10.1016/j.ica.2019.03.014.

[13] S. Kumar, A. Hansda, A. Chandra, A. Kumar, M. Kumar, M. Sithambaresan, M.S.H. Faizi, V. Kumar, R.P. John, Co(II), Ni(II), Cu(II) and Zn(II) complexes of acenaphthoquinone 3-(4-benzylpiperidyl)thiosemicarbazone: Synthesis, structural, electrochemical and antibacterial studies, Polyhedron 134 (2017) 11–21. https://doi.org/10.1016/j.poly.2017.05.055.

[14] A. Ourari, A. Alouache, D. Aggoun, R. Ruiz-Rosas, E. Morallon, Electrocatalytical reduction of bromocyclopentane and iodobenzene using Cobalt(III) and Nickel(II) Tris- and Bis-bidentates Schiff Bases Complexes, Int. J. Electrochem. Sci. 13 (2018) 5589–5602. https://doi.org/10.20964/2018.06.39.

[15] A.A. Alothman, E.S. Al-Farraj, W.A. Al-Onazi, Z.M. Almarhoon, A.M. Al-Mohaimeed, Spectral characterization, electrochemical, antimicrobial and cytotoxic studies on new metal(II) complexes containing N2O4 donor hexadentate Schiff base ligand, Arab. J. Chem. 13 (2020) 3889–3902. https://doi.org/10.1016/j.arabjc.2019.02.003.

[16] M. Kuate, E.M. Ngandung, F.A.N. Kamga, A.G. Paboudam, C.A. Mariam, C.N. Pecheu, T.K. Ignas, P.T. Ndifon, Cobalt (II), Nickel (II) and Copper (II) complexes of Tetradentate Schiff base ligands derived from 4-Nitro-O-phenylenediamine: Synthesis, Characterization, cyclic voltammetry and biological studies, Egypt. J. Chem. 65 (2022) 477–495. https://doi.org/10.21608/EJCHEM.2022.82313.4087.

[17] K. Das, G.W. Woyessa, A. Datta, B.B. Beyene, S. Goswami, E. Garribba, A. Frontera, C. Sinha, A Ni(II) derivative incorporating tetradentate Schiff base precursor: Structure, spectral, electrochemical and DFT interpretation, J. Mol. Struct. 1173 (2018) 462–468. https://doi.org/10.1016/j.molstruc.2018.07.027.

[18] M. Merzougui, K. Ouari, J. Weiss, Ultrasound assisted synthesis, characterization and electrochemical study of a tetradentate oxovanadium diazomethine complex, J. Mol. Struct. 1120 (2016) 239–244. https://doi.org/10.1016/j.molstruc.2016.05.046.

[19] M.H. Habibi, E. Askari, Synthesis, structural characterization, thermal, and electrochemical investigations of a square pyramid manganese(III) complex with a Schiff base ligand acting as N2O2 tetradentate in equatorial and as O monodendate in axial positions: Application as a pr, Synth. React. Inorganic, Met. Nano-Metal Chem. 43 (2013) 406–411. https://doi.org/10.1080/15533174.2012.740741.

[20] S. Chahmana, S. Keraghel, F. Benghanem, R. Ruíz-Rosas, A. Ourari, E. Morallón, Synthesis, spectroscopic characterization, electrochemical properties and biological activity of 1-[(4Hydroxyanilino)-methylidene] naphthalen-2(1H)-one and its Mn (III) complex, Int. J. Electrochem. Sci. 13 (2018) 175–195. https://doi.org/10.20964/2018.01.27.

[21] S. Zolezzi, E. Spodine, A. Decinti, Electrochemical studies of copper(II) complexes with Schiff-base ligands, Polyhedron 21 (2002) 55–59. https://doi.org/10.1016/S0277-5387(01)00960-3.

[22] M.A. Spackman, D. Jayatilaka, Hirshfeld surface analysis, CrystEngComm 11 (2009)

19–32. https://doi.org/10.1039/b818330a.

[23] W. ZEMAMOUCHE, Elaboration et caractérisation des produits organiques à intérêt biologique substitués par des méthyles et des halogènes ., 2021.

[24] S. Boukhssas, Y. Aouine, H. Faraj, A. Alami, A. El Hallaoui, N. Tijani, K. Yamni, H. Zouihri, D. Mrani, M. Lachkar, Hirshfeld Surface Analysis and DFT calculations of 1-phenyl-N-(benzomethyl)-N-({1-[(2-benzo-4-methyl-4,5-dihydro-1,3-oxazol-4-yl)methyl]-1H-1,2,3-triazol-4-yl}methyl)methanamine, J. Mater. Environ. Sci 9 (2018) 2254–2262. http://www.jmaterenvironsci.com.

[25] H. Chebbi, A. Boumakhla, M.F. Zid, A. Guesmi, Crystal structure and thermal and Hirshfeld surface analyses of 4-azaniumyl-2,2,6,6-tetramethylpiperidin-1-ium diperchlorate, Acta Crystallogr. Sect. E Crystallogr. Commun. 73 (2017) 1453–1457. https://doi.org/10.1107/S2056989017012695.

[26] S. Janeoo, Reenu, A. Saroa, R. Kumar, H. Kaur, Computational investigation of bioactive 2,3-diaryl quinolines using DFT method: FT- IR, NMR spectra, NBO, NLO, HOMO-LUMO transitions, and quantum-chemical properties, J. Mol. Struct. 1253 (2022) 132285. https://doi.org/10.1016/j.molstruc.2021.132285.

[27] Y. Yan, W. Li, L. Cai, B. Hou, Electrochemical and quantum chemical study of purines as corrosion inhibitors for mild steel in 1 M HCl solution, Electrochim. Acta 53 (2008) 5953–5960. https://doi.org/10.1016/j.electacta.2008.03.065.

[28] M. Murmu, S.K. Saha, N.C. Murmu, P. Banerjee, Effect of stereochemical conformation into the corrosion inhibitive behaviour of double azomethine based Schiff bases on mild steel surface in 1 mol L−1 HCl medium: An experimental, density functional theory and molecular dynamics simulation study, Corros. Sci. 146 (2019) 134–151. https://doi.org/10.1016/j.corsci.2018.10.002.

[29] A. Dutta, S.K. Saha, P. Banerjee, A.K. Patra, D. Sukul, Evaluating corrosion inhibition property of some Schiff bases for mild steel in 1 M HCl: Competitive effect of the heteroatom and stereochemical conformation of the molecule, RSC Adv. 6 (2016) 74833–74844. https://doi.org/10.1039/c6ra03521c.

[30] M.R. Noor El-Din, E.A. Khamis, Corrosion inhibition efficiency, electrochemical and quantum chemical studies of some new nonionic surfactants for carbon steel in acidic media, J. Surfactants Deterg. 17 (2014) 795–805. https://doi.org/10.1007/s11743-014-1565-6.

[31] S. Vikneshvaran, S. Velmathi, Interfacial Properties of Electron-Donating and Electron-Withdrawing Group-Substituted Chiral Schiff Bases on Mild Steel Corrosion in 1 M Hydrochloric Acid Solution, J. Bio- Tribo-Corrosion 3 (2017). https://doi.org/10.1007/s40735-017-0079-y.

[32] D.R. Joshi, N. Adhikari, An Overview on Common Organic Solvents and Their Toxicity, J. Pharm. Res. Int. 28 (2019) 1–18. https://doi.org/10.9734/jpri/2019/v28i330203.

[33] F. Chemat, M. Abert Vian, H.K. Ravi, B. Khadhraoui, S. Hilali, S. Perino, A.-S. Fabiano Tixier, Review of alternative solvents for green extraction of food and natural products: Panorama, principles, applications and prospects, Molecules 24 (2019) 3007.

[34] I.C.F.R. Ferreira, M.-J.R.P. Queiroz, M. Vilas-Boas, L.M. Estevinho, A. Begouin, G. Kirsch, Evaluation of the antioxidant properties of diarylamines in the benzo [b] thiophene series by free radical scavenging activity and reducing power, Bioorg. Med. Chem.

Lett. 16 (2006) 1384–1387.

[35] F.C. Torres, N. Brucker, S. Fernandes Andrade, D. Fabio Kawano, S. Cristina Garcia, G. Lino von Poser, V. Lucia Eifler-Lima, New insights into the chemistry and antioxidant activity of coumarins, Curr. Top. Med. Chem. 14 (2014) 2600–2623.

GENERAL CONCLUSION

General conclusion

In this work three new Schiff base compounds: 2,2'-((1E,E')-(bis(azanylylidene)bis(methanylylidene)bis(bis(4-bromophenol)(2-hydroxypropane-1,3 diyl) (H2L1), 2,2'-((1E,11E)-5,8-dioxa-2,11-diazdecaado-1,12-diyl) (H2L2), E-4-(5-bromo-2-hydroxybenzhyylidene)amino)butanoic acid (H2L3) were synthesized by simple methods with good yields and characterized by the usual spectroscopic methods UV-vis, IR, RNM 1H and 13C.

Additionally, the transition metal complexes of copper (II), manganese (II), zinc (II), and cobalt (II) were produced and studied using infrared and ultraviolet-visible spectroscopy techniques. The synthetic complexes have high melting points and are all solid and stable in the presence of air and ambient temperature. We were able to draw attention to the structures of the produced compounds via the use of these analytical procedures.

Cyclic voltammetry, based on the metal center, indicates that the process of oxidation and reduction of active sites is mono-electronic. Redox systems show reversibility of load transfers.

The crystallographic findings unequivocally demonstrate that the azomethine group's and the phenolic hydroxyl group's nitrogen donor sites are used in the coordination of the metal ions.

In order to comprehend the crystalline stack and determine the intermolecular interactions that maintain the cohesiveness of our crystal, a thorough examination of the Hirshfeld surface is provided. The most significant contribution to the interaction surface is represented by H... H type contacts, according to a thorough analysis of the Hirshfeld surface of the molecular structure..

The investigation of non-linear optical properties on the ligand (H2L2) shows a good answer.

Theoretical calculations using the Functional Theory of Density (DFT) method are performed to determine the optimized electronic structure for ligands. Load transfers are modelled in order to compare the results with the available experimental data.

Les tois séries de base de Schiff et ses complexes ont été testés in vitro pour évaluer leur activité antioxydante à l'aide des méthodes de piégeage des radicaux libres dont le test de DPPH et de ABTS ou ils sont montrés une très faible activité antioxydante.

The basic series of Schiff and its complexes were tested in vitro to assess their antioxidant activity using free radical trapping methods including DPPH and ABTS test or they showed very low antioxidant activity.

Abstract

Three series of Schiff base ligands were synthesized by a 5-bromo-2-hydroxybenzaldehyde condensation reaction with three different amines. The structural determinations were identified using UV-vis, FT-IR and 1H ,13C spectroscopic analysis. The products were obtained with excellent yields. Prepared Schiff bases have been used as tetradentate and bidentate ligands to coordinate Co(II), Cu(II), Mn(II) and Zn(II) that lead to complexes with a metal/ligand ratio of 1:1 and 1:2. The electrochemical properties of metal complexes were conducted by cyclic voltametry in DMF. The molecular structure of the single crystals obtained for certain compounds was also determined by the DRX diffraction technique on single crystals. Hirshfeld's surface analysis provided information about the existing interactions in the structure of the two products, and helped to view and understand its crystalline stacking. Theoretical calculations using the Functional Theory of Density (DFT) method were performed. The investigation of non-linear optical properties on the ligand (H2L2) shows a good answer. investigations carried out on the antioxidant capacities of our products were made from in-vitro experiments against the free radicals DPPH and ABTS.

Keywords: Schiff base, Crystallography, DFT ,X-ray diffraction, Antioxidant activity, Non-linear optical properties.

Résumé

Trois séries de ligands bases de Schiff ont été synthétisés par une réaction de condensation de 5-bromo-2-hydroxybenzaldehyde avec trois amines différentes. Les déterminations structurelles ont été identifiées à l'aide d'une analyse spectroscopiques UV-vis, FT-IR et RMN 1H ,13C. Les produits ont été obtenus avec d'excellents rendements. Les bases de Schiff préparées ont été utilisées comme des ligands tétradentates et bidentate pour coordonner Co(II) , Cu(II),Mn(II) et Zn(II) qui mènent aux complexes avec un rapport métal /ligand de 1:1 et 1:2. Les propriétés électrochimiques des complexes métalliques ont été menées par voltamétrie cyclique dans le DMF. La structure moléculaire des monocristaux obtenus pour certains composés a été également déterminée par la technique de diffraction DRX sur monocristal. L'analyse de la surface de Hirshfeld a fourni des informations sur les interactions existantes dans la structure des deux produits, et aidé à visionner et à comprendre son empilement cristallin. Des calculs théoriques utilisant la méthode de la théorie fonctionnelle de la densité (DFT) ont été effectues. L'investigation des propriétés optiques non linéaire, sur le ligand (H2L2) montre une bonne réponse . des investigations réalisées sur les capacités antioxydantes de nos produits ont été faites à partir des expériences in-vitro envers les radicaux libres DPPH et ABTS.

Mots clés : Base de Schiff , Cristallographie , Diffraction des rayons X, DFT, Activité antioxydant , Propriétés optique non linéaire .

:الملخص

تم تصنيع ثلاث سلاسل من ربيطات قاعدة شيف بواسطة تفاعل تكثيف 5-bromo-2-hydroxybenzaldehyde مع ثلاثة أمينات مختلفة. تم تحديد التحديدات الهيكلية باستخدام التحليل الطيفي للأشعة فوق البنفسجية و FT-IR و 13C1, H. تم الحصول على المنتجات بعوائد ممتازة. تم استخدام قواعد Prepress Schiff كرباط رباعي وبيدنتات لتنسيق II) Co) و II) Cu) و II) Mn) و II) Zn) التي تؤدي إلى مجمعات بنسبة معدن/رباط 1:1 و 1:2. تم إجراء الخصائص الكهروكيميائية للمجمعات المعدنية بواسطة قياس الفولتاميك cy-clique في DMF. كما تم تحديد البنية الجزيئية للبلورات المفردة التي تم الحصول عليها لبعض المركبات من خلال تقنية حيود DRX على بلورات مفردة. قدم تحليل سطح هيرشفيلد معلومات حول التفاعلات الحالية في بنية المنتجين، وساعد في عرض وفهم تكديسه البلوري. أجريت الحسابات النظرية باستخدام طريقة النظرية الوظيفية للكثافة (DFT). يُظهر التحقيق في الخصائص البصرية غير الخطية على الربيطة (H2L2) إجابة جيدة. تم إجراء التحقيقات التي أجريت على القدرات المضادة للأكسدة لمنتجاتنا من التجارب المختبرية ضد الجذور الحرة DPPH و ABTS.

الكلمات المفتاحية: قاعدة شيف، علم البلورات، حيود الأشعة السينية، نشاط مضادات الأكسدة، الخصائص البصرية غير الخطية